High-Resolution Geophysical Images of Static Crustal Structure and Time-Dependent Glacier Flow

Thesis by
Minyan Zhong

In Partial Fulfillment of the Requirements for the
Degree of
Doctor of Philosophy

CALIFORNIA INSTITUTE OF TECHNOLOGY
Pasadena, California

2022
Defended September 2, 2021

Minyan Zhong
ORCID: 0000-0002-1382-7061

ACKNOWLEDGEMENTS

It takes a village to produce a PhD, and there are many people I am indebted to. First of all, I want to thank my advisors and my thesis committee. I feel truly fortunate and thankful for working with Mark Simons who introduced me to the exciting world of satellite geodesy and glaciology. Mark is so all-rounded and experienced in research that I wish I had more discussions with him. I will miss all those mind-opening, encouraging, and fun conversations (geophysics and beyond) between us. I am particularly grateful for his patience and trust in me when we were facing unexpected problems and offering me much freedom to explore my embryonic ideas. I am truly indebted to Zhongwen Zhan who advised me on my seismological project. Working with Zhongwen was an invaluable experience to me. His passion for research, attention to detail, and creativity in solving problems always inspire me. I feel genuinely grateful to him for fostering my growth along the way. I would like to thank Rob Clayton and Andy Thompson for being on my thesis committee and being supportive whenever I needed help. Thanks to Rob for signing all my "blue cards" and giving me constructive suggestions on my projects and thesis. Thanks to Andy for the helpful comments on my research from the perspective of oceanography and pointing me to related studies. In addition, I also want to thank all the other faculty members at Seismolab and GPS. I learned a lot from their classes and research.

I am thankful to Rosemary Miller, Donna Mireles, Priscilla McLean, Kim Baker-Gatchalian, and many other staff at Seismolab. I especially want to thank Scott Dungan who was always responsive to resolving any issues on our servers and patient to answer all my questions.

The engineering aspect of satellite geodesy was involved to me early on, thus my research would not be possible without the help from many people. I have much thanks to Heresh Fattahi, Piyush Agram, and Cunren Liang for answering my many questions about SAR processing and explaining to me all the tricks/issues in the data processing package. My special thanks go to Lijun Zhu for his great work on our computational tool and discussions on many topics of high-performance computing.

I am also indebted to many people who helped me in thinking about problems in glaciology. Much thanks to Brent Minchew for always having enlightening and encouraging discussions with me no matter how busy he was. Much thanks to Victor

Tsai for a number of illuminating conversations which deepened my understanding of the problems I worked on. I am also thankful to the "glacier reading group" and all the glaciologists I met. Those discussions certainly broadened my horizon.

Over the past few years, I was fortunate to meet many outstanding postdocs and graduate students in the lab whom I learn from and work with. My special thanks go to Bryan Riel who is so kind and helpful, sharing his rich experience in various technical fields to me before and after his graduation. I thank Yunjun Zhang for introducing me to his helpful tools and sharing his experience. I also want to thank Xin Wang for his great following work of my seismological project.

The work presented in chapter 3 and 4 is possible due to the availability of raw COSMO-SkyMed SAR imagery provided by the Italian Space Agency (ASI) as part of two dedicated campaigns to image Rutford and Evans Ice Streams, respectively. I sincerely thank ASI for all their efforts in making these two campaigns successful. The work in chapter 4 also contains modified Copernicus Sentinel 1a and 1b SAR data openly provided by the European Space Agency (ESA) whom I sincerely thank as well.

My thanks go to all the friends, and current and former students at Caltech who are so important and made my stay here enjoyable. I want to thank my current and former officemates: Zhe, Xiaolin, Ollie, Vish, Erin, Ojashvi, and Vasilije for all the entertaining moments. I want to thank Zhichao, Siteng, Hao, Kangchen, Voon, Jorge, Jiashun, Junle, Yingdi, Dunzhu, Yiran, Han, and many others, for all the activities and memorable moments. I also thank the GPS softball team with whom I enjoyed fun playtimes over two summers.

I also want to thank Christina, Dennis, and their two cats and one dog. I lived with them for three years in southwest San Gabriel Valley where I enjoyed the yard, peaceful community, and wonderful food.

I am thankful to many professors back at Peking University who taught me the basics of science and engineering. I am deeply thankful to my advisor Shiyong Zhou who gave me huge support during my undergraduate research and recommended me to pursue a PhD program abroad.

My deep gratitude goes to my parents, whom I can never thank enough for their unconditional love, for always looking out for me and believing in my decisions, for their dedication and sacrifices to give me a sweet childhood and providing me with the best possible education.

Finally, my very special thanks to dear Shujuan, who fills my life with countless happiness. Her love, understanding, and encouragement are priceless. It is my great fortune to have her companion in the past and many more years to come.

ABSTRACT

The emerging availability of high-quality geophysical observations motivates the development of new methodologies to better extract the key information contained in the datasets. In this thesis, I present methodological developments utilizing two types of geophysical data. Firstly, in Chapter 2, I make use of the observations recorded at the newly-available dense seismic arrays and propose a new method for estimating the seismic receiver functions (RFs). RFs have been widely used in global seismology to probe the structural discontinuities in the interior of the Earth. By exploiting the coherency in RFs at neighboring stations, the new method adds the RF coherency as a key constraint in RF estimation, which directly addresses issues such as non-uniqueness and over-fitting in conventional ways for RF estimations. I show a pilot application of this method to real data that demonstrates its advantages on obtaining high-quality RFs on short-term (e.g., one month) high-density seismic profiles. Secondly, in Chapter 3 and Chapter 4, I take advantage of the temporally dense Synthetic-Aperture-Radar (SAR) imagery. In these two main chapters of my thesis, I focus on understanding the temporal variations in the buttress stress of Antarctic ice shelves and develop new methodologies for observing tidally-induced ephemeral grounding of ice shelves on the sub-shelf bathymetric highs. This observational study provides new insights into the buttressing effect of ice shelves and improves our understanding of the dynamics of Antarctic ice flow including the short-term (days to weeks) response to tidal forcing and the long-term (tens to hundreds of years) response to changes in climate. Specifically, in Chapter 3, I illustrate the methodological development and an application to Rutford Ice Stream (RIS), West Antarctica; in Chapter 4, I further apply the new methods to Evans Ice Stream (EIS), an ice-stream-shelf system significantly larger than the RIS with multiple upstream tributaries and complex grounding line. At both RIS and EIS, I find abundant zones of ephemeral grounding in the vicinity of the grounding zone. These two studies provide direct evidence for the asymmetric response of ice flows to tidal forcing, which causes the observed strong fortnightly variation in horizontal flow. With the projected oceanic warming, our observations of ephemeral grounding will help quantify the increase in ice flow rate in the long-term caused by the loss of buttressing stress due to ice-shelf thinning.

PUBLISHED CONTENT AND CONTRIBUTIONS

Zhong, M., M. Simons, and L. Zhu (n.d.[a]). Tidally induced sub-shelf ephemeral grounding and fortnightly variation in flow rate at Evans Ice Stream, West Antarctica. In prep.
M.Z. participated in the conception of the project, developed the methodology, processed the data, and wrote the manuscript.

Zhong, M., M. Simons, L. Zhu, and B. Minchew (n.d.[b]). Tidally induced sub-shelf ephemeral grounding at Rutford Ice Stream, West Antarctica, inferred from remotely sensed observations. In prep.
M.Z. participated in the conception of the project, developed the methodology, processed the data, and wrote the manuscript.

Zhu, L., **M. Zhong**, and M. Simons (n.d.). cuAmpcor—A GPU accelerated pixel tracking for offset estimation in satellite geodesy. In prep.
M.Z. participated in developing the software and writing the manuscript.

Wang, X., Z. Zhan, **M. Zhong**, P. Persaud, and R. W. Clayton (2021). Urban basin structure imaging based on dense arrays and bayesian array-based coherent receiver functions. In: *Journal of Geophysical Research: Solid Earth* 126.9, e2021JB022279. ISSN: 2169-9356. DOI: 10.1029/2021JB022279.
M.Z. participated in the initiation of the project.

Fielding, E. J., Z. Liu, O. L. Stephenson, **M. Zhong**, C. Liang, A. Moore, S.-H. Yun, and M. Simons (2020). Surface deformation related to the 2019 Mw 7.1 and 6.4 Ridgecrest earthquakes in California from GPS, SAR interferometry, and SAR pixel offsets. In: *Seismological Research Letters* 91.4, pp. 2035–2046. ISSN: 0895-0695. DOI: 10.1785/0220190302.
M.Z. participated in processing the data and making figures.

Zhong, M. and Z. Zhan (2020). An array-based receiver function deconvolution method: methodology and application. In: *Geophysical Journal International* 222.1. ISSN: 1365246X. DOI: 10.1093/gji/ggaa113.
M.Z. participated in the conception of the project, developed the methodology, processed the data, and wrote the manuscript.

Ross, Z., B. Idini, Z. Jia, O. Stephenson, **M. Zhong**, X. Wang, Z. Zhan, M. Simons, E. Fielding, S.-H. Yun, E. Hauksson, A. Moore, Z. Liu, and J. Jung (2019). Hierarchical interlocked orthogonal faulting in the 2019 Ridgecrest earthquake sequence. In: *Science* 366.6463. ISSN: 10959203. DOI: 10.1126/science.aaz0109.
M.Z. participated in processing the data and making figures.

TABLE OF CONTENTS

LIST OF ILLUSTRATIONS

LIST OF TABLES

Chapter 1

INTRODUCTION

Better geophysical observations of the Earth are crucial in enhancing the knowledge of many fundamental problems in Earth system, including the origin and mechanisms of natural hazards, the search for and sustainable use of natural resources, and environmental responses to climate changes. Seismological and geodesic observations are two important categories of geophysical data. Studies utilizing seismic observations can depict the Earth's interior structures and earthquakes rupture process. Studies based on geodetic observations reveal the space-time evolution of surface deformation associated with various geophysical phenomena, including seismic cycles, tides, sub-surface migration of magma and water, etc.

The availability of high-quality observations is a fundamental catalyst for advances in geophysical studies. Large sizes of datasets are currently being generated via various types of geophysical tools, including dense networks of seismometers, distributed acoustic sensing systems, earth-orbiting satellites, dense networks of GPS observations, etc. In thesis, I focus on two types of geophysical observations—the spatially dense seismic-array observations and temporally dense synthetic-aperture-radar (SAR) observations. For the seismic-array observations, there have been continuous efforts to improve the spatial resolution through deployment of dense seismic arrays, to increase the number seismic stations, and to decrease the station spacing (Figure 1.1a-d). For SAR observations, which guarantee high spatial resolution, improving the temporal resolution of SAR observations has always been a desire of the community. Last two decades have seen continuous decrease in the revisit time of SAR acquisitions. With the rapid increase in SAR missions, jointly using observations from multiple sensors can provide even higher temporal resolution (Figure 1.1e-h).

These two types of emerging datasets (Figure 1.2) offer new opportunities for obtaining geophysical observations at unprecedented spatial and temporal resolutions. However, to extract key information from these datasets, often required are new methodologies based on specific geophysical problems. The new methodologies can take advantage of the data redundancy to reduce uncertainty in estimation or can model more detailed information in the data to reveal complex geophysical

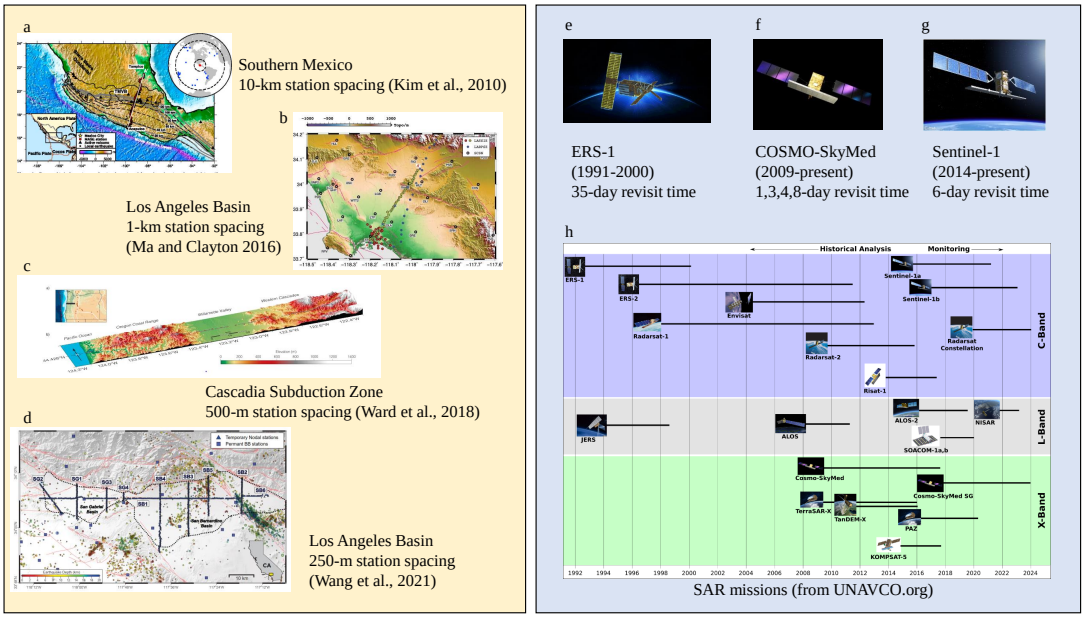

Figure 1.1: The emerging seismic and SAR observations. (a-d) The increase in the number of stations and decrease in the station spacing of dense seismic array profiles (Kim et al., 2010;Ma and Clayton, 2016;Ward et al., 2018;Wang et al., 2021). (e-g) The decrease in the revisit time of SAR observations. (h) SAR missions from 1990s to 2020s.

processes. In this thesis, I present two lines of study in which the methodological development plays a key role:

1. I propose a new technique in reflection seismology to image the structural discontinuities in Earth interior using seismic data recorded by dense nodal arrays. I demonstrate this technique by applying it to a dense network of seismic nodes in Oklahoma basin, and provide high-resolution images of the shallow sedimentary structures (Chapter 2).

2. I develop a new method employing a nonlinear time-dependent 3-D displacement model to identify and quantify tidally-induced ephemeral grounding of ice shelves on sub-shelf bathymetric highs in Antarctica, using dense Synthetic-Apeature Radar (SAR) imagery. I apply this method to two main ice-shelf-stream systems in west Antarctica and reveal abundant undocumented zones of ephemeral grounding. The observation of ephemeral grounding improves our understanding of the buttressing effect of ice shelves (Chapter 3 and Chapter 4).

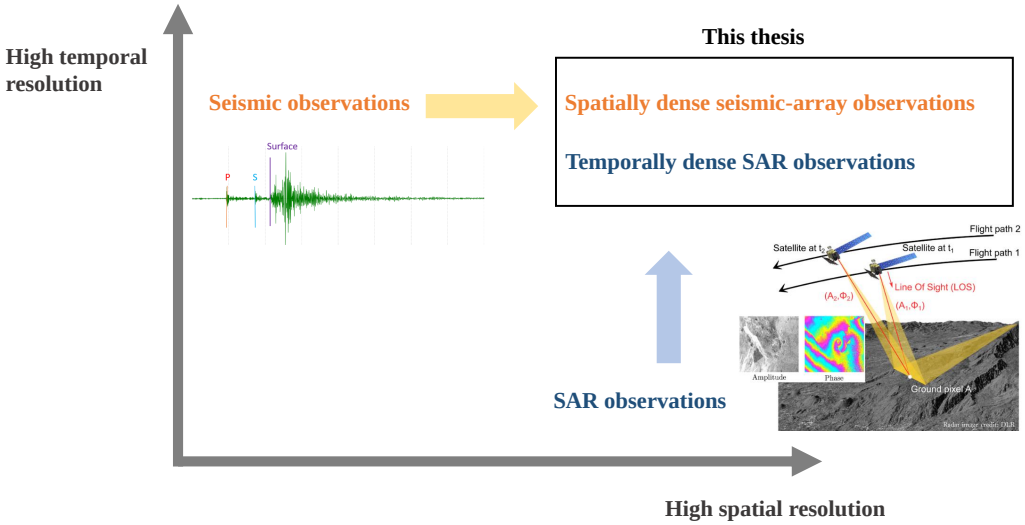

Figure 1.2: The characteristics of emerging seismic and SAR observations—increasing spatial resolution in seismic observations and increasing temporal resolution in SAR observations.

Chapter 2 is adapted from a published paper (Zhong and Zhan, 2020). For this new technique on reflection seismology proposed in this chapter, the presented imaging of the sedimentary structure in the Oklahoma basin is a pilot application. There is a follow-up work of this method that includes its optimization and further applications (Wang et al., 2021).

The main parts of this thesis are the methodology and the applications in Chapter 3 and Chapter 4 to study tide-induced sub-shelf ephemeral grounding in Antarctica. These two chapters are adapted from two manuscripts in preparation for submission as Zhong et al. (n.d.[b]) and Zhong et al. (n.d.[a]). Because we use the same methodology in Chapter 3 and Chapter 4, the methodology section in Chapter 4 is a brief review of that in Chapter 3.

In Chapter 2, I present our study on developing an array-based receiver function deconvolution method for improving the imaging of subsurface structures from emerging dense seismic-array datasets. Receiver function (RF) is an indispensable tool in global seismology to probe the structural discontinuities in Earth interior. The most widely used classical teleseismic P-wave RF isolates receiver-side structures from source and path effects by deconvolving vertical component from radial

component of recorded seismograms at one station to highlight the P-wave-to-S-wave conversions at structural discontinuities (e.g., Vinnik, 1977, Langston, 1979, Ammon, 1991). In this study, I focus on improving RF estimation along a dense profile of stations, a common layout of seismic experiments to get a cross-section of target areas (e.g., Nábelek et al., 2009, Kim et al., 2010, Ma and Clayton, 2016). The conventional practice is that RFs are estimated independently at individual stations, and are then combined to form a 2-D RF profile. The coherent phases on the profile are then tracked and interpreted as structural discontinuities. However, due to the ill-posedness of deconvolution, or more specifically non-uniqueness and data over-fitting, RFs often include spurious phases and are difficult to interpret.

I propose a new array-based RF deconvolution method towards improving RF estimation on dense arrays. Its main characteristic is to exploit the coherency of RFs at neighboring stations on dense-arrays. The advantages of exploiting coherency in RFs in the estimation stage are two folds: (1) The new constraint of coherency in RFs serves as a regularization in RF estimation which significantly reduces the non-uniqueness and over-fitting in estimation. (2) The estimated RFs only include coherent phases which makes the interpretation easier and benefits the following imaging process using the estimated RFs (e.g., migration of RFs). I first present the methodology including the inverse problem setup and the algorithm for parameter estimation. Then, I show a synthetic test, where I compare this new method with conventional RF practices. Finally, I present a real data application to the 2016 IRIS community wavefield experiment in Oklahoma, where I show the challenges the dataset poses to convention RF practices and how they are overcome by the new method.

In Chapter 3, I switch to satellite geodesy and glaciology to observe tide-induced ephemeral grounding of ice shelf on sub-shelf bathymetric highs and discuss the implications of the observed zones of ephemeral grounding for the dynamics of Antarctic ice flow. The Antarctic Ice Sheet is fringed with floating ice shelves which have contact with sub-shelf bathymetric highs that generate resistive back stress to tributary ice flows (e.g., Thomas, 1979, Gudmundsson, 2013). This resistive stress, often referred to as buttressing stress, plays an important role in regulating Antarctic ice flows (e.g., Joughin et al., 2012, Pritchard et al., 2012). It is interesting to understand how temporal variations in the buttressing stress may impact the tributaries. For instance, short-term (days to weeks) variations in buttressing stress induced by ocean tides have been proposed as an underlying mechanism to generate

strong fortnightly flow rate variation at Rutford Ice Stream (RIS), West Antarctica (Minchew et al., 2017, Robel et al., 2017). Tide-induced ephemeral grounding of ice shelves on sub-shelf bathymetric highs which modulates the buttressing stress is considered as an important underlying mechanism for this phenomenon.

In this study, I develop a new nonlinear time-dependent 3-D displacement model that explicitly accounts for ephemeral grounding in the vertical displacement to infer zones of ephemeral grounding from dense SAR imagery. The full workflow of our methodology includes two displacement models: a 3-D linear displacement model which is based on modification to the linear model used in Minchew et al. (2017) for indirectly inferring zones of ephemeral grounding, and our new 3-D nonlinear displacement model that both directly infers and quantifies the process of ephemeral grounding. The workflow of our methodology starts from the linear model, then constructs the nonlinear model using the results derived from the linear model and an independent ocean tidal model, and finally solves for vertical displacements with ephemeral grounding and horizontal flow variability.

I revisit the temporally dense 9-month long SAR dataset collected over RIS by the COSMO-SkyMed 4-satellite constellation which was used in Minchew et al. (2017). By applying our new methodology, I infer zones of ephemeral grounding as well as the spatial-temporal variation of the fortnightly flow variability. I find zones of ephemeral grounding along the western ice-shelf margin as well as a few prominent ephemeral grounding points in the central trunk of ice shelf and the vicinity of the grounding zone. Our observations provide key evidence for tide-modulated buttressing stress and the temporally asymmetric response of ice-shelf flow to tidal forcing at RIS. In the long-term, with projected ice-shelf thinning, we should expect that RIS will accelerate if the ice shelf thins sufficiently that the ephemeral grounding zones I have identified remain permanently ungrounded over the tidal cycle. Besides inferring ephemeral grounding, the new methodology also produces improved estimates of secular velocity and fortnightly flow variation at RIS which are of higher resolution and contain less artfacts compared with the reported values in Minchew et al. (2017).

In Chapter 4, I apply the methodology developed in Chapter 3 to Evans Ice Stream (EIS), West Antarctica, to infer zones of ephemeral grounding and horizontal fortnightly flow variability. Both EIS and RIS are tributary ice streams of Filchner-Ronne Ice Strean (FRIS). The California-sized FRIS situated at Weddell Sea is subjected to the largest ocean tides in Antarctica. The strong fortnightly flow vari-

ability which was first observed at RIS (Gudmundsson, 2006) was later proved to present over the entire FRIS and all adjoining ice streams (Rosier et al., 2017) including EIS by spatially sparse GPS observations. EIS and RIS, both situated on the Zumberge Coast, experience very similar tidal forcing. EIS is a significantly larger ice stream than RIS with multiple upstream tributaries and a complex grounding line. Unlike those ice streams adjoining the southern portion of FRIS, EIS is located at relatively low latitude, so it is well covered by the ongoing right-looking SAR systems (e.g., Sentinel-1 and COSMO-SkyMed). Therefore, it is both interesting and viable to expand the observation to EIS to investigate the existence and influence of zones of ephemeral grounding.

I jointly use synthetic aperture radar data (SAR) collected over EIS by Sentinel-1 two-satellite constellation and COSMO-SkyMed four-satellite constellation over a 4-year temporal coverage from 2017 to 2021. Our study, for the first time, provides complete maps of zones of ephemeral grounding zones and spatial variability of fortnightly flow variability at EIS. The inferred zones of ephemeral grounding have prevalent existence in the vicinity of the grounding zone which are the new observational evidence for the asymmetric response of the ice-shelf flow to tidal forcing at EIS. The spatial variability of fortnightly flow variability exhibits similarity with that at RIS, but the modulation of fortnightly flow rate on secular flow rate is smaller at EIS than RIS suggesting the intrinsic asymmetry in tidal response is smaller at EIS.

This inferred zones of ephemeral at EIS corroborate the observations at RIS and demonstrate that the asymmetric response to tidal forcing is not unique to a single ice stream. The abundant zones of ephemeral grounding at RIS and EIS suggest the potential of tide-induced ephemeral grounding playing an important role in explaining fortnightly flow variability over the entire FRIS. Our study motivates similar observations at other ice-shelf-stream systems and the central trunk of FRIS. The accumulation of such observations will be crucial in advancing our understanding of the buttressing effect of ice shelves and help make more realistic projections of long-term dynamic response of ice flow to ice shelf thinning at FRIS and beyond.

In summary, both lines of work in this thesis, though in distinct fields, propose new methodologies to extract key information from the emerging datasets. The proposed RF method is motivated by the recent rapid deployment of ultra-dense seismic networks. The proposed nonlinear 3-D displacement model to infer zones of ephemeral grounding over ice shelves is enabled by the recently available temporally dense SAR datasets. Our two lines of studies contribute to the respective field

and show the possibility of pushing the limits of datasets through methodological developments. Chapter 5 contains my closing thoughts on the experiences with developing and applying the methodologies as well as possible follow-up work of our studies.

BIBLIOGRAPHY

Ammon, C. J. (1991). The isolation of receiver effects from teleseismic P waveforms. In: *Bulletin of the Seismological Society of America* 81.6, pp. 2504–2510. ISSN: 0037-1106.

Gudmundsson, G. H. (2013). Ice-shelf buttressing and the stability of marine ice sheets. In: *The Cryosphere* 7.2, pp. 647–655. ISSN: 1994-0424. DOI: 10.5194/tc-7-647-2013.

Gudmundsson, G. H. (2006). Fortnightly variations in the flow velocity of Rutford Ice Stream, West Antarctica. In: *Nature* 444.7122, pp. 1063–1064. ISSN: 0028-0836. DOI: 10.1038/nature05430.

Joughin, I. et al. (2012). *Ice-sheet response to oceanic forcing*. DOI: 10.1126/science.1226481.

Kim, Y. et al. (2010). Geometry and seismic properties of the subducting Cocos plate in central Mexico. In: *Journal of Geophysical Research* 115.B6, B06310. ISSN: 0148-0227. DOI: 10.1029/2009JB006942.

Langston, C. A. (1979). Structure under Mount Rainier, Washington, inferred from teleseismic body waves. In: *Journal of Geophysical Research* 84.B9, p. 4749. ISSN: 0148-0227. DOI: 10.1029/JB084iB09p04749.

Ma, Y. and R. W. Clayton (2016). Structure of the Los Angeles Basin from ambient noise and receiver functions. In: *Geophysical Journal International* 206.3, pp. 1645–1651. ISSN: 0956-540X. DOI: 10.1093/gji/ggw236.

Minchew, B. M. et al. (2017). Tidally induced variations in vertical and horizontal motion on Rutford Ice Stream, West Antarctica, inferred from remotely sensed observations. In: *Journal of Geophysical Research: Earth Surface* 122.1, pp. 167–190. ISSN: 21699003. DOI: 10.1002/2016JF003971.

Nábelek, J. et al. (2009). Underplating in the Himalaya-Tibet collision zone revealed by the Hi-CLIMB experiment. In: *Science (New York, N.Y.)* 325.5946, pp. 1371–4. ISSN: 1095-9203. DOI: 10.1126/science.1167719.

Pritchard, H. D. et al. (2012). Antarctic ice-sheet loss driven by basal melting of ice shelves. In: *Nature* 484.7395, pp. 502–505. ISSN: 00280836. DOI: 10.1038/nature10968.

Robel, A. A. et al. (2017). "Tidal modulation of ice shelf buttressing stresses". In: *Annals of Glaciology*. Vol. 58. 74. Cambridge University Press, pp. 12–20. DOI: 10.1017/aog.2017.22.

Rosier, S. H. R. et al. (2017). Strong tidal variations in ice flow observed across the entire Ronne Ice Shelf and adjoining ice streams. In: *Earth System Science Data* 9.2, pp. 849–860. ISSN: 1866-3516. DOI: 10.5194/essd-9-849-2017.

Thomas, R. H. (1979). The dynamics of marine ice sheets. In: *Journal of Glaciology* 24.90, pp. 167–177. ISSN: 0022-1430. DOI: 10.3189/s0022143000014726.

Vinnik, L. (1977). Detection of waves converted from P to SV in the mantle. In: *Physics of the Earth and Planetary Interiors* 15.1, pp. 39–45. ISSN: 0031-9201. DOI: 10.1016/0031-9201(77)90008-5.

Wang, X. et al. (2021). Urban basin structure imaging based on dense arrays and bayesian array-based coherent receiver functions. In: *Journal of Geophysical Research: Solid Earth* 126.9, e2021JB022279. ISSN: 2169-9356. DOI: 10.1029/2021JB022279.

Ward, K. M. et al. (2018). High-Resolution Receiver Function Imaging Across the Cascadia Subduction Zone Using a Dense Nodal Array. In: *Geophysical Research Letters* 45.22, pp. 12, 218–12, 225. ISSN: 0094-8276. DOI: 10.1029/2018GL079903.

Zhong, M. and Z. Zhan (2020). An array-based receiver function deconvolution method: methodology and application. In: *Geophysical Journal International* 222.1. ISSN: 1365246X. DOI: 10.1093/gji/ggaa113.

Zhong, M. et al. (n.d.[a]). Tidally induced sub-shelf ephemeral grounding and fortnightly variation in flow rate at Evans Ice Stream, West Antarctica. In prep.

Zhong, M. et al. (n.d.[b]). Tidally induced sub-shelf ephemeral grounding at Rutford Ice Stream, West Antarctica, inferred from remotely sensed observations. In prep.

Chapter 2

AN ARRAY-BASED RECEIVER FUNCTION DECONVOLUTION METHOD FOR IMPROVING THE IMAGING OF SUBSURFACE STRUCTURAL DISCONTINUITIES

Abstract

Receiver functions (RFs) estimated on dense arrays have been widely used for the study of Earth structures across multiple scales. However, due to the ill-posedness of deconvolution, RF estimation faces challenges such as non-uniqueness and data over-fitting. In this chapter, we present an array-based RF deconvolution method in the context of emerging dense arrays. We propose to exploit the wavefield coherency along a dense array by joint inversions of waveforms from multiple events and stations for RFs with a minimum number of phases required by data. The new method can effectively reduce the instability of deconvolution and help retrieve RFs with higher fidelity. We test the algorithm on synthetic waveforms and show that it produces RFs with higher interpretability than those by the conventional RF estimation practice. Then we apply the method to real data from the 2016 Incorporated Research Institutions for Seismology (IRIS) community wavefield experiment in Oklahoma and are able to generate high-resolution RF profiles with only three teleseismic earthquakes recorded by the temporary deployment. This new method should help enhance RF images derived from short-term high-density seismic profiles.

2.1 Introduction

Receiver function (RF) has been an indispensable tool in global seismology. The classical teleseismic P-wave RF isolates receiver-side structures from source and path effects by deconvolving vertical component (Z) from radial component (R) (e.g., Vinnik, 1977, Langston, 1979, Ammon, 1991). RF has been applied routinely to study crustal and upper mantle structures, such as basins, Moho, and subduction zones (e.g., Zhu and Kanamori, 2000, Nábelek et al., 2009, Nikulin et al., 2009, Levander et al., 2011, Ma and Clayton, 2016). The classical RF has also been generalized to longer periods and S waves, to study the Lithosphere-Asthenosphere-Boundary (LAB) and the mantle transition zones (e.g., Fischer et al., 2010, Miller

and Agostinetti, 2012, Tauzin et al., 2013). In particular, wide applications of RF on dense arrays have pushed Earth structure images to unprecedented resolutions (e.g., IRIS Portable Array Seismic Studies of the Continental Lithosphere (PASSCAL) experiments in U.S., Tibet, and South America, and the EarthScope Transportable and Flexible arrays; Eagar et al., 2011, Levander and Miller, 2012, Kumar et al., 2012, Shen et al., 2013, Tauzin et al., 2013, Schulte-Pelkum and Mahan, 2014).

In this chapter, we focus on RF estimation along a dense profile of stations, a common layout of seismic experiments to get a cross-section of target areas (e.g., Nábelek et al., 2009, Kim et al., 2010, Ma and Clayton, 2016). The conventional practice is that RFs are estimated independently at individual stations and are then combined to form a 2-D RF profile. The coherent phases on the profile are then tracked and interpreted as structural discontinuities. To improve the RF resolution, it is common to stack individual RFs obtained from many events that share similar receiver-side structural responses. In RF imaging, the next step is to relate RFs to physical structures through migrating or inverting RFs for reflectivity and velocity models. (e.g., Ammon et al., 1990, Dueker and Sheehan, 1997, Zhu and Kanamori, 2000, Gilbert et al., 2003, Xu et al., 2013). The new method we present here is solely on RF estimation using arrays, not on deriving reflectivity or velocity models from the RFs.

Although dense-array RFs are widely used to reveal Earth discontinuities, it is well known that obtaining high-resolution RF profiles is far from being trivial and sometimes challenging. This reason is often related to the ill-posedness of deconvolution, or more specifically non-uniqueness and data over-fitting. As a result, RFs often include spurious phases and are difficult to interpret. These issues related to RF deconvolution have been widely recognized and there have been many efforts in overcoming the challenges, which we summarize as the following three categories:

1. Procedures for data and RF quality controls, especially for (semi-) automated systems. For example, the IRIS EARS project has a conservative system rating the RFs (Crotwell and Owens, 2005). Yang et al. (2016) developed a RF quality control system with 13 procedures. The chosen criteria need to account for the time span of seismic experiments as well as the quantity and quality of available data.

2. Improved algorithms to stabilize the RF deconvolution. The most classical

one is water-level spectral division (Clayton and Wiggins, 1976). The multi-taper approach provides optimal spectra estimates by suppressing stochastic effects thus further improving spectral division (Park and Levin, 2000). Time-domain iterative deconvolution is probably the most widely used RF method these days, due to its simplicity, robustness at suppressing ringing effects, and ability to obtain consistent RFs from events of different source spectra (Ligorría and Ammon, 1999). Gurrola et al. (1995) performed the time-domain deconvolution as a regularized simultaneous inversion of a group of events, to improve stability and suppress artifacts. Recently, more sophisticated statistical deconvolution methods are proposed, involving Bayesian inference and time series sparsity modeling (Yildirim et al., 2010, Kolb and Leki, 2014).

3. Stacking and post-processing of RFs. Stacking has been the most common approach to improve RF quality. RFs estimated from a group of events sharing receiver-side structural response are combined, often through some kind of averaging, to produce the stacked one with random noise suppressed. When it comes to RFs on dense arrays, RF post-processing can be another way towards the same goal. For example, Wilson and Aster (2005) applied frequency-wavenumber (FK) filter to 2D RF profiles to promote spatial coherency. On a dense nodal seismic array, Ward et al. (2018) averaged individual RFs within 10km to suppress noise and produce coherent RF images.

In this chapter, we propose a new RF deconvolution method towards improving RF estimation on dense arrays. Its main characteristic is to exploit the coherency of dense-array RFs. Figure 2.1 is a schematic example of an RF dense array experiment. The incoming teleseismic P wave converts to S wave at structural discontinuities. Because of the small station spacing, RFs at nearby stations correspond to similar ray paths and are coherent. The coherency exists for laterally smooth discontinuities, as well as sharp features such as offsets/steps in discontinuities or scatters due to wave diffraction. Therefore, as long as the station spacing is substantially smaller than the depth of structures, the coherency of nearby RFs is maintained.

We will demonstrate that the adoption of coherency can effectively address instabilities in deconvolution. Intuitively, this is because the noise (e.g., instrumental/ambient noise, scattering from shallow/local heterogeneities) are incoherent, while the waveforms constraining RF phases are coherent. Requiring RF to be spatially coherent on a dense array naturally excludes the incoherent parts of waveforms from estimation. Problems, such as non-uniqueness and over-fitting, which

are essentially related to noise, are thus largely suppressed. Although the idea of combining the power of dense array to RFs is not new, most previous array-based RF methods are actually on how to better translate RFs to subsurface structures (e.g., Dueker and Sheehan, 1997, Bostock and Rondenay, 1999, Chen et al., 2005). For these methods, RFs as the input are assumed to be generated from some standardized procedures. In exploration seismology, multichannel deconvolution has been established (e,g,, Wapenaar et al., 2011). However, in global seismology, deconvolution on dense-arrays has not systematically moved into an array-based fashion. The aforementioned FK filtering approach (Wilson and Aster, 2005) is an early work touching this possibility but focused on post-processing of RFs. The method we propose treats RF coherency more rigorously by integrating it into RF deconvolution.

To include RF coherency into estimation, we cast RF deconvolution as an inverse problem, in which the deconvolution at a single station involves the nearby stations to provide constraints. We design the inverse problem to be sparsity-promoting by parameterizing RFs as a finite number of coherent phases and seek the optimal solution with the minimum number of phases required by data. We also jointly invert seismic data from multiple events, instead of stacking individual RFs, for better stability and rigorous treatment of data uncertainty (Gurrola et al., 1995). We adopt the Bayesian formulation of inverse problem which provides the model posterior probability distribution. The optimal RF and RF uncertainties are indicated by the maximum a posteriori (MAP) estimation and marginal distributions of parameters.

The structure of the chapter is as follows. We first present the methodology in section 2, including the inverse problem setup and the algorithm for parameter estimation. In section 2.3, we show a synthetic test, where we compare this new method with conventional RF practices. Section 4 is a real data application to the 2016 IRIS community wavefield experiment in Oklahoma, where we show the challenges the dataset poses to convention RF practices and how they are overcome by the new method.

2.2 Methodology

2.2.1 Inverse Problem Setup: Single-Station Deconvolution

We first describe the inverse problem formulation of single-station deconvolution. It lays down the foundation for the extension to the array-based version in section 2.2. We start from the simplest form of P-wave RF. Given a pair of vertical and

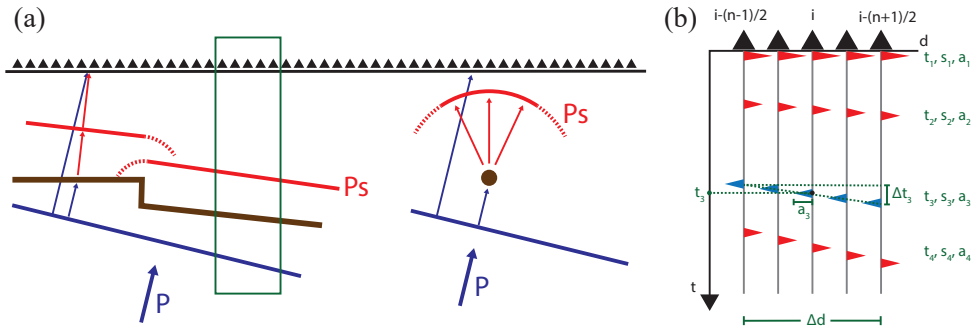

Figure 2.1: Coherency of receiver functions on dense arrays. (a) Teleseismic P wave (blue) impinges on subsurface structures below a dense seismic profile, including a step along a velocity discontinuity (brown thick lines to the left) and a single scatterer (the brown dot to the right), and generates Ps conversions (red). Due to wave diffraction, the Ps phase recorded by the dense array should be coherent at neighboring stations. (b) Illustration of coherent RFs for the five-station subarray outlined by the green box in (a). Each coherent RF phase is parameterized by timing t, slowness s, and amplitude a. For example, t_3, s_3, and a_3 characterize the negative coherent phase where $s_3 = \Delta t_3/\Delta d$.

radial component of seismic records at a single station, the problem of P-wave RF deconvolution can be expressed in frequency domain as:

$$R(\omega) = Z(\omega)E(\omega) + N(\omega) \tag{2.1}$$

where R, Z, and E are the spectra of the radial component, the vertical component, and the RF respectively, and N is the spectrum of noise in the radial component. We parameterize the RF by a finite number of delta functions with different amplitudes and timings. Similar parametrization has been widely used in RF methods and proves useful in producing consistent RFs from events of various source spectra (e.g., Ligorría and Ammon, 1999, Kolb and Leki, 2014, Wang et al., 2016). With this parameterization, $E(\omega)$ can be written as:

$$E(\omega; a_i, t_i) = \sum_{i=1}^{m} a_i \exp(-i\omega t_i) \tag{2.2}$$

where m is the number of phases, and t_i and a_i are the timing and amplitude of the i-th spike. For simplicity, we ignore the normalization factor in the Fourier transform, which is eventually cancelled out in deconvolution. Using equation (2.2), we can rewrite equation (2.1) as:

$$R(\omega) = Z(\omega) \sum_{i=1}^{m} a_i \exp(-i\omega t_i) + N(\omega). \tag{2.3}$$

We can then solve for the RF parameters t_i, a_i $(i = 1, 2, \cdots, m)$ by minimizing the squared misfit of data and model prediction if m is known:

$$\text{argmin} \left\| R(\omega) - Z(\omega) \sum_{i=1}^{m} a_i \exp(-i\omega t_i) \right\|_2^2 . \tag{2.4}$$

We can find the optimal m through approaches such as L-curve (e.g., Hansen, 1992) or cross-validation (e.g., Aster et al., 2018).

2.2.2 Inverse Problem Setup: Array-Based Deconvolution

Array-based deconvolution is built upon the single-station formulation with the consideration of RF coherency. Here, we assume that any specific RF phase has constant amplitude and slowness across a subarray (Figure 2.1b). With this assumption, deconvolution at a particular station involves a subarray of stations to provide constraints. For each phase, besides timing and amplitude, now we have an additional parameter, slowness (s). For a subarray with n stations, the spectrum of RF at the j-th station $(j = 1, 2, \cdots, n)$ is:

$$E_j(\omega) = \sum_{i=1}^{m} a_i \exp(-i\omega(t_i + s_i(x_j - x_c))) \tag{2.5}$$

where x_j and x_c are the coordinates of station j and the center station. Therefore, the array version of (2.3) for the j-th station is

$$R_j(\omega) = Z_j(\omega) \sum_{i=1}^{m} a_i \exp(-i\omega(t_i + s_i(x_j - x_c))) + N_j(\omega) \ (j = 1, 2, \cdots, n). \tag{2.6}$$

Putting all the n stations within the subarray together, we can write (2.6) into matrix form

$$\mathbf{R} = \mathbf{Z}\mathbf{E}(\boldsymbol{\theta}) + \mathbf{N}. \tag{2.7}$$

Here, $\mathbf{R} = [\mathbf{R}_1^T, \mathbf{R}_2^T, \cdots, \mathbf{R}_n^T]^T$ is a column vector formed by concatenation of the spectra of the radial components at the n stations, where $\mathbf{R}_j (1 \le j \le n)$ is a column vector of the spectrum of the radial component at the j-th station. $\mathbf{Z} = [\mathbf{Z}_1^T, \mathbf{Z}_2^T, \cdots, \mathbf{Z}_n^T]^T$ is a diagonal matrix filled by the spectra of the vertical components at the n stations where $\mathbf{Z}_j (1 \le j \le n)$ is a column vector of the spectrum of the vertical component at the j-th station. $\mathbf{E} = [\mathbf{E}_1^T, \mathbf{E}_2^T \cdots, \mathbf{E}_n^T]^T$ is a column vector formed by concatenation of the spectra of the n RFs. The RF spectra are parameterized by $\boldsymbol{\theta}$: t_i, s_i and a_i $(i = 1, 2, \cdots, m)$ through equation (2.5).

We adopt the Bayesian formulation of inverse problem (Tarantola, 2005). Assuming zero-mean Gaussian uncertainties and uniform priors for all parameters, we have the model posterior probability distribution

$$P(\boldsymbol{\theta}|\mathbf{R}) \propto P(\mathbf{R}|\boldsymbol{\theta}) = \exp(-\frac{1}{2}(\mathbf{R} - \mathbf{ZE}(\boldsymbol{\theta}))^T \mathbf{C}_d^{-1}(\mathbf{R} - \mathbf{ZE}(\boldsymbol{\theta}))) \tag{2.8}$$

where $\mathbf{C}_d$ is the data covariance matrix. We use a diagonal $\mathbf{C}_d$ without consideration of covariance between different frequency. The diagonal entries of $\mathbf{C}_d$ are the measurement error variances estimated from the pre-event noise and control how data are weighted. Data is transformed into the frequency domain and all frequencies within the chosen frequency band are jointly inverted for the final RFs. The choice of frequency band depends on the scale of structures, noise level, instrument response, etc, in the same way as in conventional RF estimations.

The pursuit of more sophisticated $\mathbf{C}_d$ and the incorporation of modeling error (i.e., noise in the vertical components) are potentially important and left for future work (Yagi and Fukahata, 2008, Duputel et al., 2012).

We can find the maximum a posterior (MAP) model estimation through

$$\text{argmin}_{\boldsymbol{\theta}}(\mathbf{R} - \mathbf{ZE}(\boldsymbol{\theta}))^T \mathbf{C}_d^{-1}(\mathbf{R} - \mathbf{ZE}(\boldsymbol{\theta}))). \tag{2.9}$$

The formulation (equation 2.7 and 2.8) above can be extended to jointly invert data from events with similar receiver-side structural responses (Gurrola et al., 1995). We prefer joint inversion to stacking the individual inversions for two reasons. First, we can ingest our prior knowledge of the data quality into the estimation rigorously through appropriate design of $\mathbf{C}_d$. Second, joint inversion helps promote model sparsity by taking all events into consideration simultaneously to constrain the RF phases.

Finally, the choice of subarray size, n, needs to account for two factors. First, the subarray aperture needs to be substantially smaller than the depths of target structures to satisfy our assumption of phase coherency, which states that the phases within a subarray have the same slowness. Second, there needs to be enough stations in the subarray to suppress non-uniqueness and over-fitting. Therefore, a seismic profile with average station spacing substantially smaller than the depth of target structures would be ideal for applying this array-based deconvolution method. For the synthetic and real-data experiment shown in this chapter, we find a five-station subarray setup is optimal. At the two edges of an array, we skip stations that do not have enough nearby stations on both sides to form a subarray.

2.2.3 Solving the Inverse Problem: Parameter Estimation

We employ a derivative-free search method—Neighborhood Algorithm (NA) to find the optimal model by solving (2.9). NA is a non-linear optimization algorithm developed in Sambridge (1999a). It conducts direct search in the multi-dimensional parameter space in an iterative fashion. Given a set of initial models, in each iteration, N_s new models are generated from the neighborhood of the best N_r existing models from the previous iteration. Since NA searches in the full parameter space, the computation complexity increases exponentially with the number of parameters. For computational efficiency, we take advantage of the linearity of the amplitude terms in (2.5) and rewrite $\mathbf{E}(\boldsymbol{\theta})$ in equation (2.7) to separate the amplitudes from the nonlinear parameters of timing and slowness:

$$\mathbf{E}(\boldsymbol{\theta}) = \mathbf{B}(t_1, t_2, \cdots, t_m, s_1, s_2, \cdots, s_m)\mathbf{A} \tag{2.10}$$

where $\mathbf{B}$ is the matrix containing the unit spike spectra $\exp(-i\omega(t_i + s_i(x_j - x_c)))$ constructed from the parameters of timing and slowness given the station coordinates $x_1, x_2, \cdots, x_n$, and $\mathbf{A} = [a_1, \ldots, a_m]^T$ is a column vector of phase amplitudes. Given any particular set of timing and slowness parameters, we can directly find the optimal $\mathbf{A}$ through

$$\mathbf{A} = ((\mathbf{ZB})^T \mathbf{C}_d^{-1} (\mathbf{ZB}))^{-1} (\mathbf{ZB})^T \mathbf{C}_d^{-1} \mathbf{R}. \tag{2.11}$$

This separation of linear and nonlinear parameters reduces the number of parameters for the NA non-linear optimization by one third and therefore increases the overall computation efficiency significantly.

To quantify the uncertainty of the RF parameters, we make use of the NA ensemble of searched models, each of which is a sample of the model posterior probability distribution (PPD) given by equation (2.8). We employ the ensemble appraisal approach introduced in Sambridge (1999b). It first defines an approximate model PPD by interpolating all the samples via Voronoi cells in model space. Gibbs sampler is then used to perform efficient importance sampling of this approximate PPD, from which we can readily find the marginal distribution of parameters.

2.2.4 Solving the Inverse Problem: Iterative Strategy and Number of Phases

One key parameter in our inverse problem is the number of phases m. It not only controls the computational complexity, but also reflects how many phases the data suggests. We want to design an objective approach to determine m with the goal of

sparsity promotion–finding the RF with the smallest number of phases required by data. Our strategy is to iteratively add new phases into the model, until the misfit reduction from adding a new phase is statistically insignificant. In each iteration, we solve for the three parameters (i.e., amplitude, timing, and slowness) of the newly added phase, while still adjusting the parameters for the existing phases around their optimal values from the previous iteration. The adjustment of existing phases, which is not included in conventional iterative RF methods (e.g., Ligorría and Ammon, 1999), is important because of the possible trade-offs between the new and the existing ones.

As more phases are added to the subarray RFs, the objective function, i.e., the function to minimize in equation (2.9), will stabilize/converge. Beyond certain number of phases, any new phases added are overfitting the data. In the conventional iterative time domain method, the number is often set to be large (e.g., 100) to ensure convergence of RF (Ligorría and Ammon, 1999). Instead, we stop adding new phases when the distribution of residuals is statistically indistinguishable from the converged/stabilized residual distribution with a large number of phases. Assuming a zero-mean Gaussian data uncertainty $N(0, \sigma^2)$, our stopping criterion is equivalent to when the σ_m estimated for the RF with m phases is within certain confidential interval of the σ_c estimated for the converged RF. In practice, we first estimate σ_c by adding phases to inversion until convergence. Then we estimate the standard deviation of σ_c for the number of data points we included in inversion by parametric bootstrapping. Finally, we choose the smallest number of phases that bring the σ_m within one standard deviation of σ_c.

Note that the starting assumption of this strategy is that the residuals in the frequency domain follow zero-mean Gaussian distribution. If the spectral power distribution is strongly frequency-dependent, this assumption may not be appropriate. However, additional data preprocessing steps, such as simultaneous spectral whitening of the radial and vertical component, can help mitigate this issue.

2.3 Synthetic Test

2.3.1 Model and Synthetics

The synthetic test model is based on a 2-D flat subduction scenario (Figure 2.2a), with reference to the central Mexico subduction zone. The oceanic plate first subducts underneath the continental plate with a dipping angle of 17°then goes flat at 50 km depth for 100 km, and finally plunges into the mantle at 75°. For the continental

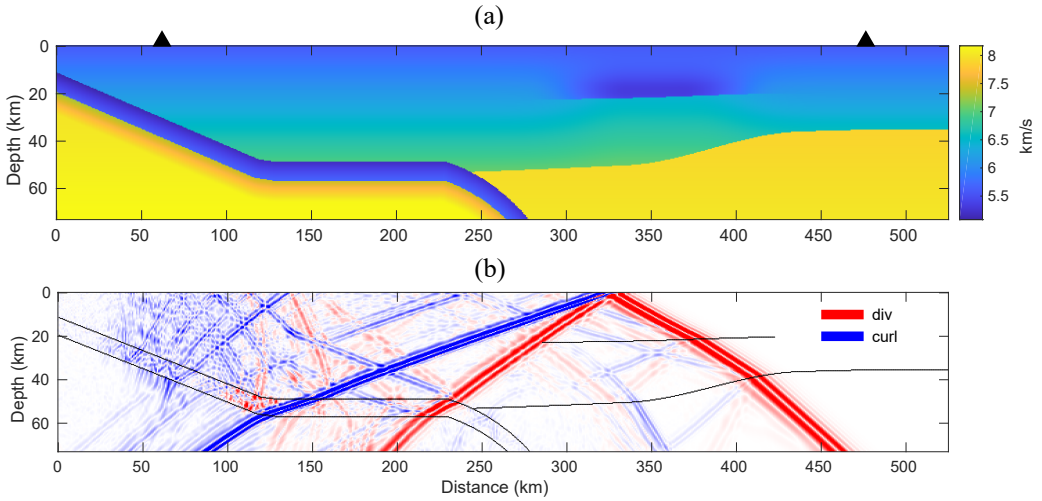

Figure 2.2: Setup of the synthetic test for array-based RFs. (a) The P-wave velocity model based on a flat subduction scenario to generate synthetic data. The two black triangles indicate the first and last station of the virtual dense seismic array. Main features to be captured by a RF profile include the low-velocity oceanic crust, the continental Moho with a smooth topography, and a mid-crust discontinuity on the continental side. (b) A snapshot of the simulated wavefield, with the divergence and curl showing the P-wave and S-wave fields, respectively.

plate, we set the Moho to have a smooth topography and add a 100 km-long mid-crust discontinuity. The station distribution is similar to the Meso-America Subduction Project (MASE) (Kim et al., 2010), with an even spacing of 5 km, substantially smaller than the depths of the target structures. We use a 2-D finite difference method (Li et al., 2014) to simulate the wavefield from a cluster of seven teleseismic events with the same azimuth aligned with the profile. The epicenter distances are centered at 40°with 2 km spacing. Figure 2.2b is a snapshot of the simulated wavefield for one of the events. Each event has its unique source time function and therefore different frequency contents. We apply a 1 Hz low-pass filter to all the synthetic data and add noise to the radial components. The noise is generated by first filtering the white noise in the same frequency band as the data, and then scaled according to a pre-defined signal-to-noise ratio (8.7 dB).

2.3.2 RF Estimation

We first estimate RFs from the noise-free synthetics as a proxy to the "true" RFs, by applying conventional iterative time-domain deconvolution at individual stations (Figure 2.3a). The "true" RFs show features as expected, including negative and positive phases related to the top and bottom edges of the oceanic crust. On the

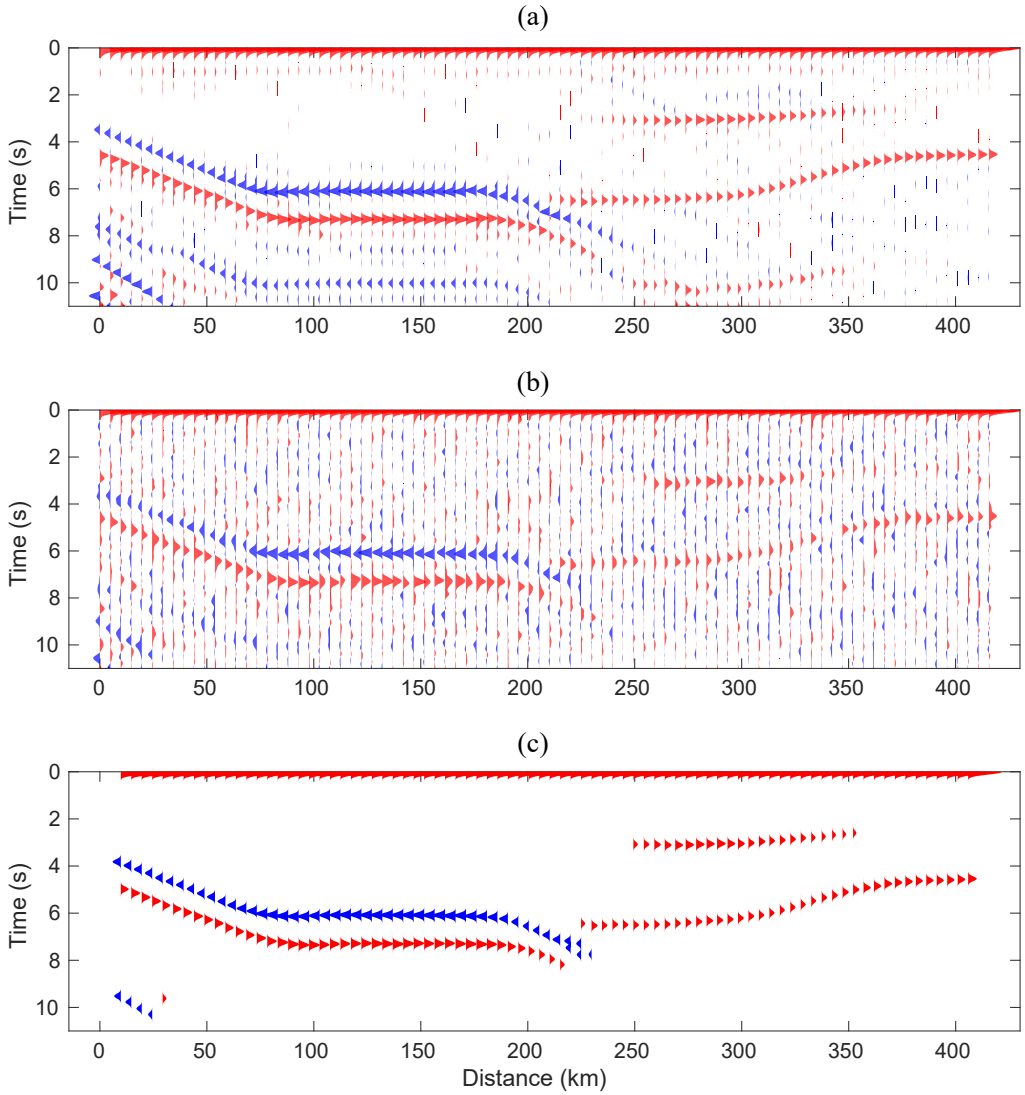

Figure 2.3: Synthetic test: full-array RFs. (a) Reference RFs estimated from the noise-free synthetics of the center event at 40° using the iterative time-domain deconvolution method. (b) Conventional RFs obtained by stacking the RFs estimated separately from the noisy synthetic data of the seven events with noise. (c) RFs estimated with the new array-based method by jointly inverting the noisy synthetic data of all seven events.

continental side, Ps phases track well the lateral variation of Moho topography and the mid-crust discontinuity. We then estimate RFs from the noisy synthetics using conventional practices. We use the iterative time domain deconvolution for individual RFs and stack the RFs from the seven events for the final RFs (Figure 2.3b). Compared with the "true" RFs (Figure 2.3a), main phases in Figure 2.3b are trackable. However, weaker phases (e.g., mid-crust discontinuity) are distorted

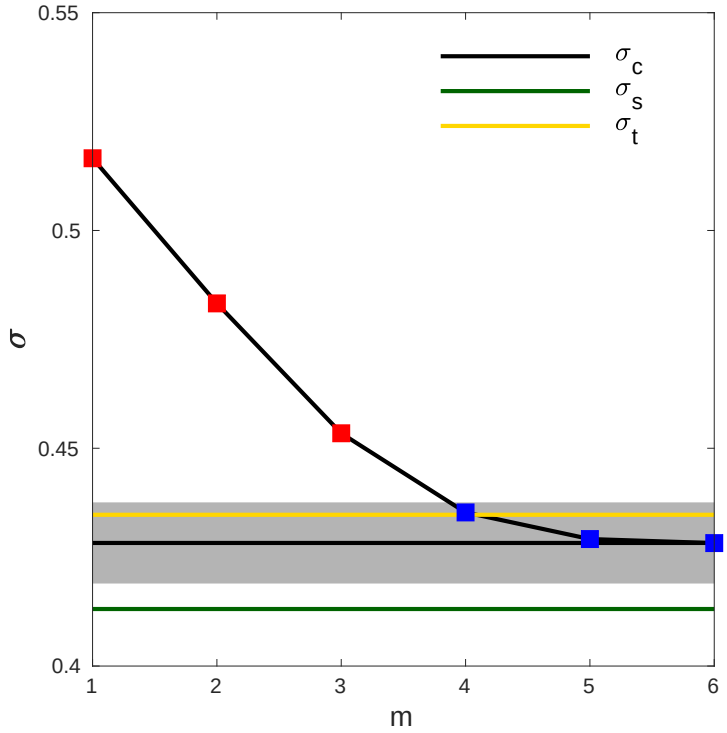

Figure 2.4: Standard deviation of residuals σ versus the number of phases m included in the RF inversions. Black line indicates the converged/stabilized value σ_c. The gray zone shows the bootstrapping $1-\sigma$ confidence interval around σ_c, given the number of data points used in the inversion. We pick the first blue square within the gray zone with $m = 4$ as our preferred RF. The yellow and green lines indicate the residual standard deviation for the "true" RFs (σ_t) and the conventional stacked RFs (σ_s), respectively.

and less coherent among nearby stations. In the meanwhile, a larger number of small incoherent phases downgrade the overall resolution of the image. Because the incoherent phases are not related to any real subsurface discontinuities, we attribute them to noise introduced by the deconvolution operations.

Finally, we estimate RFs from the same noisy data but using our new array-based deconvolution method. At each station, we joint invert the data from a subarray of five stations and all seven events for a RF with a minimum number of phases required by data. Figure 2.4 shows an example of the iterative process at one subarray, with a four-phase RF providing a residual distribution statistically indistinguishable from a fully converged RF. In other words, this synthetic data set with noise can only resolve four phases in RF. Interestingly, the standard deviation of the residuals (σ_c) for our converged RF is close to that of the "true" RFs (σ_t), while the one for conventional

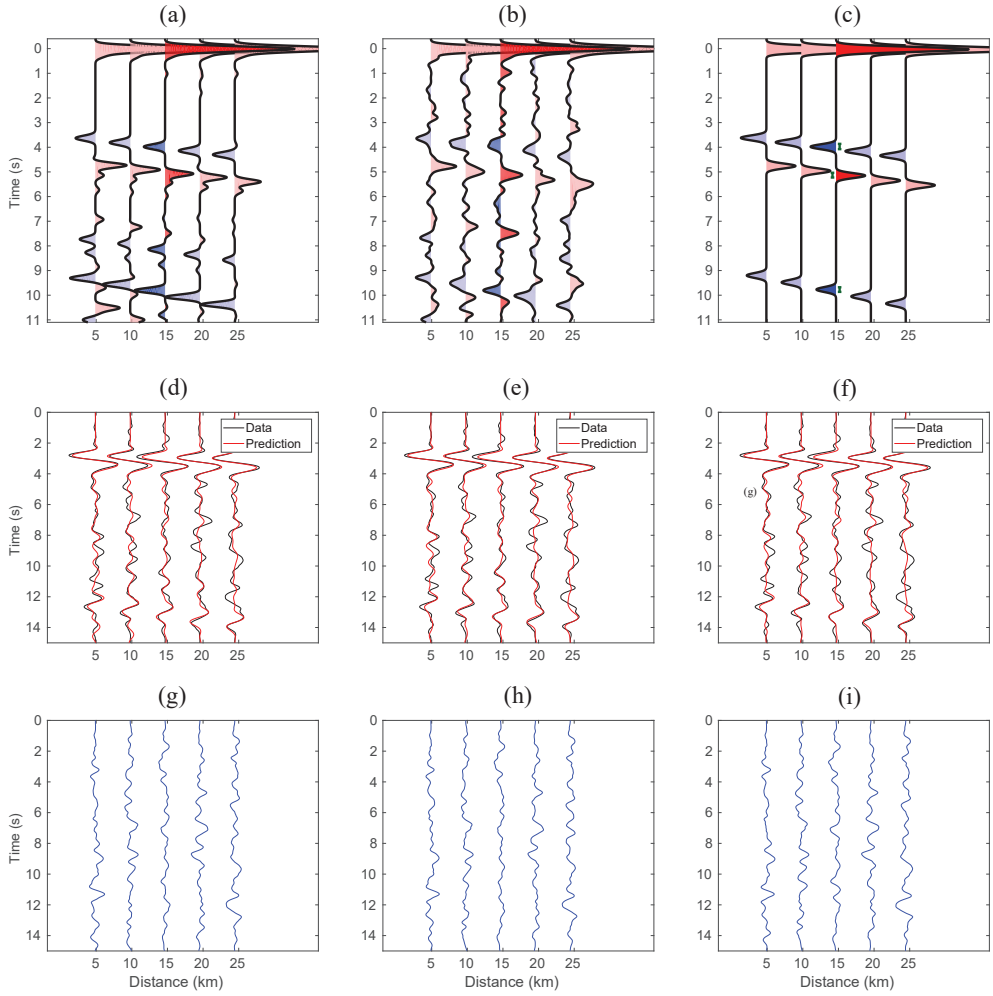

Figure 2.5: Synthetic test: a subarray example of RFs and data-fitting. (a, b, c) display the true RFs, the conventional stacked RFs, and the array-based RFs for one five-station subarray, respectively. The phases at center station are showed in darker colors. The green bars next to the phases in (c) indicate the 68% confidence interval of the phase timing. (d, e, f) Waveform fitting for the true RFs, the stacked RFs and the array-based RFs, respectively for the center event at 40°. The waveform in black is the radial component and waveform the red is the predicted radial component by convolving the vertical component with the estimated RF. (g, h, i) Waveform residuals (i.e. the difference between radial component and the prediction) for the true RFs, the stacked RFs, and the array-based RFs.

RFs (Figure 2.3b) is substantially lower (σ_s), suggesting data over-fitting by the large number of phases included in the time-domain iterative deconvolution method. Figure 2.5 shows the three sets of RFs for the subarray and their waveform fittings. The array-based RFs are much simpler, yet are able to fit the data equally well as the

reference and the conventional ones. Several weak phases in the "true" RFs (e.g., the negative phase at ~8 s) that are free-surface multiples are missing in our RFs. These missing phases do not improve data fitting in a statistically significant way and are considered un-resolvable in our method. To resolve them we will need to either include more data or reduce the data uncertainty.

The full array-based RF image (Figure 2.3c) agree well with the reference RF image (Figure 2.3a), with major phases from the low-velocity oceanic crust and the continental Moho well resolved and tracked along the profile. Weaker phases, such as those corresponding to the mid-crust discontinuity, are now clearly resolved along the right distance range with the right amplitudes. At small distance range, the phases at ~10 s is the only resolvable free-surface multiple. Other multiples, for example, the negative phase at ~10 s between 50 km and 200 km, are not included into the image according to our criterion of determining the number of phases. Moreover, incoherent noise is completely absent in the image and the whole profile is of better interpretability.

In this synthetic test, our input subsurface structures are laterally coherent, such that our assumptions on RF coherence are largely true. For point diffractors or sharp lateral discontinuities (e.g., Figure 2.1a), the assumptions may not hold unless the diffracted wave is well sampled by a dense array. Otherwise, the array-based RF estimation may suppress the sharpness of the structure.

2.4 Application

Recent deployments of large-N arrays demonstrated the importance of capturing full seismic wavefields in future seismic imaging projects (e.g., Lin et al., 2013, Ward and Lin, 2017, Liu et al., 2018). Here we apply our array-based RF method to the data from the 2016 IRIS community wavefield experiment in northern Oklahoma (Sweet et al., 2018) to demonstrate the benefit of applying our method to dense arrays. Conventional RF estimation relies on stacking many RFs to suppress noise and artifacts. This is feasible because broadband seismic experiments often last for a few months to a few years and record tens to hundreds of teleseismic events. However, nodal-type sensors typically operate for only a few weeks due to battery life, limiting the number of available events. How to retrieve high quality RFs from dense but short-duration deployments is a key challenge.

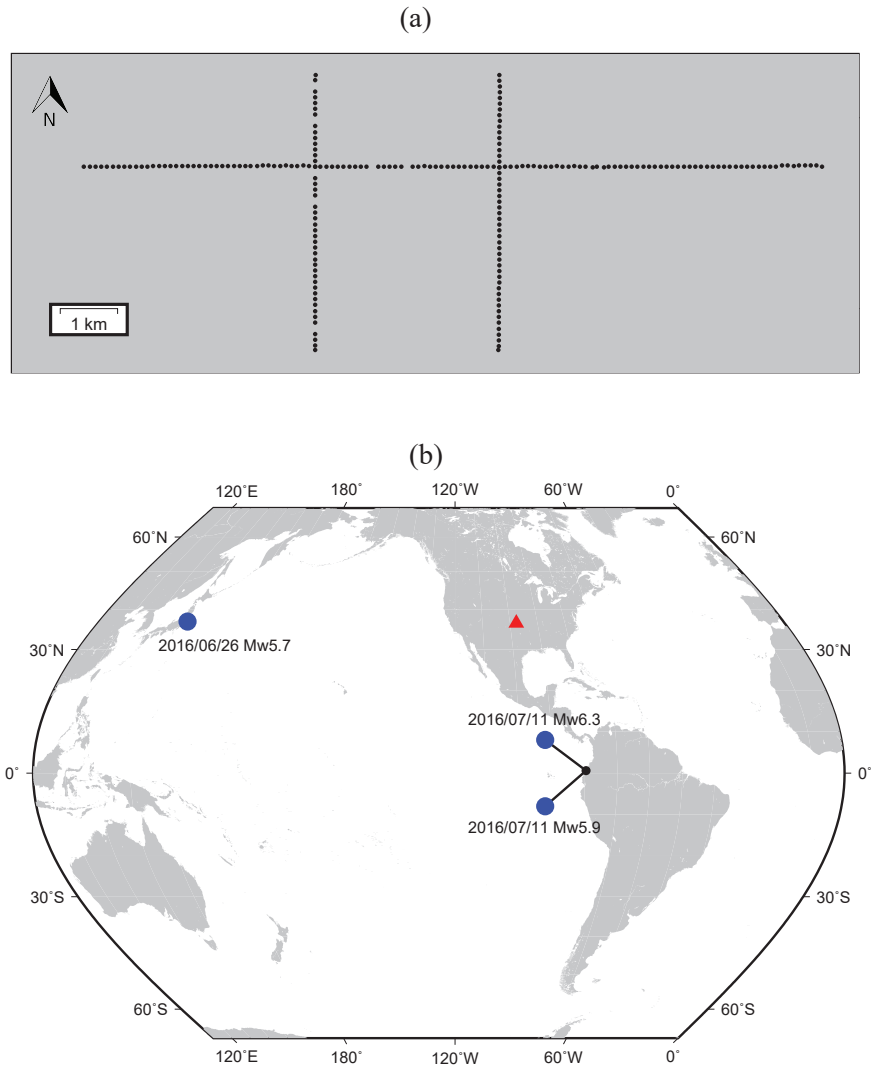

Figure 2.6: [Application to real data: arrays and earthquakes. (a) Three nodal seismic lines deployed in the IRIS community wavefield experiment in Oklahoma. The station spacing is about 100 m. There are 129 and 49 nodes in the WE and NS profiles, respectively. (b) The three teleseismic events (blue dots) we use for the RF estimations: the 2016 July 11th earthquake doublet in Ecuador and the 2016 June 26th earthquake in Japan.

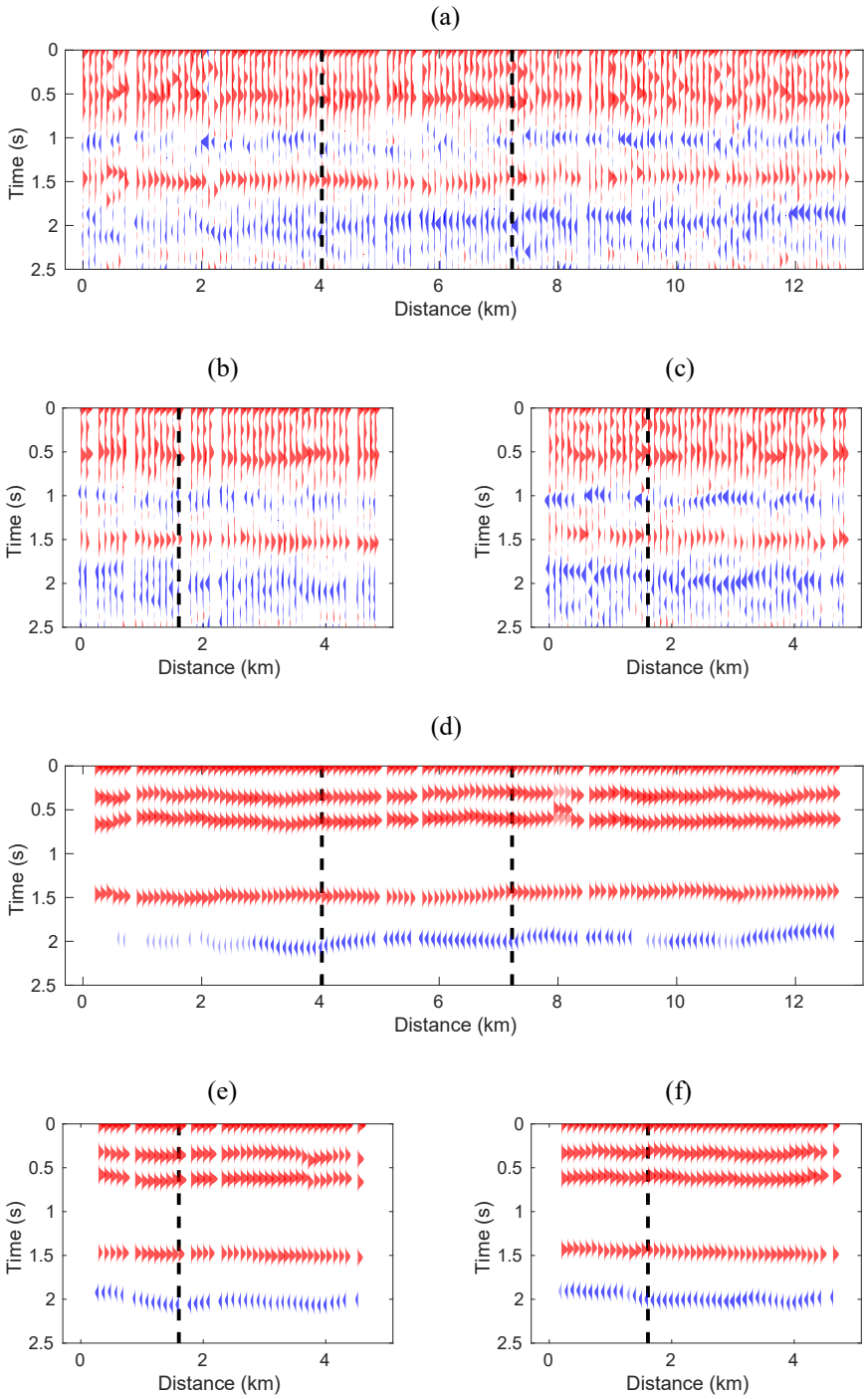

Figure 2.7: Application to real data: full-array RFs. (a, b, c) Conventional stacked RFs along the W-E line, western N-S line and eastern N-S line of the IRIS wavefield experiment, respectively. The black dashed lines show the cross points of the profiles. (d, e, f) The same as (a, b, c) but for our array-based RFs. For parts of the RF profiles, light blue or light red colors indicate phases added after one more iteration beyond the stopping criteria. In other words, they are not as well resolved as the ones in blue or red colors.

2.4.1 RF Estimation

One major component of the IRIS experiment is three dense profiles of three-component nodal seismic sensors, with an even spacing of about 100 m (Figure 2.6a). Given the small station spacing and array aperture, we focus on using RF to probe the shallow sedimentary structures. During the 1-month experiment, there were three $M_w \geq 5.5$ teleseismic events with good signal-to-noise ratios, two from Ecuador, and one from Japan (Figure 2.6b). We assume the station-side structural response of the three events are the same, because the piercing points of their incoming P-waves for the shallow sedimentary structures are very close. This allows us to jointly invert the data from the three events. To resolve the shallow structures, we include more high frequency waveforms (0.2 Hz – 2.5 Hz) in the inversion. In order to model the residuals with Gaussian distributions, we find it necessary to perform spectral whitening. We estimate the spectrum power of vertical component and divide it from both radial and vertical components.

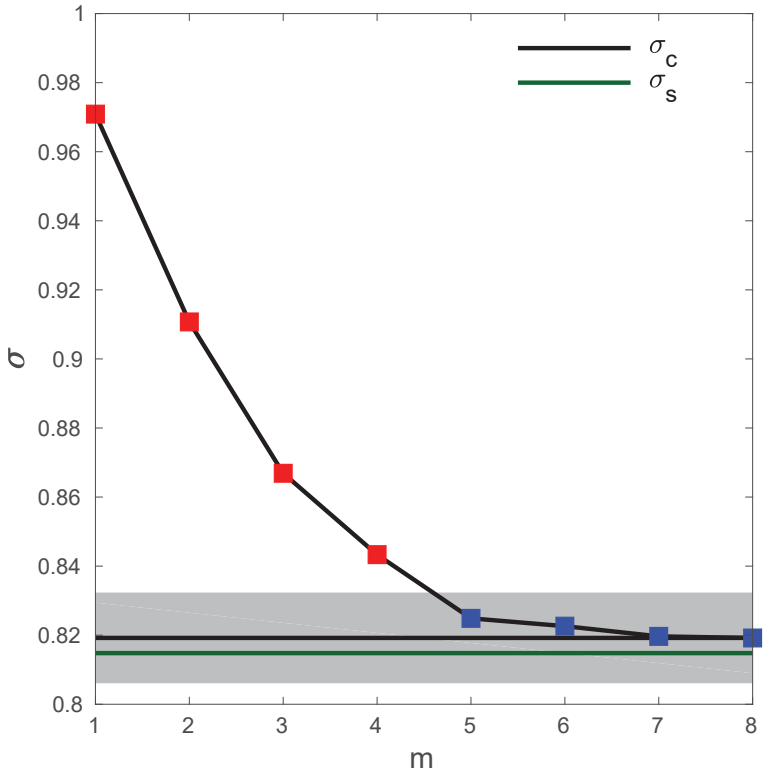

Figure 2.8: The same as Figure 2.4 but for the real data application to one subarray in the IRIS wavefield experiment. We pick the first blue square within the gray zone with $m = 5$ as our preferred RF, with exceptions of $m = 4$ at several subarrays.

We first estimate RFs using the conventional practices: we derive individual RFs through iterative time domain deconvolution for each event-station pair and then stack. The resulting RFs along the three profiles (Figure 2.7a-c) consistently show a weak first P phase and several closely following positive phases before 1 s, suggesting the existence of shallow slow structures. However, the phases are not coherent and hard to interpret. Later in the time window, we can see a few other phases that display better coherency across the array: a weak negative phase at 1 s, a strong positive phase at 1.5 s followed by some less coherent negative phases between 1.8 s and 2.3 s. The coherency of these phases across the arrays and consistency of the three RF profiles suggests approximately flat layered shallow structures beneath the arrays. However, more detailed interpretation for structures is difficult, because of the limited resolution.

We then apply our array-based RF deconvolution method to the same data. Each RF estimation is done by joint inversion of the three events recorded by a five-station subarray. Figure 2.8 shows an example of the iterative process for one subarray, where five coherent phases produce a residual distribution statistically indistinguishable from RF with more phases. The corresponding conventional RF produces slightly smaller residuals, but still statistically indistinguishable from that of the array-based RF. In Figure 2.9, we show the two sets of RFs and their corresponding waveform fittings for the subarray. The conventional RFs are of lower resolution, especially in the first 1 s. Spurious phases are introduced due to over-fitting. In contrast, the array-based RFs are simple and of high resolution. The uncertainty of phase timing is indicated by the green bar next to the phase representing 68% confidence interval.

The full array-based RF profile in Figure 2.7d-f show high phase coherency and essentially flat structures. The first 1 s following the direct P phases of the RFs, which the conventional method resolve poorly, now consists of two distinct positive phases trackable throughout the three profiles. We also obtain coherent positive and negative phase at about 1.5 s and 2 s, respectively, consistent with the smeared features in the conventional RFs. Interestingly, the weak but seemingly coherent negative phases at ~1 s in the conventional RF profiles are absent in the array-based RF profiles. We carefully examine this phase and conclude that it is a spurious phase caused by ringing effect, i.e., side-lobes, in the conventional method of deconvolution. The negative phase has opposite polarity and strong trade-offs with the two nearby positive phases. As a greedy algorithm without adjustment to

existing phases, conventional iterative time-domain deconvolution cannot account for this trade-off and may produce this spurious phase before contributions from other phases are fully accounted for.

Our array-based RF profiles suggest relatively simple and uniform shallow structures beneath this region. We suggest that the two positive phases closely following first P phase are Ps phases linking to two shallow sedimentary discontinuities. The later positive phase at 1.5 s and the negative phase at 2 s can be the multiples i.e., PpPs and PpSs/PsPs, or represent two shallow crustal discontinuities with increasing and decreasing velocity downwards, respectively. Further geological interpretation would benefit from other geophysical measurements (e.g., surface wave dispersions, boreholes) and the local geological history.

Besides showing the overall improved clarity of the RF profile, this real data application demonstrates that our new method has advantages over conventional methods in resolving more features, especially interfering phases, and removing noise introduced by the side-lobe effects of deconvolution. Indeed, compared with the conventional method, our proposed method is more complex and computationally more costly to deliver these advantages. In practice, sufficient stacking of conventional RFs (e.g., long-term or permanent stations) might produce RF images of high quality at lower cost. However, for short-term dense-array deployments (e.g., one month) where only a limited number of earthquakes are available, strong artifacts can exist in conventional RF profiles due to insufficient stacking. Our new method provides a solution to such scenarios.

2.5 Conclusions

Motivated by the emerging three-component large-N arrays, we develop a new array-based RF deconvolution method toward coherent RF profiles with only phases required by data. To address common issues such as non-uniqueness and data over-fitting in conventional deconvolution methods, we cast RF estimation as a sparsity-prompting inverse problem and exploit the wavefield coherency on dense arrays. Synthetic test shows that this new method outperforms conventional practices and produces RF profiles with higher fidelity and resolution. The real-data application to dense nodal seismic profiles also demonstrates the new method's advantages over conventional practices in producing higher-quality RF images with small amounts of data available on short term dense deployments. Compared with the conventional method, our method comes with higher computational cost due to

non-linear inversion and the sampling of parameter space.

Uncertainty estimation of phase timings is valuable new information provided by this method. Theoretically, estimating RFs as an inverse problem allows us to rigorously quantify RF uncertainties, which can be valuable during geological interpretations. As discussed in section 2.3 and section 2.4, we analyze the NA ensembles and the residual statistics to estimate the uncertainties. However, our experiments show that NA's efficiency drops quickly as the number of phases increases (e.g., beyond 10). Furthermore, NA does not perform importance sampling of the model posterior probability distribution, and the accuracy of the ensemble appraisal approach we use relies on thorough exploration of the model space (Sambridge, 1999b). Therefore, our current RF uncertainty estimation approach may be biased, especially when a large number of phases are required by data. In the future, we may use more efficient algorithms, for example, parallel Metropolis-Hastings algorithm (e.g., Jacob et al., 2010), to sample the model space and improve the uncertainty estimates.

Acknowledgements

We thank the team of IRIS community wavefield experiment for deployments and making the data readily accessible. We thank Rob Clayton and YoungHee Kim for helpful conversations. We thank Elmer Ruigrok and an anonymous reviewer for providing constructive reviews. This research is financially supported by NSF grant 1722879.

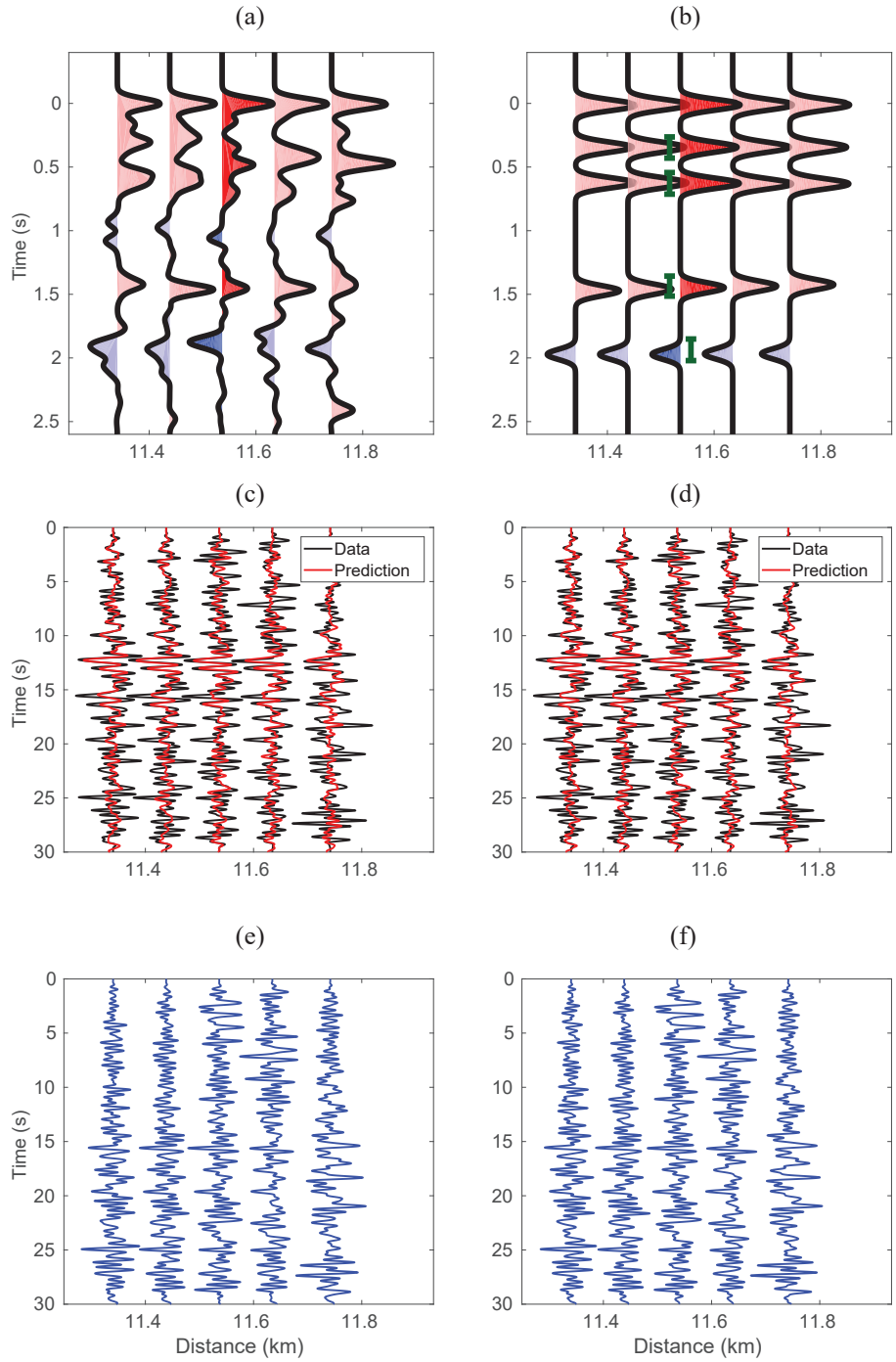

Figure 2.9: Similar to Figure 2.5 but for the real data application to one subarray in the IRIS wavefield experiment. (a, c, e) are for the conventional stacked RFs and (b, d, f) are for our array-based RFs. (c,e,d,f) are based on the waveforms of Mw 6.3 event.

BIBLIOGRAPHY

Ammon, C. J. (1991). The isolation of receiver effects from teleseismic P waveforms. In: *Bulletin of the Seismological Society of America* 81.6, pp. 2504–2510. ISSN: 0037-1106.

Ammon, C. J. et al. (1990). On the nonuniqueness of receiver function inversions. In: *Journal of Geophysical Research* 95.B10, p. 15303. ISSN: 0148-0227. DOI: 10.1029/JB095iB10p15303.

Aster, R. C. et al. (2018). *Parameter Estimation and Inverse Problems*. Elsevier.

Bostock, M. G. and S. Rondenay (1999). Migration of scattered teleseismic body waves. In: *Geophysical Journal International* 137.3, pp. 732–746. ISSN: 0956-540X. DOI: 10.1046/j.1365-246x.1999.00813.x.

Chen, L. et al. (2005). A wave equation migration method for receiver function imaging: 2. Application to the Japan subduction zone. In: *Journal of Geophysical Research: Solid Earth* 110.B11. ISSN: 01480227. DOI: 10.1029/2005JB003666.

Clayton, R. W. and R. Wiggins (1976). Source shape estimation and deconvolution of teleseismic bodywaves. In: *Geophysical Journal International* 47.1, pp. 151–177. ISSN: 0956-540X. DOI: 10.1111/j.1365-246X.1976.tb01267.x.

Crotwell, H. P. and T. J. Owens (2005). Automated receiver function processing. In: *Seismological Research Letters* 76.6, pp. 702–709. ISSN: 0895-0695. DOI: 10.1785/gssrl.76.6.702.

Dueker, K. G. and A. F. Sheehan (1997). Mantle discontinuity structure from midpoint stacks of converted P to S waves across the Yellowstone hotspot track. In: *Journal of Geophysical Research: Solid Earth* 102.B4, pp. 8313–8327. ISSN: 01480227. DOI: 10.1029/96JB03857.

Duputel, Z. et al. (2012). Uncertainty estimations for seismic source inversions. In: *Geophysical Journal International* 190.2, pp. 1243–1256. ISSN: 0956540X. DOI: 10.1111/j.1365-246X.2012.05554.x.

Eagar, K. C. et al. (2011). Crustal structure beneath the High Lava Plains of eastern Oregon and surrounding regions from receiver function analysis. In: *Journal of Geophysical Research* 116.B2, B02313. ISSN: 0148-0227. DOI: 10.1029/2010JB007795.

Fischer, K. M. et al. (2010). The lithosphere-asthenosphere boundary. In: *Annual Review of Earth and Planetary Sciences* 38.1, pp. 551–575. ISSN: 0084-6597. DOI: 10.1146/annurev-earth-040809-152438.

Gilbert, H. J. et al. (2003). Receiver functions in the western United States, with implications for upper mantle structure and dynamics. In: *Journal of Geophysical Research: Solid Earth* 108.B5. ISSN: 01480227. DOI: 10.1029/2001JB001194.

Gurrola, H. et al. (1995). Simultaneous time-domain deconvolution with application to the computation of receiver functions. In: *Geophysical Journal International* 120.3, pp. 537–543. ISSN: 0956540X. DOI: 10.1111/j.1365-246X.1995.tb01837.x.

Hansen, P. C. (1992). Analysis of discrete ill-posed problems by means of the L-curve. In: *SIAM Review* 34.4, pp. 561–580. ISSN: 0036-1445. DOI: 10.1137/1034115.

Jacob, P. et al. (2010). Using parallel computation to improve Independent Metropolis–Hastings based estimation. In: arXiv: 1010.1595.

Kim, Y. et al. (2010). Geometry and seismic properties of the subducting Cocos plate in central Mexico. In: *Journal of Geophysical Research* 115.B6, B06310. ISSN: 0148-0227. DOI: 10.1029/2009JB006942.

Kolb, J. M. and V. Leki (2014). Receiver function deconvolution using transdimensional hierarchical Bayesian inference. In: *Geophysical Journal International* 197.3, pp. 1719–1735. DOI: 10.1093/gji/ggu079.

Kumar, P. et al. (2012). USArray receiver function images of the lithosphere-asthenosphere boundary. In: *Seismological Research Letters* 83.3, pp. 486–491. ISSN: 0895-0695. DOI: 10.1785/gssrl.83.3.486.

Langston, C. A. (1979). Structure under Mount Rainier, Washington, inferred from teleseismic body waves. In: *Journal of Geophysical Research* 84.B9, p. 4749. ISSN: 0148-0227. DOI: 10.1029/JB084iB09p04749.

Levander, A. et al. (2011). Continuing Colorado plateau uplift by delamination-style convective lithospheric downwelling. In: *Nature* 472.7344, pp. 461–465. ISSN: 0028-0836. DOI: 10.1038/nature10001.

Levander, A. and M. S. Miller (2012). Evolutionary aspects of lithosphere discontinuity structure in the western U.S. In: *Geochemistry, Geophysics, Geosystems* 13.7, n/a–n/a. ISSN: 15252027. DOI: 10.1029/2012GC004056.

Li, D. et al. (2014). Global synthetic seismograms using a 2-D finite-difference method. In: *Geophysical Journal International* 197.2, pp. 1166–1183. ISSN: 1365-246X. DOI: 10.1093/gji/ggu050.

Ligorría, J. P. and C. J. Ammon (1999). Iterative deconvolution and receiver-function estimation. In: *Bulletin of the Seismological Society of America*. ISSN: 00371106.

Lin, F.-C. et al. (2013). High-resolution 3D shallow crustal structure in Long Beach, California: Application of ambient noise tomography on a dense seismic array. In: *GEOPHYSICS* 78.4, Q45–Q56. ISSN: 0016-8033. DOI: 10.1190/geo2012-0453.1.

Liu, G. et al. (2018). Structure of the northern Los Angeles basins revealed in teleseismic receiver functions from short-term nodal seismic arrays. In: *Seismological Research Letters* 89.5, pp. 1680–1689. ISSN: 0895-0695. DOI: 10.1785/0220180071.

Ma, Y. and R. W. Clayton (2016). Structure of the Los Angeles Basin from ambient noise and receiver functions. In: *Geophysical Journal International* 206.3, pp. 1645–1651. ISSN: 0956-540X. DOI: 10.1093/gji/ggw236.

Miller, M. S. and N. P. Agostinetti (2012). Insights into the evolution of the Italian lithospheric structure from S receiver function analysis. In: *Earth and Planetary Science Letters* 345-348, pp. 49–59. ISSN: 0012-821X. DOI: 10.1016/J.EPSL.2012.06.028.

Nábelek, J. et al. (2009). Underplating in the Himalaya-Tibet collision zone revealed by the Hi-CLIMB experiment. In: *Science (New York, N.Y.)* 325.5946, pp. 1371–4. ISSN: 1095-9203. DOI: 10.1126/science.1167719.

Nikulin, A. et al. (2009). Receiver function study of the Cascadia megathrust: Evidence for localized serpentinization. In: *Geochemistry, Geophysics, Geosystems* 10.7, n/a–n/a. ISSN: 15252027. DOI: 10.1029/2009GC002376.

Park, J. and V. Levin (2000). Receiver functions from multiple-taper spectral correlation estimates. In: *Bulletin of the Seismological Society of America* 90.6, pp. 1507–1520. ISSN: 0037-1106. DOI: 10.1785/0119990122.

Sambridge, M. (1999a). Geophysical inversion with a neighbourhood algorithm-I. Searching a parameter space. In: *Geophysical Journal International* 138.2, pp. 479–494. ISSN: 0956540X. DOI: 10.1046/j.1365-246X.1999.00876.x.

Sambridge, M. (1999b). Geophysical inversion with a neighbourhood algorithm-II. Appraising the ensemble. In: *Geophysical Journal International* 138.3, pp. 727–746. ISSN: 0956540X. DOI: 10.1046/j.1365-246x.1999.00900.x.

Schulte-Pelkum, V. and K. H. Mahan (2014). A method for mapping crustal deformation and anisotropy with receiver functions and first results from USArray. In: *Earth and Planetary Science Letters* 402, pp. 221–233. ISSN: 0012-821X. DOI: 10.1016/J.EPSL.2014.01.050.

Shen, W. et al. (2013). A 3-D model of the crust and uppermost mantle beneath the Central and Western US by joint inversion of receiver functions and surface wave dispersion. In: *Journal of Geophysical Research: Solid Earth* 118.1, pp. 262–276. ISSN: 21699313. DOI: 10.1029/2012JB009602.

Sweet, J. R. et al. (2018). A community experiment to record the full seismic wavefield in Oklahoma. In: *Seismological Research Letters* 89.5, pp. 1923–1930. ISSN: 0895-0695. DOI: 10.1785/0220180079.

Tarantola, A. (2005). *Inverse problem theory and methods for model parameter estimation*. Society for Industrial and Applied Mathematics, p. 342. ISBN: 0898715725.

Tauzin, B. et al. (2013). Multiple transition zone seismic discontinuities and low velocity layers below western United States. In: *Journal of Geophysical Research: Solid Earth* 118.5, pp. 2307–2322. ISSN: 21699313. DOI: 10.1002/jgrb.50182.

Vinnik, L. (1977). Detection of waves converted from P to SV in the mantle. In: *Physics of the Earth and Planetary Interiors* 15.1, pp. 39–45. ISSN: 0031-9201. DOI: 10.1016/0031-9201(77)90008-5.

Wang, L. et al. (2016). Seismic sparse-spike deconvolution via Toeplitz-sparse matrix factorization. In: *GEOPHYSICS* 81.3, pp. V169–V182. ISSN: 0016-8033. DOI: 10.1190/geo2015-0151.1.

Wapenaar, K. et al. (2011). Seismic interferometry by crosscorrelation and by multidimensional deconvolution: a systematic comparison. In: *Geophysical Journal International* 185.3, pp. 1335–1364. ISSN: 0956540X. DOI: 10.1111/j.1365-246X.2011.05007.x.

Ward, K. M. and F.-C. Lin (2017). On the viability of using autonomous three-component nodal geophones to calculate teleseismic Ps receiver functions with an application to old Faithful, Yellowstone. In: *Seismological Research Letters* 88.5, pp. 1268–1278. ISSN: 0895-0695. DOI: 10.1785/0220170051.

Ward, K. M. et al. (2018). High-Resolution Receiver Function Imaging Across the Cascadia Subduction Zone Using a Dense Nodal Array. In: *Geophysical Research Letters* 45.22, pp. 12, 218–12, 225. ISSN: 0094-8276. DOI: 10.1029/2018GL079903.

Wilson, D. and R. Aster (2005). Seismic imaging of the crust and upper mantle using regularized joint receiver functions, frequency–wave number filtering, and multimode Kirchhoff migration. In: *Journal of Geophysical Research* 110.B5, B05305. ISSN: 0148-0227. DOI: 10.1029/2004JB003430.

Xu, Z. J. et al. (2013). Crustal and uppermost mantle S velocity structure under Hi-CLIMB seismic array in central Tibetan Plateau from joint inversion of surface wave dispersion and receiver function data. In: *Tectonophysics* 584, pp. 209–220. ISSN: 0040-1951. DOI: 10.1016/J.TECTO.2012.08.024.

Yagi, Y. and Y. Fukahata (2008). Importance of covariance components in inversion analyses of densely sampled observed data: an application to waveform data inversion for seismic source processes. In: *Geophysical Journal International* 175.1, pp. 215–221. ISSN: 0956540X. DOI: 10.1111/j.1365-246X.2008.03884.x.

Yang, X. et al. (2016). A quality control method for teleseismic P-Wave receiver functions. In: *Bulletin of the Seismological Society of America* 106.5, pp. 1948–1962. ISSN: 0037-1106. DOI: 10.1785/0120150347.

Yildirim, S. et al. (2010). A Bayesian Deconvolution Approach for Receiver Function Analysis. In: *IEEE Transactions on Geoscience and Remote Sensing* 48.12, pp. 4151–4163. ISSN: 0196-2892. DOI: 10.1109/TGRS.2010.2050327.

Zhu, L. and H. Kanamori (2000). Moho depth variation in southern California from teleseismic receiver functions. In: *Journal of Geophysical Research: Solid Earth* 105.B2, pp. 2969–2980. ISSN: 01480227. DOI: 10.1029/1999JB900322.

Chapter 3

TIDE-INDUCED EPHEMERAL GROUNDING AT RUTFORD ICE STREAM, WEST ANTARCTICA, INFERRED FROM REMOTELY SENSED OBSERVATIONS

Abstract

Antarctic ice-shelves play a key role in regulating the rate of flow in tributary ice streams. Temporal variations in the associated buttressing stress clearly impact the flow in tributaries. For instance, short-term variations in buttressing stress induced by ocean tides have been proposed as an underlying mechanism to generate strong fortnightly flow rate variation at Rutford Ice Stream (RIS), West Antarctica. Ephemeral grounding induced by tides is considered as an important mechanism for modulating the buttressing stress. Here, we develop an approach to inferring variations in 3-D surface displacements at the ice-shelf-stream system that explicitly accounts for ephemeral grounding. Using a temporally dense 9-month long SAR image acquisition campaign collected over RIS by the COSMO-SkyMed 4-satellite constellation, we infer the ephemeral grounding zones and the spatial-temporal variation of the fortnightly flow variability. Expanding on previous results, we find ephemeral grounding zones along the western ice-shelf margin as well as a few prominent ephemeral grounding points in the central trunk and in the vicinity of the grounding zone. Our observations provide evidence for tide-modulated buttressing stress and the temporally asymmetric response of ice-shelf flow to tidal forcing. We should expect that RIS will accelerate if the ice shelf thins sufficiently that the ephemeral grounding zones we have identified remain permanently ungrounded over the tidal cycle.

3.1 Introduction

The Antarctic Ice Sheet is fringed with floating ice shelves which have contact with sub-shelf bathymetric highs that generate resistive back stress to tributary ice flows (e.g., Thomas, 1979; Gudmundsson, 2013). This resistive stress, often referred to as buttressing stress, plays an important role in regulating Antarctic ice flows (e.g., Joughin et al., 2012; Pritchard et al., 2012). With ongoing and projected ice shelf thinning, the loss of buttressing stress will result in retreat, acceleration, and dynamic thinning of glaciers, and may eventually lead to catastrophic mass loss of

the Antarctic Ice Sheet (e.g., Pritchard et al., 2009; Joughin et al., 2012; Alley et al., 2015). More detailed observation of the sub-shelf bathymetry, especially where ice shelves contact the seafloor, and better understanding of how the buttressing stress influences the ice-shelf-stream system are important for projecting the future evolution Antarctic ice sheet in response to changes in climate. Here, we focus on how the ocean tides influence the ice flow rate by modulating the buttressing stress.

Rutford Ice Stream (RIS), situated on the east of Ellsworth mountain range, is one of the major ice streams flowing into Filchner-Ronne Ice Shelf (FRIS) (Figure 3.1). RIS is about 300-km-long and 30-km-wide with a typical ice thickness of order 2 km over its grounded portion and 1.5 km over its floating portion. The bed of RIS lies more than 1.5 km below sea level and has a sinuous grounding line associated with a bathymetric ridge (Rignot et al., 2011b; King et al., 2016). The peak-to-peak tidal amplitude on the downstream ice shelf exceeds 7 m with the primary tidal constituents being semi-diurnal lunar and solar tides M_2 (12.42 h) and S_2(12.00 h), respectively (Table 3.1). The tidal forcing gives rise to a strong horizontal ice flow rate variation (~20% of the mean flow speed) at the fortnightly period M_{sf} (14.77 day), which corresponds to the beating of the two primary semi-diurnal constituents M_2 and S_2 (e.g., Gudmundsson, 2006; Murray et al., 2007).

Using synthetic aperture radar data collected by a 9-month COSMO-SkyMed (CSK) observation campaign over RIS, Minchew et al. (2017) inferred the spatial variability of the amplitude and phase of this fortnightly flow and found that it originated within the floating ice shelf and propagated upstream. This observation suggests that tidal forcing of the ice shelf processes is responsible for horizontal flow variability of the ice stream. Several models have been proposed to explain these observations including ephemeral grounding of the ice shelf, ice shelf margin widening, and grounding line migration (Minchew et al., 2017; Robel et al., 2017; Rosier and Gudmundsson, 2020; Warburton et al., 2020). All of these models suggest that the ocean tide modulates the contact of the ice shelf with the seafloor, and hence influences the buttressing stress to generate flow variability thereby causing temporal variability in flow.

Observation of the proposed tide-induced sub-shelf processes will improve our understanding of sub-shelf bathymetry and ice-shelf buttressing. Here, we focus on the tide-induced sub-shelf ephemeral grounding (Figure 3.2a). At RIS, there is a previously documented ephemeral grounding point 10 km downstream of the grounding line in the central trunk (Figure 3.1b, Goldstein et al., 1993; Rignot,

1998; Schmeltz et al., 2001). However, a modeling study on the buttressing effect of this single ephemeral grounding point, which is ~1.5 m beneath the ice shelf central trunk, suggests that it has limited impact on modulating the ice flow (Schmeltz et al., 2001). More zones of ephemeral grounding which have not yet been documented may exist at RIS.

Synthetic Apeture Radar (SAR) images can be used to measure the displacement of ice over a given time interval in two orthogonal directions, one of which is purely horizontal along and parallel to the satellite orbit (azimuth) direction, and the other which is parallel to the radar line-of-sight (LOS) direction. The measurement in the LOS direction is sensitive to vertical motion. When SAR data has sufficiently high revisit rates and is collected from multiple viewing angles over the same point, one may infer the tide-induced time-dependent 3-D motions from a time series of displacements (Minchew et al., 2017). Minchew et al. (2017) parameterized the temporal behavior of the displacement as the sum of sinusoidal functions at known tidal periods and thus were by construction unable to observe any ephemeral grounding. In other words, ephemeral grounding produces temporal asymmetry that is not captured by such a simple parameterization.

Here, we develop new methods to map the ephemeral grounding zone and estimate the level of ephemeral grounding at RIS. We model the vertical displacements considering all relevant major tidal constituents and introduce the level of ephemeral grounding level, or so called clipping, as an additional parameter. We demonstrate and validate our methods using realistic synthetic tests and then apply the methods to the improved displacement dataset. We present the inferred displacement including maps of ephemeral grounding as well as updated estimates of the fortnightly flow variability at RIS.

3.2 SAR Data and Displacement Fields

As described in Minchew et al. (2017), the COSMO-SkyMed (CSK) SAR satellite constellation, which is operated by the Italian Space Agency (ASI), collected SAR data over RIS for approximately 9 months beginning in August 2013. The data acquisition plan covers all of the grounded ice and landward ~100 km of the floating ice shelf from 32 unique tracks (Figure 3.1b). All four CSK satellites collected data, each repeating a given orbit track every 16 days. CSK satellite orbits are offset from one another with timespan between subsequent SAR acquisitions of 1, 3, 4, and 8 days. All CSK satellites carry nearly identical X-band (3.1 cm wavelength; 9.6

GHz) SAR systems. We use the Stripmap-HIMAGE products, which provide raw spatial resolution as fine as 3 m.

We processed the CSK data using the InSAR Scientific Computing Environment 2 (ISCE2), a radar-processing software package developed primarily at NASA's Jet Propulsion Laboratory (Rosen et al., 2012). We first focused the raw images to single-look complex (SLC) images and then used the stack processing tools in ISCE2 (Fattahi et al., 2017) to coregister all the same-track SLC images using Antarctica digital elevation model BedMachine Version 2 (Morlighem et al., 2020). To calculate displacement fields from coregistered images, we prescribed the 2-D cross-correlation windows to be 480×240 pixels (range $\times$ azimuth) with a step size of 120 and 60 pixels in range and azimuth direction, respectively. The cross-correlation window takes into account that the ratio of the dimensions of a full resolution pixel is approximately 1:2. The cross-correlation window size is significantly larger than the one used in Minchew et al. (2017) (64×64 pixels). The use of large cross-correlation window significantly increases the number of quality displacement measurements. We post-filter/adjust the resulting displacement fields by (1) masking out the displacement values if they differ from the prior Antarctica ice velocity model (Mouginot et al., 2012) beyond a prescribed threshold, (2) applying a moving-window median filter, and (3) adjusting for reference frame issue caused by the miscoregistration using tie points on stagnant ice. This approach keeps as many valid measurements as possible from noisy displacement fields. Using this scheme, we derived ~2500 displacement fields along 32 tracks from acquisitions with intervals no greater than 8 days.

Using dense cross-correlation on the SLC images to estimate displacement fields is computationally expensive, especially when using large cross-correlation windows. To overcome this computational challenge, we have developed a new tool employing GPUs for estimating the displacement fields. This GPU-enabled software accelerates this expensive computation by factors of 10 to 100 and makes it viable to use large cross-correlation windows, such as 480×240 pixels. This new tool has been included as part of the publicly released version of ISCE2 (Zhu et al., in prep).

3.3 Methodology

3.3.1 Ocean tides, Bathymetry and Ephemeral Grounding

Ocean tides cause changes in instantaneous sea level from the mean sea level. By convention, positive tide height corresponds to a rise in sea level, and zero tide

height corresponds to mean sea level. Ice shelves rise and fall synchronously with ocean tide. At any point on ice shelf, the sub-shelf water column thickness (wct) is the distance between the underlying seafloor and the bottom of ice shelf when tide height is zero. Ephemeral grounding occurs when the impact of tide on the instantaneous level of the bottom of ice shelf exceeds wct such that the bottom of ice shelf contacts the seafloor. Figure 3.2 2a1 and 2a2 is an example of ephemeral grounding on a sub-shelf bathymetric pinning point where the wct is 1 m.

At any point, the vertical displacement at the surface of ice shelf is the same as the vertical displacement of the bottom of the ice shelf (assuming negligible vertical extension and compression), if we define the zero displacement for both to be the their levels when tide height is zero, respectively. Hereafter, unless mentioned explicitly, vertical displacement refers to displacement at surface which SAR observations have direct sensitivity to. The vertical displacement is typically the same as the tide height due to hydrostatic balance between ice shelf and ocean (Figure 3.2a1), for example, in the central trunk of the ice shelf. In the vicinity of the grounding zone, the amplitude of surface vertical displacement gradually decreases to zero towards the grounded ice due to the flexure of ice-shelf (e.g., Vaughan 1995).

Ephemeral grounding on sub-shelf bathymetric highs induces clipping on the vertical displacement. We define the level of ephemeral grounding as the level of clipping (Figure 3.2b1). In the example shown in Figure 3.2, the vertical displacement at the point indicated by the gray GPS station is clipped at -1 m because the seafloor is 1 m below the mean level of the bottom of ice shelf. The level of ephemeral grounding is typically negative and is equivalent to be negative of the wct. A higher level of grounding corresponds to higher sub-shelf bathymetry and thinner wct, and vice versa. If the range of vertical displacement is smaller than the wct, ephemeral grounding does not occur. We note the difference between grounding zone and zones of ephemeral grounding. Grounding zone refers to the transition region between the fully grounded ice to the free floating ice shelf (e.g., Fricker et al., 2009). While zones of ephemeral grounding are likely to exist in the vicinity of the grounding zone due to the shallow bathymetry, they can also exist far from the grounding zone, for example, an isolated localized bathymetric high point in the central trunk of the ice shelf.

3.3.2 An Overview of Displacement Models and Workflow

Our approach includes two displacement models: a linear 3-D displacement model for indirectly inferring ephemeral grounding and a nonlinear 3-D displacement model for quantifying the level of ephemeral grounding. The workflow starts from the linear model, then constructs the nonlinear model using the results derived from the linear model and an independent ocean tidal model, and finally solves for vertical displacements with ephemeral grounding and horizontal flow variability (Figure 3.3).

The linear model is in the same framework as the model developed in Minchew et al. (2017), but is modified to improve the estimation of the vertical displacements on ice-shelf and to identify zones of ephemeral grounding. A key improvement is the inclusion of the vertical displacement at fortnightly period into the inference. In section 3.3.3, we show the connection between ephemeral grounding and the inferred vertical displacement at fortnightly period. The main limitation of the linear model is that only a subset of tidal periods can be inferred (e.g., M_2, O_1), in particular, those which are not aliased in the satellite observations which occur at the same time of a day. As a consequence, this linear model is unable to constrain the level of ephemeral grounding (Figure 3.2a) which depends on knowledge of the total displacement field, not just selected tidal constituents.

To quantify the level of ephemeral grounding, the displacement model needs to consider the absolute vertical displacement on the ice-shelf, which is the superposition of vertical displacement at all tidal periods (Table 3.1). Our strategy is to combine inferred vertical displacements derived from the linear model and the vertical displacements extracted from the ocean tidal model. The former has high spatial resolution but misses key aliased tidal constituents. The latter is complete including all major tidal constituents but does not have sufficient spatial resolution for resolving ephemeral grounding in the vicinity of the grounding zone. By combination of the two, we construct a nonlinear vertical displacement model accounting for ephemeral grounding.

The full workflow consists of two parts which include two models and four steps (Figure 3.3). Part I is associated with the linear 3-D displacement model. We apply this model to real data and infer vertical displacements at the selected tidal periods (Step 1). Then, we obtain the theoretical bias in the estimated vertical displacements from a realistic synthetic test and correct for this bias in the inferred values (Step 2). Part II describes the nonlinear 3-D displacement model. We construct the nonlinear

vertical displacement model accounting for ephemeral grounding using the bias-corrected inferred vertical displacements from the linear model and the ocean tidal model (Step 3). Using this new vertical displacement model and inheriting the horizontal displacement model from the linear 3-D displacement model, we arrive at the final nonlinear 3-D displacement model. Using this model, we infer the vertical displacements with ephemeral grounding and horizontal flow variability (Step 4).

3.3.3 Identifying Zones of Ephemeral Grounding

3.3.3.1 A Linear Model for Inferring 3-D Periodic Displacements

We start with reviewing the methodology developed in Minchew et al. (2017) which forms the basic foundation for our methodological development. In this review, we include our modification to the original inverse problem formulation which makes the model more suitable for our use. We are interested in the tide-induced displacements of ice stream and ice shelf system. We consider the instantaneous 3-D displacement vector $\mathbf{u}$ on the ice surface at location $\mathbf{r}$ and at time t as the sum of a secular term and a tide-induced term in east ($\hat{e}$), north ($\hat{n}$), and up component ($\hat{u}$), such that

$$\mathbf{u}(\mathbf{r},t) = \mathbf{v}(\mathbf{r})t + \mathbf{w}(\mathbf{r},t) = \begin{bmatrix} v^{\hat{e}}(\mathbf{r}) \\ v^{\hat{n}}(\mathbf{r}) \\ v^{\hat{u}}(\mathbf{r}) \end{bmatrix} t + \begin{bmatrix} w^{\hat{e}}(\mathbf{r},t) \\ w^{\hat{n}}(\mathbf{r},t) \\ w^{\hat{u}}(\mathbf{r},t) \end{bmatrix} \tag{3.1}$$

where $\mathbf{v}(\mathbf{r})$ is the secular velocity and $\mathbf{w}(\mathbf{r},t)$ is the tide-induced displacement vector.

Assuming the tide-induced displacement to be sinusoidal for all periods of tidal forcing, we parameterize $\mathbf{w}(\mathbf{r},t)$ as the sum of a family of sinusoidal functions $i = 1, 2, ..., k$, such that

$$w^{\hat{\zeta}}(\mathbf{r},t) = \sum_{i=1}^{k} a_i^{\hat{\zeta}} \sin(\omega_i t + \phi_i^{\hat{\zeta}}) \quad \text{for } \hat{\zeta} = [\hat{e}, \hat{n}, \hat{u}] \tag{3.2}$$

where sinusoid i has angular frequency ω_i, amplitude $a_i^{\hat{\zeta}}(\mathbf{r})$, and phase $\phi_i^{\hat{\zeta}}(\mathbf{r})$ corresponding to different tidal constituents. We can rewrite equation (3.2) as the linear displacement model

$$w^{\hat{\zeta}}(\mathbf{r},t) = \sum_{i=1}^{k} c_i^{\hat{\zeta}} \cos(\omega_i t) + s_i^{\hat{\zeta}} \sin(\omega_i t) \tag{3.3}$$

where

$$c_i^{\hat{\zeta}} = a_i^{\hat{\zeta}} \sin(\phi_i^{\hat{\zeta}}) \tag{3.4}$$

$$s_i^{\hat{\xi}} = a_i^{\hat{\xi}} \cos(\phi_i^{\hat{\xi}}). \tag{3.5}$$

At any point $\mathbf{r}$, the measured displacement $d_j (j = 1, 2, \cdots, q)$ from q pairs of SAR scenes is

$$d_j(\hat{\mathbf{l}}_j, \mathbf{r}, t_j^a, t_j^b) = \hat{\mathbf{l}}_j \cdot (\mathbf{u}(\mathbf{r}, t_j^b)) - \mathbf{u}(\mathbf{r}, t_j^a)) \tag{3.6}$$

where $\hat{\mathbf{l}}_j$ is observational unit vector (in LOS or azimuth direction) and t_j^a and t_j^b are the acquisition times of the primary and secondary scenes of the SAR pair.

Equation (3.6) relates model parameters ($\mathbf{v}$, $c_i^{\hat{\xi}}$, $s_i^{\hat{\xi}}$) to the observed displacements. To infer the model parameters, we cast it as a linear inverse problem for a given location $\mathbf{r}$ and arrive at the matrix form

$$\mathbf{d} = \mathbf{G}\mathbf{m} \tag{3.7}$$

where $\mathbf{d}$ is the vector of observed displacement, $\mathbf{m}$ is the model vector, and $\mathbf{G}$ is the design matrix. Model vector $\mathbf{m}$ has the form

$$\mathbf{m} = \begin{bmatrix} \mathbf{v} & \mathbf{c}_1 & \mathbf{s}_1 & \mathbf{c}_2 & \mathbf{s}_2 & \dots & \mathbf{c}_k & \mathbf{s}_k \end{bmatrix}^T \tag{3.8}$$

$$\mathbf{c}_i = \begin{bmatrix} c_i^{\hat{e}} & c_i^{\hat{n}} & c_i^{\hat{u}} \end{bmatrix}, i = 1, 2, .., k \tag{3.9}$$

$$\mathbf{s}_i = \begin{bmatrix} s_i^{\hat{e}} & s_i^{\hat{n}} & s_i^{\hat{u}} \end{bmatrix}, i = 1, 2, .., k \tag{3.10}$$

and the corresponding design matrix has the form

$$\mathbf{G} = \begin{bmatrix} \hat{\mathbf{l}}_1 \Delta t_1 & \hat{\mathbf{l}}_1 \Delta p_{1_1}^{\cos} & \hat{\mathbf{l}}_1 \Delta p_{1_1}^{\sin} & \dots & \hat{\mathbf{l}}_1 \Delta p_{k_1}^{\cos} & \hat{\mathbf{l}}_1 \Delta p_{k_1}^{\sin} \\ \vdots & & & \ddots & & \vdots \\ \hat{\mathbf{l}}_q \Delta t_q & \hat{\mathbf{l}}_q \Delta p_{1_q}^{\cos} & \hat{\mathbf{l}}_q \Delta p_{1_q}^{\sin} & \dots & \hat{\mathbf{l}}_q \Delta p_{k_q}^{\cos} & \hat{\mathbf{l}}_q \Delta p_{k_q}^{\sin} \end{bmatrix} \tag{3.11}$$

where

$$\Delta t_j = t_j^b - t_j^a \tag{3.12}$$

$$\Delta p_{i_j}^{\cos} = \cos(\omega_i t_j^b) - \cos(\omega_i t_j^a) \tag{3.13}$$

$$\Delta p_{i_j}^{\sin} = \sin(\omega_i t_j^b) - \sin(\omega_i t_j^a). \tag{3.14}$$

To solve the inverse problem, we adopt Bayesian formulation assuming Gaussian distributions for all uncertainties, so the optimal (maximum a posteriori) model estimation is (Tarantola, 2005)

$$\tilde{\mathbf{m}} = (\mathbf{G}^T \mathbf{C}_\chi^{-1} \mathbf{G} + \mathbf{C}_m^{-1})^{-1} (\mathbf{C}_\chi^{-1} \mathbf{G}^T \mathbf{d} + \mathbf{C}_m^{-1} \mathbf{m}_0) \tag{3.15}$$

where $\mathbf{m}_0$ is the prior model vector, $\mathbf{C}_m$ is the prior model covariance matrix, and $\mathbf{C}_\chi$ is the error covariance matrix, also referred to as the misfit covariance. In the original formulation, the error covariance matrix is denoted as $\mathbf{C}_d$, because only the measurement error in data is considered. Here, we consider both measurement error and modeling (or prediction) error, $\mathbf{C}_p$, such that $\mathbf{C}_\chi = \mathbf{C}_m + \mathbf{C}_p$. Details of $\mathbf{C}_\chi$ are discussed in section 3.3.5.

In the original design of the model prior, $\mathbf{C}_m$ is a diagonal matrix with the diagonal values constraining the amplitude of the corresponding variation. Two reference frequencies were chosen for the horizontal and vertical variation, respectively, and diagonal values scale inversely with the difference between the corresponding frequency and the reference frequency. This approach was motivated by the fact the vertical and horizontal motion at RIS are primarily at short-period (semi-diurnal and diurnal) and at long-period (fortnightly), respectively. Here, we remove the dependence on reference frequency and generalize the model so that both the short-period and long-period variation can be modeled. The modified $\mathbf{C}_m$ is still diagonal and structured as follows:

$$\mathbf{C}_m^{-1} = \mathrm{diag}[\Omega_{\mathbf{v}}\ \Omega_{\mathbf{c}_1}\ \Omega_{\mathbf{s}_1}\ \cdots\ \Omega_{\mathbf{c}_k}\ \Omega_{\mathbf{s}_k}\ ] \tag{3.16}$$

$$\Omega_{\mathbf{v}} = [\Omega_{\mathbf{v}\hat{\mathbf{e}}}\ \Omega_{\mathbf{v}\hat{\mathbf{n}}}\ \Omega_{\mathbf{v}\hat{\mathbf{u}}}\ ] \tag{3.17}$$

$$\Omega_{\mathbf{c}_i} = [\Omega_{c_i^{\hat{e}}}\ \Omega_{c_i^{\hat{n}}}\ \Omega_{c_i^{\hat{u}}}], \tag{3.18}$$

$$\Omega_{\mathbf{s}_i} = [\Omega_{s_i^{\hat{e}}}\ \Omega_{s_i^{\hat{n}}}\ \Omega_{s_i^{\hat{u}}}] \tag{3.19}$$

$$\Omega_\rho = \begin{cases} \frac{1}{\epsilon^2} & \rho \text{ is constrained to be close to the prior value} \\ 0 & \rho \text{ is unconstrained} \end{cases} \quad (\rho = v^{\hat{\xi}},\ c_i^{\hat{\xi}},\ s_i^{\hat{\xi}}) \tag{3.20}$$

where ϵ is a pre-defined value of small variation in parameters. Constraining the variations of certain components to be small can be helpful to stabilize the inversion when the unconstrained inversion shows strong trade-offs between certain components (Minchew et al., 2017).

The posterior model covariance matrix

$$\tilde{\mathbf{C}}_m = (\mathbf{G}^T \mathbf{C}_\chi^{-1} \mathbf{G} + \mathbf{C}_m^{-1})^{-1} \tag{3.21}$$

provides the estimates of formal errors in $\tilde{\mathbf{m}}$. The estimates of formal errors in amplitude $a_i^{\hat{\zeta}}$ and phase $\phi_i^{\hat{\zeta}}$ can be calculated from the formal errors of $c_i^{\hat{\zeta}}$ and $s_i^{\hat{\zeta}}$ by applying the following relations derived in Minchew et al. (2017):

$$\sigma^2_{a_i^{\hat{\zeta}}} = \frac{\sigma^2_{c_i^{\hat{\zeta}}} \sin^2(\phi_i^{\hat{\zeta}}) - \sigma^2_{s_i^{\hat{\zeta}}} \cos^2(\phi_i^{\hat{\zeta}})}{\sin^4(\phi_i^{\hat{\zeta}}) - \cos^4(\phi_i^{\hat{\zeta}})} \tag{3.22}$$

$$\sigma^2_{\phi_i^{\hat{\zeta}}} = \frac{-\sigma^2_{c_i^{\hat{\zeta}}} \cos^2(\phi_i^{\hat{\zeta}}) + \sigma^2_{s_i^{\hat{\zeta}}} \sin^2(\phi_i^{\hat{\zeta}})}{(a_i^{\hat{\zeta}})^2(\sin^4(\phi_i^{\hat{\zeta}}) - \cos^4(\phi_i^{\hat{\zeta}}))} \tag{3.23}$$

3.3.3.2 An Approach to Infer the Presence of Ephemeral Grounding

3.3.3.2.1 Candidate Tidal Constituents

We choose the family of sinusoids in the model according to our prior knowledge of the tide-induced displacement variations at EIS. The vertical motion on the ice shelf is dominated by semi-diurnal and diurnal constituents (Table 3.1). However, the time interval of the SAR acquisitions is always within seconds of being integer days, which prevents any sensitivity to constituents S_2, K_2, K_1, and P_1 whose periods are or very close to 12 h or 24 h. Thus, we are left with M_2(12.42 h period), N_2(12.66 h period), O_1(25.82 h period), and Q_1(26.87 h period).

3.3.3.2.2 Ephemeral Grounding and the Vertical M_{sf} Sinusoid

When the ice shelf ephemerally grounds on the seafloor (Figure 3.2a), the vertical displacement is the time series of the tide height clipped at the grounding level (Figure 3.2b1-3.2b2). Compared with the original time series, such clipping introduces new frequency content at fortnightly periods which can be seen in the amplitude spectrum (Figure 3.2b3- 3.2b4). Therefore, we include the vertical M_{sf} period into the model and consider it as a proxy for ephemeral grounding. If the inferred amplitude of the vertical M_{sf} sinusoid is significantly larger than the expected amplitude (less than 1 cm at RIS), the vertical displacement can be assumed to be ephemerally grounded. Later, in section 3.3.4, we will explicitly include the clipping effect in the model parameterization, but this makes the model nonlinear.

3.3.3.3 Tests with Synthetic Data

We use synthetic tests to explore how to best identify ephemeral grounding and to assess any bias in the linear approach. Within the context of linear model, we

construct our synthetic model as follows:

1. Secular velocity: We prescribe the east and north component of the secular velocity, $v^{\hat{e}}$, and, $v^{\hat{n}}$, using the latest Antarctic Ice velocity Model (Rignot et al., 2011b; Mouginot et al., 2012). We prescribe the up component, $v^{\hat{u}}$, to be zero everywhere.

2. Vertical tidal displacement: We prescribe the vertical motion on the ice shelf with ephemeral grounding as:

$$w^{\hat{u}}(\mathbf{r}, t) = \max(S(\mathbf{r})h_{\text{ref}}(t), K(\mathbf{r})) \tag{3.24}$$

   where $h_{\text{ref}}(t)$ is tide height time series extracted at a reference point in the ice shelf trunk (Figure 3.1b) from the CATS2008 ocean tidal model (Padman et al., 2002), $S(\mathbf{r})$ is a linear amplitude scaling factor, and $K(\mathbf{r})$ is the level of ephemeral grounding. $S(\mathbf{r})$ is 1 in the ice shelf central trunk, gradually decreasing in the vicinity of the grounding zone and is 0 over the grounded ice. We adopt this parameterized form using a reference point because the tidal model does not have data available everywhere in our observational domain and it does not have sufficient resolution near grounding zones. This form for the synthetic model assumes negligible variation in phase over the ice-shelf, a reasonable approximation according to both the tidal model and our eventual inferred values from real data.

3. Horizontal tidal displacements: We prescribe the temporal variation in horizontal flow rate, $\Delta\mathbf{v}^{\text{horiz}}(\mathbf{r}, t)$, to be only in the same direction as the secular velocity ("along-flow") and to scale with the horizontal secular speed as

$$\begin{aligned}\Delta\mathbf{v}^{\text{horiz}}(\mathbf{r}, t) &= [\Delta v^{\hat{e}}(\mathbf{r}, t), \Delta v^{\hat{n}}(\mathbf{r}, t)] \\ &= \begin{cases} (v^{\text{horiz}}(\mathbf{r})/v_0) \sum_\xi a_\xi \sin(\omega_\xi t + \phi_\xi) & \text{along-flow} \\ 0 & \text{cross-flow} \end{cases}\end{aligned} \tag{3.25}$$

   where the a_ξ and ϕ_ξ are reported amplitude (unit: m/d) and phase of the flow rate variation at the period of tidal constituent ξ by GPS measurements at RIS (Murray et al., 2007), $v^{\text{horiz}}(\mathbf{r}) = \sqrt{v^{\hat{e}2}(\mathbf{r}) + v^{\hat{n}2}(\mathbf{r})}$ is the prescribed horizontal secular speed, and v_0 is the reference horizontal secular speed in the central trunk of RIS, which we choose to be 1 m/d.

4. Synthetic displacement data: We create synthetic displacement data which has the same temporal and spatial sampling as our actual observations (see section 3.2). Add uncorrelated Gaussian noise with standard deviation 10 cm to both the LOS and azimuth synthetic displacements.

We conduct synthetic tests exploring models with different families of sinusoids, different settings of model priors, and both sub-shelf grounding and no-grounding scenarios. In the no-grounding case, $K(\mathbf{r})$ is prescribed as lower than lowest tide height (e.g., −0.5 m). In the ephemeral grounding case, we prescribe $K(\mathbf{r})$ to −1.5 m everywhere. We conclude that the optimal model contains sinusoids M_2, N_2, O_1, and M_{sf}, adopts prior model $\mathbf{m}_0 = 0$, and prior model covariance matrix constraining the horizontal variations at short periods (M_2, N_2, O_1) to be small ($\epsilon = 1$ mm in equation 3.20). The result and discussion of synthetic tests are provided in the supporting information (S3.7.1). These demonstrate that the inferred amplitude of vertical M_{sf} can be used as a proxy for detecting, but not quantifying ephemeral grounding. By comparing the inferred values with the prescribed values, the synthetic tests also provide estimates of the bias in the inferred values. The bias estimates are important for interpreting and using the results inferred with real data.

3.3.4 Quantifying of Level of Ephemeral Grounding

3.3.4.1 A Vertical Displacement Model with Ephemeral Grounding

In order to identify zones of ephemeral grounding, as well as to constrain the level of ephemeral grounding, we need to develop a new vertical displacement model for $w^{\hat{u}}(\mathbf{r}, t)$ in equation (3.1). Compared with the linear model, the new model needs to consider the absolute ocean tide height i.e., the superposition of all major constituents (Table 3.1). However, as previously noted, we are not able to directly infer a few major constituents (e.g., S_2, K_1) with periods at or close to 12h and 24h, since they are aliased in the CSK observations. To overcome this limitation, we refer to the existing ocean tidal models which can provide a starting point from which we can infer the aliased constituents. The ocean tidal models provide the tie between the constituents we can observe and those we cannot. The major limitation of tidal models at RIS is that they do not have sufficient spatial resolution in the vicinity of the grounding zone where we expect amplitudes to gradually decrease towards the grounded ice due to ice-shelf flexure as well as possible variations in phase as observed in Minchew et al. (2017).

The new vertical displacement model we develop combines the completeness of the

ocean tidal model with the high spatial resolution of inferred displacement variation at M_2, N_2, and O_1 periods from our CSK data using the linear model (section 3.3.3). We use the CATS2008 tidal model (Padman et al., 2002), which is shown to agree well with local GPS measurements (Padman et al., 2018). We separately construct the spatial phase and amplitude maps for the 10 major tidal constituents listed in Table 3.1 over the ice-shelf, from which we have the absolute tidal displacement. Then, we introduce ephemeral grounding level as an additional parameter which clips the absolute tidal displacement to arrive at our final vertical displacement model. We present this model in three parts as follows:

1. Spatial phase variation
   We denote the spatial phase variation for a given constituent ξ, as $\phi_\xi(\mathbf{r})$ and define its relative spatial phase variations as:

$$\Delta\phi_\xi(\mathbf{r}) = \phi_\xi(\mathbf{r}) - \phi_\xi(\mathbf{r}_0) \tag{3.26}$$

   where $\mathbf{r}_0$ is a chosen reference point in the central trunk of the ice shelf (Figure 3.1b). Using the inferred spatial phase variation of M_2, N_2, and O_1 from the linear model, we have an estimate of the relative spatial phase variation, which we denote as $\Delta\tilde{\phi}_{M_2}(\mathbf{r})$, $\Delta\tilde{\phi}_{N_2}(\mathbf{r})$, and $\Delta\tilde{\phi}_{O_1}(\mathbf{r})$, where the tilde symbol on top signifies an estimated value. We assume that constituents with similar periods have a similar physical response, so that they share the same relative phase variation. This assumption leads us to the following assumptions on the other 5 semi-diurnal and diurnal constituents:

$$\begin{aligned} \Delta\tilde{\phi}^{\hat{u}}_{S_2}(\mathbf{r}) &= \Delta\tilde{\phi}^{\hat{u}}_{K_2}(\mathbf{r}) = \Delta\tilde{\phi}^{\hat{u}}_{M_2}(\mathbf{r}) \\ \Delta\tilde{\phi}^{\hat{u}}_{K_1}(\mathbf{r}) &= \Delta\tilde{\phi}^{\hat{u}}_{P_1}(\mathbf{r}) = \Delta\tilde{\phi}^{\hat{u}}_{Q_1}(\mathbf{r}) = \Delta\tilde{\phi}^{\hat{u}}_{O_1}(\mathbf{r}) \end{aligned}. \tag{3.27}$$

   Our choice of pairing S_2 and K_2 with M_2 is because the phase of M_2 is better constrained than N_2 due to its larger amplitude. As will be shown when using the actual data, $\Delta\tilde{\phi}_{M_2}(\mathbf{r})$ and $\Delta\tilde{\phi}_{N_2}(\mathbf{r})$ are similar. The linear inversion does not provide access to the phase of M_f and M_m. Because their amplitudes are significantly smaller than other constituents (Table 3.1), there is little impact if we ignore their phase variations.

   We estimate the spatial variations in phase for all tidal constituents by combining the phase at the reference point with the estimated relative phase variation:

$$\phi_\xi(\mathbf{r}) = \phi_\xi(\mathbf{r}_0) + \Delta\tilde{\phi}_\xi(\mathbf{r}) \tag{3.28}$$

where $\phi_\xi(\mathbf{r}_0)$ is the phase of constituent ξ at the reference point and is set by the value extracted from the tide model.

2. Spatial amplitude variation
   The inferred amplitude maps in both Minchew et al. (2017) and our new results (section 3.4.1) suggest that the spatial variations of amplitude in the vicinity of the grounding zone due to ice-shelf flexure are very similar for M_2, N_2, O_1. Therefore, we empirically assume the same normalized spatial amplitude variation for all tidal periods and adopt the following form for the spatial amplitude variation:

$$a_\xi(\mathbf{r}) = A(\mathbf{r})a_\xi(\mathbf{r}_0). \tag{3.29}$$

   Here, $a_\xi(\mathbf{r}_0)$ is the amplitude of constituent ξ at the reference point and is set by the value from the tide model. $A(\mathbf{r})$, a new parameter, is the linear scaling of the amplitude at $\mathbf{r}$ to account for the decreasing amplitude in the vicinity of the grounding zone. We present a more detailed discussion on using $A(\mathbf{r})$ in the supporting information S3.7.6.

3. Ephemeral grounding level
   A new parameter, $K(\mathbf{r})$, denotes the ephemeral grounding level (section 3.3.1 and Figure 3.2b). Given the formulated spatial variations of the phase and the amplitude for all constituents, we arrive at the final vertical displacement model including ephemeral grounding:

$$w^{\hat{u}}(\mathbf{r}, t) = \max(\sum_\xi A(\mathbf{r})a_\xi(\mathbf{r}_0)\sin(\omega_\xi t + \phi_\xi(\mathbf{r})), K(\mathbf{r})) \tag{3.30}$$

   where $a_\xi(\mathbf{r})$ and $\phi_\xi(\mathbf{r})$ are given by equations (3.28) and (3.29). The parameters characterizing the vertical displacement are $A(\mathbf{r})$ and $K(\mathbf{r})$. The inclusion of $K(\mathbf{r})$ causes this new displacement model to be nonlinear.

3.3.4.2 Model for Inferring Ephemeral Grounding Level

Applying the new vertical displacement model to the vertical component of tide-induced displacement (equation 3.2), we arrive at the new model for simultaneously inferring the 3-D surface displacement variation with ephemeral grounding level explicitly taken into account. At any point $\mathbf{r}$, given q displacement observations d_j $(j = 1, 2, \cdots, q)$ with the corresponding observational unit vector $\hat{\mathbf{l}}_j$, and the

acquisition time of primary scene t_j^a and secondary scene t_j^b, we denote this nonlinear model as

$$\begin{aligned}\mathbf{d} &= \mathbf{g}(\mathbf{m}) \\ &= \mathbf{g}(\mathbf{v}, \mathbf{m}^{\hat{e}}, \mathbf{m}^{\hat{n}}, A, K)\end{aligned} \tag{3.31}$$

where $\mathbf{d}$ is the vector of displacement, $\mathbf{m}$ is the model parameter vector, and $\mathbf{g}$ represents the forward function relating the parameters to the observations. The model parameters consist of secular velocity $\mathbf{v} = \begin{bmatrix} v^{\hat{e}} & v^{\hat{n}} & v^{\hat{u}} \end{bmatrix}^T$, parameters for the tide-induced sinusoidal horizontal displacement variation in east and north component $\mathbf{m}^{\hat{e}} = \begin{bmatrix} c_1^{\hat{e}} & s_1^{\hat{e}} & \dots & c_k^{\hat{e}} & s_k^{\hat{e}} \end{bmatrix}^T$, $\mathbf{m}^{\hat{n}} = \begin{bmatrix} c_1^{\hat{n}} & s_1^{\hat{n}} & \dots & c_k^{\hat{n}} & s_k^{\hat{n}} \end{bmatrix}^T$, and the amplitude scaling A and ephemeral grounding level K for the vertical displacement. Given the point $\mathbf{r}$, the forward function $\mathbf{g}(\mathbf{m})$ is formulated as follows:

The observed displacement d_j is the 3-D displacement over $[t_j^a, t_j^b]$ projected onto $\hat{\mathbf{l}}_j$, such that

$$\mathbf{g}(\mathbf{v}, \mathbf{m}^{\hat{e}}, \mathbf{m}^{\hat{n}}, A, K) = \begin{bmatrix} \hat{\mathbf{l}}_1^T \cdot \Delta\mathbf{u}_1 \\ \hat{\mathbf{l}}_2^T \cdot \Delta\mathbf{u}_2 \\ \vdots \\ \hat{\mathbf{l}}_q^T \cdot \Delta\mathbf{u}_q \end{bmatrix} \tag{3.32}$$

where $\Delta\mathbf{u}_j$ is the 3-D displacement vector over the corresponding time interval. We stack the transpose of these vectors by row and form a matrix

$$\begin{bmatrix} \Delta\mathbf{u}_1^T \\ \Delta\mathbf{u}_2^T \\ \vdots \\ \Delta\mathbf{u}_q^T \end{bmatrix} = \begin{bmatrix} \Delta u_1^{\hat{e}} & \Delta u_1^{\hat{n}} & \Delta u_1^{\hat{u}} \\ \Delta u_2^{\hat{e}} & \Delta u_2^{\hat{n}} & \Delta u_2^{\hat{u}} \\ \vdots & \vdots & \vdots \\ \Delta u_q^{\hat{e}} & \Delta u_q^{\hat{n}} & \Delta u_q^{\hat{u}} \end{bmatrix} \tag{3.33}$$

where the three columns are the east, north, and up component of the displacement vectors.

For the east and north component, the relationship with parameters is linear:

$$\begin{bmatrix} \Delta u_1^{\hat{\eta}} \\ \Delta u_2^{\hat{\eta}} \\ \vdots \\ \Delta u_q^{\hat{\eta}} \end{bmatrix} = \begin{bmatrix} u^{\hat{\eta}}(t_1^b) - u^{\hat{\eta}}(t_1^a) \\ u^{\hat{\eta}}(t_2^b) - u^{\hat{\eta}}(t_2^a) \\ \vdots \\ u^{\hat{\eta}}(t_q^b) - u^{\hat{\eta}}(t_q^a) \end{bmatrix} = \begin{bmatrix} \Delta t_1 \\ \Delta t_2 \\ \vdots \\ \Delta t_q \end{bmatrix} v^{\hat{\eta}} + \begin{bmatrix} \Delta t_1 & \Delta p_{1_1}^{\cos} & \Delta p_{1_1}^{\sin} & \dots & \Delta p_{k_1}^{\cos} & \Delta p_{k_1}^{\sin} \\ \vdots & & & \ddots & & \vdots \\ \Delta t_q & \Delta p_{1_q}^{\cos} & \Delta p_{1_q}^{\sin} & \dots & \Delta p_{k_q}^{\cos} & \Delta p_{k_q}^{\sin} \end{bmatrix} \mathbf{m}^{\hat{\eta}} \tag{3.34}$$

where $\hat{\eta} = [\hat{e}, \hat{n}]$, $\mathbf{m}^{\hat{\eta}}$ is the corresponding model parameter vector, Δt_j, $\Delta p_{i_j}^{\cos}$, $\Delta p_{i_j}^{\sin}$ ($i = 1, 2, .., k,\ j = 1, 2, ..., q$) are defined in equation (3.12) to (3.14).

For the up component, the secular term remains the same, but the tide-induced term is set by the new nonlinear vertical displacement model:

$$\begin{bmatrix} \Delta u_1^{\hat{u}} \\ \Delta u_2^{\hat{u}} \\ \vdots \\ \Delta u_q^{\hat{u}} \end{bmatrix} = \begin{bmatrix} \Delta t_1 \\ \Delta t_2 \\ \vdots \\ \Delta t_q \end{bmatrix} v^{\hat{u}} + \begin{bmatrix} w^{\hat{u}}(t_1^b) - w^{\hat{u}}(t_1^a) \\ w^{\hat{u}}(t_2^b) - w^{\hat{u}}(t_2^a) \\ \vdots \\ w^{\hat{u}}(t_q^b) - w^{\hat{u}}(t_q^a) \end{bmatrix} \tag{3.35}$$

where $w^{\hat{u}}(t)(A, K)$ is defined in equation (3.30).

3.3.4.3 A Necessary Condition for Constraining Ephemeral Grounding Level

Ephemeral grounding occurs at lower tides when the total low tide height exceeds the sub-shelf water column thickness. To constrain the ephemeral grounding level, we need satellite data acquired during the period of grounding. Considering that SAR data is temporally sparse (i.e., time interval of a few days), it is possible that little or no data is acquired during periods of ephemeral grounding, especially when the grounding level is low. For any location, a necessary condition for constraining the level of ephemeral grounding is that at least one SAR scene is acquired during ephemeral grounding.

This necessary condition is also reflected in the formulation of the displacement model. Equation (3.35) indicates that the vertical displacement model is constructed by discrete vertical displacement values at the acquisition times of the SAR scenes $w^{\hat{u}}(t)(t = t_1^a, t_1^b, t_2^a, t_2^b, \cdots, t_q^a, t_q^b)$. At any location $\mathbf{r}$, according to equation (3.30), for the ephemeral grounding level K_{true} to take effect in constructing the model, we need

$$\exists t^* \in \{t_1^a, t_1^b, t_2^a, t_2^b, \cdots, t_q^a, t_q^b\} \quad \text{s.t.} \quad K_{\text{true}} > \sum_{\xi} A a_\xi \sin(\omega_\xi t^* + \phi_\xi). \tag{3.36}$$

Equation (3.36) implies that the lowest ephemeral grounding level that the data can constrain in theory is

$$K_{\min} = \min\Big(\sum_{\xi} A a_\xi^{\hat{u}} \sin(\omega_\xi t^* + \phi_\xi^{\hat{u}}) \quad | \quad t^* \in \{t_1^a, t_1^b, t_2^a, t_2^b, \cdots, t_q^a, t_q^b\}\Big) \tag{3.37}$$

and the necessary condition to constrain ephemeral grounding level K_{true} is

$$K_{\text{true}} > K_{\min}. \tag{3.38}$$

At locations, where the vertical displacement without clipping is the same as tide height (e.g., the central trunk of ice shelf), $A = 1$ in equation (3.36), and the necessary condition can be described as the level of ephemeral grounding being higher than the minimum of all sampled tide heights. At locations, where the vertical displacement is damped to be smaller than the tide height (e.g., the vicinity of the grounding zone), we can still use the sampled tide heights at this location to assess the ability of SAR data in detecting ephemeral grounding, because a lower sampled tide height always corresponds to a lower sampled level of vertical displacement, unless already being clipped at a higher level.

If the ephemeral grounding level cannot be constrained, there are two possibilities: (1) there is no ephemeral grounding, or (2) there is ephemeral grounding, but the grounding level K_{true} is so low that the necessary condition is not satisfied. The second possibility implies that any region of ephemeral grounding zone we infer is a lower bound on the actual extent of ephemeral grounding. In section 3.5.3, we present further discussion on the implication of this necessary condition.

3.3.4.4 Formulating and Solving the Inverse Problem

We adopt a Bayesian formulation of the inverse problem assuming Gaussian distributions for all uncertainties. The posterior probability distribution of the model parameters is (Tarantola, 2005):

$$P(\mathbf{m}|\mathbf{d}) \propto P(\mathbf{d}|\mathbf{m})P(\mathbf{m}) \tag{3.39}$$

$$P(\mathbf{d}|\mathbf{m}) \propto \exp(-\frac{1}{2}(\mathbf{d}-\mathbf{g}(\mathbf{m}))^T\mathbf{C}_\chi^{-1}(\mathbf{d}-\mathbf{g}(\mathbf{m}))) \tag{3.40}$$

where $P(\mathbf{m})$ is model prior, $P(\mathbf{d}|\mathbf{m})$ is the data likelihood, and $\mathbf{C}_\chi$ is the error covariance matrix discussed in section 3.3.5. The model prior for secular velocity and horizontal displacement variations is the same as those in the linear model. We adopt a uniform prior for amplitude scaling A in the range of $[0, 2]$ and a uniform prior for the ephemeral grounding K in the range of minimal and maximal tide height at RIS.

We consider each location to be independent of other locations. The total number of grid points are $10^5 \sim 10^6$ depending on the chosen resolution. For nonlinear Bayesian inverse problems, Markov Chain Monte Carlo (MCMC) sampling methods are commonly used for parameter estimations, but performing this method repeatedly at all the grid points is computationally very expensive. To address this computational

difficulty, we use an alternative and equivalent form of the vertical displacement model

$$w^{\hat{u}}(\mathbf{r}, t) = A(\mathbf{r}) \max(\sum_{\xi} \tilde{a}_i \sin(\omega_\xi t + \phi_\xi), K'(\mathbf{r})) \tag{3.41}$$

$$K(\mathbf{r}) = A(\mathbf{r}) K'(\mathbf{r}) \tag{3.42}$$

In the original form (equation 3.41), there are two parameters $A(\mathbf{r})$ and $K(\mathbf{r})$ in the max operator. In this alternative form, $A(\mathbf{r})$ is moved outside of the max operator leaving $K'(\mathbf{r})$ to be the only nonlinear parameter. Once $K'(\mathbf{r})$ is fixed, we can solve for the remaining parameters efficiently using the closed-form solutions for linear problem. Thus, we take the following approach to solve the nonlinear inverse problem problem:

1. Discretize K' with a sampling interval significantly smaller than its intrinsic uncertainty (e.g., 1 cm). We denote the n enumerated values as $K'^{(i)}$, where $i = 1, 2, ..., n$.

2. For every $K'^{(i)}$, solve for remaining parameters and obtain the corresponding model likelihood $P^{(i)}(K'|\mathbf{d})$.

3. The index of the optimal model is $s = \text{argmax}(P^{(i)}(K'|\mathbf{d}), i = 1, 2, \cdots, n)$ and the corresponding optimal enumerated ephemeral grounding level is $K'^{(s)}$. Using the equation (3.42), we get the optimal grounding level K.

4. We obtain the approximate posterior marginal probability distribution of K' from $P^{(i)}(K'|\mathbf{d})$, where $i = 1, 2, \cdots, n$. The marginal distribution quantifies the uncertainty in estimated K' and informs whether the ephemeral grounding level is well constrained.

The revision in the formulation of the inverse problem after introducing K' can be arrived naturally by plugging equation (3.41) into equation (3.35). We describe the revised formulation in the supporting information (S3.7.2).

Besides the computational efficiency, introducing K' has the advantage that it normalizes the ephemeral grounding level in the problem with respect to the amplitude. Clipping on the tidal displacement without amplitude scaling $A(\mathbf{r})$, K' is the normalized version of K, such that it is not sensitive to the amplitude of tidal displacement. The distribution of K' is advantageous over K in evaluating the existence and uncertainty in ephemeral grounding, because a consistent criterion, for example, the

threshold of determining the existence of grounding, can be used in both large and small tidal amplitude scenarios. This advantage can also be viewed as K' automatically scaling the range and sampling interval in the enumeration of grounding level with the amplitude of tidal displacement. Hereafter, unless mentioned explicitly, the distribution and statistics related to ephemeral grounding are all referred to K'.

The linearization of the original nonlinear inverse problem guarantees the solution to be optimal and enables efficiently solving the problem accelerating the computation by many orders of magnitude compared with applying MCMC sampling methods. Although there is the disadvantage that the solution is approximate due to the discretization of K', we can reduce this approximation error to be significantly smaller than the intrinsic uncertainty in the parameters by refining the discretization around the optimum.

3.3.4.5 Tests with Synthetic Data

We test the developed model with the same synthetic RIS model in section 3.3.3.3. For the inference, we use the new vertical displacement model (equation 3.41) and follow the approach in section 3.3.4.4 to solve the inverse problem by enumerating K'. In the synthetic tests, we explore different strategies for enumerating K', quantifying the uncertainty, and determining the whether the ephemeral grounding exists. Our optimization strategy is as follows:

1. Discretize K' in the tidal range $[-4.0\,\mathrm{m}, 4.0\,\mathrm{m}]$ starting with the spacing at 10 cm and iteratively refine the spacing around the optimum down to 1 cm. Resolution of 1 cm is significantly smaller than the intrinsic uncertainty in K'.

2. Calculate the approximate marginal posterior probability distribution of K' from enumerated $P(K'|\mathbf{d})$ and find the 68% credible interval around the optimum (supporting information S3.7.3).

3. Consider the ephemeral grounding as well-constrained if the necessary condition (section 3.3.4.3) is satisfied and the 68% credible interval of K' is smaller than the prescribed threshold 60 cm.

Figure 3.4 shows the result from applying the nonlinear model to synthetic data. For the vertical displacement, both the linear amplitude scaling $A(\mathbf{r})$ and grounding level $K(\mathbf{r})$ are in good agreement with the prescribed values. Comparing with the

result of the linear model (Figure S3.13), the bias in the estimated amplitude and phase of horizontal M_{sf} displacement variation is greatly reduced.

3.3.5 Error Model

In both the linear model (section 3.3.3) and nonlinear model (section 3.3.4), we consider both the measurement error and modeling error. Under the assumption of Gaussian distributions for all uncertainties, we have the following relationship (Tarantola, 2005)

$$\mathbf{C}_\chi = \mathbf{C}_d + \mathbf{C}_p \tag{3.43}$$

where $\mathbf{C}_d$ is the data measurement covariance matrix and $\mathbf{C}_p$ is the covariance matrix for modeling error, which is also referred to as prediction error.

We use cross-correlation methods to calculate displacement from SAR scenes (see section 3.2). The variance of the measured displacement $\mathbf{C}_d$ is estimated from the curvature of the correlation surface (Joughin, 2002) denoted as $\hat{\mathbf{C}}_d$. The modeling error $\mathbf{C}_p$ can come from multiple sources including but not limited to (1) error in amplitude and phase values of the tidal constituents used to model vertical displacement, (2) error in our assumption of the relative phase variation (equation 3.27), (3) error from not modeling M_f and short-period horizontal flow variability. We do not have a good prior model for $\mathbf{C}_\chi$.

A χ^2 residual analysis provides an empirical way to estimate $\mathbf{C}_\chi$. More specifically, the normalized misfit r_i, $r_i = (d_i - (\mathbf{Gm})_i)/\sigma_i$, should be roughly normally distributed with standard deviation one, where i is the i-th data point and σ_i is its standard deviation in the error model (e.g., Aster et al., 2018). Thus, the square of residual $d_i - (\mathbf{Gm})_i$ should be on the same scale as $\mathbf{C}_\chi$.

We assume the error to be independent (i.e., $\mathbf{C}_\chi$ is diagonal) and employ the following approach for inversion:

1. Assuming 10 cm error for all displacement data, conduct a first inversion and find the residual of each data point.

2. For the data on the same grid point, group the data points according to the observational unit, which is determined by track and range/azimuth measurement. Assuming data in the same group share the error model, calculate the error for each group using the residual from the initial inversion. The diagonal entries of $\hat{\mathbf{C}}_\chi$ are the variances of the residual in the corresponding groups.

3. Conduct a second inversion using the empirically estimated error model $\hat{\mathbf{C}}_\chi$.

Using this empirical approach residual, we have found that the modeling error dominates the measurement error ($\hat{\mathbf{C}}_d \ll \hat{\mathbf{C}}_\chi$) in the inversion with real data. Our experiences with exploring $\hat{\mathbf{C}}_\chi$ shows that inclusion of modeling error and adoption of the empirically estimated $\hat{\mathbf{C}}_\chi$ is important for reducing artifacts in the results and making realistic quantification of uncertainty.

3.4 Results

We apply both the linear model (section 3.3.3) and nonlinear model (section 3.3.4) to the processed ~2500 displacement fields. The two models both infer the secular velocity and horizontal displacement variation at M_{sf} period, but differ in the inference of vertical displacement. We note that in all figures, phase values are centered at the mean phase in the observational domain and converted to the unit of minutes or days based on the period of the tidal constituent. The fortnightly flow variation is shown in displacement domain.

3.4.1 Application of the Linear Model

We describe the inferred vertical displacements including short-period M_2, N_2, and O_1 and the key diagnostic long-period M_{sf} that reveals ephemeral grounding. We leave discussions of the inferred secular velocity and horizontal M_{sf} displacement variation in the supporting information (S3.7.5). Note that in Minchew et al. (2017), M_2 and O_1 displacement were inferred and reported, but N_2 was not. Based on the inferred amplitude at M_2 period, we also derive an updated grounding line which has better accuracy than the existing grounding line data (Rignot et al., 2011a; Fretwell et al., 2013). We show this derived grounding line and compare it with the existing grounding line data in the supporting information S3.20 and include the data in the supporting information (Grounding line - RIS) as well. We use this new grounding line in all the figures.

3.4.1.1 Semidiurnal and Diurnal Component

The spatial variability in M_2, N_2, and O_1 components are similar in terms of amplitude (Figure 3.5a1-c1), but the spatial variability of the phase differ from component to component (Figure 3.5a2-c2). The displacement amplitude of the three components in the central trunk is about 1.6 m, 0.3 m and 0.4 m, respectively. These values are consistent with the CATS2008 tidal model (Table 3.1). The

inferred amplitude is uniform in the central trunk and decreases in the vicinity of the grounding zone sharing similar spatial patterns supporting the assumption we use in the nonlinear model that all tidal constituents share the normalized spatial variability of amplitude. The strongest feature is the circular zone about 10 km in diameter in the middle on the west margin where the amplitude is only 20% of its central trunk amplitude. The phase estimates for M_2 and N_2 lag ($\phi < 0$) by approximately 20 min within 10 km of grounding zone. The phase lag is more pronounced in the two horns of the grounding line than the ice shelf margins. O_1 does not exhibit lagging phases in the grounding zone, but has prevalent and uniform leading phase by approximately 20 min over the upstream half of the ice-shelf in our observational domain. This variation of O_1 phase is likely to be spurious because it is similar in both the value and the shape to the theoretical bias in O_1 phase estimation found in our synthetic test (Figure S3.11). There is a zone of M_2 leading phase in the central trunk 20 km downstream of the grounding line, which is consistent with the previously reported ephemeral grounding point (Schmeltz et al., 2001). The leading phase at this known ephemeral grounding zone is consistent with our synthetic test which shows that the linear model can produce spurious leading/lagging phase because ephemeral grounding is not explicitly accounted for (Figure S3.13). Phase estimates at all three tidal periods show significant leading and lagging phase (leading or lagging more than 50 min) within the low-amplitude circular zone on the west margin, suggesting that this is a pronounced ephemeral grounding zone.

3.4.1.2 M_{sf} Component and Ephemeral Grounding

Inference of a large-amplitude vertical M_{sf} component indicates the existence of ephemeral grounding (Figure 3.5d1-3.5d2). Because this fortnightly component does not correspond to any existing tidal forcing, its phase variation does not have immediate physical meaning. Here we only focus on the amplitude map which reveals three primary ephemeral grounding zones:

A. An isolated circular zone in the central trunk 20 km downstream of the grounding line. This zone was previously reported in Schmeltz et al. (2001).

B. An approximately 5-km-wide zone along the west margin of the ice shelf, extending to the southern end of our observational domain. There is a pronounced circular zone with relatively large M_{sf} amplitude in the middle.

C. An approximately 5-km-wide and 20-km-long zone within the eastern horn of the grounding line in the vicinity of the eastern half of the U-shaped bend of the grounding line. The southern end of this zone connects to the bathymetric ridge at the corner of the grounding line that pins the grounded ice.

The detection and quantification of ephemeral grounding confirms the prior suggestion of such zones at RIS. However, we also recognize that some of the observed strong variations in the phase of vertical displacement are artifacts due to not accounting for ephemeral grounding in the model.

3.4.1.3 Comparison of Tidal Model and Inference from the Linear Model

We compare our inferred amplitude and phase values of vertical displacement at M_2, N_2, and O_1 periods with the CATS2008 tidal model (Padman et al., 2002) at a reference point (82.0°W, 78.8°S) chosen to be away from the vicinity of any grounding (Figure 3.1b). Given the theoretical bias in our estimation from the synthetic test (section 3.3.3.3), we also compare the bias-corrected amplitude and phase values to the tidal model (Table 3.2 and 3.3). Although the comparison is made at one point, it is representative of the ice shelf central trunk in our observational domain because the tidal displacement is spatially uniform.

We find that the estimated amplitude and phase at all three tidal periods agree well with the tidal model. We also find that the theoretical bias in the estimation explains the relatively large difference between the estimation and the tidal model, such as the amplitude of O_1 and the phase of N_2. This comparison validates our inferred values and shows that the inferred bias in the synthetic test is realistic and can be used to adjust inferred values from the linear model.

3.4.2 Application of the Nonlinear Model

We now describe the inference of amplitude scaling and ephemeral grounding level using the nonlinear model. In terms of the horizontal secular velocity, our updated results agree well with Minchew et al. (2017) albeit with fewer artifacts in the vertical component. Details can be found in the supporting information (S3.7.9). The final spatial resolution of the reported fields is determined by the processed displacement fields and is approximately 500 m. Animations showing the vertical motion (Movie RIS-V) and the horizontal ice flow (Movie RIS-H) are provided in the supporting information.

3.4.2.1 Construction of the Vertical Displacement Model

To apply the nonlinear model, we construct the vertical displacement model (equation 3.30) by jointly using the CATS2008 tidal model and the inferred vertical displacement at M_2, N_2, and O_1 periods from the linear model (section 3.3.4). We set the reference point $\mathbf{r}_0$ at (82.0°W, 78.8°S) (Figure 3.1b) where we have shown that the tidal model agrees with the bias-corrected estimation of M_2, N_2, and O_1 in both amplitude and phase (section 3.4.1.3). To use the results from the linear model, we correct for the bias in all inferred values using the bias inferred from the synthetic tests (supporting information S3.7.1). We construct the vertical displacement model following the methodology in section 3.3.4.1. For details, see supporting information (S3.7.7).

3.4.2.2 Vertical Displacement with Ephemeral Grounding

The inferred amplitude scaling, $A(\mathbf{r})$, representing the amplitude of vertical displacement at all tidal periods, is uniform in the central trunk, gradually decreases in the vicinity of the grounding zone and is zero on the grounded ice (Figure 3.6a). The amplitude scaling typically decreases from 1 to 0 over distances of approximately 5 km on both the western and eastern ice shelf margins. The circular zone in the middle of ice shelf western margin has an amplitude approximately 20% the amplitude in the central trunk. Near the grounding line horns, the amplitude starts to decrease towards the U-shaped bend of grounding line and gradually decrease to zero within in the two horns (Figure 3.6a).

The ephemeral grounding zones are consistent with the inferred amplitude of the vertical M_{sf} component from the linear model (section 3.4.1.2). Here, we discuss the three primary ephemeral grounding zones (Figure 3.6b-c):

A. For the isolated ephemeral grounding zone in the central trunk (A), the grounding level is approximately -1.7 m at its center and gradually decreases towards the periphery. The lowest grounding level detected is approximately -2.5 m at on the northern end. As described in section 3.3.4.3, the inferred ephemeral grounding zone is the minimum spatial extent of the actual ephemeral grounding zone.

B. The grounding level on the western margin is relatively high, ranging from -1 m to 0 m. The northern portion (B1) is approximately 5-km-wide with

the grounding level increasing towards the grounding line. The width of this zone decreases towards the south. The low-amplitude circular-zone (B2) has a relatively high grounding level near 0 m. We find no ephemeral grounding to the north and less ephemeral grounding to the south of this zone. The southern portion (B3) has a similar grounding level as the northern portion.

C. The grounding level of the ephemeral grounding zone in the eastern horn of the grounding line (C1) ranges from −0.5 m to 0 m, increasing as one approaches towards the grounding line. This whole zone is slightly wider than the zone on the western margin and exhibits a smaller gradient in the change of grounding level. Within the western horn of the grounding line, a small ephemeral grounding zone (C2) exists at the northern end with the level of ephemeral grounding close to 0 m.

We find the zones of ephemeral grounding primarily exist in the vicinity of the grounding zone along the western margin of RIS. The spatial distribution of zones of ephemeral grounding should reflect the current bathymetry beneath RIS. On the western side, the seaward slopes of the bed should be relatively small which introduce relatively wider grounding zone and more abundant existence of ephemeral grounding. On the eastern side, the bed should be steep which makes the grounding zone to be narrow and limits the existence of ephemeral grounding.

Considering the total area and the grounding level, the main ephemeral grounding zone is on the western margin (B1-B3). This zone should contribute most to the tide-modulated buttressing stress compared with other zones. That the southern portion of this zone extends to the southern end of our observational domain suggests that zones of ephemeral grounding extend further the downstream. Observations have shown that the grounded portion of the RIS upstream of the grounding line is deeper on its western margin (Fretwell et al., 2013; Morlighem et al., 2020), so the thickness of the ice shelf downstream should also be thicker on the western side. Whether the ephemeral grounding on the western margin downstream of the grounding line is caused by the increased ice-shelf thickness or variations in sub-shelf bathymetry remains an open question.

3.4.2.3 Horizontal Fortnightly Flow Variability

Here, we present the inferred variations in flow and the derived strain rates. In the 2-D horizontal plane, we define along-flow and cross-flow as the directions along

(parallel to) and cross (perpendicular to) the inferred direction of secular velocity. The cross-flow direction is 90° counter-clockwise from the along-flow direction.

This updated version of fortnightly flow is consistent with the results in Minchew et al. (2017) in terms of the major features and has improvement in three aspects: (1) There were artifacts in Minchew et al. (2017) which are the discontinuities of variation at SAR acquisition track boundaries and some extreme values caused by the instability in the inversion due to lack of data. This new version has less artifacts and enables deriving variations in strain rates. (2) The inferred heterogeneity of the fortnightly flow in Minchew et al. (2017) may be overestimated due to the aforementioned artifacts. This version shows that the fortnightly flow has smoother spatial variation. (3) This version includes better resolved cross-flow component and shows the periodic divergence and convergence of the flow.

3.4.2.3.1 Variation in the Along-Flow Component

The along-flow variation is highest over the ice shelf with an amplitude of approximately 40 cm and varies smoothly in space (Figure 3.7a). The trend of increasing amplitude downstream suggests that this variation is not local on the observed portion of the ice shelf. The low amplitudes along the western margin should be primarily due to the low mean flow speed.

Leading phase values are present over the ice-shelf (Figure 3.7b) and are relatively uniform. The prominent circular ephemeral grounding zone in the middle along the western margin (B2) has the most leading phase values. The isolated ephemeral grounding zone in the central trunk of the ice-shelf (A) also exhibits leading phases. In addition, phases at the ice-shelf margins, where ephemeral grounding are likely to exist, generally lead the phases in the ice-shelf central trunk. All these observations suggest that ephemeral grounding plays an important role in the generation of fortnightly flow variation.

3.4.2.3.2 Variation in the Cross-Flow Component

The amplitude of the cross-flow variation on the ice shelf ranges from 5 cm in the central trunk to 15 cm located along the western and eastern ice shelf margins and near the U-shaped bend of the grounding line (Figure 3.7c). The phase of this variation is anti-symmetric with the maximum difference of phase values on the western and eastern sides at half of the fortnightly period (approximately 7.4 days). We find that the large amplitudes near the margin and anti-symmetry in phase together lead

the periodic divergence and convergence of the ice flow during acceleration and deceleration (Movie RIS-H).

3.4.2.3.3 Strain-Rate Variations

The longitudinal strain rate ($\dot{\epsilon_{xx}}(t) = \partial(v_x(t) - \bar{v}_x)/\partial x$, where x is in the along-flow direction) calculated from the fortnightly flow rate shows extension and compression of the ice in the along-flow direction during acceleration and deceleration (Movie RIS-H). At the centerline of RIS, the amplitude of variation is approximately 5μ/day. The localized high strain-rates are present at the central bathymetric ridge that pins the grounding line at the downstream extent of the U-shaped bend and near the circular zone of pronounced ephemeral grounding on the western ice-shelf margin (Figure 3.8 and 3.9). Large negative strain rates with amplitude larger than 10μ/day are present when the ice is accelerating suggesting that the ephemeral grounding provides resisting stress to ice flow.

The transverse strain rate ($\dot{\epsilon_{yy}}(t) = \partial(v_y(t) - \bar{v}_y)/\partial y$ where y is in the cross-flow direction) shows the extension and compression of ice in the cross-flow direction during acceleration and deceleration which corresponds to the ice-flow divergence and convergence (Movie RIS-H). The strain rates with amplitudes of approximately 10μ/day are present in two-bands along ice-shelf flow with less variation in the center (Figure 3.8 and 3.9). Near the circular zone on the western margin where the pronounced ephemeral grounding is located, there is compression during acceleration which is presumably driven by basal pinning (Movie RIS-H).

The second invariant of areal strain rate measuring the magnitude of strain rate ($\frac{1}{2}(\text{trace}(\epsilon^2) - \text{trace}(\epsilon \cdot \epsilon))$) shows the dominant strain rate in the shear strain in the western and eastern margins. The strain rate along the western margin is more dispersed and has more spatial variations due to the more complicated margin geometry, ephemeral grounding, and the inflow of the Minnesota Glacier (MG) that intersects RIS (Figure 3.1b). The eastern grounding line horn where the ephemeral grounding exists experiences a higher magnitude of strain rate than the western horn.

3.5 Discussion

3.5.1 Asymmetric Response to Tidal Forcing

Previous studies have suggested that the M_{sf} signal over the ice-shelf-stream at RIS is driven by the asymmetric response of ice shelf flow to the high and low tide. By studying the variation of the lateral shear strain rate, Minchew et al. (2017) proposed that the ephemeral (periodic) grounding of the ice shelf during low tide along the ice

shelf margin leads to the tide-modulated contact area of the ice shelf with the bed changing the effective ice shelf width, with the resulting temporal evolution of the basal shear traction and the buttressing stress giving rise to the observed variations flow rate. Motivated by the theoretical model on the tide-modulated asymmetric grounding line migration (Tsai and Gudmundsson, 2015) and the observations of the ephemeral grounding at RIS (Schmeltz et al., 2001; Minchew et al., 2017; Robel et al., 2017) proposed that the ice shelf buttressing stress to be an asymmetric function of the tide height with the high tide corresponds more significant buttressing stress decrease than the equivalent low tide corresponds to the buttressing stress increase. Employing this buttressing stress model, they were able to reproduce the amplitude and phase of the observed fortnightly flow rate variation in a 1-D model using Maxwell viscoelastic rheology. Using extensive GPS records, Rosier et al. (2017) showed that this fortnightly flow rate variation is prevalent over the entire Filchner-Ronne Ice Shelf (FRIS) and all the adjoining ice streams including RIS. The amplitude of this variation increases downstream to the ice shelf front suggesting that the underlying mechanism is not particular to a certain ice stream. Using the realistic geometry of FRIS and a 3-D full Stokes viscoelastic model, Rosier and Gudmundsson (2020) were able to reproduce the amplitude of this fortnightly flow rate variation by modeling the asymmetric grounding line migration (Tsai and Gudmundsson, 2015; Minchew et al., 2017) and the nonlinear dependence of the flow rate on the ice shelf width. Warburton et al. (2020) developed a mathematical model showing that grounding line migration is dependent on the permeability and drainage speed of the subglacial hydrological system. The effective grounding line can be pinned at the point of the high tide for low-permeability system resulting in asymmetric widening and shrinking of grounding zone and leading to the fortnightly flow variability.

While all the aforementioned mechanisms point to the asymmetric response of the ice shelf flow to the tidal forcing, the observational evidence has been limited. Our study here focuses on observing the ephemeral grounding of the ice shelf, a potentially important mechanism for generating the tide-modulated buttressing (Minchew et al., 2017; Robel et al., 2017), and shows that the ephemeral grounding at RIS is not limited to the pinning point detected by Schmeltz et al. (2001), but also present in significantly larger zones including the western ice shelf margin and the eastern grounding line horn. This observation provides direct evidence for the tide-modulated grounding of the ice-shelf and provides support for mechanisms dependent on the evolution in basal shear traction. The ephemeral grounding

on the western margin also suggests the existence of more ephemeral grounding downstream outside of our observational domain and the potential for explaining the fortnightly flow rate variation outside RIS.

3.5.2 Long-Term Response to Ice Shelf Thinning

The western Antarctic ice-sheet (WAIS) is unstable in response to the ongoing oceanic warming and ice-shelf melting (e.g., Joughin et al., 2012; Alley et al., 2015). Buttressing stress from the ice shelves plays an important role in regulating the ice-sheet discharge (e.g., Thomas, 1979; Dupont and Alley, 2005; Gudmundsson, 2013). However, with ice-shelf thinning and grounding line retreat, the resulting reduction in basal traction allows the ice flow to speed up and thin, and the grounding line to retreat, especially where the bed is prone to marine ice-sheet instability (Weertman, 1974; Schoof, 2007; Cuffey and Paterson, 2010). Such dynamic response of the ice flow to ice shelf thinning has been observed at multiple glaciers, such as Pine Island Glacier and Thwaites Glacier, along the Amundsen coast where the flow acceleration currently accounts for most of the ice discharge increase from the western Antarctica (e.g., Joughin et al., 2014; Sutterley et al., 2014; Gardner et al., 2018). Unlike the ice shelves in Amundson sea sector, FRIS currently has a net mass loss close to zero, resulting in almost constant ice thickness and no increase in ice discharge (e.g., Pritchard et al., 2012; Paolo et al., 2015). However, studies have shown that sub-shelf ocean currents below FRIS could transition from cold to warm by the end of the century increasing the basal melting by more than a order of magnitude (Hellmer et al., 2012). Such change can lead to decrease of the buttressing stress and increase outflows from the adjoining ice streams, and potentially removing large portions of WAIS.

The tide-induced ephemeral grounding is the intermediate state between a grounded and an ungrounded state. Compared with permanent pinning points, the buttressing effect of the ephemeral grounding zones is more sensitive to ice-shelf thinning which causes immediate shrinkage of the grounding zone area and the further transition into an ungrounded state. Thus, quantifying the buttressing effect of the ephemeral grounding zone and the loss of the buttressing due to ice-shelf thinning is important for predicting the future response of Antarctic glaciers to oceanic warming and ice shelf thinning.

The secular loss of this buttressing should in turn be compensated for by increased drag upstream. Given a decrease in longitudinal stress $\Delta\tau_{xx}$ due to decreased

buttressing, the predicted increase in longitudinal ice-flow rate is

$$\Delta v_x = \Delta \dot{\epsilon}_{xx} \cdot L = \frac{\Delta \tau_{xx}}{2\eta} \cdot L \tag{3.44}$$

where $\dot{\epsilon}_{xx}$ is the longitudinal strain rate, L is a characteristic length scale ($L = 100\,\mathrm{km}$ for RIS), and η is the effective dynamic viscosity which is inferred to be $\sim 10^{15}\mathrm{Pa} \cdot \mathrm{s}$ at RIS (Minchew et al., in prep.).

We can estimate current variations in longitudinal stress using the measured flow variability. Using the laterally confined ice stream model, Minchew et al. (in prep.) developed a theoretical model characterizing the relationship between the variation in longitudinal stress and variation in velocity. Using this relationship, we estimate the variation in longitudinal stress to be approximately 100 KPa (see the supporting information S3.7.10). Assuming that the current tide-induced buttressing stress variation is mainly associated with the sub-shelf bathymetry and can be largely reduced by the future ice-shelf thinning, the current variation in longitudinal stress is the lower bound the of the decrease in longitudinal stress. This 100 KPa decrease in longitudinal stress corresponds to an increase in ice flow rate by approximately 0.5 m/day at RIS (equation 3.44), which corresponds to a 50% increase relative to characteristic present-day secular rates of approximately 1 m/d.

3.5.3 Mapping Ephemeral Grounding Zone with SAR Observations

We demonstrate a methodology for identifying uncharted ephemeral grounding zones and quantifing the grounding level using temporally dense SAR observations. The identification of sub-shelf pinning points has previously relied on the detection of surface elevation changes, including ice rises and ice rumples, using satellite imagery (e.g., Scambos et al., 2007; Matsuoka et al., 2015). Feature tracking on synthetic aperture radar and optical images can reveal modulated ice flow by the pinning points (e.g., Rignot, 2002). Because ephemeral grounding does not introduce significant surface expression or modulated ice flow that traditional approaches rely on, there has not been comprehensive documentation of ephemeral grounding zones. The few observations of ephemeral grounding are limited to the ephemeral grounding points in the ice shelf central trunk which can be are revealed by the localized “bull’s eye” patterns in the interferograms (e.g., Schmeltz et al., 2001; Milillo et al., 2019). However, this approach does not work well for detecting ephemeral grounding in the vicinity of the grounding zone or large regions devoid of localized patterns in the radar data.

The key characteristic that determines the capability of SAR observations on constraining the ephemeral grounding is how much and how well we sample low tide. The sampling is determined by the SAR acquisition times and the corresponding tidal displacement. Analysis of the suite of observations at RIS reveals the lowest sampled tide at any spatial point and shows that different tracks have different sensitivity to low tides (Figure 3.10). Because of the periodic nature of tides, the efficacy of any future the future observation campaign for study ephemeral grounding can be easily evaluated and optimized in the planning stage.

3.6 Conclusions

Building upon the linear geodetic model for inferring 3-D surface velocity variations from temporally dense SAR observations (Minchew et al., 2017), we fuse information from a tidal model and satellite observations to develop a new nonlinear geodetic model which simultaneously infers variations in the 3-D displacement field and tide-induced ephemeral grounding. With the increasing availability of temporally dense satellite observation (e.g., the Sentinel-1 mission, the NASA-ISRO SAR mission), the developed geodetic model for constraining the ephemeral grounding demonstrates the possibility of studying more complex (e.g., nonlinear) temporally-dependent displacement variations. The special case of tidal phenomenon also reveals the limitations of integer-day repeating times, as widely employed by space-borne SAR missions and motivates planning more observations with flexibility in choosing repeat-pass time intervals.

Our study at RIS improves on the previous result in Minchew et al. (2017) and explicitly identifies ephemeral grounding zones. The inferred ephemeral grounding zones provide new observational evidence for the asymmetric response of the ice-shelf flow to the high and low tides, which is a key component in all proposed mechanisms for generating the observed fortnightly flow variability. With continued oceanic warming and ice-shelf thinning, the loss of this ephemeral grounding will decrease buttressing stress. For RIS, we estimate that just the loss of the presently identified ephemeral grounding zones will result in at least a 50% increase ice flux. Actual increases would presumably be larger as some fully grounded regions will become ephemeral as the ice thins.

Acknowledgements

The presented work is possible due to the availability of raw COSMO-SkyMed SAR imagery provided by the Italian Space Agency (ASI) as a dedicated campaign to

image Rutford Ice Stream. We sincerely thank ASI for all their efforts in making this campaign successful.

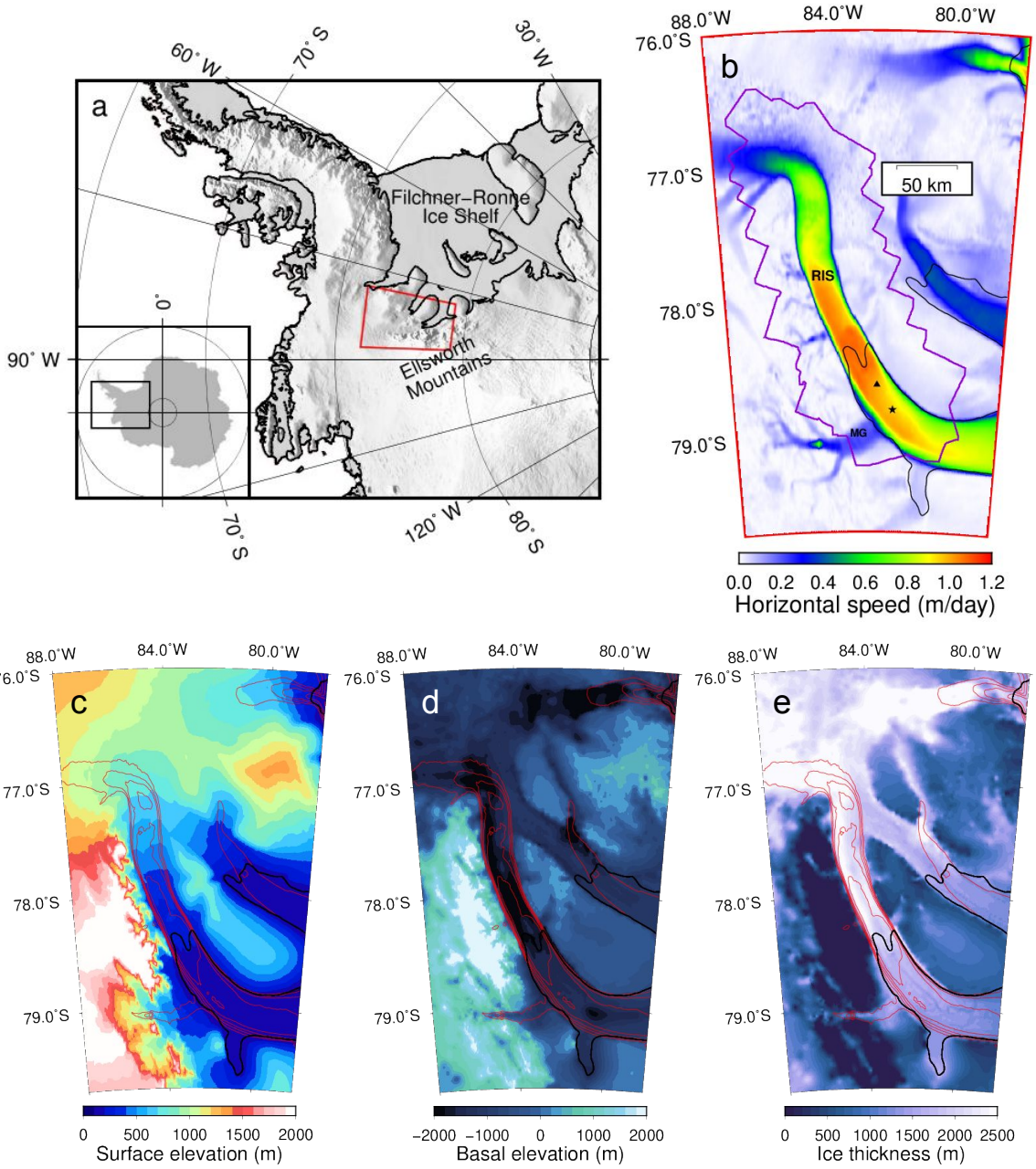
a
60° W
70° S
30° W
Filchner–Ronne
Ice Shelf
0°
90° W
Ellsworth
Mountains
70° S
120° W
80° S
b
88.0°W
84.0°W
80.0°W
76.0°S
77.0°S
78.0°S
79.0°S
50 km
RIS
MG
0.0 0.2 0.4 0.6 0.8 1.0 1.2
Horizontal speed (m/day)
c
0 500 1000 1500 2000
Surface elevation (m)
d
−2000 −1000 0 1000 2000
Basal elevation (m)
e
0 500 1000 1500 2000 2500
Ice thickness (m)

Figure 3.1: (a) Shaded relief map of RIS and surrounding area. Red box indicates the region shown in Figures 1b–1e. (b) Horizontal velocity from Mouginot et al. (2012). Purple outline indicates the extent of the CSK observations used in this study. The black star and triangle in the ice shelf central trunk indicate the reference point used in our study and the ephemeral grounding point reported in Schmeltz et al. (2001), respectively. MG indicates Minnesota Glacier flowing into RIS. (c and d) Surface and basal elevation relative to mean sea level. (e) Ice thickness. Red contour lines in Figures 1c–1e indicate horizontal surface velocity from Figure 1b in 0.2 m/d increments. In all panels, irregular black lines indicate the grounding line. All the elevation data is from BedMachine V2(Morlighem et al., 2020). In all panels, irregular black lines indicate grounding line from Bedmap2 (Fretwell et al., 2013). This figure is adapted from Figure 1 in Minchew et al. (2017) with updates of elevation data from Bedmap2 to BedMachine V2.

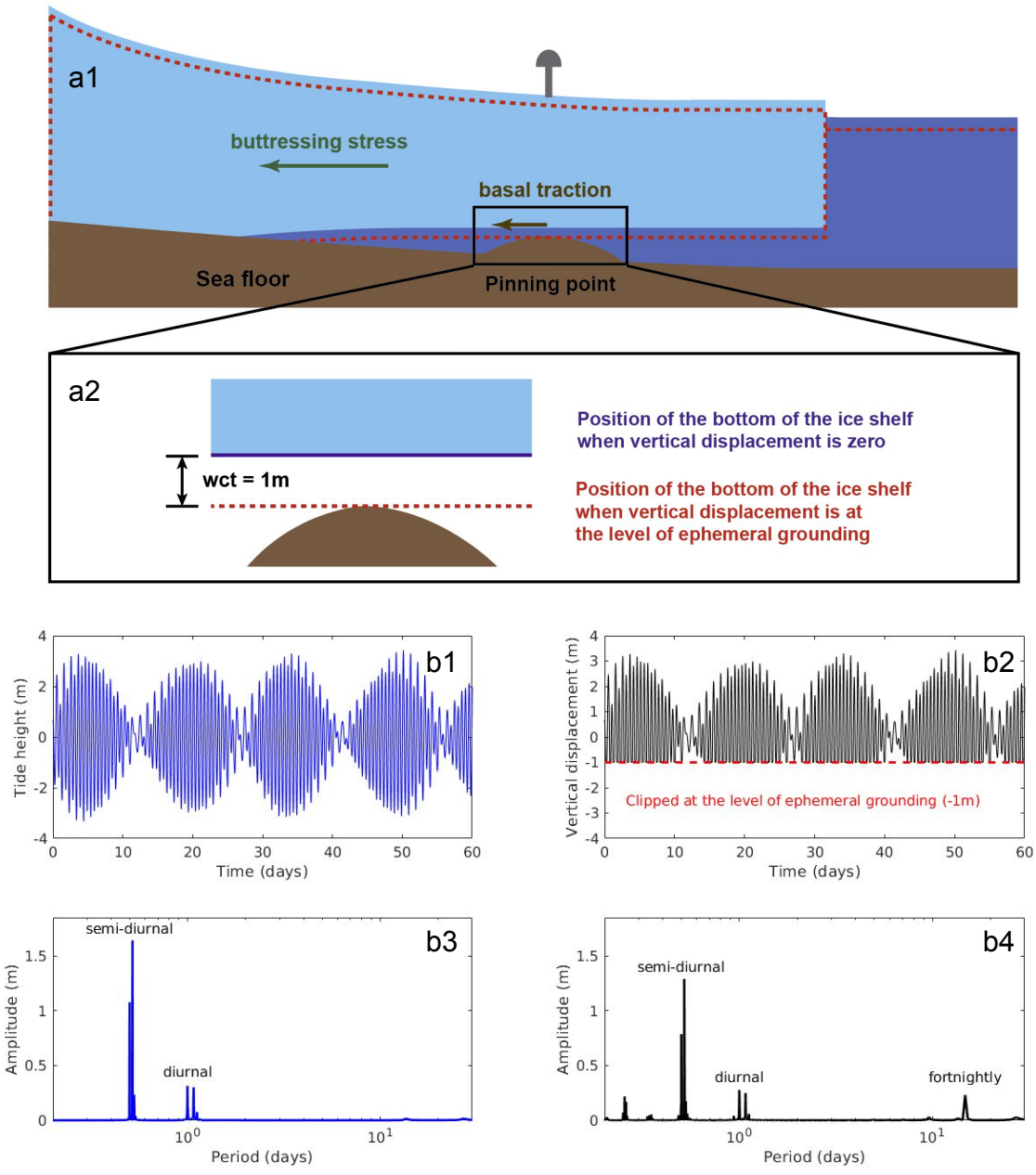
a1
buttressing stress
basal traction
Sea floor
Pinning point
a2
wct = 1m
Position of the bottom of the ice shelf
when vertical displacement is zero
Position of the bottom of the ice shelf
when vertical displacement is at
the level of ephemeral grounding
b1
Tide height (m)
Time (days)
b2
Vertical displacement (m)
Clipped at the level of ephemeral grounding (-1m)
Time (days)
b3
semi-diurnal
diurnal
Amplitude (m)
Period (days)
b4
semi-diurnal
diurnal
fortnightly
Amplitude (m)
Period (days)

Figure 3.2: (a1) Schematic view of tide-induced ephemeral grounding on a sub-shelf pinning point. The red dashed line indicates the location of the ice-shelf in hydrostatic balance with the ocean during at the level of ephemeral grounding. The brown arrow indicates the basal traction induced by the ephemeral grounding. The green arrow indicates the ice shelf buttressing stress. (a2) The level of the bottom of ice shelf when tide height is at mean sea level (solid blue) and at the level of ephemeral grounding (dashed red). (b1) Tidal height at RIS from the CATS2008 tidal model at a reference point in the central trunk (Figure 3.1b). (b2) Vertical displacement at the point indicated by the gray GPS station which is at the surface point of the shown sub-shelf pinning point. The level of clipping induced by ephemeral grounding is -1 m, which is defined as the level of ephemeral grounding. (b3-b4) Amplitude spectrum of the time series of displacement in b1 and b2.

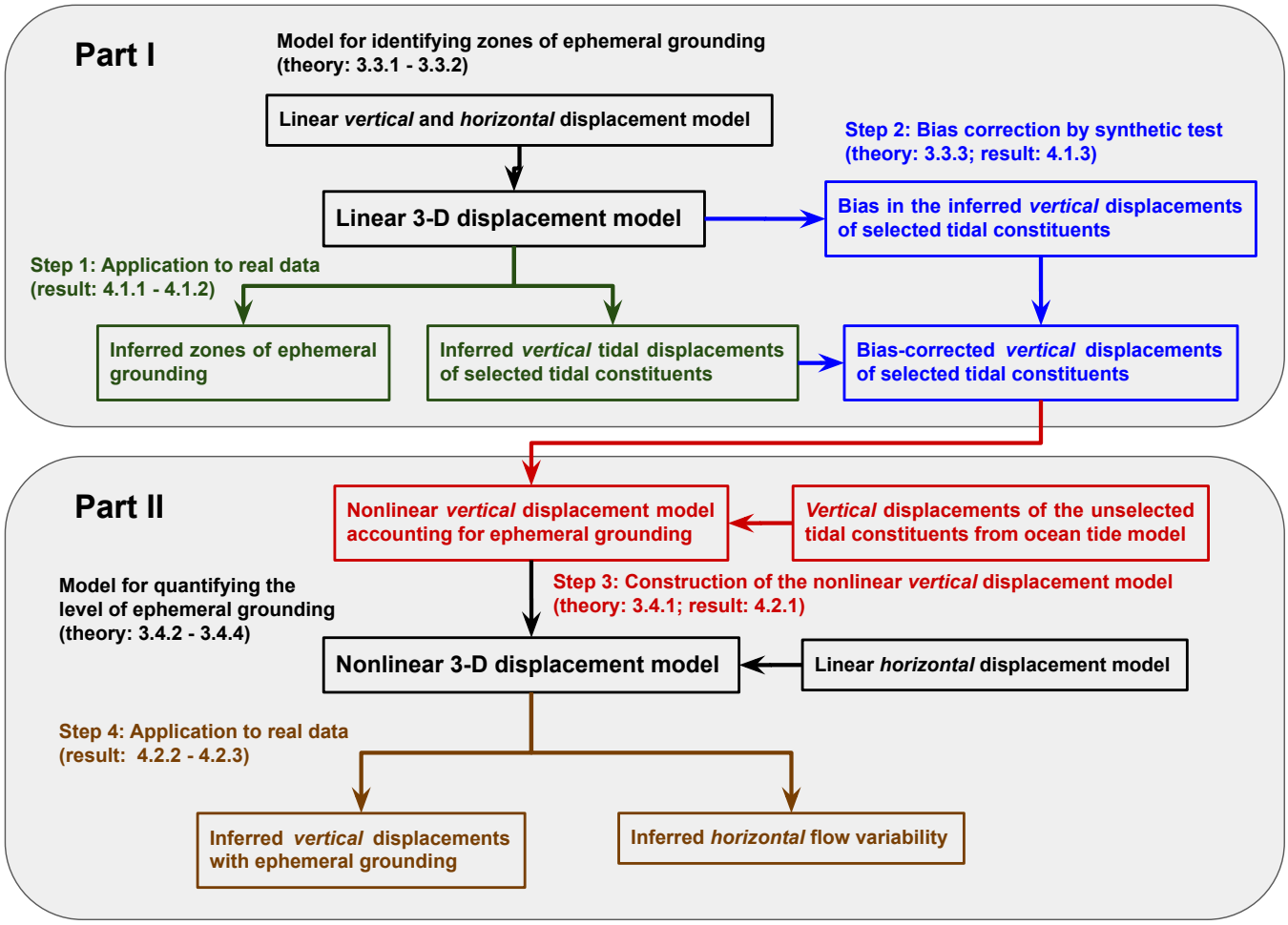

Figure 3.3: Outline of the workflow described herein. The workflow has two parts which are associated with a linear 3-D displacement model in the upper panel and the a nonlinear 3-D displacement model in the lower panel, respectively. The full workflow consists of the two models and four steps. For each model and step, we direct the corresponding section numbers in this paper.

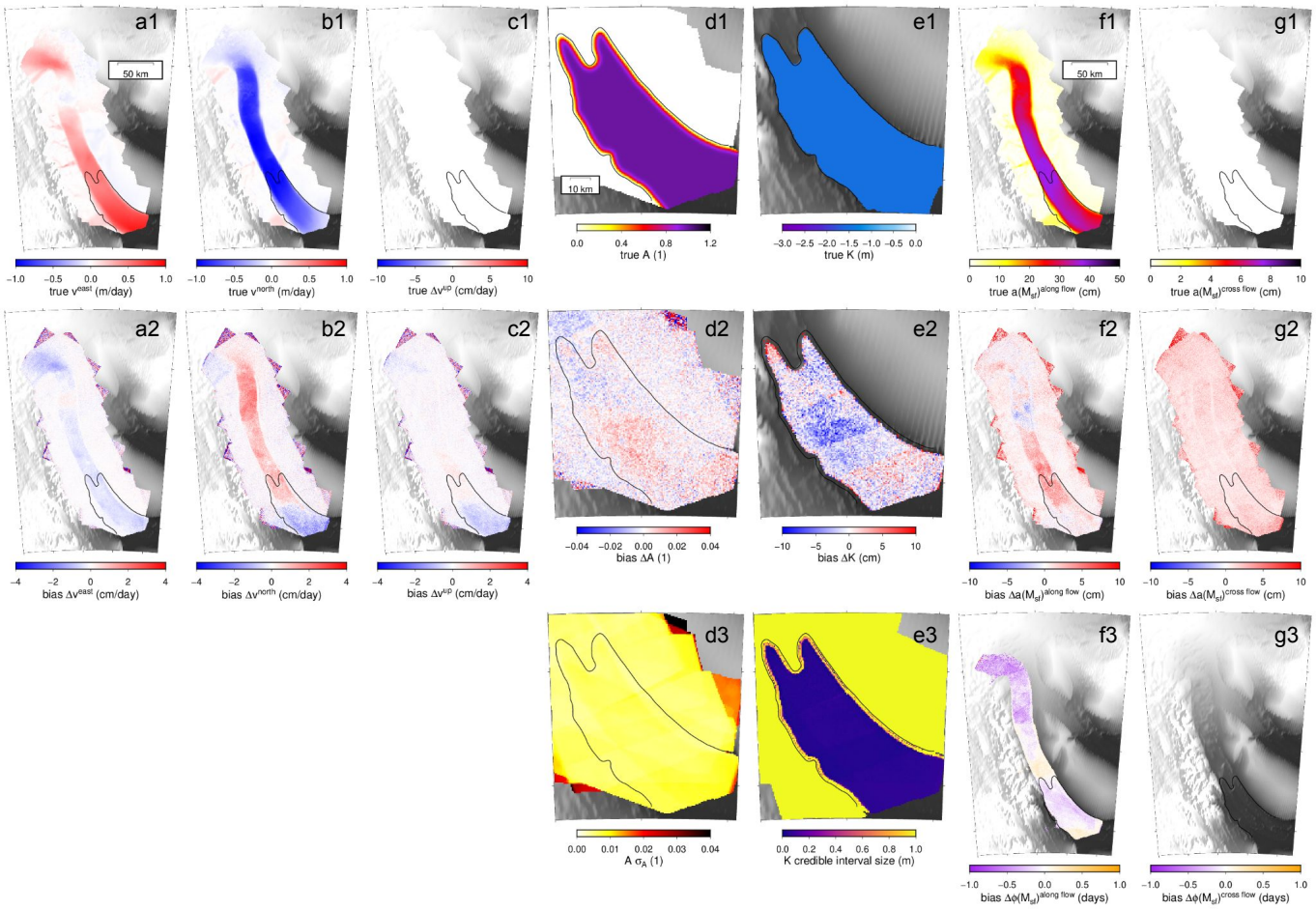

Figure 3.4: Results of synthetic tests. Input and bias of estimated secular velocity and tide-induced displacement using the nonlinear model assuming the seafloor is 1.5 m beneath the mean level of ice-shelf base. (a1-c1) Input horizontal and vertical secular velocity. (d1) Input vertical amplitude scaling. (e1) Input ephemeral grounding level. (f1-g1) Input horizontal sinusoidal displacement at M_{sf} period. (a2-c2) Bias of estimated secular velocity. (d2) Bias of estimated vertical amplitude scaling. (e2) Bias of estimated ephemeral grounding level. Only grounding level values with the credible interval size smaller than 60 cm is considered valid and shown. (d3) Formal error (1-σ) of vertical amplitude scaling. (e3) Credible interval (68%) size of the posterior probability distribution of grounding level. (f2-g2) Bias of estimated amplitude of horizontal displacement. (f3) Bias of estimated phase of horizontal sinusoidal displacement. (g3) Bias in estimated phase for cross-flow M_{sf} is not available because the input phase is undefined due to zero amplitude. The background is shaded surface elevation from Morlighem et al. (2020).

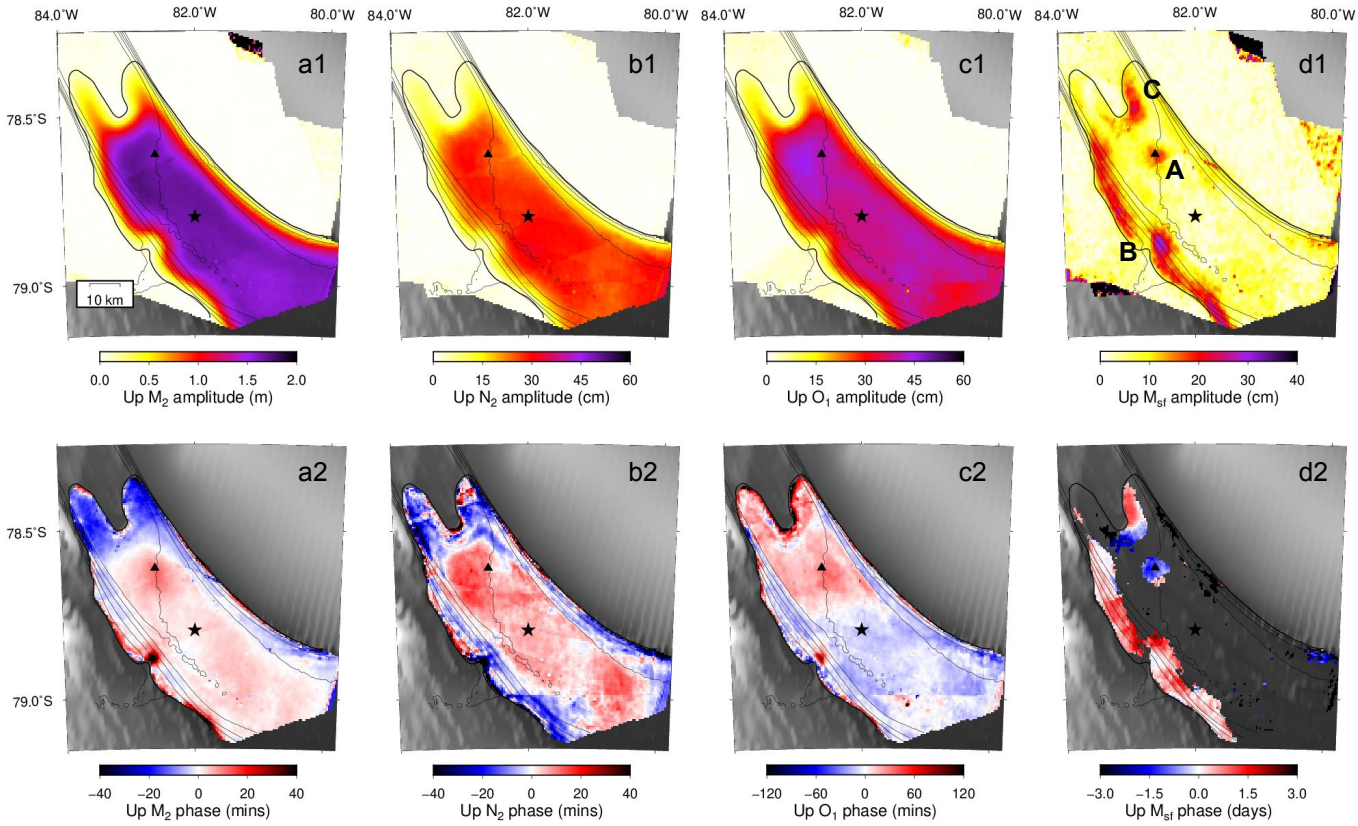

Figure 3.5: The tide-induced vertical displacement variation at M_2, N_2, O_1, and M_{sf} periods. (a1-d1) Amplitude variations of the vertical displacement. (a2-d2) Phase variations of the vertical displacement centered at the mean phase. Phase estimates with small amplitude (< 10 cm) are not shown. Grounding lines are derived from the amplitude of M_2 using the 5 cm amplitude contour. Black star and triangle indicate the reference point and the ephemeral grounding point reported in Schmeltz et al. (2001). Black contour lines are inferred horizontal speed in 0.2 m/d increments. The background is shaded surface elevation from Morlighem et al. (2020).

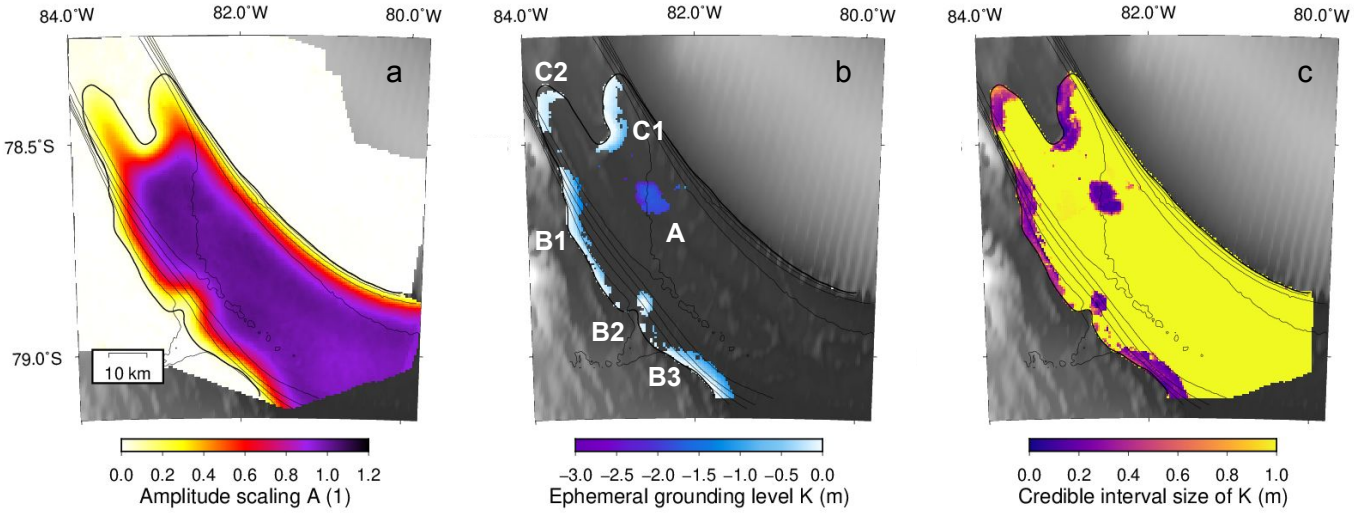

Figure 3.6: Vertical displacement inferred from the nonlinear model. (a) Amplitude scaling $A(\mathbf{r})$ for all constituents. (b) Ephemeral grounding level $K(\mathbf{r})$. Only the estimated values with credible interval size < 60 cm) are shown. (c) The credible interval size of the normalized ephemeral grounding level. Black contour lines are inferred horizontal speed in 0.2 m/d increments. The background is shaded surface elevation from Morlighem et al. (2020).

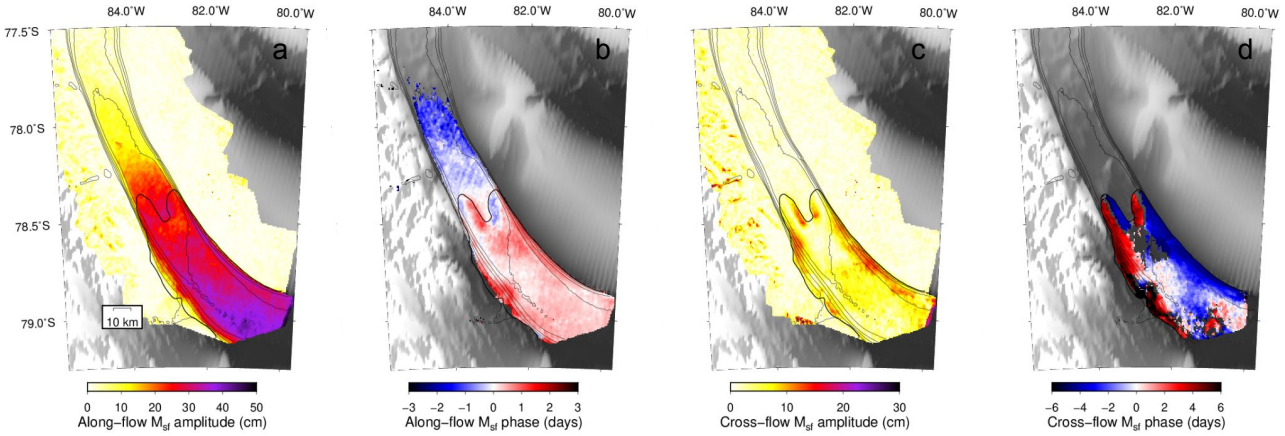

Figure 3.7: Along-flow and cross-flow horizontal displacements at M_{sf} (14.77 day) period. (a) Amplitude of the along-flow displacement. (b) Phase of the along-flow displacement. (c) Amplitude of the cross-flow displacement. (d) Phase of the cross-flow displacement. Black contour lines are inferred horizontal speed in $0.2\,\mathrm{m/d}$ increments. The background is shaded surface elevation from Morlighem et al. (2020).

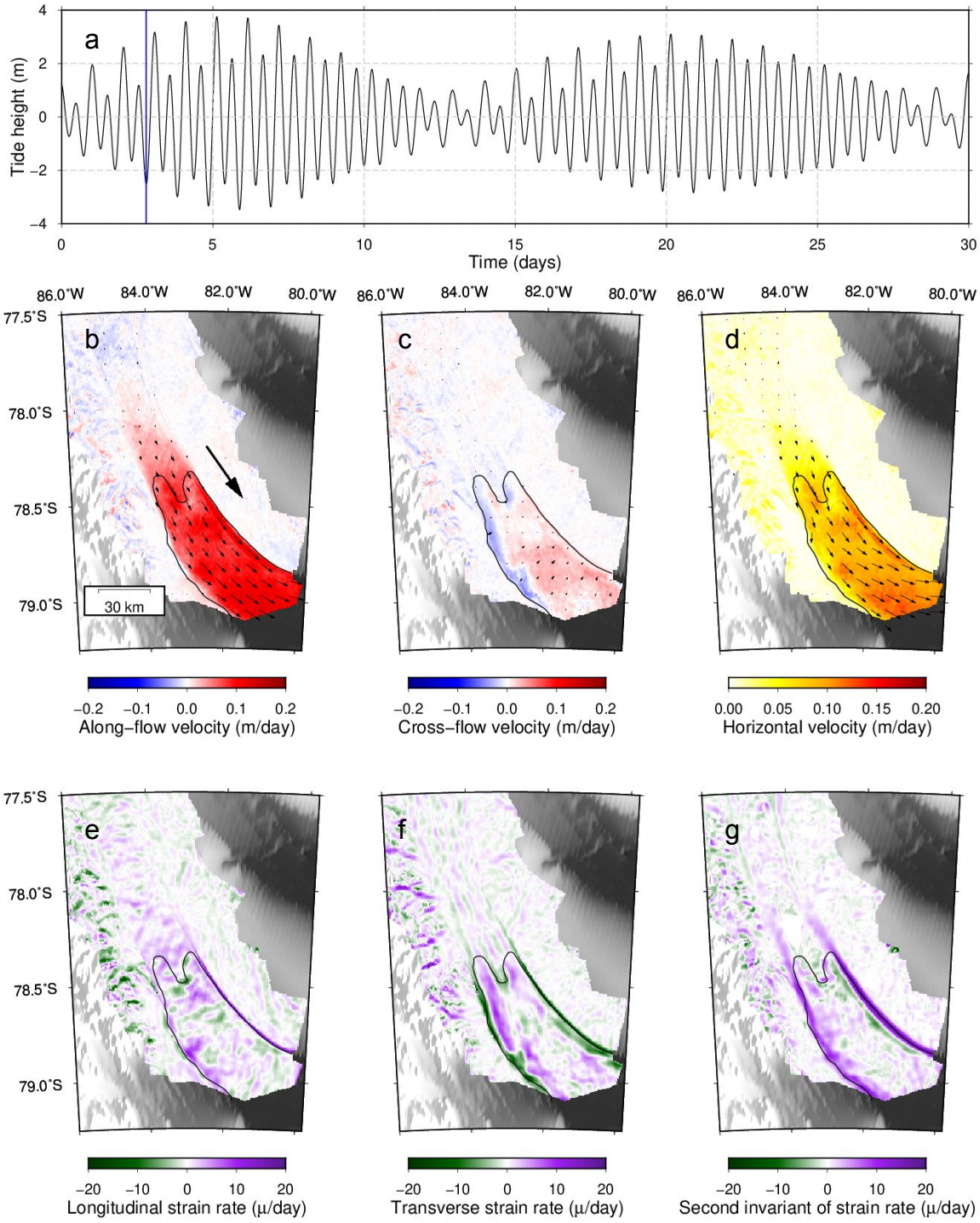
a
Tide height (m)
Time (days)
b
c
d
30 km
Along−flow velocity (m/day)
Cross−flow velocity (m/day)
Horizontal velocity (m/day)
e
f
g
Longitudinal strain rate (μ/day)
Transverse strain rate (μ/day)
Second invariant of strain rate (μ/day)

Figure 3.8: A snapshot of tide-induced velocity and strain rate variation during flow acceleration (secular velocity removed). (a) Tidal displacement at the reference point in the central trunk where the red line indicates time of the snapshot. (b) Along-flow velocity. Arrows indicate the along-flow direction whose sizes scale with the speed. The big arrow indicates the direction of secular flow. (c) Cross-flow velocity. Arrows indicate the cross-flow variation whose sizes scale with the speed. (d) Total velocity variation. Color indicates the speed of fortnightly flow velocity. Arrows indicate direction and scale with speed. (e) Longitudinal strain rate. (f) Transverse strain rate. (g) Second invariant of the areal strain rate tensor variation. The background is shaded surface elevation from Morlighem et al. (2020).

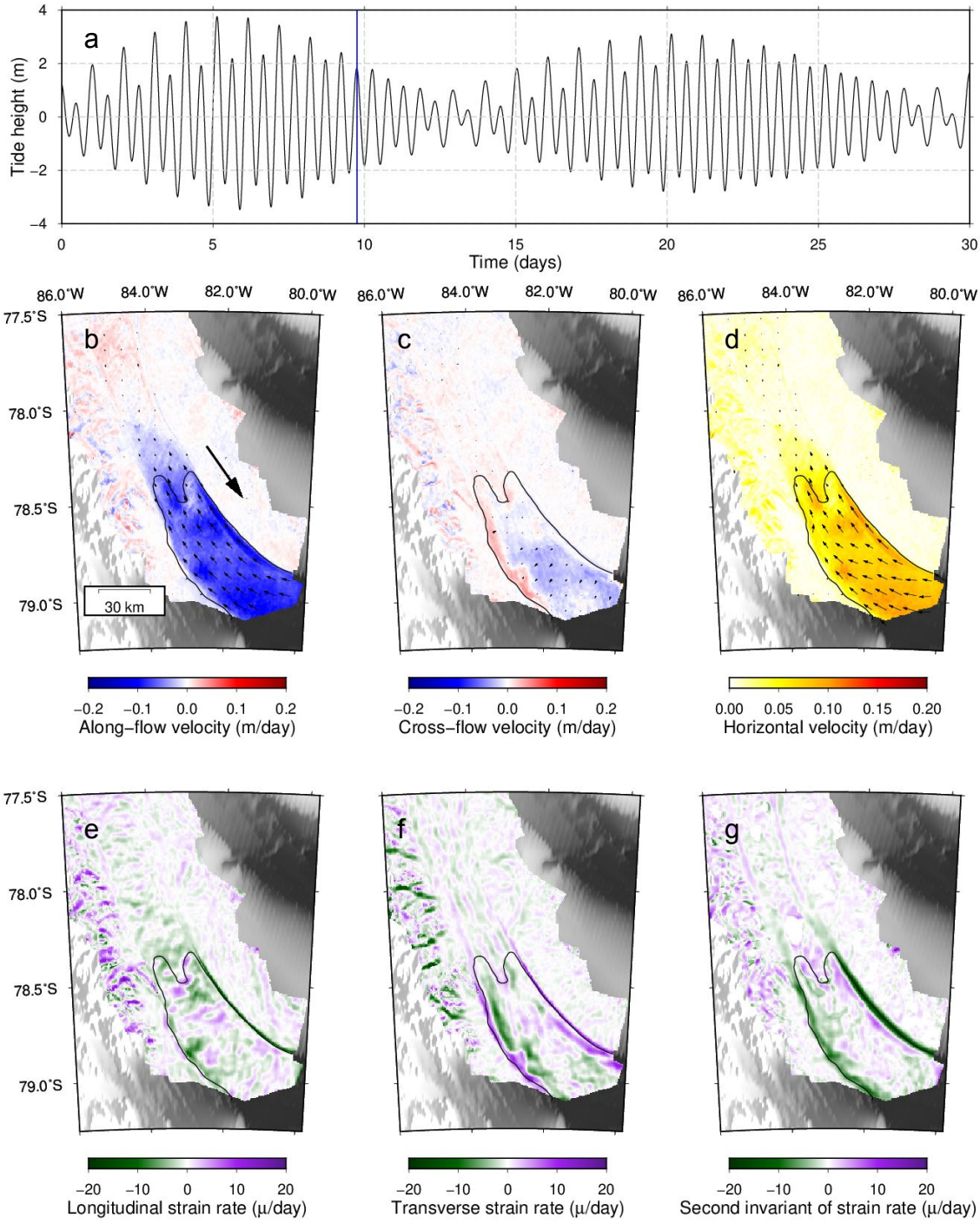

Figure 3.9: A snapshot during flow deceleration. The layout of panels is the same as in Figure 3.8.

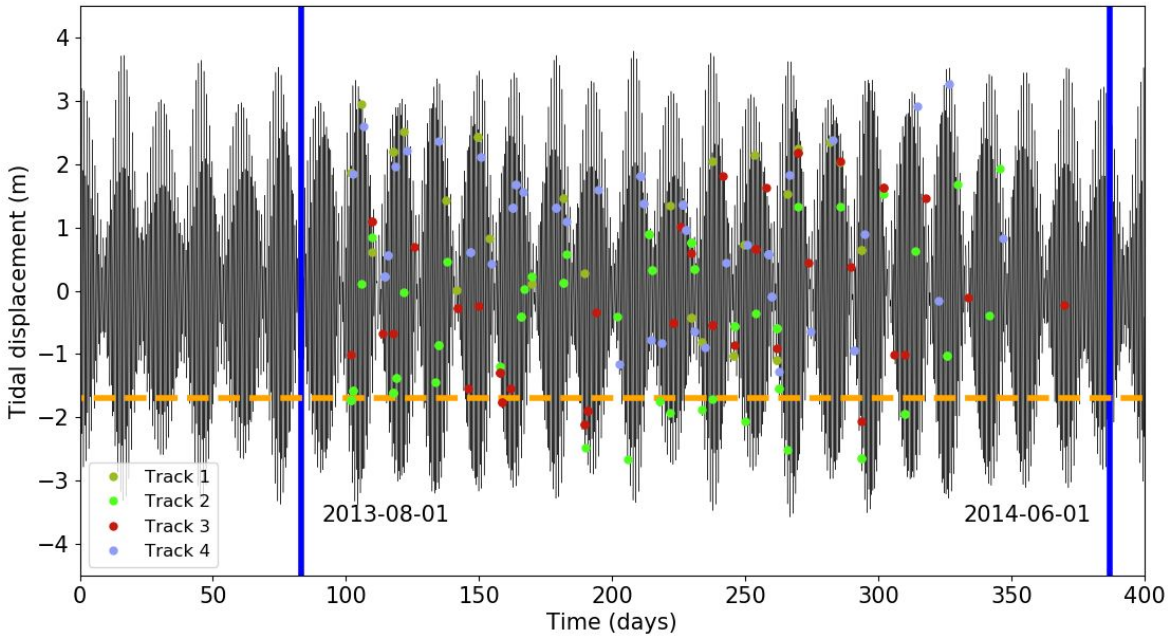

Figure 3.10: Tidal displacement time series (CATS2008 tidal model) and the temporal sampling of the SAR observations, sampled at the ephemeral grounding point in the central trunk where the inferred level of ephemeral grounding is approximately -1.7 m. Each SAR acquisition is shown at its timing and corresponding tide height. Colors indicate observations from different satellite ground tracks. The dashed orange line indicates the inferred level of ephemeral grounding. The two blue lines indicate the approximate start and end of the observation campaign.

Constituent	Period (days)	Reference Amplitude (m)	Reference Phase (°)	Inferred Amplitude (m)	Inferred Phase (°)
M_2	0.5175	1.647	120.69	1.666	119.63
S_2	0.5000	1.087	-10.82	-	-
N_2	0.5274	0.277	24.60	0.278	25.00
K_2	0.4986	0.238	-162.11	-	-
K_1	0.9973	0.374	36.99	-	-
O_1	1.0758	0.352	113.82	0.368	112.65
P_1	1.0027	0.140	12.92	-	-
Q_1	1.1195	0.079	10.72	-	-
M_f	13.6608	0.020	5.32	-	-
M_m	27.5546	0.017	11.99	-	-

Table 3.1: Reference amplitude and phase values from the CATS2008 tidal model at the reference point in the central trunk of RIS. Inferred amplitude and phase values with bias-correction at the reference point are from the linear model.

Amplitude (m)

Constituent ξ	$\hat{a}(\xi)$	$\Delta\tilde{a}(\xi)$	$\tilde{a}(\xi)$ - $\hat{a}(\xi)$	$\tilde{a}(\xi)$ - $\Delta\tilde{a}(\xi)$ - $\hat{a}(\xi)$
M_2	1.647	-0.003	0.016	0.019
N_2	0.277	0.005	0.006	0.001
O_1	0.352	0.020	0.036	0.016

Table 3.2: Comparison of the inferred amplitude and the reference amplitude at the reference point. $\hat{a}(\xi)$: reference amplitude from the CATS2008 tidal model. $\Delta\tilde{a}(\xi)$: estimated bias in the inferred amplitude. $\tilde{a}(\xi) - \hat{a}(\xi)$: difference between inferred amplitude and reference amplitude. $\tilde{a}(\xi) - \Delta\tilde{a}(\xi) - \hat{a}(\xi)$: difference between bias-corrected inferred amplitude and reference amplitude.

Phase (°)

Constituent ξ	$\hat{\phi}(\xi)$	$\Delta\tilde{\phi}(\xi)$	$\tilde{\phi}(\xi)$ - $\hat{\phi}(\xi)$	$\tilde{\phi}(\xi)$ - $\Delta\tilde{\phi}(\xi)$ - $\hat{\phi}(\xi)$
M_2	120.69	0.29	-0.77	-1.06
N_2	24.60	7.27	7.66	0.40
O_1	113.82	1.95	0.77	-1.17

Table 3.3: Comparison of the inferred phase and the reference phase at the reference point. $\hat{\phi}(\xi)$: reference phase from the CATS2008 tidal model. $\Delta\tilde{\phi}(\xi)$ estimated bias in inferred phase. $\tilde{\phi}(\xi) - \hat{\phi}(\xi)$: difference between inferred phase and reference phase. $\tilde{\phi}(\xi) - \Delta\tilde{\phi}(\xi) - \hat{\phi}(\xi)$: difference between bias-corrected inferred phase and reference phase.

S3.7 Supplementary Information

S3.7.1 Synthetic Test of the Linear Model

We discuss the results of the optimal model for no-grounding (Figure S3.11 and Figure S3.12) and grounding scenarios (Figure S3.13 and Figure S3.14). In the no-grounding scenario, the bias of amplitude estimation for M_2, N_2, O_1, and M_{sf} is less than 5 cm. Bias in the phase estimation of M_2 is close to zero; for N_2, there is an approximately +20 min bias uniformly across the entire ice shelf; for O_1, there is approximately +20 min bias on the upstream half of the ice shelf except the western and eastern margins. Near the southern end of the area of observation where the available viewing angles are limited, the bias in the estimation can increase. In the grounding scenario, the estimates of the vertical displacement for M_2, N_2, and O_1 has moderate difference when compared with the no-grounding scenario. The estimated amplitude of these three are systematically underestimated and has bias at -20 cm, -10 cm, and -5 cm, respectively. For the phase estimation, there is an approximately 10 min bias for M_2, an approximately +20 min bias for N_2, and an approximately +40 min bias for O_1 in upstream half similar to no-grounding scenario. Due to the grounding, the amplitude of the key vertical M_{sf} increases from less than 5 cm in the no-grounding scenario to approximately 25 cm. The two synthetic tests show that the vertical displacement at M_2, N_2, and O_1 can be well estimated. More importantly, they demonstrate that the vertical M_{sf} constituent can serve as a diagnostic proxy for the existence of ephemeral grounding.

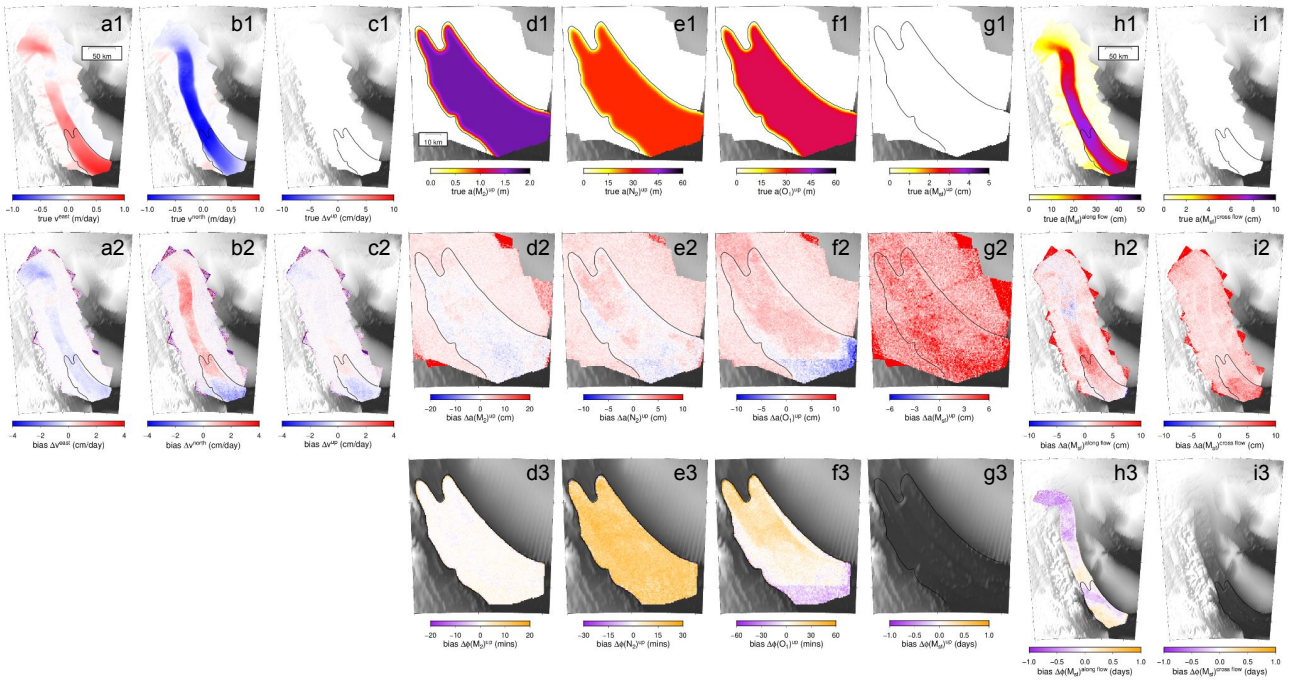

Figure S3.11: Input and the bias of estimated secular and tide-induced displacement using the linear model when there is no ephemeral grounding. (a1-c1) Input secular horizontal and vertical velocity. (d1-g1) Input amplitude of vertical sinusoidal displacement at M_2, N_2, O_1, and M_{sf} period. (h1-i1) Input amplitude of horizontal sinusoidal displacement at M_{sf} period. Input phases of all sinusoidal displacement are spatially constant and are not shown. The bias of estimation is defined as the inferred value minus the input value. (a2-c2) Bias of estimated secular velocity. (d2-g2) Bias of estimated amplitude of vertical sinusoidal displacements. (d3-g3) Bias of estimated phase of sinusoidal vertical displacements. (h2-i2) Bias of estimated amplitude of horizontal sinusoidal displacement. (h3-i3) Bias of estimated of phase of horizontal sinusoidal displacement. Phase estimates which correspond to small amplitude estimates and large uncertainties are not shown.

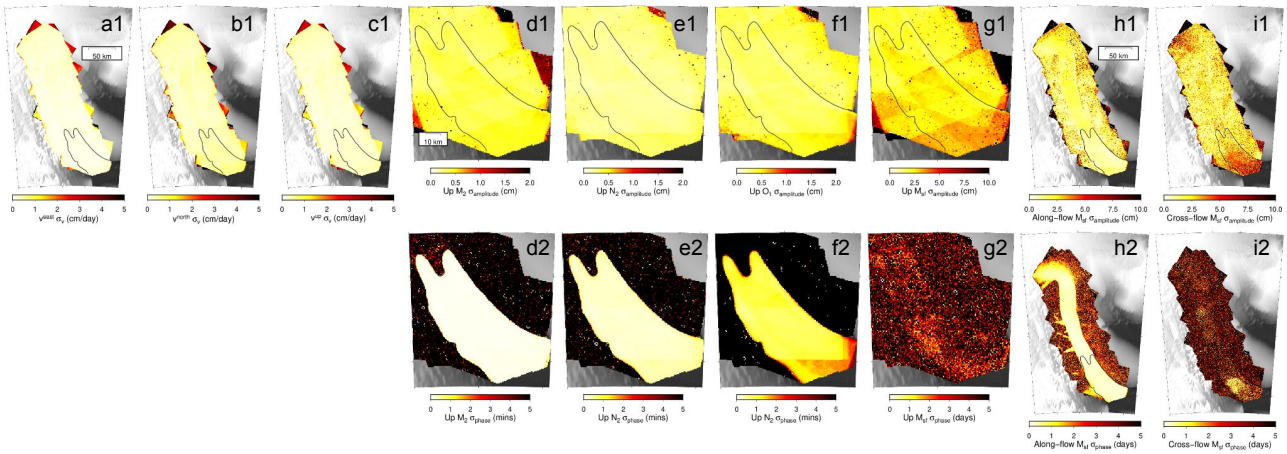

Figure S3.12: Formal errors in estimated secular velocity, vertical displacement, and horizontal displacement variations in the synthetic test without ephemeral grounding inferred by the linear model. (a1-c1) Standard deviation of estimated secular east, north, up velocity. (d1-g1) Standard deviation of estimated vertical displacement amplitude at M_2, N_2, O_1, M_{sf} periods. (h1-i1) Standard deviations of along-flow and cross-flow displacement amplitude at M_{sf} period. (d1-g1) Standard deviation of estimated vertical displacement amplitude at M_2, N_2, O_1, M_{sf} periods. (h2-i2) Standard deviation of estimated along-flow and cross-flow displacement phase at M_{sf} period.

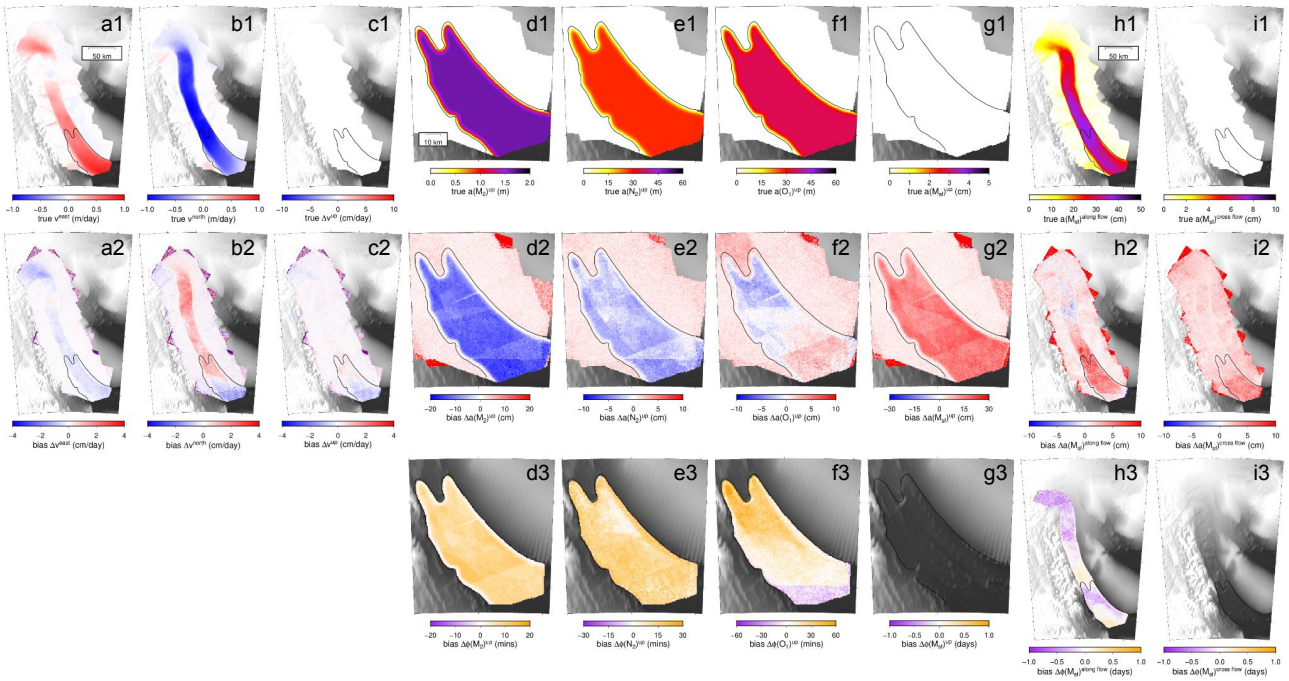

Figure S3.13: Input and the bias of estimated secular and tide-induced displacement using the linear model assuming the seafloor is 1.5 m beneath the ice-shelf. Ephemeral grounding occurs when the low tide is smaller than −1.5 m. The layout of the panels is the same as Figure S3.11.

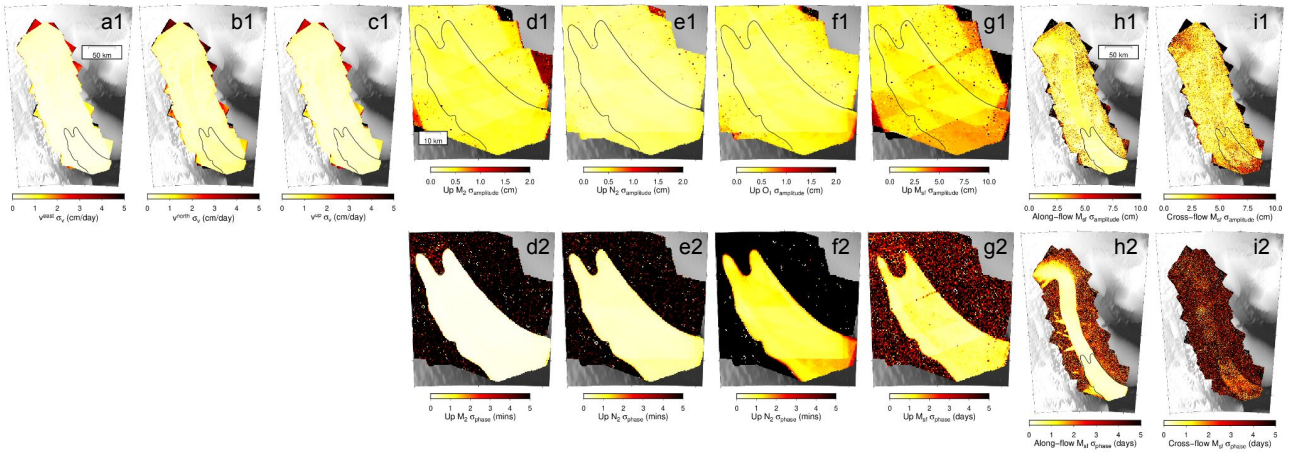

Figure S3.14: Formal errors in estimated secular velocity, vertical displacement, and horizontal displacement variations in the synthetic test with ephemeral grounding inferred by the linear model. The layout of the panels is the same as Figure S3.12.

S3.7.2 Formulation of the Linearized Inverse Problem

Let $E(t) = \max(\sum_{\xi} \tilde{a}_{\xi} \sin(\omega_{\xi} t + \phi_{\xi}), K'(\mathbf{r}))$, then we can write the up component of displacement vector as

$$\begin{bmatrix} \Delta u_1^{\hat{u}} \\ \Delta u_2^{\hat{u}} \\ \vdots \\ \Delta u_q^{\hat{u}} \end{bmatrix} = \begin{bmatrix} \Delta t_1 \\ \Delta t_2 \\ \vdots \\ \Delta t_q \end{bmatrix} v^{\hat{u}} + \begin{bmatrix} E(t_1^b) - E(t_1^a) \\ E(t_2^b) - E(t_2^a) \\ \vdots \\ E(t_q^b) - E(t_q^a) \end{bmatrix} A. \tag{S3.45}$$

We can arrive at the form of the linear inverse problem for the remaining parameters naturally combining the linear form of all three components and projecting the displacement vectors onto the observational unit vectors:

$$\mathbf{d} = \mathbf{G}'\mathbf{m}' \tag{S3.46}$$

where $\mathbf{d}$ is observed displacement, the $\mathbf{G}'$ is the design matrix, and $\mathbf{m}'$ includes all parameters except K. We can find the optimal model using the closed-form solutions

$$\tilde{\mathbf{m}}' = (\mathbf{G}'^T \mathbf{C}_{\chi}^{-1} \mathbf{G}' + \mathbf{C}_{m'}^{-1})^{-1} \mathbf{C}_{\chi}^{-1} \mathbf{G}'^T \mathbf{d} \tag{S3.47}$$

$$\tilde{\mathbf{C}}_{m'} = (\mathbf{G}'^T \mathbf{C}_{\chi}^{-1} \mathbf{G}' + \mathbf{C}_{m'}^{-1})^{-1} \tag{S3.48}$$

where $\mathbf{C}_{m'}$ is the prior model covariance matrix for parameters expect K.

S3.7.3 The Computation of Credible Interval

We calculate the highest posterior density interval (HPDI) as the credible interval. The formal definition of HPDI is as follows:

Let $f(x)$ be the density function of a random variable X. Then the $100(1-\alpha)\%$ HPDI is the subset $R(f_\alpha)$ of the sample space of X such that

$$R(f_\alpha) = \{x : f(x) \geq f_\alpha\} \tag{S3.49}$$

where f_α is the largest constant such that $P(X \in R(f_\alpha)) \geq 1 - \alpha$.

In our case X is the ephemeral grounding level K' defined on the real line and $\alpha = 0.05$. We use the measure of $100(1-\alpha)\%$ HPDI on the real line as the size of the credible interval.

S3.7.4 Formal Errors in the Synthetic Test of the Nonlinear Model

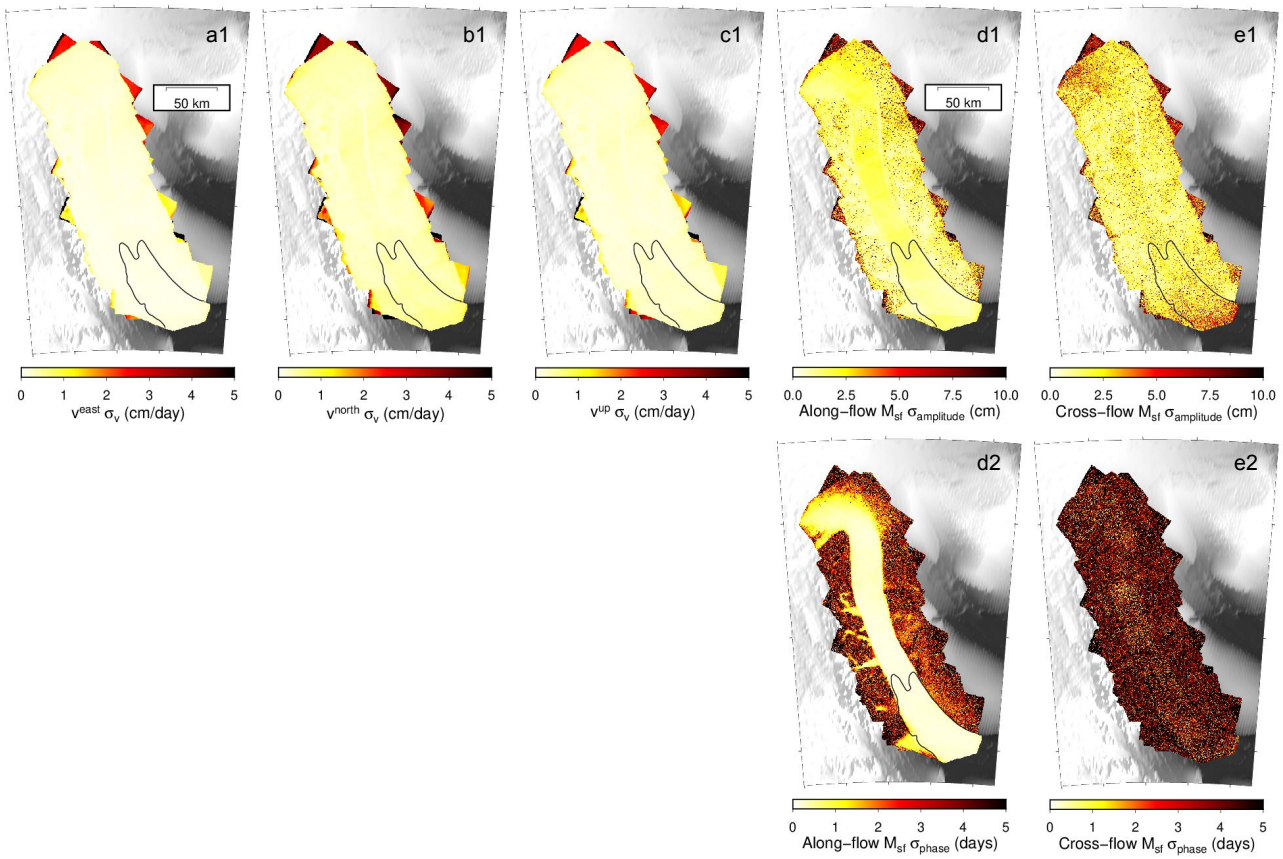

Figure S3.15: Formal errors in the synthetic test of the nonlinear model. (a1-c1) Standard deviation of estimated secular east, north, up velocity. (d1-e1) Standard deviations of along-flow and cross-flow displacement amplitude at M_{sf} period. (d2-e2) Standard deviation of estimated along-flow and cross-flow displacement phase at M_{sf} period.

S3.7.5 Additional Results Inferred from the Linear Model

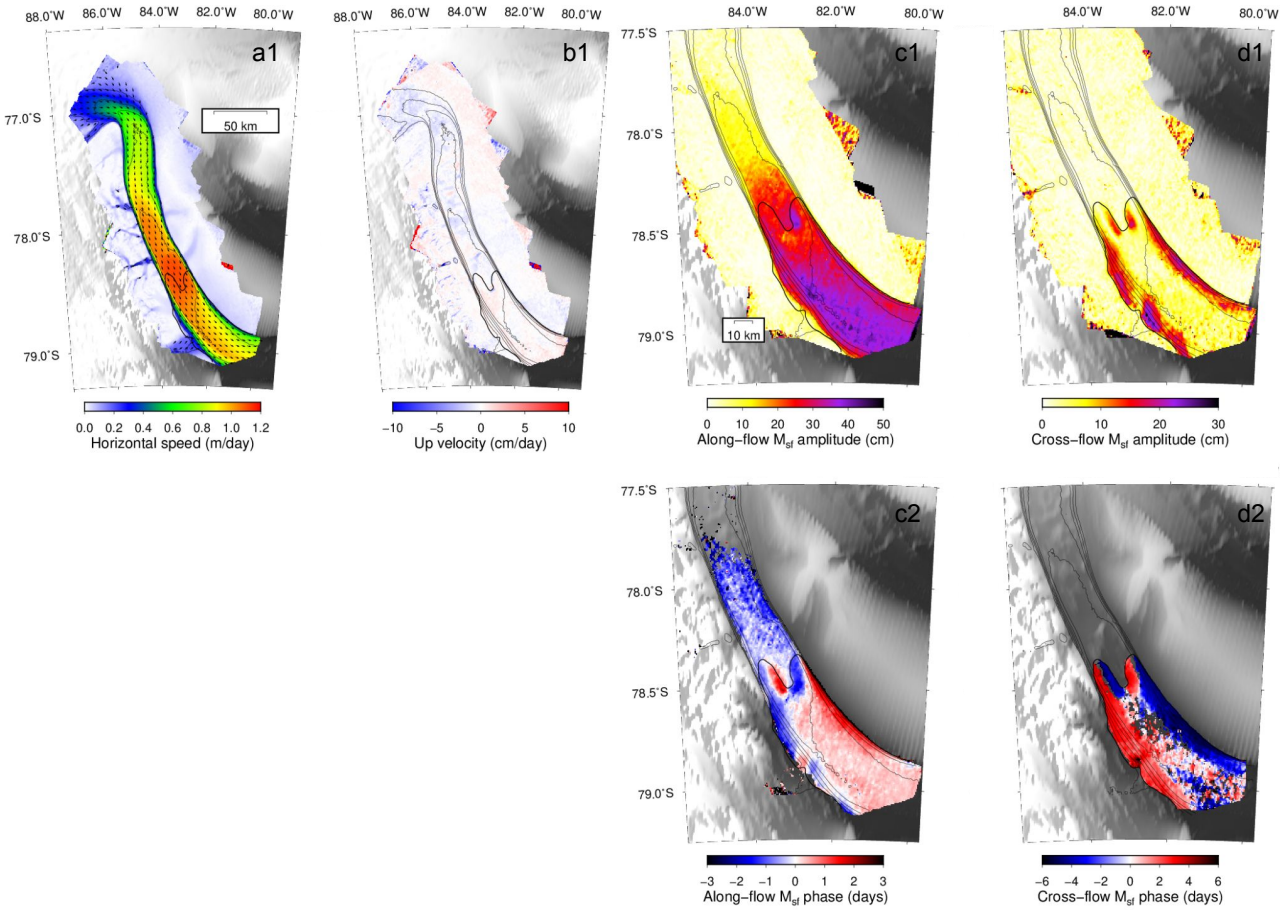

Figure S3.16: (a1) Horizontal velocity where the color indicates speed and arrows show flow direction (b1) Vertical velocity, where the positive values indicate moving upward. (c1-d1) The amplitude of horizontal displacement variation at M_{sf} period. (c2-d2) The phase of horizontal displacement variation at M_{sf} period.

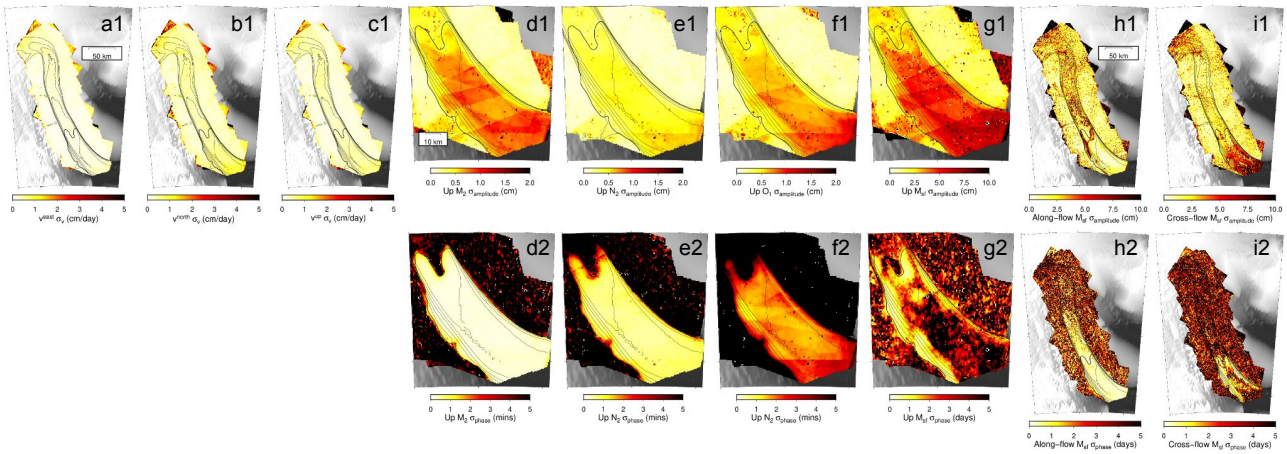

Figure S3.17: Formal errors in estimated secular velocity, vertical displacement and horizontal displacement variations by the linear model. (a1-c1) Standard deviation of estimated secular east, north, up velocity. (d1-g1) Standard deviation of estimated vertical displacement amplitude at M_2, N_2, O_1, M_{sf} periods. (h1-i1) Standard deviations of along-flow and cross-flow displacement amplitude at M_{sf} period. (d1-g1) Standard deviation of estimated vertical displacement amplitude at M_2, N_2, O_1, M_{sf} periods. (h2-i2) Standard deviation of estimated along-flow and cross-flow displacement phase at M_{sf} period.

S3.7.6 Discussion of Vertical Amplitude Scaling $A(\mathbf{r})$

We present a discussion on the displacement amplitude of vertical M_2, N_2, and O_1 as well as the motivation of the using a lumped parameter $A(\mathbf{r})$ to describe the amplitude variation of all tidal constituents. Figure S3.18a-c show the normalized spatial variation in amplitude of vertical M_2, N_2 and O_1, calculated by dividing the inferred amplitude $a(\mathbf{r})$ by the amplitude at the reference point $a(\mathbf{r}_0)$ (Figure 3.1b). M_2, N_2 and O_1 demonstrate similar normalized spatial variation in amplitude ($a(\mathbf{r})/a(\mathbf{r}_0)$) with the difference between every two tidal constituents shown in Figure S3.18d-f. Thus, we make an empirical assumption that all tidal constituents share similar normalized spatial variation in amplitude and use a lumped parameter $A(\mathbf{r})$ to describe this spatial variation. The use of $A(\mathbf{r})$ enables the linearization of the nonlinear inverse problem.

The inferred $A(\mathbf{r})$ is mainly constrained by the major semi-diurnal constituents (e.g., M_2) because they are a few time larger in amplitude than the major diurnal constituents (e.g, O_1). The difference in normalized amplitude between the two semidiurnal constituents (M_2 and N_2) and the diurnal constituent O_1 is ~0.1. Given the amplitude of two major diurnal constituents K_1 and O_1 is approximately 35 cm, the mean error of ignoring the possible difference between the amplitude variation of semi-dirunal and dirunal constituents translates to be only ~5 cm. This is a few times smaller than the sum of measurement error and modeling error in data which is typically larger than 20 cm.

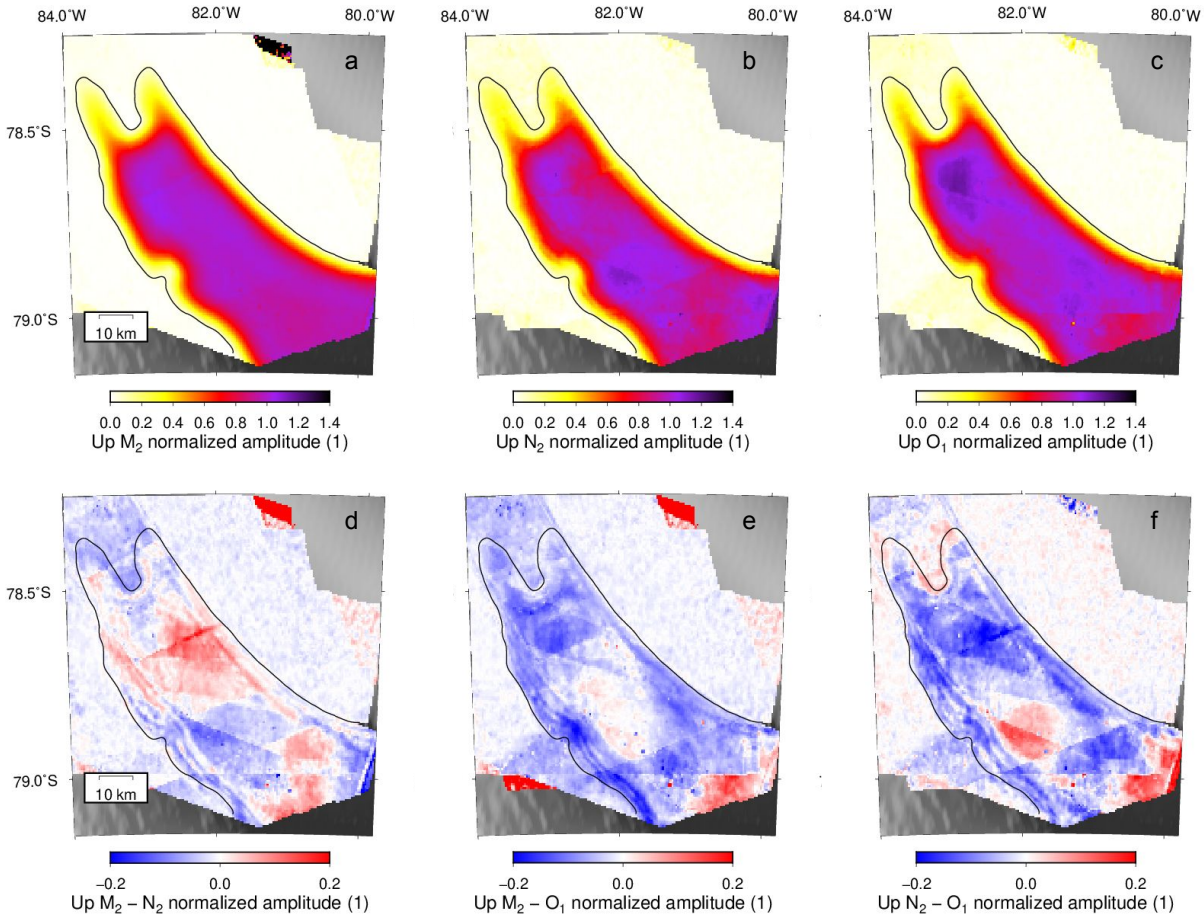

Figure S3.18: (a-c) The normalized displacement amplitude of vertical M_2, N_2 and O_1. (d-f) The difference of normalized displacement amplitude between M_2, N_2 and O_1.

S3.7.7 Construction of the Nonlinear Vertical Displacement Model

We derive the relative spatial phase variations for M_2, N_2, and O_1 which inform the relative phase variation of the other 5 semi-diurnal and diurnal variations. Because the inferred phase maps for these three contains the bias in estimation, spurious phase variation caused by the ephemeral grounding and noise, we apply the following post-processing procedures on the original inferred maps and then obtain the relative phase variation (Figure S3.19):

1. Correct for the bias estimated by the synthetic test.
2. Remove the phase variation related to the ephemeral grounding including the isolated ephemeral grounding zone in central trunk and the low-amplitude node on the west margin.
3. Apply median filter (7x7) to further reduce the noise.
4. Calculate phase difference relative to the reference point.

Because the only strong phase variation in O_1 phase map has the similar shape and magnitude as the synthetic test (Figure S3.11), we simply assume that there is no phase variation in O_1.

The spatial amplitude variation of each constituent is defined as its amplitude at the reference point $\tilde{a_\xi}(\mathbf{r}_0)$ multiplied by the spatial scaling parameter $A(\mathbf{r})$. Same as the phase, we use the measured amplitude value at reference point for M_2, N_2, and O_1, and CATS2008 amplitude value for the rest.

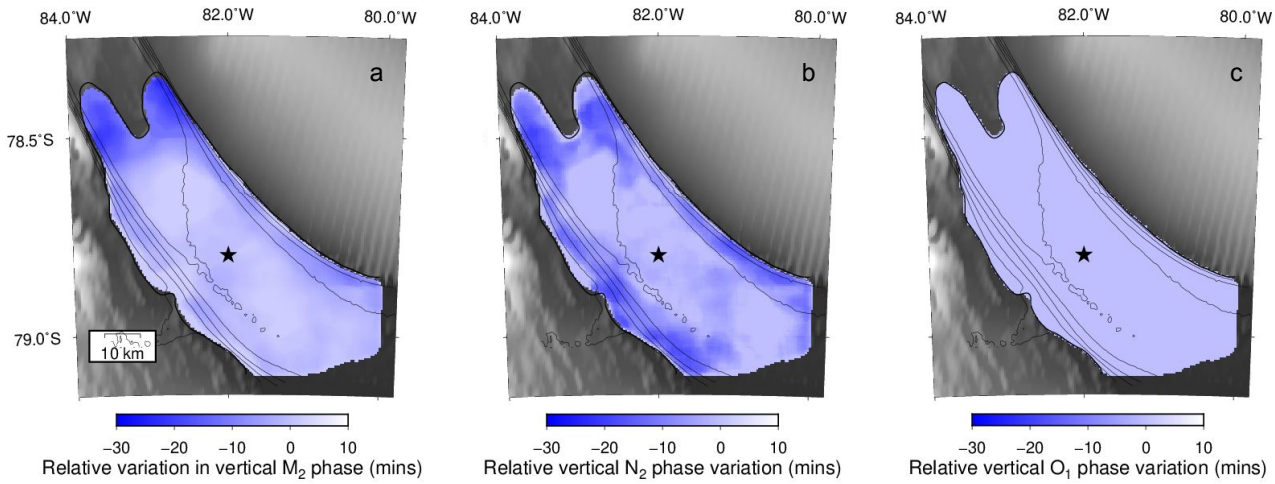

Figure S3.19: The relative phase variation of M_2, N_2, and O_1 derived from the result inferred by the linear model.

S3.7.8 Derived Grounding Line from M_2 Displacement Amplitude

We derive updated grounding line at Rutford Ice Stream using the 10 cm contour of M_2 vertical displacement amplitude. The updated grounding line has better accuracy at the two horns of the grounding line and on the western margin of the ice shelf.

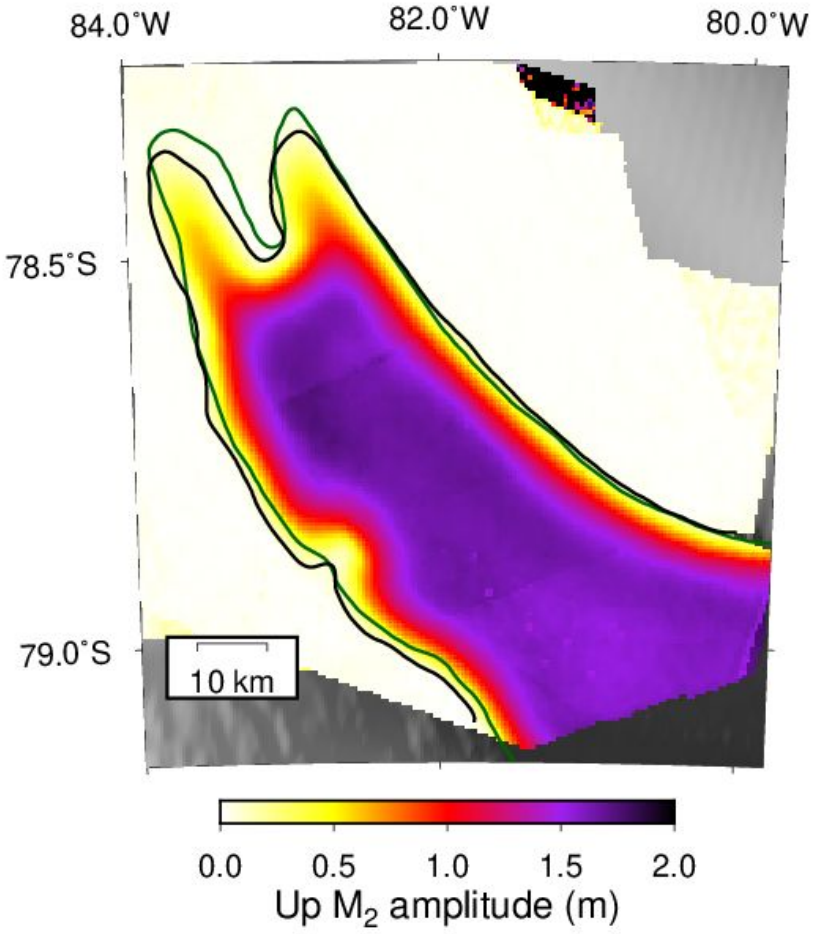

Figure S3.20: Grounding line at Rutford Ice Stream. Grounding line derived from M_2 displacement amplitude is in black. Grounding line from Bedmap2 (Fretwell et al., 2013) is in green.

S3.7.9 Additional Results Inferred from the Nonlinear Model

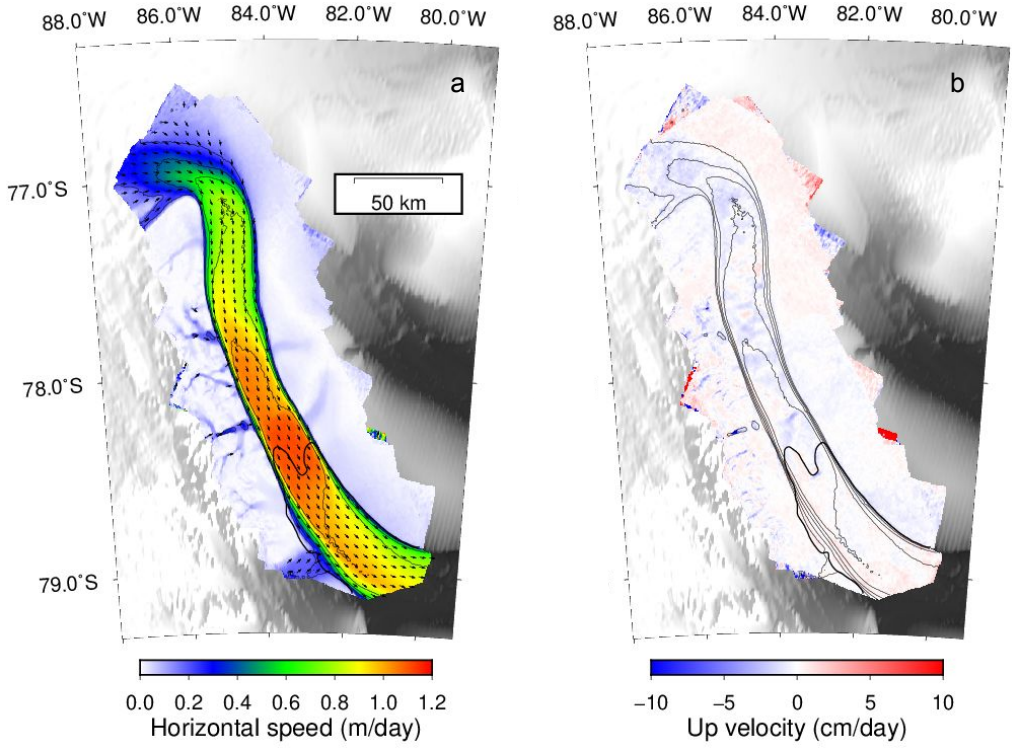

Figure S3.21: (a) Horizontal velocity where the color indicates speed and arrows show flow direction (b) Vertical velocity, where the positive values indicate moving upward.

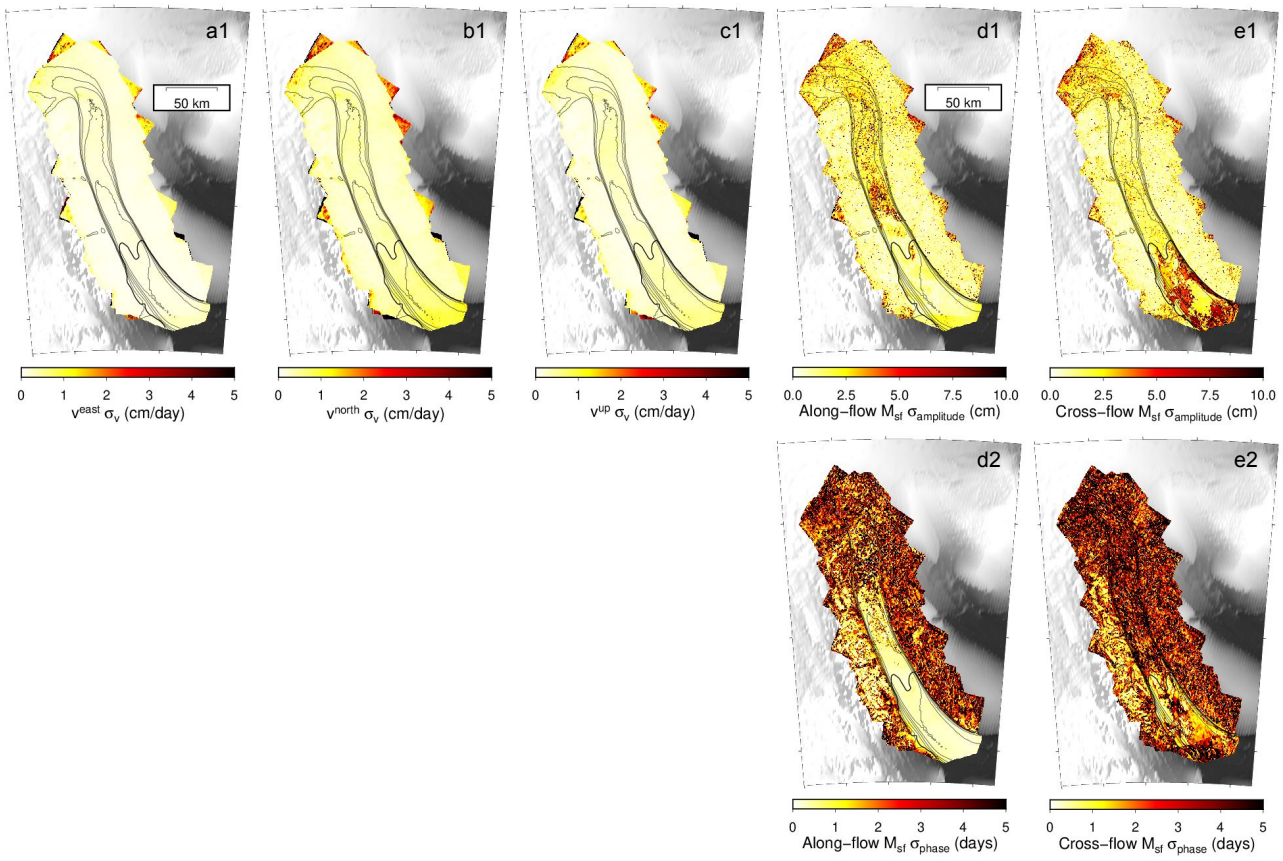

Figure S3.22: Formal errors in the synthetic test of the nonlinear model. (a1-c1) Standard deviation of estimated secular east, north, up velocity. (d1-e1) Standard deviations of along-flow and cross-flow displacement amplitude at M_{sf} period. (d2-e2) Standard deviation of estimated along-flow and cross-flow displacement phase at M_{sf} period.

S3.7.10 Estimation of Variation in Longitudinal Stress

The estimation is based on work in Minchew et al. (in prep.). The derived effective dynamic modulus relates the variation in longitudinal stress to the variation in longitudinal flow rate.

$$\frac{\hat{\tau}_{xx}}{\hat{u}} = \frac{2\bar{\eta}k}{n}\left(\frac{-\mathrm{De}+i}{\theta^2}\right) \tag{S3.50}$$

where τ_{xx} is the amplitude of sinusoidal variation in longitudinal stress, $\hat{u}$ is the amplitude of sinusoidal variation in flow rate, $\bar{\eta}$ is the effective dynamic viscosity which is considered as a constant, De is Deborah number, $\theta = \sqrt{1+\mathrm{De}^2}$, n is the exponent is Glen-Nye's flow law, and k is angular wavenumber.

Let $\bar{T}_r$ be the viscoelastic relaxation time characterizing the decay upstream stress decay. We have

$$\bar{T}_r = \frac{\bar{\eta}}{E} \tag{S3.51}$$

where $E \sim 10^9$ Pa is ice Young's modulus, and

$$\mathrm{De} = \omega \bar{T}_r. \tag{S3.52}$$

The observable angular wavenumber is

$$k = \frac{\omega}{v_p} + i\frac{1}{l} \tag{S3.53}$$

where ω is angular frequency of the flow rate variation, v_p is the phase velocity of the upstream propagation, and l is the upstream decay distance in amplitude.

$\bar{T}_r$ has the following relationships with the observables (Minchew et al., in prep.):

$$\bar{T}_r = \frac{1}{\omega}\sqrt{\left(\frac{1+\Theta}{1-\Theta}\right)^2 - 1} \tag{S3.54}$$

$$\Theta = \left(\frac{\omega l}{v_p}\right)^2 = \frac{\theta - 1}{\theta + 1} \tag{S3.55}$$

At RIS, observations indicate $\omega = 2\pi/14.7\,\mathrm{d}$, $l = 45\,\mathrm{km}$, and $v_p = 24\mathrm{km/d}$. Plugging in these values yields $\Theta = 0.64$, $\theta = 4.6$, $\mathrm{De} = 4.49$, and $\bar{T}_r = 10\,\mathrm{d}$.

Further plugging in these values and $\hat{u} = 0.2\mathrm{m/d}$, $n = 3$ into equation (S3.50), the estimated $\hat{\tau}_{xx}$ is approximately 100 KPa.

BIBLIOGRAPHY

Alley, R. B. et al. (2015). Oceanic forcing of ice-sheet retreat: West Antarctica and more. In: *Annual Review of Earth and Planetary Sciences* 43.1, pp. 207–231. ISSN: 0084-6597. DOI: 10.1146/annurev-earth-060614-105344.

Cuffey, K. and W. S. B. Paterson (2010). *The Physics of Glaciers*. 4th Editio. Academic Press. ISBN: 9780123694614.

Dupont, T. K. and R. B. Alley (2005). Assessment of the importance of ice-shelf buttressing to ice-sheet flow. In: *Geophysical Research Letters* 32.4, pp. 1–4. ISSN: 00948276. DOI: 10.1029/2004GL022024.

Fattahi, H. et al. (2017). InSAR time-series estimation of the ionospheric phase delay: An extension of the split range-spectrum technique. In: *IEEE Transactions on Geoscience and Remote Sensing* 55.10, pp. 5984–5996. ISSN: 0196-2892. DOI: 10.1109/TGRS.2017.2718566.

Fretwell, P. et al. (2013). Bedmap2: improved ice bed, surface and thickness datasets for Antarctica. In: *The Cryosphere* 7.1, pp. 375–393. ISSN: 1994-0424. DOI: 10.5194/tc-7-375-2013.

Fricker, H. A. et al. (2009). Mapping the grounding zone of the Amery Ice Shelf, East Antarctica using InSAR, MODIS and ICESat. In: *Antarctic Science* 21.5, pp. 515–532. ISSN: 09541020. DOI: 10.1017/S095410200999023X.

Gardner, A. S. et al. (2018). Increased West Antarctic and unchanged East Antarctic ice discharge over the last 7 years. In: *Cryosphere* 12.2, pp. 521–547. ISSN: 19940424. DOI: 10.5194/tc-12-521-2018.

Goldstein, R. M. et al. (1993). *Satellite radar interferometry for monitoring ice sheet motion: Application to an Antarctic ice stream*. DOI: 10.1126/science.262.5139.1525.

Gudmundsson, G. H. (2013). Ice-shelf buttressing and the stability of marine ice sheets. In: *The Cryosphere* 7.2, pp. 647–655. ISSN: 1994-0424. DOI: 10.5194/tc-7-647-2013.

Gudmundsson, G. H. (2006). Fortnightly variations in the flow velocity of Rutford Ice Stream, West Antarctica. In: *Nature* 444.7122, pp. 1063–1064. ISSN: 0028-0836. DOI: 10.1038/nature05430.

Hellmer, H. H. et al. (2012). *Twenty-first-century warming of a large Antarctic ice-shelf cavity by a redirected coastal current*. DOI: 10.1038/nature11064.

Joughin, I. (2002). Ice-sheet velocity mapping: A combined interferometric and speckle-tracking approach. In: *Annals of Glaciology* 34, pp. 195–201. ISSN: 02603055. DOI: 10.3189/172756402781817978.

Joughin, I. et al. (2012). *Ice-sheet response to oceanic forcing*. DOI: 10.1126/science.1226481.

Joughin, I. et al. (2014). Marine ice sheet collapse potentially under way for the thwaites glacier basin, West Antarctica. In: *Science* 344.6185, pp. 735–738. ISSN: 10959203. DOI: 10.1126/science.1249055.

King, E. C. et al. (2016). Subglacial landforms beneath Rutford Ice Stream, Antarctica: detailed bed topography from ice-penetrating radar. In: *Earth System Science Data* 8.1, pp. 151–158. ISSN: 18663516. DOI: 10.5194/essd-8-151-2016.

Matsuoka, K. et al. (2015). *Antarctic ice rises and rumples: Their properties and significance for ice-sheet dynamics and evolution*. DOI: 10.1016/j.earscirev.2015.09.004.

Milillo, P. et al. (2019). Heterogeneous retreat and ice melt of thwaites glacier, West Antarctica. In: *Science Advances* 5.1, eaau3433. ISSN: 23752548. DOI: 10.1126/sciadv.aau3433.

Minchew, B. M. et al. (2017). Tidally induced variations in vertical and horizontal motion on Rutford Ice Stream, West Antarctica, inferred from remotely sensed observations. In: *Journal of Geophysical Research: Earth Surface* 122.1, pp. 167–190. ISSN: 21699003. DOI: 10.1002/2016JF003971.

Morlighem, M. et al. (2020). Deep glacial troughs and stabilizing ridges unveiled beneath the margins of the Antarctic ice sheet. In: *Nature Geoscience* 13.2. ISSN: 17520908. DOI: 10.1038/s41561-019-0510-8.

Mouginot, J. et al. (2012). Mapping of ice motion in Antarctica using synthetic-aperture radar data. In: *Remote Sensing* 4.9, pp. 2753–2767. ISSN: 2072-4292. DOI: 10.3390/rs4092753.

Murray, T. et al. (2007). Ice flow modulated by tides at up to annual periods at Rutford Ice Stream, West Antarctica. In: *Geophysical Research Letters* 34.18, p. L18503. ISSN: 0094-8276. DOI: 10.1029/2007GL031207.

Padman, L. et al. (2002). A new tide model for the Antarctic ice shelves and seas. In: *Annals of Glaciology* 34, pp. 247–254. ISSN: 02603055. DOI: 10.3189/172756402781817752.

Padman, L. et al. (2018). Ocean tide influences on the Antarctic and Greenland Ice Sheets. In: *Reviews of Geophysics* 56.1, pp. 142–184. ISSN: 19449208. DOI: 10.1002/2016RG000546.

Paolo, F. S. et al. (2015). Volume loss from Antarctic ice shelves is accelerating. In: *Science* 348.6232, pp. 327–331. ISSN: 10959203. DOI: 10.1126/science.aaa0940.

Pritchard, H. D. et al. (2012). Antarctic ice-sheet loss driven by basal melting of ice shelves. In: *Nature* 484.7395, pp. 502–505. ISSN: 00280836. DOI: 10.1038/nature10968.

Pritchard, H. D. et al. (2009). Extensive dynamic thinning on the margins of the Greenland and Antarctic ice sheets. In: *Nature* 461.7266, pp. 971–975. ISSN: 00280836. DOI: 10.1038/nature08471.

Rignot, E. et al. (2011a). Antarctic grounding line mapping from differential satellite radar interferometry. In: *Geophysical Research Letters* 38.10, n/a–n/a. ISSN: 00948276. DOI: 10.1029/2011GL047109.

Rignot, E. et al. (2011b). Ice flow of the antarctic ice sheet. In: *Science* 333.6048, pp. 1427–1430. ISSN: 00368075. DOI: 10.1126/science.1208336.

Rignot, E. (1998). Radar interferometry detection of hinge-line migration on Rutford Ice Stream and Carlson Inlet, Antarctica. In: *Annals of Glaciology* 27, pp. 25–32. ISSN: 0260-3055. DOI: 10.3189/1998AoG27-1-25-32.

Rignot, E. (2002). Ice-shelf changes in Pine Island Bay, Antarctica, 1947-2000. In: *Journal of Glaciology* 48.161, pp. 247–256. ISSN: 00221430. DOI: 10.3189/172756502781831386.

Robel, A. A. et al. (2017). "Tidal modulation of ice shelf buttressing stresses". In: *Annals of Glaciology*. Vol. 58. 74. Cambridge University Press, pp. 12–20. DOI: 10.1017/aog.2017.22.

Rosier, S. H. R. et al. (2017). Strong tidal variations in ice flow observed across the entire Ronne Ice Shelf and adjoining ice streams. In: *Earth System Science Data* 9.2, pp. 849–860. ISSN: 1866-3516. DOI: 10.5194/essd-9-849-2017.

Rosier, S. H. and G. H. Gudmundsson (2020). Exploring mechanisms responsible for tidal modulation in flow of the Filchner-Ronne Ice Shelf. In: *Cryosphere* 14.1, pp. 17–37. ISSN: 19940424. DOI: 10.5194/tc-14-17-2020.

Scambos, T. A. et al. (2007). MODIS-based Mosaic of Antarctica (MOA) data sets: Continent-wide surface morphology and snow grain size. In: *Remote Sensing of Environment* 111.2, pp. 242–257. ISSN: 00344257. DOI: 10.1016/j.rse.2006.12.020.

Schmeltz, M. et al. (2001). Ephemeral grounding as a signal of ice-shelf change. In: *Journal of Glaciology* 47.156, pp. 71–77. ISSN: 0022-1430. DOI: 10.3189/172756501781832502.

Schoof, C. (2007). Marine ice-sheet dynamics. Part 1. The case of rapid sliding. In: *Journal of Fluid Mechanics* 573, p. 27. ISSN: 0022-1120. DOI: 10.1017/S0022112006003570.

Sutterley, T. C. et al. (2014). Mass loss of the Amundsen Sea Embayment of West Antarctica from four independent techniques. In: *Geophysical Research Letters* 41.23, pp. 8421–8428. ISSN: 0094-8276. DOI: 10.1002/2014GL061940.

Tarantola, A. (2005). *Inverse problem theory and methods for model parameter estimation*. Society for Industrial and Applied Mathematics, p. 342. ISBN: 0898715725.

Thomas, R. H. (1979). The dynamics of marine ice sheets. In: *Journal of Glaciology* 24.90, pp. 167–177. ISSN: 0022-1430. DOI: 10.3189/s0022143000014726.

Tsai, V. C. and G. H. Gudmundsson (2015). An improved model for tidally modulated grounding-line migration. In: *Journal of Glaciology* 61.226, pp. 216–222. ISSN: 0022-1430. DOI: 10.3189/2015JoG14J152.

Warburton, K. L. P. et al. (2020). Tidal grounding-line migration modulated by subglacial hydrology. In: *Geophysical Research Letters* 47.17, e2020GL089088. ISSN: 0094-8276. DOI: 10.1029/2020GL089088.

Weertman, J. (1974). Stability of the Junction of an Ice Sheet and an Ice Shelf. In: *Journal of Glaciology* 13.67, pp. 3–11. ISSN: 0022-1430. DOI: 10.3189/S0022143000023327.

Chapter 4

TIDE-INDUCED EPHEMERAL GROUNDING AND FORTNIGHTLY VARIATION IN FLOW RATE AT EVANS ICE STREAM, WEST ANTARCTICA

Abstract

Ocean tides cause strong fortnightly flow variability over Filchner-Ronne Ice Shelf (FRIS), West Antarctica. Tide-induced temporal variations in buttressing stress due to ephemeral grounding on sub-shelf bathymetric highs can induce such fortnightly flow variability. Following the approach of a previous study identifying zones of ephemeral grounding at Rutford Ice Stream (RIS), we infer zones of ephemeral grounding as well as the fortnightly flow variability at Evans Ice Stream (EIS) using synthetic-aperture-radar data collected by both Sentinel-1 two-satellite constellation and COSMO-SkyMed four-satellite constellation over EIS from 2017 to 2021. EIS is significantly larger than RIS with multiple upstream tributaries and complex grounding lines. We find prevalent ephemeral grounding in the vicinity of the grounding zone and the largest fortnightly flow modulation in areas of of ephemeral grounding. We also observe the upstream propagation of the fortnightly flow variability from the floating ice shelf to grounded ice through one large upstream tributary. As zones of ephemeral grounding are most sensitive to the projected oceanic warming and ice shelf thinning, our study highlights the importance of and motivates further studies on the buttressing effect provided by the previously poorly observed zones of ephemeral grounding at FRIS.

4.1 Introduction

Ocean tides cause strong variations in ice flow rate near the marine margins in Antarctica (e.g., Padman et al., 2018). The response of different ice streams/ice shelves to these tidal forcings is heterogeneous (e.g., Doake et al., 2002; Bindschadler et al., 2003; Gudmundsson, 2006; Lipovsky and Dunham, 2017; Wiens et al., 2008, Minchew et al., 2017). Improving our understanding of the underlying physical mechanisms that generate these variations can illuminate key processes that impact the dynamics of glacier flow in Antarctica, such as rheology of ice, mechanics of the bed, and the buttressing effect of ice shelves, and will benefit the development of more realistic ice sheet models used to project the future evolution of Antarctic

Ice Sheet in response to changes in climate. Here, we are focused on improving our understanding of the tide-induced fortnightly flow over Filchner-Ronne Ice Shelf System, West Antarctica.

The California-sized Filchner-Ronne Ice Shelf (FRIS) situated on the edge of the Weddell Sea is subjected to the largest ocean tides in Antarctica, predominately at two semi-diurnal periods M_2 (12.42 h) and S_2(12.00 h). The peak-to-peak tidal amplitude exceeds 7 m along the Zumberge Coast (Padman et al., 2002) where Rutford Ice Stream (RIS), Evans Ice Stream (EIS), and Carlson inlet flow into the western Ronne Ice Shelf (Figure 4.1a). However, strong temporal variations in horizontal flow rate occurs at the fortnightly M_{sf} (14.77 day) period. This period corresponds to the beating of the two primary semi-diurnal constituents M_2 and S_2. M_{sf} flow variability was first observed at RIS (Gudmundsson, 2006) and identified over the entire FRIS and all adjoining ice streams (Rosier et al., 2017) by GPS observations.

Several studies have explored the possible underlying physical mechanisms responsible for generating the fortnightly flow (e.g., Gudmundsson, 2007; Rosier et al., 2014; Thompson et al., 2014; Robel et al., 2017). Minchew et al. (2017) used synthetic-aperture-radar (SAR) data collected by a 9-month COSMO-SkyMed (CSK) observation campaign over RIS to infer the spatial-temporal variation of this fortnightly flow variability. They found that this flow modulation originated within floating ice shelf and propagated upstream to grounded ice, from which they infer that tidal forcing of the ice shelf is responsible for generating horizontal flow variability of RIS. Several models have been proposed to explain this phenomenon including ephemeral grounding of the ice shelf, ice shelf margin widening, and grounding line migration (Minchew et al., 2017; Robel et al., 2017; Rosier and Gudmundsson, 2020; Warburton et al., 2020). All of these models suggest that the ocean tide modulates the contact of the ice shelf with the seafloor and hence influences the buttressing stress to cause temporal variability in flow. Chapter 3 extends the methodology used in Minchew et al. (2017) and identifies zones where ice shelf ephemerally grounds on sub-shelf bathymetric highs over tidal cycles as well as quantifies the level of ephemeral grounding at RIS. The observation of sub-shelf ephemeral grounding at RIS provides key evidence for tide-modulated buttressing stress in ice-shelf and motivates expanding similar observational study to other tributary ice streams of FRIS where strong fortnightly flow variability is also present.

In this study, we focus on Evans Ice Stream (EIS), another ice stream along the Zumberge Coast. EIS is the largest ice stream flowing into FRIS draining a 104 000 km^2 catchment from Ellsworth Land (Figure 4.1a, Bamber et al., 2000; Joughin and Bamber, 2005). Upstream of EIS are six major tributaries among which Drewry Ice Stream (DIS) is the longest (> 150 km) and widest (> 30 km) (Figure 4.1b). Compared with the other tributaries, DIS is believed to have the shallowest bed at −1 km below sea level, the smallest bed slope, and the highest secular flow speed at ∼1.8 m/d near the grounding line. At the three northern tributaries (Trib. 2,3,4) and two western tributaries (Trib. 5,6), the bed deepens to −2 km below sea level resulting in reverse bed slopes. The two western tributaries have flow speeds of approximately 1 m/d with the grounding line slightly extending into the ice stream inlets. The three northern tributaries, which are far from the grounding line and largely join DIS at higher latitudes, have relatively slow flow speeds of approximately 0.5 m/d. The ice thickness is approximately 1.5 km at DIS, increases gradually from eastern to western tributaries, and reaches more than 2.5 km at Trib. 5 and Trib. 6. Downstream of EIS, the central trunk of the floating ice shelf is about 500-km-long with the width increasing from 50 km to 100 km and thickness decreasing from 1.5 km to 1 km downstream. The secular flow speed of ice shelf is approximately 2 m/d at the western and central portion and decreases to 1.5 m/d at the eastern portion. The grounding line of EIS is sinuous on both the western and eastern ends. This sinuosity is likely due to localized changes in sub-shelf bathymetry. There are a few documented pinning points underneath the ice shelf at EIS including two pronounced pinning points downstream of Trib. 8 and a few more at Cape Zumberge (Matsuoka et al., 2015).

We adopt the same methodology including the displacement models and workflow as in Chapter 3 to infer sub-shelf ephemeral grounding as well as the spatial-temporal variation of fortnightly flow variability at EIS. A key difference is the availability of SAR data collected over EIS by both the Sentinel-1 two-satellite constellation and COSMO-SkyMed four-satellite constellation over a 4-year temporal coverage from 2017 to 2021.

4.2 SAR Data and Displacement Fields

Synthetic Apeture Radar (SAR) images can be used to measure the displacement of ice over a given time interval in two orthogonal directions of which the first is along a path parallel to the satellite orbit (azimuth) direction and the second is along the radar line-of-sight (LOS) or range direction. The measurement in LOS direction is

sensitive to the vertical motion.

Sentinel-1, which is operated by the European Space Agency (ESA), collected SAR data over EIS beginning in June 2017 until the present. The data acquisition plan covers all of the grounded and floating portion of EIS including data from six tracks with 6-day revisit times and one track with a 12-day revisit time (Figure S4.9a). Both Sentinel-1A and 1B carry nearly identical C-band (5.5 cm wavelength; 5.4 GHz) SAR systems. We use Level-1 Interferometric Wide Swath SLC (single-look complex) Products (250-km-swath) which provides SLC images with pixel size at 2.3 m in the range direction and 14 m in the azimuth direction. We use all available SAR data starting from June 2017 until April 2021. The total number of Sentinel-1 SAR acquisitions is ~1200 (see the supporting information S4.7.1).

The COSMO-SkyMed (CSK) SAR constellation is operated by the Italian Space Agency (ASI) and collected SAR data over EIS beginning in November 2017. The data acquisition plan covers all of the grounded ice including the all upstream tributaries and ~150 km of the floating portion of the ice shelf downstream of the grounding line. The data is acquired from 11 ascending tracks and 11 descending tracks (Figure S4.9b). All four CSK satellites collected data, each repeating a given orbit track every 16 days, and are offset from one another with timespans between subsequent SAR acquisitions of 1, 3, 4, and 8 days. All CSK satellites carry nearly identical X-band (3.1 cm wavelength; 9.6 GHz) SAR systems. We use the Level-0 Stripmap-HIMAGE products and focus them to SLC images with pixel size of 0.9 m in the range direction and 2.2 m in the azimuth direction. We use ~500 CSK acquisitions in our study (see the supporting information S4.7.1).

The domain of our study is indicated in (Figure 4.1b) and spans the entire EIS, including the six upstream tributaries, the floating portion of ice shelf with two additional tributaries (Trib. 7 and Trib. 8), and extends to Cape Zumberge where another tributary (Trib. 9) flows into the ice shelf. We processed both S1 and CSK data using the InSAR Scientific Computing Environment 2 (ISCE2), a radar-processing software package developed primarily at NASA's Jet Propulsion Laboratory (Rosen et al., 2012). We used the stack processing tools in ISCE2 (Fattahi et al., 2017) to coregister all the same-track SLC images using Antarctica digital elevation model BedMachine Version 2 (Morlighem et al., 2020).

We use a feature tracking algorithm (Joughin, 2002) to measure the displacement from pairs of same-track coregistered SLC images. For feature tracking on S1 SLC images, we use 2-D cross-correlation windows of 480×120 pixels (range $\times$ azimuth)

with a step size of 240 and 60 pixels in the range and azimuth directions. For feature tracking on CSK SLC images, we use 2-D cross-correlation windows of 480×240 pixels (range $\times$ azimuth) with a step size of 120 and 60 pixels in the range and azimuth directions. We have implemented the feature tracking algorithm employing GPUs (Zhu et al., in prep.) which accelerates the computationally expensive feature tracking calculation by several orders of magnitude. We post-filter/adjust the resulting displacement fields by (1) masking out the displacement values if they differ from the prior displacement values calculated using Antarctica ice velocity model (Mouginot et al., 2012) beyond a prescribed threshold, (2) applying a moving-window median filter, and (3) adjusting for reference frame issue caused by the miscoregistration using tie points on stagnant ice. Using this scheme, we derived ~2200 displacement fields along 7 S1 tracks from acquisitions with time spans no greater than 12 days and ~600 displacement fields along 22 CSK tracks from acquisitions with time spans no greater than 8 days. Because the number of S1 displacement fields is ~4 times the number of CSK displacement fields and S1 scenes are significantly larger than CSK scenes (750 km v.s. 40 km in swath width), S1 displacement fields constitutes more than $> 90\%$ of our displacement dataset (see the supporting information S4.7.1).

4.3 Methodology

4.3.1 Overview

We adopt the methodology described in Chapter 3 which includes a linear 3-D displacement model and a nonlinear 3-D displacement model. The workflow starts from the linear model, then constructs the nonlinear model using the inferred vertical displacements at selected tidal periods and an independent ocean tidal model, and finally solves for vertical displacements with ephemeral grounding and horizontal flow variability (Figure 4.2). Part I of the workflow is to infer the vertical displacement at selected tidal periods from the linear model. Compared with the Part I in Chapter 3, we simplified two aspects of the estimation: (1) We do not estimate the vertical displacement at M_{sf} period, the inferred amplitude of which was used identify zones of ephemeral grounding (Chapter 3), and (2) we do not perform bias-correction to inferred values using estimated bias from synthetic tests. We explain the reasons for not following the original workflow on these two aspects in section 4.3.2. Part II of the workflow, which is the same as Chapter 3, is to infer vertical displacement with ephemeral grounding and horizontal flow variability.

Ephemeral grounding occurs when the impact of tide on the instantaneous level of

the bottom of ice shelf exceeds sub-shelf water column thickness (wct) such that the bottom of ice shelf contacts the seafloor. Figure 4.3 is an example of ephemeral grounding on a sub-shelf bathymetric pinning point. We adopt the same definition of the level of ephemeral grounding as in Chapter 3. For any given point on the surface of ice shelf, if ephemeral grounding occurs, the level of ephemeral grounding is the level of clipping (Figure 4.3b1) on the vertical displacement at this point. By convention, vertical displacement is zero when tide height is zero. In the shown example, the level of ephemeral grounding, defined in Figure 4.3a2, is -1 m. The level of ephemeral grounding is typically negative and is equivalent to be negative of the wct. A higher level of grounding corresponds to higher sub-shelf bathymetry and thinner wct, and vice versa. If the range of vertical displacement is smaller than the wct, ephemeral grounding does not occur.

4.3.2 The Linear 3-D Displacement Model

4.3.2.1 Formulation and Parameter Estimation

We are interested in the tide-induced displacements of an ice-shelf-stream system. We consider the instantaneous 3-D displacement vector $\mathbf{u}$ on the ice surface at location $\mathbf{r}$ and at time t as the sum of a secular term and a tide-induced term in east ($\hat{e}$), north ($\hat{n}$), and up component ($\hat{u}$), such that

$$\mathbf{u}(\mathbf{r},t) = \mathbf{v}(\mathbf{r})t + \mathbf{w}(\mathbf{r},t) = \begin{bmatrix} v^{\hat{e}}(\mathbf{r}) \\ v^{\hat{n}}(\mathbf{r}) \\ v^{\hat{u}}(\mathbf{r}) \end{bmatrix} t + \begin{bmatrix} w^{\hat{e}}(\mathbf{r},t) \\ w^{\hat{n}}(\mathbf{r},t) \\ w^{\hat{u}}(\mathbf{r},t) \end{bmatrix} \tag{4.1}$$

where $\mathbf{v}(\mathbf{r})$ is the secular velocity and $\mathbf{w}(\mathbf{r},t)$ is the tide-induced displacement vector.

Assuming the tide-induced displacement to be sinusoidal for all periods of tidal forcing, we parameterize $\mathbf{w}(\mathbf{r},t)$ as the sum of a family of sinusoidal functions $i = 1, 2, ..., k$, such that

$$w^{\hat{\zeta}}(\mathbf{r},t) = \sum_{i=1}^{k} a_i^{\hat{\zeta}} \sin(\omega_i t + \phi_i^{\hat{\zeta}}) \quad \text{for } \hat{\zeta} = [\hat{e}, \hat{n}, \hat{u}] \tag{4.2}$$

where sinusoid i has angular frequency ω_i, amplitude $a_i^{\hat{\zeta}}(\mathbf{r})$, and phase $\phi_i^{\hat{\zeta}}(\mathbf{r})$ corresponding to different tidal constituents (Minchew et al., 2017).

We can rewrite this to be a linear displacement model

$$w^{\hat{\zeta}}(\mathbf{r},t) = \sum_{i=1}^{k} c_i^{\hat{\zeta}} \cos(\omega_i t) + s_i^{\hat{\zeta}} \sin(\omega_i t) \tag{4.3}$$

where

$$c_i^{\hat{\xi}} = a_i^{\hat{\xi}} \sin(\phi_i^{\hat{\xi}}) \tag{4.4}$$

$$s_i^{\hat{\xi}} = a_i^{\hat{\xi}} \cos(\phi_i^{\hat{\xi}}). \tag{4.5}$$

At any point $\mathbf{r}$, the measured displacement $d_j (j = 1, 2, \cdots, q)$ from q pairs of SAR scenes is

$$d_j(\hat{\mathbf{l}}_j, \mathbf{r}, t_j^a, t_j^b) = \hat{\mathbf{l}}_j \cdot (\mathbf{u}(\mathbf{r}, t_j^b)) - \mathbf{u}(\mathbf{r}, t_j^a)) \tag{4.6}$$

where $\hat{\mathbf{l}}_j$ is observational unit vector (in range or azimuth direction) and t_j^a and t_j^b are the acquisition times of the primary and secondary scene of the SAR pair.

Equation (4.6) relates model parameters ($\mathbf{v}$, $c_i^{\hat{\xi}}$, $s_i^{\hat{\xi}}$) to the observed displacements. To infer the model parameters, we cast it as a linear inverse problem for a given point $\mathbf{r}$ and arrive at the matrix form

$$\mathbf{d} = \mathbf{G}\mathbf{m} \tag{4.7}$$

where $\mathbf{d}$ is the vector of observed displacement, $\mathbf{m}$ is the model vector and $\mathbf{G}$ is the design matrix. The detailed forms of $\mathbf{G}$ and $\mathbf{m}$ can be found in Minchew et al. (2017).

To solve the inverse problem, we adopt a Bayesian formulation assuming Gaussian distributions for all uncertainties, so the optimal (maximum a posteriori) model estimation is (Tarantola, 2005)

$$\tilde{\mathbf{m}} = (\mathbf{G}^T \mathbf{C}_\chi^{-1} \mathbf{G} + \mathbf{C}_m^{-1})^{-1} (\mathbf{C}_\chi^{-1} \mathbf{G}^T \mathbf{d} + \mathbf{C}_m^{-1} \mathbf{m}_0) \tag{4.8}$$

where $\mathbf{m}_0$ is the prior model vector, $\mathbf{C}_m$ is the prior model covariance matrix, and $\mathbf{C}_\chi$ is the error covariance matrix, also referred to as the misfit covariance. $\mathbf{C}_m$ is diagonal and able to constrain certain parameters to be close to the prior values. The error covariance matrix considers both measurement error $\mathbf{C}_d$ and modeling (or prediction) error, $\mathbf{C}_p$, such that $\mathbf{C}_\chi = \mathbf{C}_m + \mathbf{C}_p$ (Tarantola, 2005). We refer readers to Chapter 3 for the detailed design of $\mathbf{C}_m$ and $\mathbf{C}_\chi$. The estimation of $\mathbf{C}_\chi$ for our inference at EIS is in the supporting information (S4.7.6).

The posterior model covariance matrix

$$\tilde{\mathbf{C}}_m = (\mathbf{G}^T \mathbf{C}_\chi^{-1} \mathbf{G} + \mathbf{C}_m^{-1})^{-1} \tag{4.9}$$

provides the estimates of formal errors in $\tilde{\mathbf{m}}$. The estimates of formal errors in amplitude $a_i^{\hat{\xi}}$ and phase $\phi_i^{\hat{\xi}}$ can be calculated from the formal errors of $c_i^{\hat{\xi}}$ and $s_i^{\hat{\xi}}$ using known relations derived in Minchew et al. (2017).

4.3.2.2 The Linear Displacement Model at EIS

We choose the family of sinusoids in the model according to our prior knowledge of the tide-induced displacement at EIS. The vertical displacement at EIS is dominated by semi-diurnal and diurnal constituents (Table 4.1). Sparse GPS observations at EIS show strong horizontal displacements at the M_{sf} period, similar in amplitude to those found at RIS (0.3 m~0.4 m). Unlike RIS, EIS also has short-period horizontal variations. For example, the M_2 amplitude is ~0.3 m at EIS. After excluding the tidal constituents with periods close to 12 h and 24 h (e.g., S_2, K_1), which are aliased in our SAR observations whose revisit time is always within seconds of being integer days, we arrive at the final candidate tidal constituents we consider: M_2, N_2, O_1, Q_1, M_{sf}, and M_f. The vertical M_{sf} displacement is a special component of the linear model. If the inferred amplitude of the vertical M_{sf} sinusoid is significantly larger than its supposed amplitude which is smaller than 1 cm at EIS, the vertical displacement can be assumed to be clipped due to ephemeral grounding (Chapter 3).

We perform synthetic tests to explore different choices of families of tidal periods to find the optimal model. The accuracy of vertical displacement is most important, since they are then used for constructing the nonlinear displacement model. We create the synthetic tests in the same way as our RIS study (Chapter 4). Details of synthetic tests are described in the supporting information (S4.7.2). We conclude that the optimal model contains sinusoids M_2, N_2, O_1, and M_{sf}, prior model $\mathbf{m}_0 = 0$ and prior model covariance matrix constraining the horizontal displacement variations at short periods (M_2, N_2, O_1) to be small and vertical displacement variations at long period, M_{sf}, to be small. Unlike the optimal model we use for RIS (Chapter 3) in which we include vertical M_{sf} sinusoid to detect ephemeral grounding, we do not include vertical M_{sf} sinusoid for EIS, since the covariance between horizontal and vertical M_{sf} sinusoid makes it an unreliable diagnostic proxy for indicating ephemeral grounding.

4.3.3 The Nonlinear 3-D Displacement Model

4.3.3.1 The Nonlinear Vertical Displacement Model with Ephemeral Grounding

To infer zones of ephemeral grounding and constrain the level of ephemeral grounding, we adopt the 3-D nonlinear displacement model developed in Chapter 3, which is built on the nonlinear vertical displacement model that explicitly accounts for

ephemeral grounding. This nonlinear vertical displacement model considers all relevant tidal constituents (Table 4.1) including those aliased in SAR observations which therefore cannot be inferred directly. The construction of the nonlinear vertical displacement model is through combining the inferred vertical displacements at M_2, N_2, and O_1 periods from the linear displacement model and an independent ocean tide model which provides a starting point to infer the remaining aliased tidal constituents (Chapter 3). The combination relies on the assumption that constituents with similar periods have a similar physical response, so that they share the same relative variation in phase. The nonlinear displacement model has the form

$$w^{\hat{u}}(\mathbf{r}, t) = \max(\sum_{\xi} A(\mathbf{r}) w_0^{\hat{u}}(\mathbf{r}, t), K(\mathbf{r})) \tag{4.10}$$

where $w_0^{\hat{u}}(\mathbf{r}, t)$ is the constructed vertical displacement which is the superposition of tidal displacements at all relevant tidal periods, $A(\mathbf{r})$ is the amplitude scaling to account for the decrease in amplitude in the vicinity of the grounding zone, and $K(\mathbf{r})$ is the level of ephemeral grounding. We refer readers to the supporting information (S4.7.3) for the details of constructing $w_0^{\hat{u}}(\mathbf{r}, t)$.

4.3.3.2 Formulation and Parameter Estimation

Applying the nonlinear vertical displacement model to the vertical component of tide-induced displacement (equation 4.2), we arrive at the nonlinear 3-D displacement simultaneously inferring vertical displacement with ephemeral grounding and variability of horizontal flow. At any point $\mathbf{r}$, given q displacement observations d_j ($j = 1, 2, \cdots, q$) with the corresponding known observational unit vectors and the acquisition times of primary and secondary scenes, we denote this nonlinear model as

$$\begin{aligned} \mathbf{d} &= \mathbf{g}(\mathbf{m}) \\ &= \mathbf{g}(\mathbf{v}, \mathbf{m}^{\hat{e}}, \mathbf{m}^{\hat{n}}, A, K) \end{aligned} \tag{4.11}$$

where $\mathbf{d}$ is the vector of displacement, $\mathbf{m}$ is the model parameter vector and $\mathbf{g}$ represents the forward function relating the parameters to the observations. The model parameters consist of secular velocity $\mathbf{v} = \begin{bmatrix} v^{\hat{e}} & v^{\hat{n}} & v^{\hat{u}} \end{bmatrix}^T$, parameters for the tide-induced sinusoidal horizontal displacement variation in east and north component $\mathbf{m}^{\hat{e}} = \begin{bmatrix} c_1^{\hat{e}} & s_1^{\hat{e}} & \dots & c_k^{\hat{e}} & s_k^{\hat{e}} \end{bmatrix}^T$, $\mathbf{m}^{\hat{n}} = \begin{bmatrix} c_1^{\hat{n}} & s_1^{\hat{n}} & \dots & c_k^{\hat{n}} & s_k^{\hat{n}} \end{bmatrix}^T$, and the amplitude scaling A and ephemeral grounding level K for the vertical displacement. The detailed forms of equation (4.11) are in in Chapter 3.

We adopt a Bayesian formulation of inverse problem for parameter estimation assuming Gaussian distribution for all uncertainties. The posterior probability distribution of the model parameters is (Tarantola, 2005):

$$P(\mathbf{m}|\mathbf{d}) \propto P(\mathbf{d}|\mathbf{m})P(\mathbf{m}) \tag{4.12}$$

$$P(\mathbf{d}|\mathbf{m}) \propto \exp(-\frac{1}{2}(\mathbf{d}-\mathbf{g}(\mathbf{m}))^T\mathbf{C}_\chi^{-1}(\mathbf{d}-\mathbf{g}(\mathbf{m}))) \tag{4.13}$$

where $P(\mathbf{m})$ is model prior, $P(\mathbf{d}|\mathbf{m})$ is the data likelihood and $\mathbf{C}_\chi$ is the error covariance matrix (supporting information S4.7.6). The model prior for secular velocity and horizontal displacement variations is the same as those in the linear model. We adopt uniform prior for amplitude scaling A in the range of $[0, 2]$ and uniform prior for the ephemeral grounding K in range of minimal and maximal tide height at EIS.

To solve the inverse problem, we adopt an alternative and equivalent form of equation (3.30),

$$w^{\hat{u}}(\mathbf{r}, t) = A(\mathbf{r}) \max(w_0^{\hat{u}}(\mathbf{r}, t), K'(\mathbf{r})) \tag{4.14}$$

$$K(\mathbf{r}) = A(\mathbf{r})K'(\mathbf{r}) \tag{4.15}$$

so that we can have only one unknown parameter $K'(\mathbf{r})$ within the max operator. By discretizing $K'(\mathbf{r})$, we can linearize the inverse problem. Linearization of the original nonlinear Bayesian inverse problem guarantees the optimum of the solution and makes solving the inverse problem at all grid points computationally tractable (Chapter 3).

4.3.3.3 The Nonlinear Displacement Model at EIS

We test the nonlinear 3-D displacement model with the same synthetic data used for the linear model (section 4.3.2.2) following the strategy in Chapter 3 in discretizing $K'(\mathbf{r})$. We present the synthetic tests in the supporting information (S4.7.5). Synthetic tests show that, for the vertical displacement, both the linear amplitude scaling $A(\mathbf{r})$ and grounding level $K(\mathbf{r})$ have good agreement with the prescribed values. Comparing with the tests for the linear model, the bias in the estimated amplitude and phase of horizontal M_{sf} displacement variation is greatly reduced.

4.4 Results

We apply both the linear model (section 4.3.2) and nonlinear model (section 4.3.3) to the processed displacement fields from CSK and S1 SAR data. We first present

inferred vertical displacements at selected tidal periods by the linear 3-D displacement model which are used to construct the nonlinear vertical displacement model and set up the nonlinear 3-D displacement model. Then, we present our inferred secular velocity, vertical displacements with ephemeral grounding, and fortnightly horizontal flow variability from the nonlinear 3-D displacement model. In all figures, phase values are centered at the mean phase in the observational domain and converted to the unit of minutes or days based on the period of the tidal constituent. The fortnightly flow variation is shown in displacement domain.

4.4.1 Application of the Linear Model

We report inferred variations in vertical displacements at M_2, N_2, and O_1 periods. We leave the inferred secular velocity and horizontal M_{sf} flow rate variation in the supporting information (S4.7.7). Based on the inferred amplitude of displacement at M_2 period, we derive an updated grounding line. We show this derived grounding line and compare it with the existing grounding line data in the supporting information S4.22 and include the data the supporting information (Grounding line - EIS) as well. We use this new grounding line in all the figures.

4.4.1.1 Inferred Semidiurnal and Diurnal Vertical Displacements

The spatial variability in M_2, N_2, and O_1 components are similar in terms of amplitude (Figure 4.4a1-c1), but the spatial variability of the phase differ more from component to component (Figure 4.4a2-c2). The displacement amplitude of the three components in the central trunk of ice shelf is approximately 1.2 m, 0.2 m, and 0.4 m, respectively, which is consistent with the CATS2008 tidal model (Table 4.1). The inferred amplitude is uniform in the central trunk and decreases in the vicinity of the grounding zone. The main features in the spatial variability of M_2 and N_2 phases are similar. The phase of the ice shelf east of 70°W lags ($\phi < 0$) the phase of the central trunk by 10 min to 40 min, with the lag increasing eastwards and being quite pronounced near Cape Zumberge. Lagging phase also exists in the vicinity of the grounding zone at lower latitudes. For example, near the northwestern end of the ice shelf, the phase estimates for M_2 and N_2 lag ($\phi < 0$) the phase in the central trunk by approximately 20 min. Compared with M_2, leading phase values for N_2 are present over the western portion of the ice shelf between 76.5°S and 77.2°S. The inferred leading phase values of N_2 in this region are unlikely to be physical but artifacts from the bias in the estimates which also exist in the synthetic tests (supporting information S4.7.2). Phase values for O_1 are uniform within our

observational domain, which is consistent with expected small phase variations for diurnal tides (Padman et al., 2002; Rosier et al., 2017). While there is a region of leading phase in the southwestern portion of the ice-shelf, the boundary of the region matches the boundary of phase variations in N_2. This leading phase is spurious due to the bias in estimates from the covariance between estimates of N_2 and O_1.

The synthetic test for the linear displacement model shows that ephemeral grounding can introduce pronounced bias in the estimated phase because the clipping of the vertical displacement due to ephemeral grounding is not accounted for. Here, in the phase maps of the three constituents, especially O_1, zones of localized leading/lagging phases are present in the vicinity of the grounding zone, especially where the grounding line is sinuous suggesting the existence of sub-shelf ephemeral grounding. We will directly infer zones of ephemeral grounding and quantify the level of grounding using the nonlinear model next in section 4.4.2.

4.4.1.2 Comparison with Tidal Model

We compare our inferred amplitude and phase values of vertical displacement at M_2, N_2 and O_1 periods with the CATS2008 tidal model (Padman et al., 2002) at the reference point (Figure 4.1b). This point is chosen to be away from the vicinity of the grounding line. Although the comparison is made at one point, it is representative of the ice shelf central trunk in our observation domain because the tidal displacement is spatially uniform west of 70°W. We find good agreement between our inferred values and the reference values from the tide model (Table 4.1).

In Chapter 3, the theoretical bias in the estimation are obtained from synthetic tests and the bias-corrected amplitude and phase values have better agreement with the reference values than the originally inferred values. Here, we do not find that this bias-correction improves agreement between our inferred values and the tidal model. The main reason for this lack of improvement is that our synthetic test at EIS is not as realistic as that at RIS due to lack of existing observations at EIS, so the estimated bias is also less realistic (supporting information S4.7.2). In addition, reference values obtained from the CATS2008 tidal model at EIS are not as accurate as those at RIS, due to the paucity of GPS observations at EIS (Padman et al., 2018).

4.4.2 Application of the Nonlinear Model

We now describe the inference of vertical displacements with explicit ephemeral grounding as well as horizontal flow variability using the nonlinear model. The final

spatial resolution of the reported fields is determined by the processed displacement fields and is approximately 1000 m. Animations showing the vertical motion (Movie EIS-V) and the horizontal ice flow (Movie EIS-H) are provided in the supporting information.

4.4.2.1 Construction of Vertical Displacement Model

To apply the nonlinear model, we construct the vertical displacement model (equation 4.10) by jointly using the CATS2008 tidal model and the inferred vertical displacement at M_2, N_2, and O_1 periods from the linear model. We construct the vertical displacement model following the methodology in the supporting information (S4.7.3) and present the details of the constructed vertical displacement model in the supporting information (S4.7.9).

4.4.2.2 Secular Velocity

4.4.2.2.1 Horizontal Velocity

The inferred horizontal velocity qualitatively agrees with previously published velocity fields over EIS (Mouginot et al., 2012, see differential maps in the supporting information S4.7.10). Horizontal speeds range from near zero in the upstream tributaries at the northern extent of our observational domain to approximately 1.5 m/d at DIS and 1 m/d at Trib. 5 and Trib. 6 near the grounding zone, and to approximately 2 m/d over the central trunk of ice shelf. The directions of the tributary ice flow are given by the field of arrows in Figure 4.5a.

Upstream tributaries display complex geometry and flow patterns. On the eastern side, along the grounding zone where DIS flows into the ice shelf, the ice flow varies from being perpendicular to parallel to the grounding line. The relatively slow-flowing northern tributaries Trib. 2, Trib. 3, and Trib. 4 first join into a larger ice stream at higher latitude and then join into the fast-flowing DIS. On the western side, the grounding line extends further north connecting to Trib. 5 and Trib. 6. One high-frequency feature is a region of localized fast-flowing ice that exists in Trib. 2 indicated by the contour in Figure 4.5a), which is associated with localized increase in bed elevation and thinning of ice thickness (Figure 4.1d).

Downstream, the ice shelf has relatively smooth variation in secular velocity. The direction of ice flow curves eastward by approximately 90°within our observational domain. The regions of faster ice flow lie primarily along the western side of the ice shelf, where the deeper bathymetry and thicker ice abut the mountains of the

Flower Peninsula (Figure 4.1). There are three tributaries (Trib. 7, Trib. 8, and Trib. 9) flowing into the main trunk of the ice shelf which are associated with localized sinuosity of grounding lines.

4.4.2.2.2 Vertical Velocity

The inferred secular vertical velocity which is the vertical component of the secular ice flow along the surface slope is near zero over most of the observational domain ($\leq 5\,\mathrm{cm/d}$) consistent with the shallow surface slope at EIS. However, we find that the inferred values are highly dependent on the direction and magnitude of horizontal secular flow, which implies that the inferred values may not reflect the actual surface slope, but are rather artifacts due to covariance with horizontal secular velocity. At RIS, similar artifacts in secular vertical velocity were also observed and discussed in Minchew et al. (2017), but were largely reduced in Chapter 3 with the improvement in the displacement dataset. The artifacts we observe here should be caused by the non-ideal viewing geometry of and insufficient constraint from available SAR data at EIS (supporting information S4.7.11).

4.4.2.3 Vertical Displacement with Ephemeral Grounding

The inferred amplitude scaling, $A(\mathbf{r})$ (Figure 4.6a), representing the amplitude of vertical displacement at all tidal periods, is approximately in the range of 0.9~1.1 and decreases downstream. In the vicinity of the grounding zone, the amplitude scaling gradually decreases to 0 over distances of 5 km to 10 km. High-frequency low-amplitude features are observed downstream of Trib. 8 and Trib. 9 suggesting zones of ephemeral grounding induced by sub-shelf pinning points.

The inferred zones of ephemeral grounding (Figure 4.6b) are prevalent in the vicinity of the grounding zone in our observational domain, but are not present in the central trunk of the ice shelf. The spatial distribution of ephemeral grounding has noticeably good agreement with the sinuosity of the grounding line where localized bathymetric highs pin the grounded ice and induce ephemeral grounding. We identify more zones of ephemeral grounding on the eastern margin than the western margin of the ice shelf. The inferred level of ephemeral grounding, $K(\mathbf{r})$, is typically in the range from -1.5 m to 0 m increasing towards to grounding line. The ephemeral grounding is pronounced at multiple zones with a relatively high level of ephemeral grounding above -0.5 m.

Our observation reveals many more existing zones of ephemeral grounding than

existing documentation of ice rumples at EIS (Matsuoka et al., 2015) which only indicates the two isolated pinning points downstream of Trib. 8 and a few more pinning points near Cape Zumberge. We note that the identified zones of ephemeral grounding are the lower bound of the actual extent of ephemeral grounding (S4.7.4). The spatially continuous area of zones of ephemeral grounding in the vicinity of the grounding zone within our observational domain suggests that more areas of ephemeral grounding may exist downstream.

4.4.2.4 Horizontal Fortnightly Flow Variability

We present the inferred fortnightly variation in horizontal flow at EIS. In the 2-D horizontal plane, we define along-flow and cross-flow as the direction along (parallel to) and cross (perpendicular to) the inferred direction of secular velocity. Cross-flow direction is 90° counter-clockwise from along-flow direction.

4.4.2.4.1 Variation in the Along-Flow Component

The large amplitude values of the along-flow fortnightly variation span the ice shelf south of 76.2°S, vary smoothly in space, and increase from 20 cm upstream to 45 cm downstream near Cape Zumberge (Figure 4.7a). The inferred amplitudes agree with the reported values from sparse GPS stations over EIS (Rosier et al., 2017). The inferred amplitude values decrease upstream and are near zero over the upstream grounded tributaries with the exception of the relatively large amplitude of ~10 cm at DIS. The good agreement between the amplitude of along-flow component and horizontal secular speed is expected according to our understanding of the generation of fortnightly flow variability, which we will discuss in section 4.5.

The inferred phase values (Figure 4.7b) show that the M_{sf} component in the floating ice shelf leads relative to the upstream tributaries. The phase values over the central trunk of the ice shelf are relatively uniform within EIS inlet and increase by approximately 0.5 day east of 72°W where an increase in amplitude values is also found. In the vicinity of the grounding zone, a number of areas of leading phase are present, many of which match well the zones of ephemeral grounding we have identified.

4.4.2.4.2 Variation in the Cross-Flow Component

The inferred amplitude of the fortnightly cross-flow variation is 0 km~10 cm in our observational domain which is small and comparable to the uncertainty in estimation (Figure 4.7c). As with the along-flow, the amplitude of cross-flow

increases downstream. We find relatively large amplitude values at the southeastern end of the observational domain. The phase of cross-flow component varies from +3 day upstream at DIS continuously to −3 day at the eastern end of observational domain, which is presumably associated with the 90°eastward bend of the ice flow.

4.4.2.4.3 Upstream Propagation

The fortnightly variation is communicated through the grounding zone and to a maximum of 70 km upstream at DIS with a propagation speed of ~30 km/d, while the fortnightly variation is negligible at Trib. 5 and Trib. 6. At DIS, the inferred basal traction from surface and bed elevation data (Joughin et al., 2006) is only 8 KPa and the subglacial material is inferred to be weak dilated till from in-situ seismic experiments (Vaughan et al., 2003). The flat and weak bed at DIS should facilitate the upstream propagation of stress changes. In contrast, at Trib. 5 and Trib. 6, where the bed is deep and ice is thick, the bed is inferred to be much harder than the bed of DIS with basal shear stresses inferred to exceed 100 KPa (Joughin et al., 2006).

4.5 Discussion

4.5.1 Asymmetric Response to Tidal Forcing and M_{sf} Modulation

4.5.1.1 Evans Ice Stream and Rutford Ice Stream

Previous studies at RIS have suggested that the M_{sf} signal over the ice-shelf-stream system is driven by the asymmetric response of ice shelf flow to the high and low tide. Several tide-induced ice shelf processes are proposed to explain this asymmetry including sub-shelf ephemeral grounding (Minchew et al., 2017; Robel et al., 2017) and asymmetric migration of grounding line (Robel et al., 2017; Warburton et al., 2020) which give rise to tide-modulated temporal variations in buttressing stress. Chapter 3 provided direct observation of ephemeral grounding at RIS and the key evidence for asymmetric response of ice-shelf flow to tidal forcings caused by ephemeral grounding.

Our new observations for EIS show tide-induced ephemeral grounding and fortnightly flow variability similar to that found at RIS. The two ice streams exhibit noticeable similarities including the spatial variability of the amplitude and phase of the fortnightly flow and the prevalent existence of areas of ephemeral grounding in the vicinity of the grounding zone. Hence, RIS and EIS, two major ice streams at Zumberge Coast, have a similar asymmetric response to tidal forcings and sub-shelf

ephemeral grounding.

With ocean tide modulating the variations in buttressing stress that influence the flow rate, the fortnightly flow variability presumably comes from the difference between the magnitude of increase in ice flow rate w.r.t. to high tide (i.e., decrease in buttress stress) and the magnitude of decrease in ice flow rate w.r.t. to low tide (i.e., increase in buttress stress) (e.g., Rosier et al., 2017). The magnitude of this difference, which determines the magnitude of the fortnightly flow variability, scales with both the mean flow speed and the intrinsic asymmetry in the ice shelf tidal response which is associated with ice shelf processes such as ephemeral grounding and asymmetric migration of grounding line. If we consider two ice streams experiencing the same tidal forcing and the same variation in buttressing stress caused by ephemeral grounding, the ice stream with a higher mean flow speed will exhibit a larger amplitude of fortnightly flow. Therefore, we use the ratio of fortnightly flow speed to the secular speed, M^*_{sf}, as a proxy to the magnitude of intrinsic asymmetry in the ice shelf tidal response.

M^*_{sf} in the central trunk of the ice shelf at EIS is ~10% in along-flow component and less than ~5% in cross-component, but significantly larger M^*_{sf} (> 20%) is present in the vicinity of the grounding zone, especially in areas of ephemeral grounding. The agreement between zones of relatively large M^*_{sf} and zones of ephemeral grounding reinforce the connection between tide-induced ephemeral grounding and fortnightly flow.

M^*_{sf} at RIS exhibits similarities with that at EIS, with areas of large M^*_{sf} corresponding to areas of ephemeral grounding. However, the tidal amplitude at RIS is only ~30% larger than that at EIS, but the M^*_{sf} at the central trunk of the ice shelf at RIS is at least two times larger than that at EIS. This difference implies that the intrinsic asymmetry to tidal response is more significant at RIS, which is likely to be associated with the larger area of zones of ephemeral grounding relative to the spatial extent of RIS.

4.5.1.2 Filchner-Ronne Ice Shelf System

Using extensive GPS observations over FRIS, Rosier et al. (2017) shows that the amplitude of fortnightly signal increases downstream from the tributary ice streams to the central trunk of FRIS, and all the way to the ice shelf front, but M^*_{sf} decreases downstream, with the largest values of M^*_{sf} seen where major tributary ice streams, such as EIS and RIS, begin to float. The increase in mean flow speed downstream

is likely to be the primary reason for the increase in the amplitude of M_{sf} described in Rosier et al. (2017). The large M^*_{sf} observed at the tributary ice streams is likely to be associated with the shallow bathymetry underneath these inlets of the FRIS system, where areas of ephemeral grounding exist.

Tide-induced ephemeral grounding may be one of the several ice shelf processes that can give rise to asymmetric tidal response. Multiple mechanisms can coexist including ephemeral grounding and asymmetric migration of the grounding line. Evaluating the importance of individual mechanism requires further observations and new modeling studies.

4.5.2 Long-Term Response to Ice Shelf Thinning

The thinning of ice shelves can result in the retreat of grounding lines and decrease in basal traction, and thus cause acceleration and thinning of glaciers, which can lead to further catastrophic mass loss in the settings prone to the marine ice-sheet instability. This dynamic response to ice shelf thinning has been observed along Amundsen Coast where the outlet glaciers account for most of the ice discharge increase from the western Antarctica (e.g., Joughin et al., 2014; Sutterley et al., 2014; Gardner et al., 2018). Although the current FRIS has a net mass loss close to zero resulting in almost constant ice thickness, studies have shown that sub-shelf ocean currents below FRIS could transition from cold to warm by the end of the century increasing the sub-shelf basal melting by more than an order of magnitude (Hellmer et al., 2012).

Quantifying the decrease in the buttress effect in ice shelves due to ice shelf thinning is critical for projecting increase in ice flow rate due to oceanic warming. However, we do not have direct measurement of the basal traction provided by zones of ephemeral grounding. Assuming that basal traction from ephemeral grounding is the primary mechanism for the asymmetric response to tidal forcing, the variation in the longitudinal stress is the lower bound of the increase in longitudinal stress if the thinning of the ice shelf fully ungrounds the ice from the current zones of ephemeral grounding. This estimate is a lower bound because the actual increase in longitudinal stress will be higher as some fully grounded regions will become ephemeral, resulting in further decrease in buttressing stress (Chapter 3). The increase in longitudinal stress can be projected as the increase in secular flow speed.

Adopting a theoretical model of laterally confined ice stream on the relationship between in variation in longitudinal stress and variation in flow rate (Minchew et

al., in prep.), we estimated the variation in longitudinal stress to be ~100 KPa at RIS using the spatial variability of the upstream propagating M_{sf} signal. In the settings discussed above, the loss of current ephemeral grounding zones results in ~0.5 m/d of flow rate increase in response to ice shelf thinning removing the current zones of ephemeral grounding at RIS. Applying the same calculation to EIS is difficult because of the complex geometry which violates the model assumptions. However, considering that the inferred amplitude and phase of the upstream propagating M_{sf} signal at DIS is similar to that at RIS, the estimated increase in flow rate (~0.5 m/d) due to loss of ephemeral grounding may serve as a starting point of the projection at EIS. We note that in longer term, with substantial thinning of ice shelf, massive mass loss may come from the western and northern tributaries which are prone to marine ice sheet instability due to the reverse bed slopes, while DIS may stay relatively stable with moderate increases in ice flow rate.

4.5.3 The Joint Use of Sentinel-1 and COSMO-SkyMed Observations

We jointly use SAR data collected over EIS from the Sentinel-1 (S1) observational campaign operated by European Space Agency (ESA) and COSMO-SkyMed (CSK) observational campaign operated by Italian Space Agency (ASI). Both S1 and CSK observation have unique advantages and complements the other. The synoptic-scale S1 data has an advantage in spatial extent providing a complete coverage of the entire EIS system and a portion of the Ronne-Ice-Shelf downstream. Besides, S1 data is also freely available Open Data, so that we are able to use the entire dataset collected from 2017 to 2021. Although, the CSK data only constitutes a small amount compared with S1 data in our inversion, the CSK data provides unique advantage that it happens to have better sensitivity to low tide than S1 data because of the timing of acquisitions (supporting information S4.7.12). In the region of the ice shelf imaged by CSK, we are able to resolve zones of ephemeral grounding with grounding level below −1 m (e.g., the periphery of ephemeral grounding points downstream of Trib. 8). In a more general comparison of the two types of data that we have, CSK data (X-band, acquired in Stripmap mode by a 4-satellite constellation) has shorter revisit intervals, higher spatial resolution, and higher coherency over ice than S1 data (C-band, acquired in Terrain Observation with Progressive Scan mode by a 2-satellite constellation) (see section 4.2).

The rapid increase in the availability of SAR observations has seen an increase in the fusion of data from multiple sensors (e.g., Velotto et al., 2016; Milillo et al., 2019). Compared with single-sensor observations, the cross-sensor observations

have advantages in both spatial coverage/resolution and temporal sensitivity. Our study is an example demonstrating the benefits of utilizing cross-sensor observations for resolving complex surface displacement/deformation.

4.6 Conclusions

Adopting the same methodology as Chapter 3, we infer vertical displacement with ephemeral grounding and horizontal fortnightly flow variability at EIS. We jointly use SAR data acquired by both the Sentinel-1 and COSMO-SkyMed constellations.

Our study documents areas of sub-shelf ephemeral grounding and spatial variability of fortnightly flow at EIS. The inferred areas of ephemeral grounding are prevalent in the vicinity of the grounding zone which provides new observational evidence for the asymmetric response of the ice-shelf flow to the high and low tide. The inferred fortnightly (M_{sf}) variability at EIS is relatively large over the floating ice shelf and propagates upstream to the grounded ice, similarity to what has been seen at RIS. The spatial agreement between the zones of relatively large M^{*}_{sf} and areas of ephemeral grounding suggests that tide-induced ephemeral grounding is an important mechanisms for the generation of fortnightly flow variability. With ongoing oceanic warming and ice-shelf thinning, the loss of ephemeral grounding will decrease buttressing stress leading to an increase in ice flow rate. We expect the lower bound of the increase in ice flow rate to be comparable to our estimation at RIS which is $0.5\,\mathrm{m/d}$.

Acknowledgements

The presented work is possible due to the availability of raw COSMO-SkyMed SAR imagery and provided by the Italian Space Agency (ASI) and Copernicus Sentinel 1a and 1b SAR imagery openly provided by the European Space Agency (ESA) as two dedicated campaigns to image Evans Ice Stream. We sincerely thank ASI and ESA for all their efforts in making these campaigns successful.

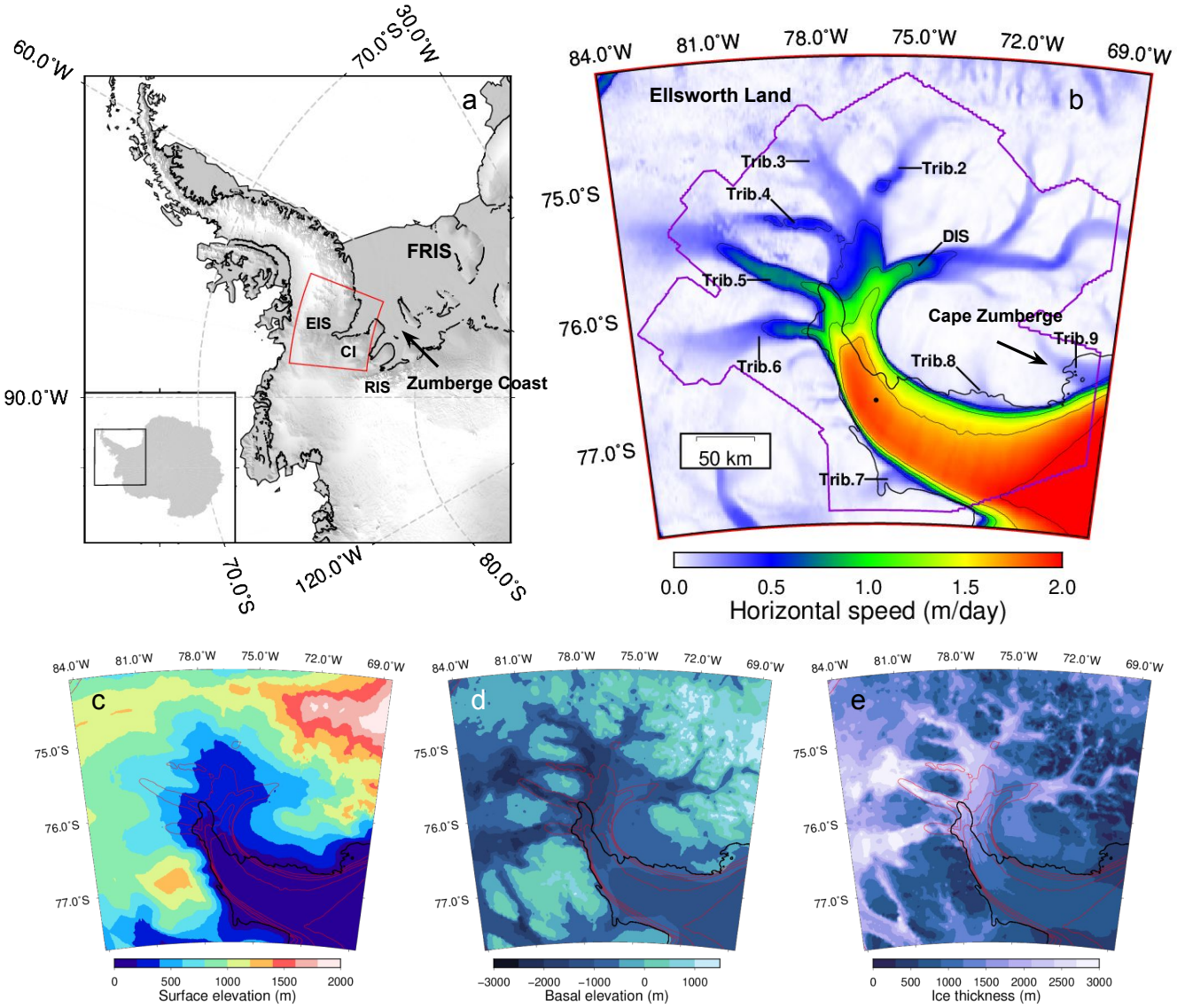

Figure 4.1: (a) Shaded relief map of EIS and surrounding area. EIS: Evans Ice Stream. RIS: Rutford Ice Stream. CI: Carlson Inlet. FRIS: Filchner-Ronne Ice Shelf. Red box indicates the region of EIS shown in Figures 1b–1e. (b) Horizontal velocity from Mouginot et al. (2012). The purple outline indicates the observational domain in this study. (c and d) Surface and basal elevation relative to mean sea level. (e) Ice thickness. Red contour lines in Figures 1c–1e indicate horizontal surface velocity from Figure 1b in 0.4 m/d increments. In all panels, irregular black lines indicate the grounding line. All the elevation data is from BedMachine V2(Morlighem et al., 2020). In all panels, irregular black lines indicate grounding line from Bedmap2 (Fretwell et al., 2013).

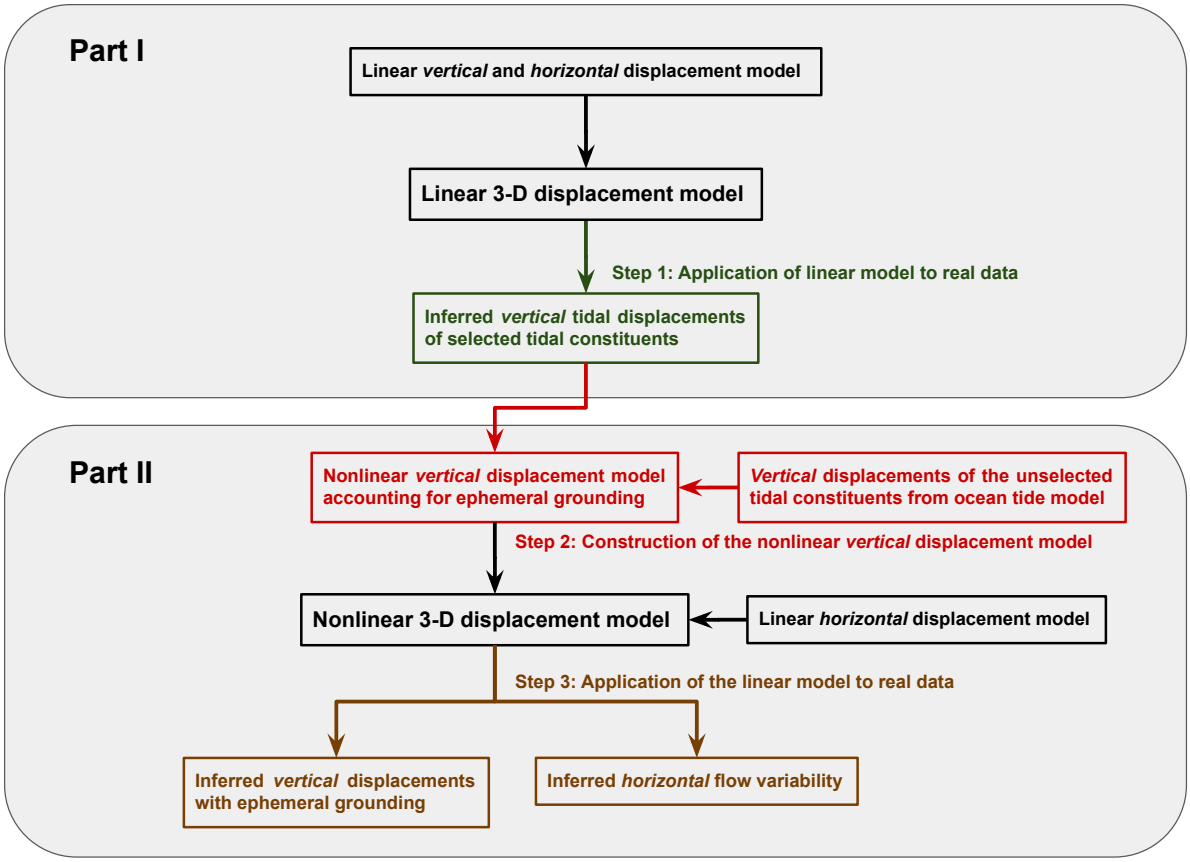

Figure 4.2: Outline of the workflow described herein. The workflow has two parts which are associated with a linear 3-D displacement model in the upper panel and a nonlinear 3-D displacement model in the lower panel, respectively. The full workflow consists of the two models and three steps.

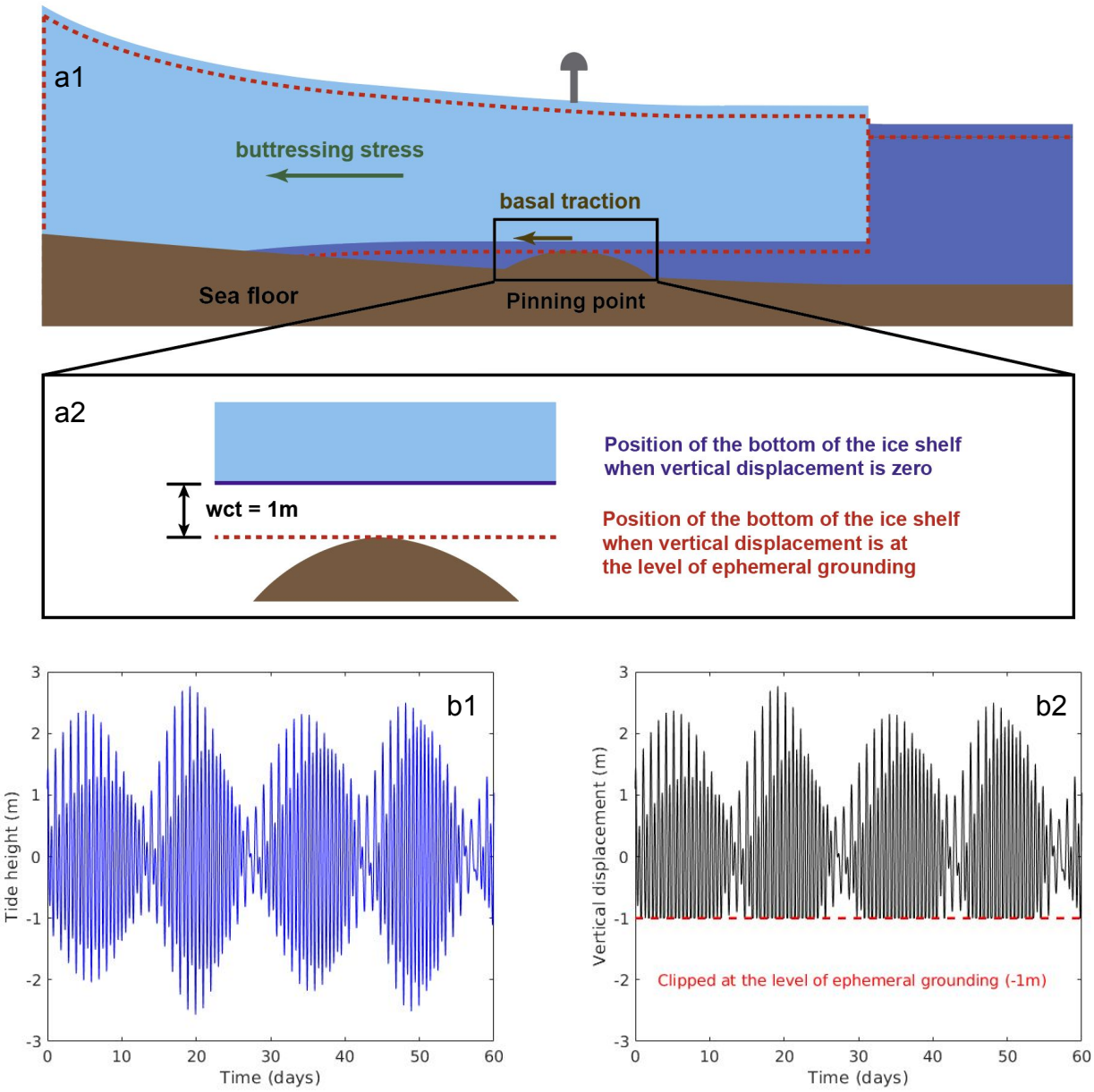

Figure 4.3: (a1) Schematic view of tide-induced ephemeral grounding on a sub-shelf pinning point. The red dashed line indicates the location of the ice-shelf in hydrostatic balance with the ocean during at the level of ephemeral grounding. The brown arrow indicates the basal traction induced by the ephemeral grounding. The green arrow indicates the ice shelf buttressing stress. (a2) The level of the bottom of ice shelf when tide height is at mean sea level (solid blue) and at the level of ephemeral grounding (dashed red). (b1) Tidal height at EIS from the CATS2008 tidal model at a reference point in the central trunk (Figure 4.1b).

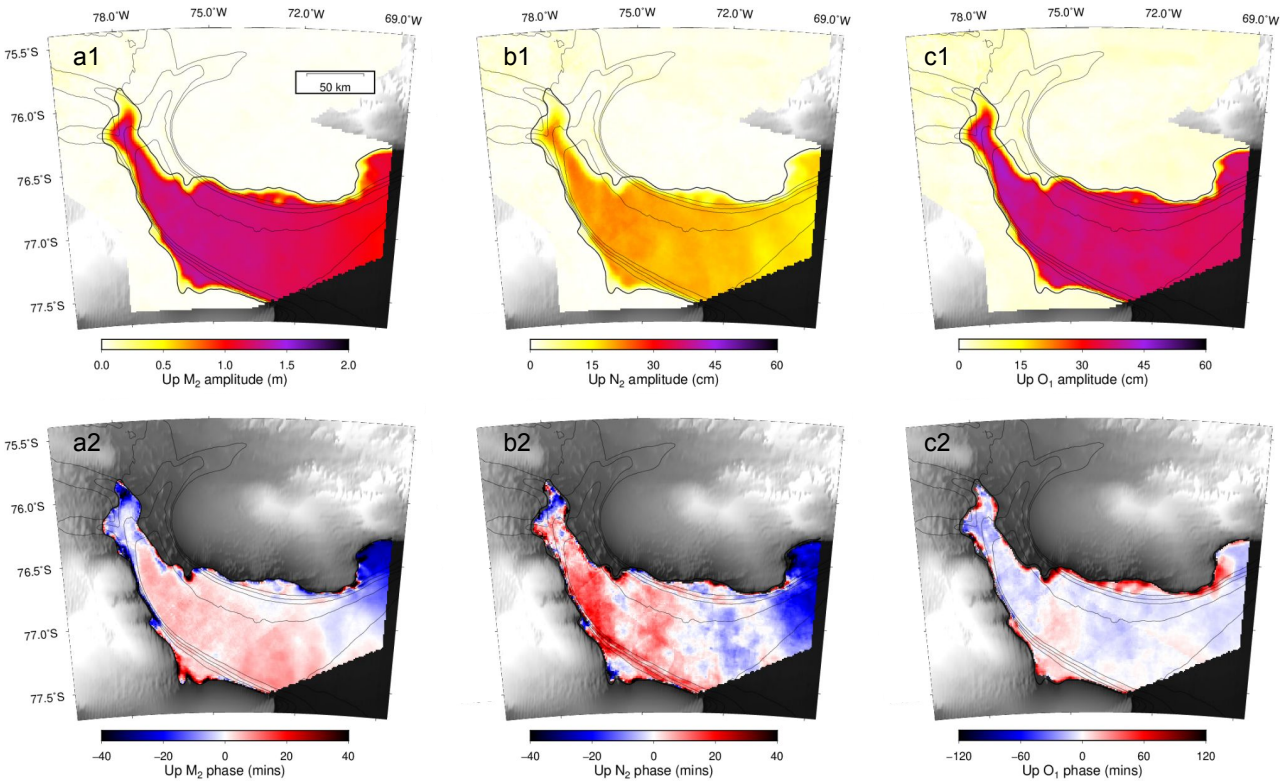

Figure 4.4: The tide-induced vertical displacement variation at M_2, N_2, O_1 periods. (a1-c1) Amplitude variations of the vertical displacement (a2-c2) Phase variations of the vertical displacement centered at the mean phase. Grounding line is derived from the 10 cm contour of M_2 amplitude. Phase estimates outside of ice shelf are not shown. The background is shaded surface elevation from Morlighem et al. (2020).

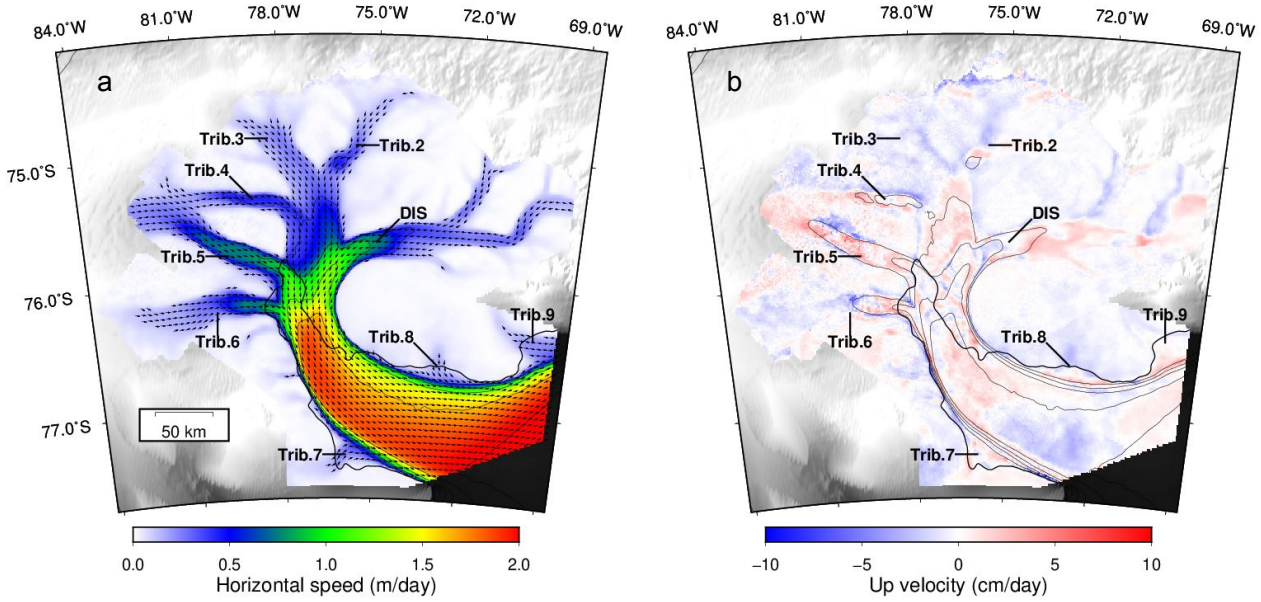

Figure 4.5: Secular velocity components. (a) Horizontal velocity where colors indicate speed and arrows indicate flow direction. Vector lengths are constant. (b) Vertical velocity, where positive values are moving upward. The background is shaded surface elevation from Morlighem et al. (2020).

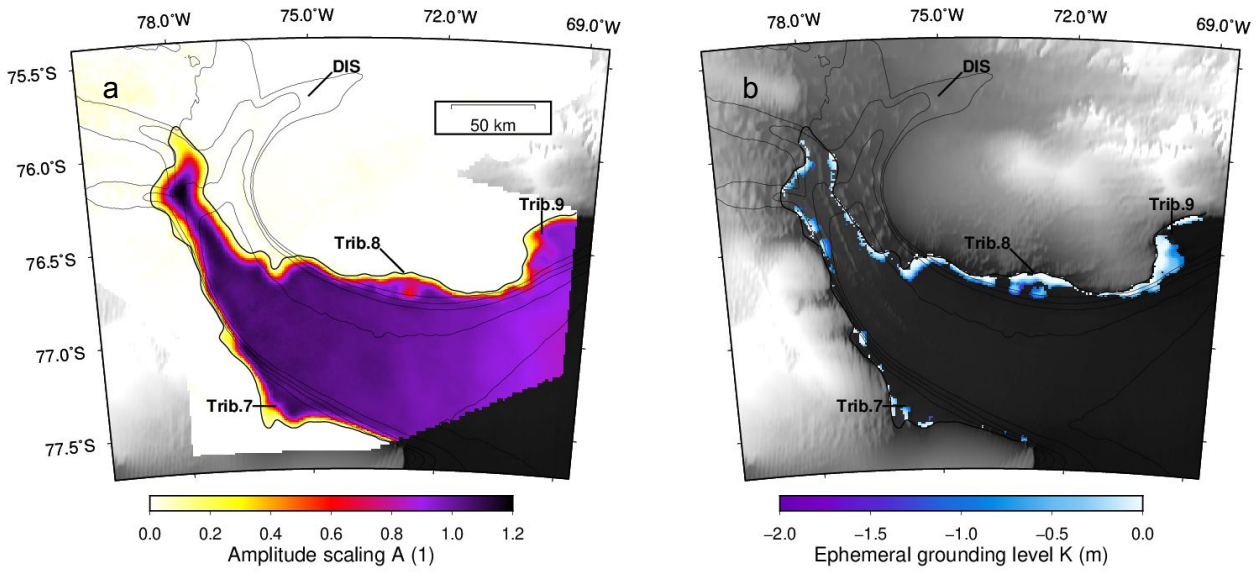

Figure 4.6: Vertical displacement inferred from the nonlinear model. (a) Amplitude scaling A for all constituents. (b) Ephemeral grounding level. Only the estimated values with credible interval size $< 60\,\mathrm{cm}$ are shown. Black contour lines are inferred horizontal speed in $0.4\,\mathrm{m/d}$ increments. The background is shaded surface elevation from Morlighem et al. (2020).

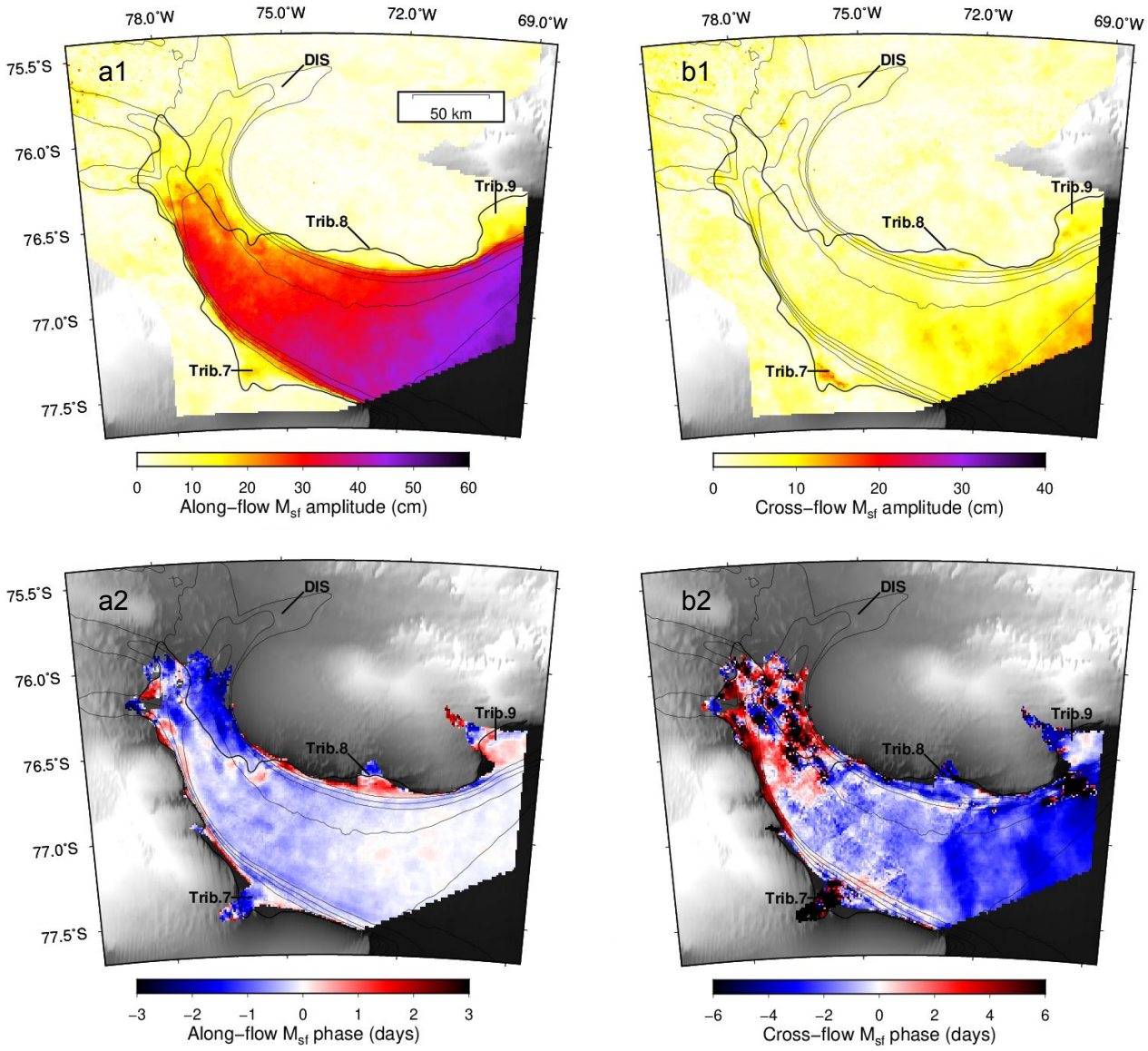

Figure 4.7: Along-flow and cross-flow horizontal displacement variation velocity at M_{sf} (14.77 day) period. (a) Along-flow displacement amplitude. (b) Along-flow displacement phase. (c) Cross-flow displacement amplitude. (d) Cross-flow displacement phase. Phase values of grid points defined in Figure 4.8 by M_{sf} modulation are shown. Black contour lines are inferred horizontal speed in 0.2 m/d increments. The background is shaded surface elevation from Morlighem et al. (2020).

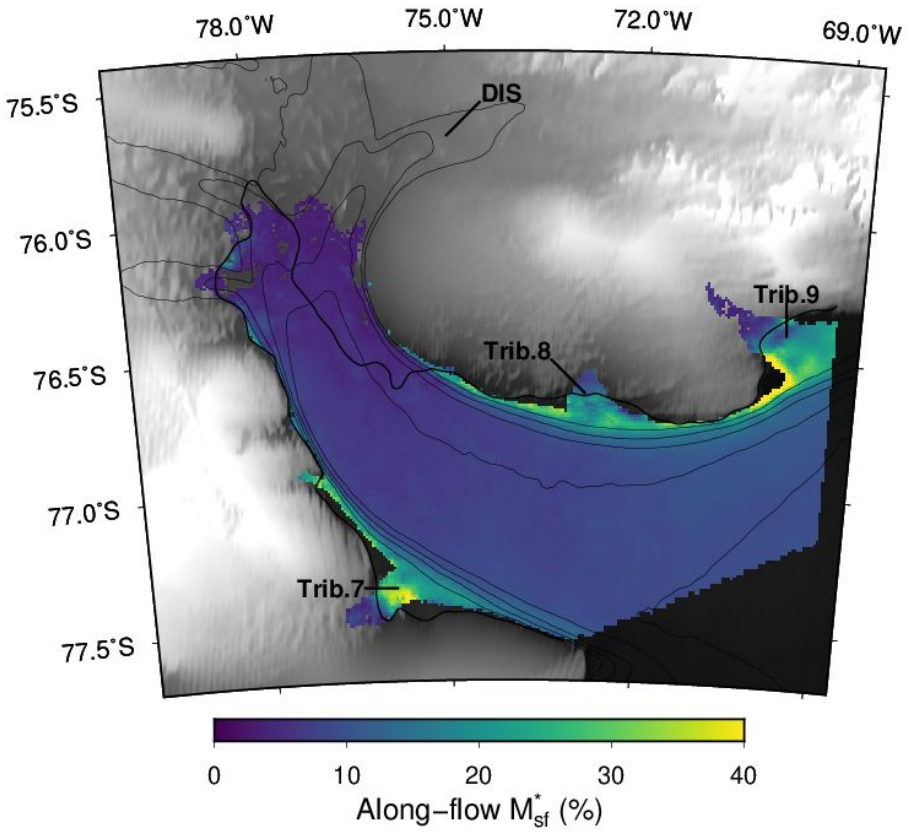

Figure 4.8: The ratio of along-flow fortnightly variation in flow velocity to secular flow velocity (M^*_{sf}). Grid points with along-flow component of M^*_{sf} larger than 3% and secular velocity larger than 10 cm/d are shown. The background is shaded surface elevation from Morlighem et al. (2020).

Constituent	Period (days)	Reference Amplitude (m)	Reference Phase (°)	Inferred Amplitude (m)	Inferred Phase (°)
M_2	0.5175	1.184	105.99	1.264	104.62
S_2	0.5000	0.765	-23.47	-	-
N_2	0.5274	0.197	9.97	0.211	10.82
K_2	0.4986	0.198	159.22	-	-
K_1	0.9973	0.361	18.36	-	-
O_1	1.0758	0.365	126.54	0.380	125.41
P_1	1.0027	0.126	8.05	-	-
Q_1	1.1195	0.082	23.50	-	-
M_f	13.6608	0.026	-32.71	-	-
M_m	27.5546	0.016	11.60	-	-

Table 4.1: Reference amplitude and phase values are from the CATS2008 tidal model at the reference point in the central trunk of EIS.

S4.7 Supplementary Information

S4.7.1 Additional Information of SAR Data and Displacement Fields

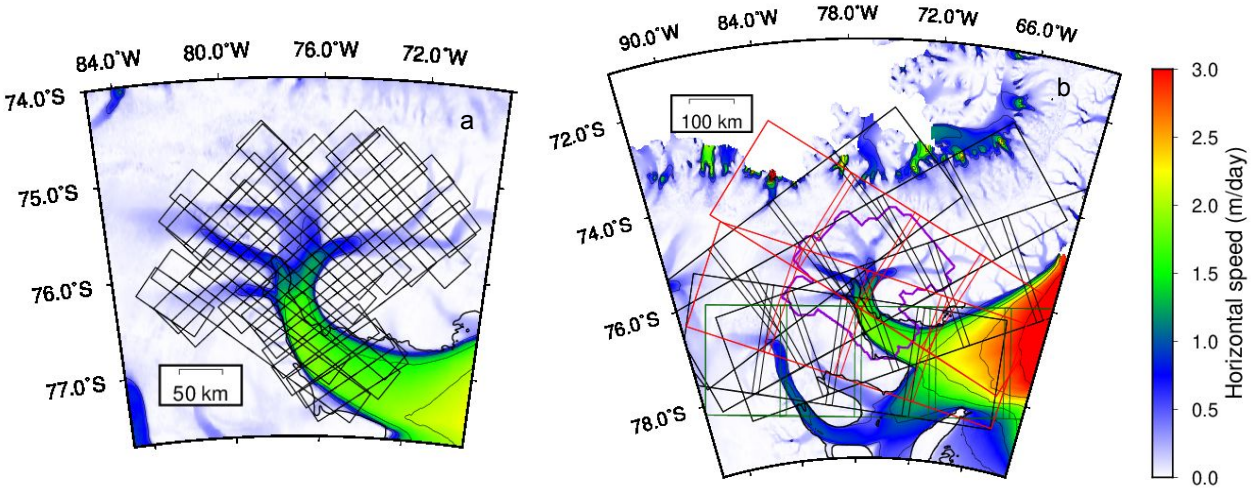

Figure S4.9: (a) Footprints of CSK acquisitions over 11 ascending and 11 descending tracks at EIS. (b) Footprints of S1 acquisitions over 6 tracks at EIS. Data from the four black tracks have a 6-day repeating time intervals with a time span from July, 2017 to the present. Data from the green track have a 12-day repeating time interval with a time span from July, 2017 to the present. Data from the two orange tracks have a 6-day repeating time interval with a time span from June, 2019 to the present.

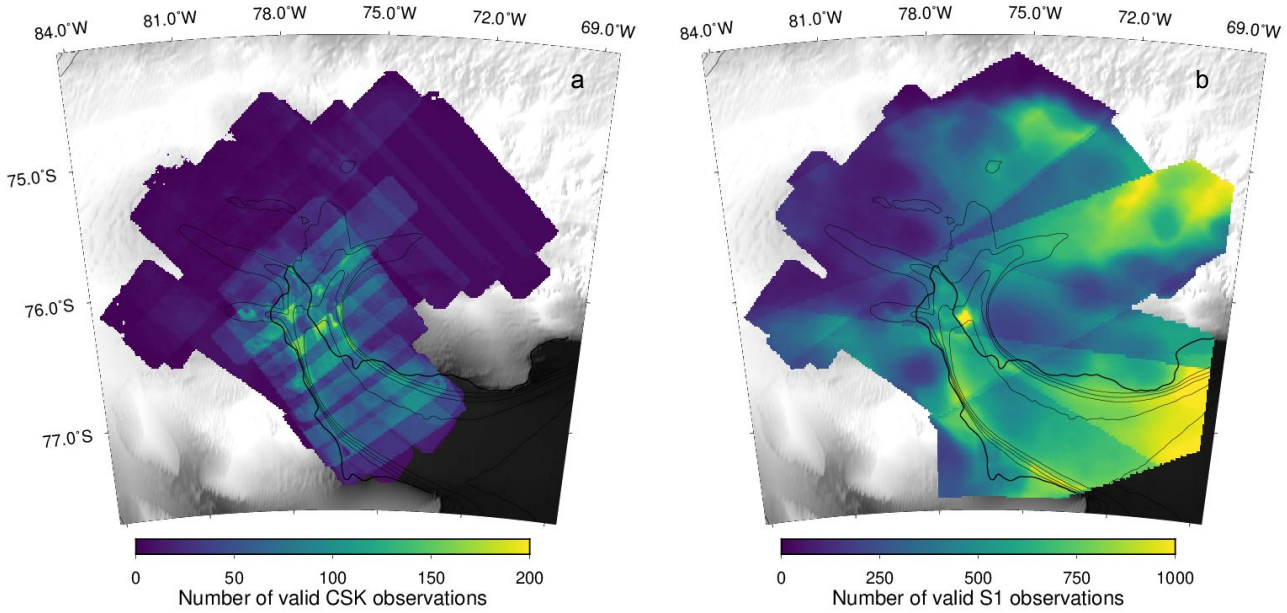

Figure S4.10: Number of valid (a) CSK observations and (b) S1 observations over EIS. One observation corresponds to a pair of displacement measurements in range and azimuth direction.

S4.7.2 Synthetic Tests of the Linear Model

We conduct synthetic tests considering all four combinations of ephemeral grounding and vertical M_{sf}. In the tests with ephemeral grounding, the level of ephemeral grounding is set as -5 m everywhere.

We find that vertical M_{sf} is not a reliable diagnostic proxy for ephemeral grounding. In the "without ephemeral grounding - with vertical M_{sf}" test, the inferred amplitude of vertical M_{sf} is 5 cm~10 cm which is larger than that from synthetic tests for RIS which is less than 5 cm. In the "with ephemeral grounding - with vertical M_{sf}" test, although the level ephemeral grounding is the same everywhere, the inferred amplitude M_{sf} has large variations ranging from 10 cm to 60 cm. The large amplitudes of M_{sf} located at the upstream portion of the ice shelf are associated with large amplitudes of horizontal M_{sf} suggesting large covariance between the two components. Unlike this synthetic test at EIS, the corresponding synthetic test at RIS finds that the amplitude of M_{sf} is uniform over the entire ice shelf, and no strong variations in amplitudes of horizontal M_{sf} are introduced.

S4.7.2.1 Without ephemeral grounding - without vertical M_{sf}

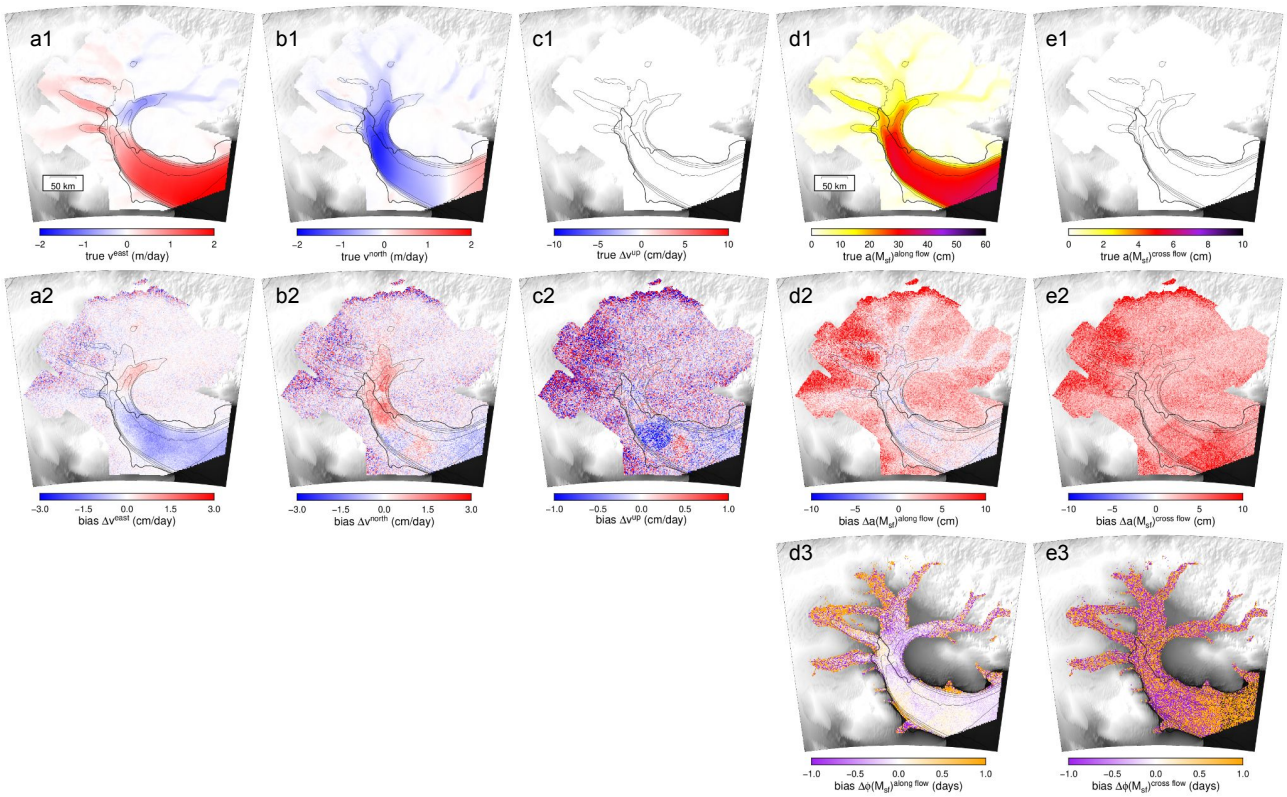

Figure S4.11: Input and the bias of estimated secular and tide-induced M_{sf} displacement using the linear model without ephemeral grounding or vertical M_{sf} in the model. (a1-c1) Input secular horizontal and vertical velocity. (d1-e1) Input amplitude of horizontal sinusoidal displacement at M_{sf} period. Input phases of all sinusoidal displacement are spatially constant and are not shown. The bias of estimation is defined as the inferred value minus the input value. (a2-c2) Bias of estimated secular velocity. (d2-f2) Bias of estimated amplitude of vertical sinusoidal displacements. (d3-e3) Bias of estimated of phase of horizontal sinusoidal displacement. Phase estimates at where amplitude is small has large uncertainty and are not shown. The input M_{sf} cross-flow displacement has zero amplitude, so the input phase the bias of phase estimates are not available.

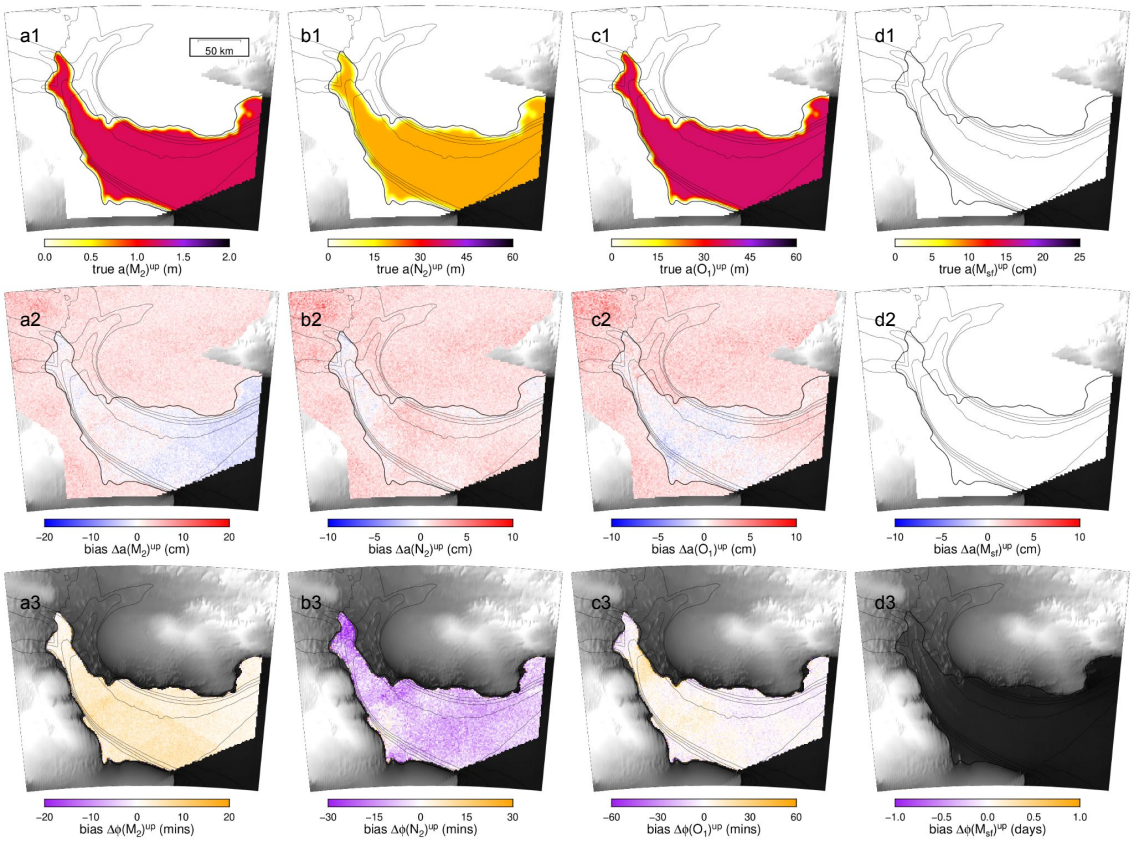

Figure S4.12: Input and the bias of estimated vertical displacement using the linear model without ephemeral grounding or vertical M_{sf} in the model. (a1-d1) Input amplitude of vertical displacement at M_2, N_2, O_1, and M_{sf} periods. (a2-d2) Bias of inferred amplitude of vertical displacement at M_2, N_2, O_1, and M_{sf} periods. (a3-d3) Bias of inferred phase of vertical displacement at M_2, N_2, O_1, and M_{sf} periods.

S4.7.2.2 Without ephemeral grounding - with vertical M_{sf}

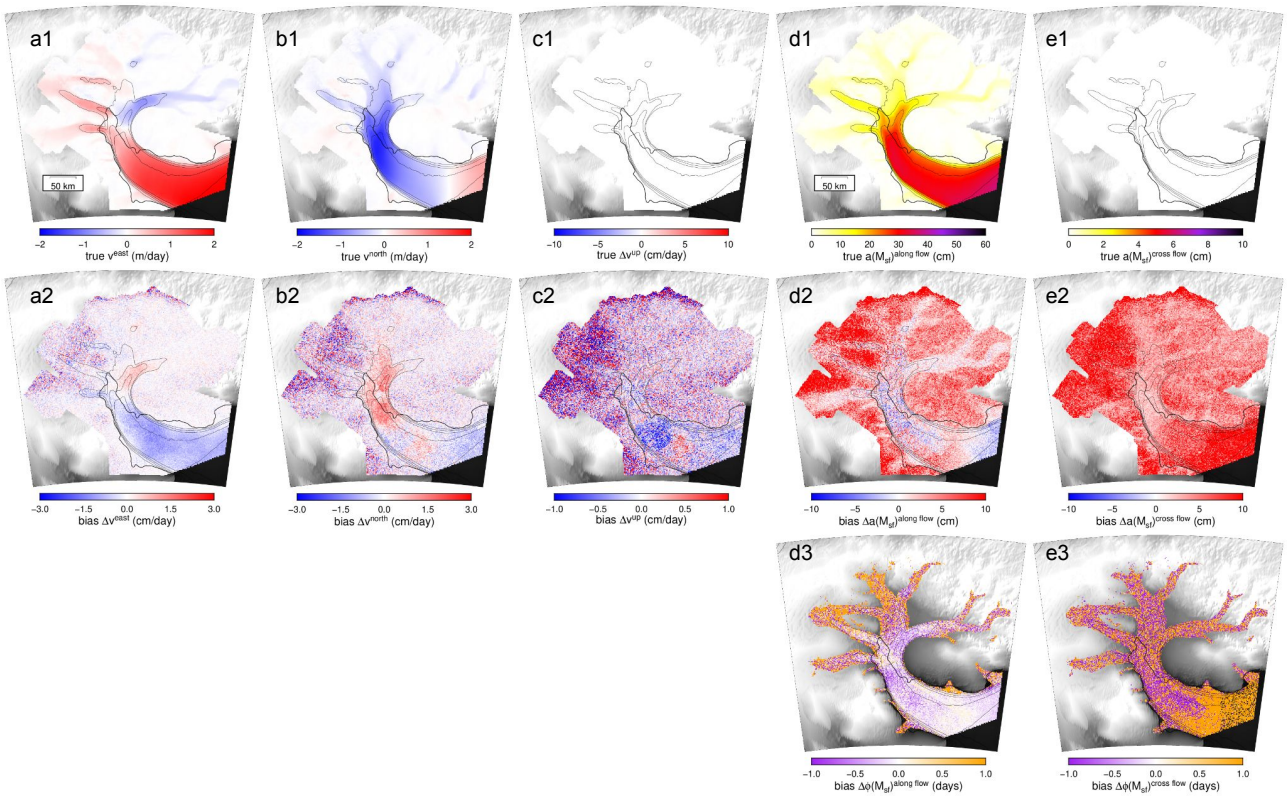

Figure S4.13: Input and the bias of estimated secular and tide-induced M_{sf} displacement using the linear model without ephemeral grounding but with vertical M_{sf} in the model. The layout of panels is the same as Figure S4.11.

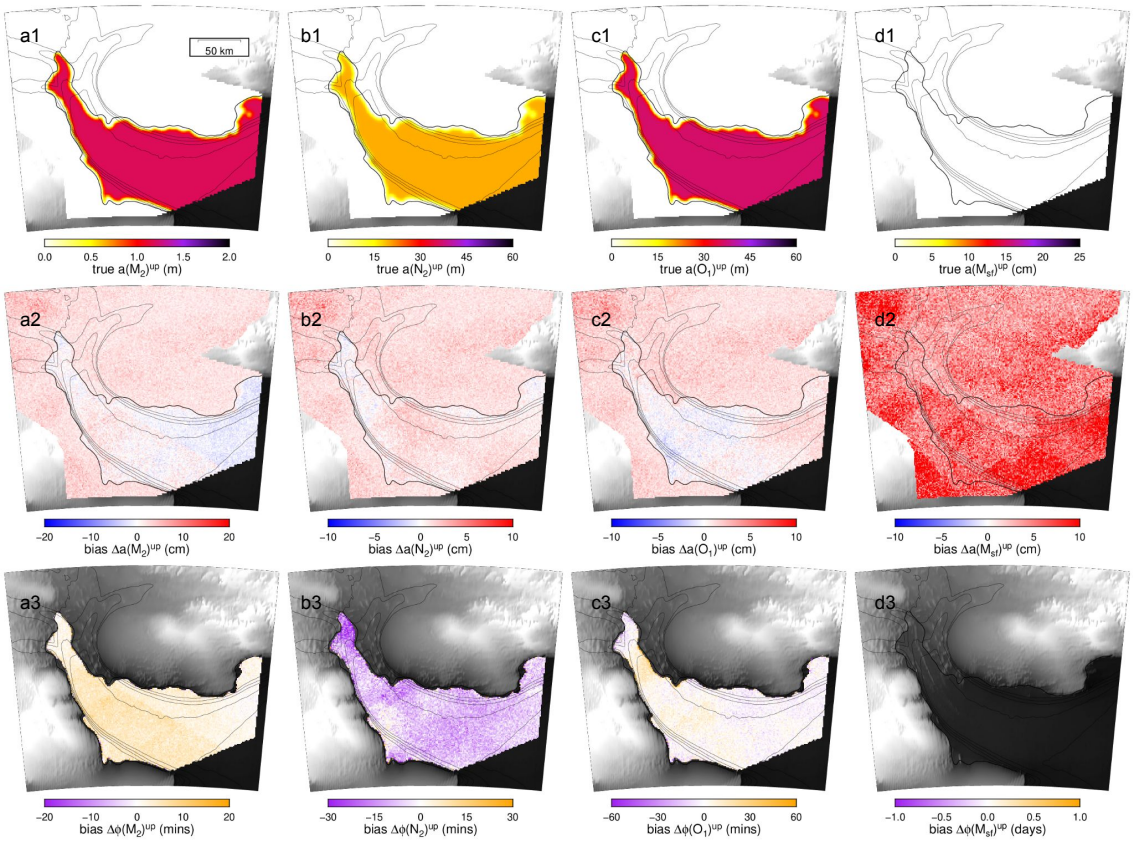

Figure S4.14: Input and the bias of estimated vertical displacement using the linear model without ephemeral grounding but with vertical M_{sf} in the model. The layout of panels is the same as Figure S4.12.

S4.7.2.3 With ephemeral grounding - without vertical M_{sf}

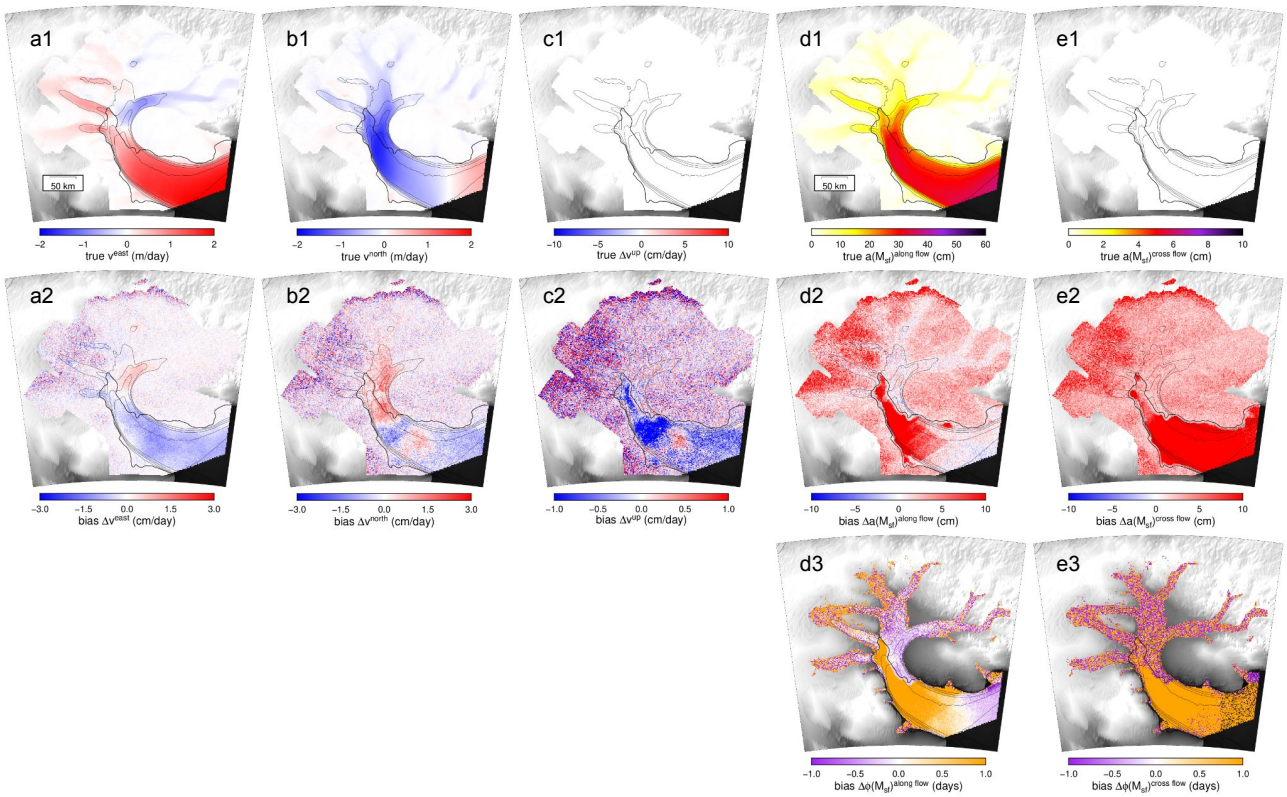

Figure S4.15: Input and the bias of estimated secular and tide-induced M_{sf} displacement using the linear model with ephemeral grounding but without vertical M_{sf} in the model. The layout of panels is the same as Figure S4.11.

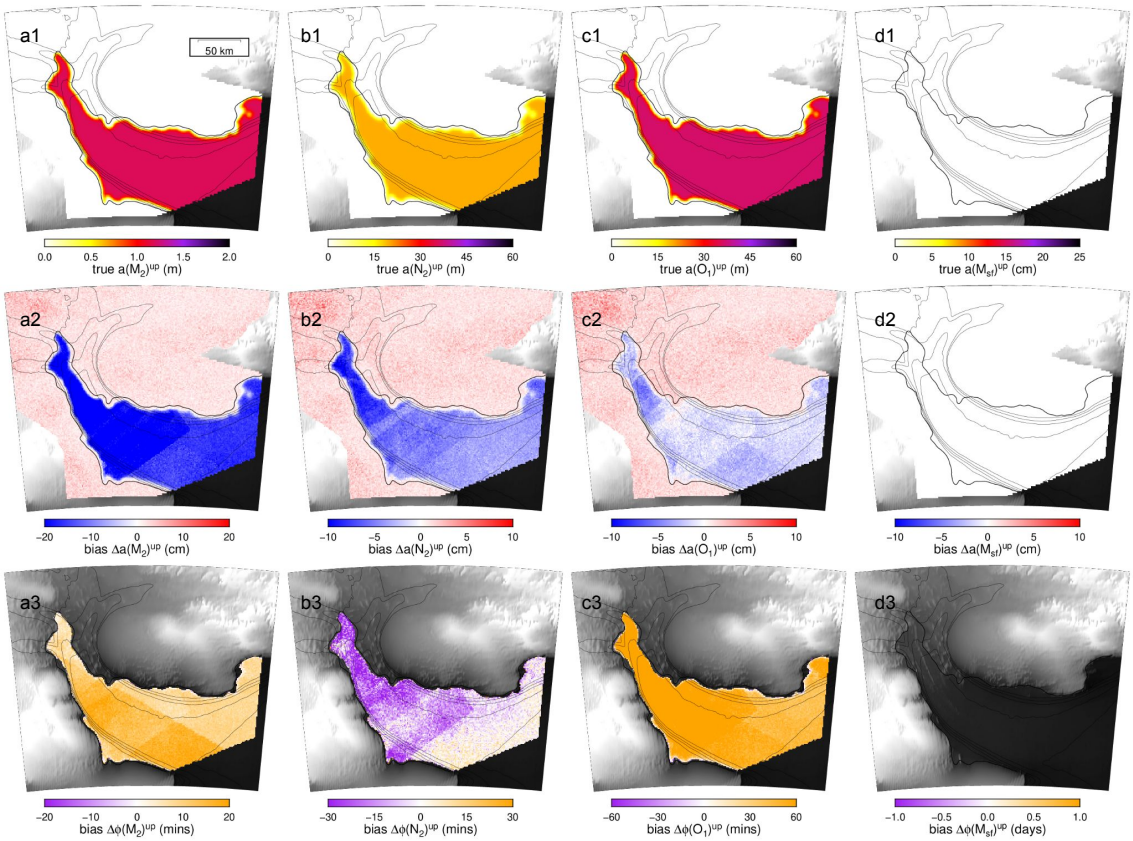

Figure S4.16: Input and the bias of estimated vertical displacement using the linear model with ephemeral grounding but without vertical M_{sf} in the model. The layout of panels is the same as Figure S4.12.

S4.7.2.4 With ephemeral grounding - with vertical M_{sf}

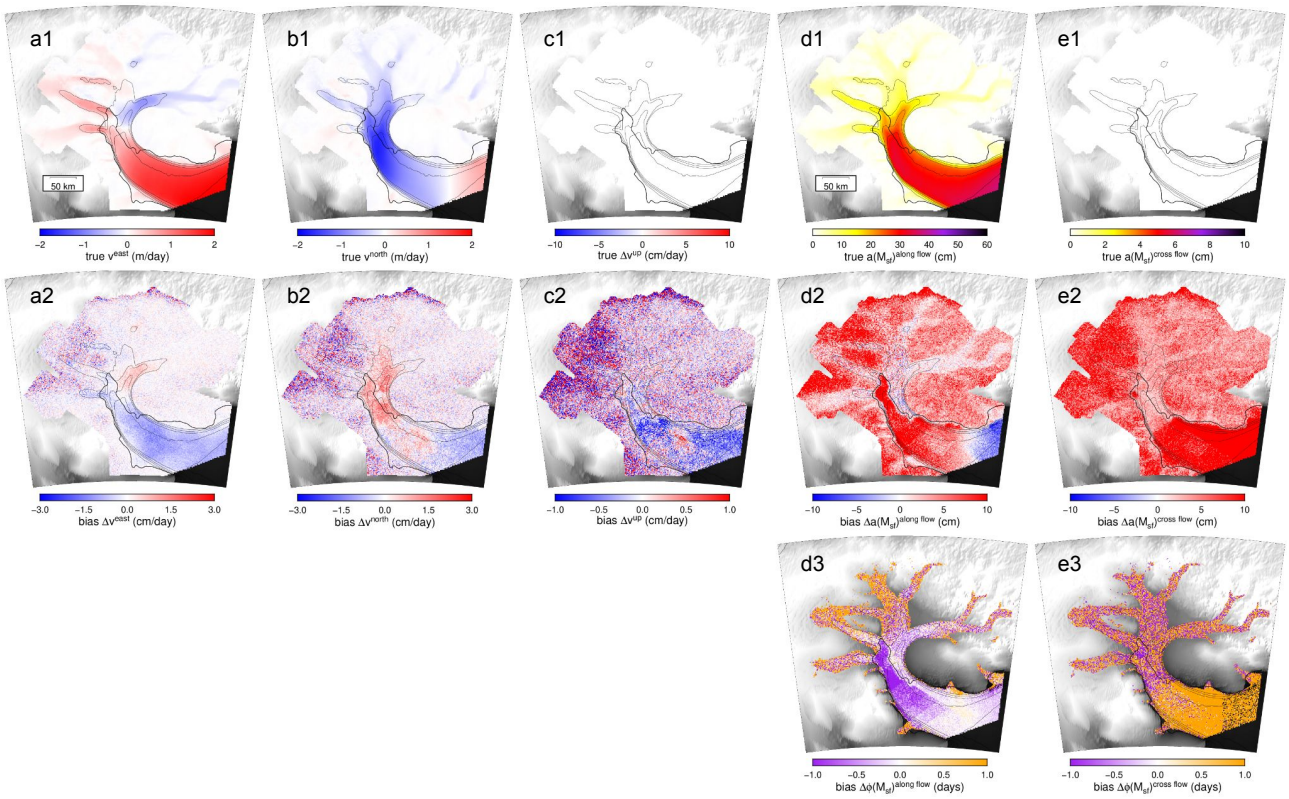

Figure S4.17: Input and the bias of estimated secular and tide-induced M_{sf} displacement using the linear model with ephemeral grounding and vertical M_{sf} in the model. The layout of panels is the same as Figure S4.11.

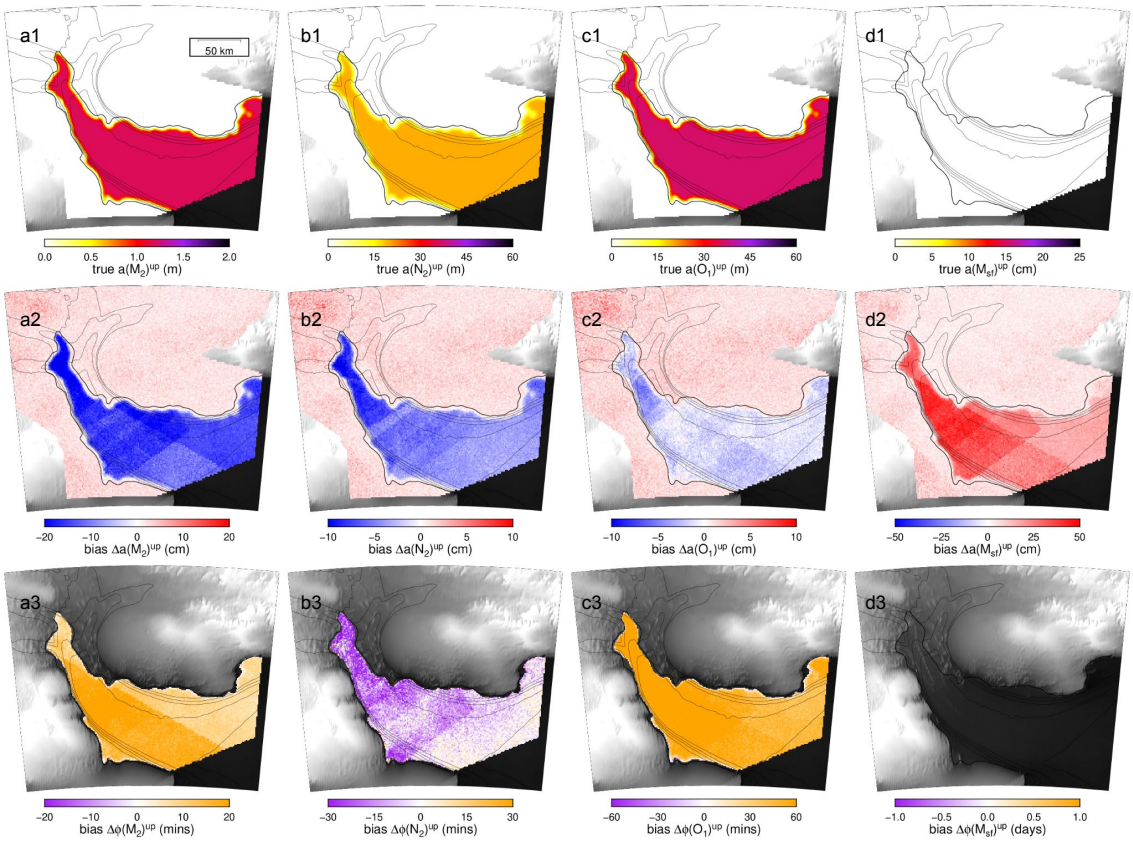

Figure S4.18: Input and the bias of estimated vertical displacement using the linear model with ephemeral grounding and vertical M_{sf} in the model. The layout of panels is the same as Figure S4.12.

S4.7.3 Theory of the Nonlinear Vertical Displacement Model

Please refer to Chapter 3, section 3.4.1.

S4.7.4 A Necessary Condition for Constraining Ephemeral Grounding Level

Please refer to Chapter 3, section 3.4.3.

S4.7.5 Synthetic Tests of the Nonlinear Model

The synthetic data is the same as in section S4.7.2 with the level of ephemeral grounding at $-0.5\,\mathrm{m}$. Our optimal strategy for solving the inverse problem is as follows:

1. Discretize K' in the tidal range $[-3.0\,\mathrm{m}, 3.0\,\mathrm{m}]$ starting with spacing $10\,\mathrm{cm}$, and iteratively refine the spacing around the optimum down to $1\,\mathrm{cm}$. Resolution at $1\,\mathrm{cm}$ is significantly smaller than the intrinsic uncertainty in K'.

2. Calculate the approximate marginal posterior probability distribution of K' from enumerated $P(K'|\mathbf{d})$, and find the 68% credible interval of around the optimum.

3. Consider the ephemeral grounding as well-constrained if the necessary condition (supporting information S4.7.4) is satisfied and the 68% credible interval of K' is smaller than the prescribed threshold $60\,\mathrm{cm}$.

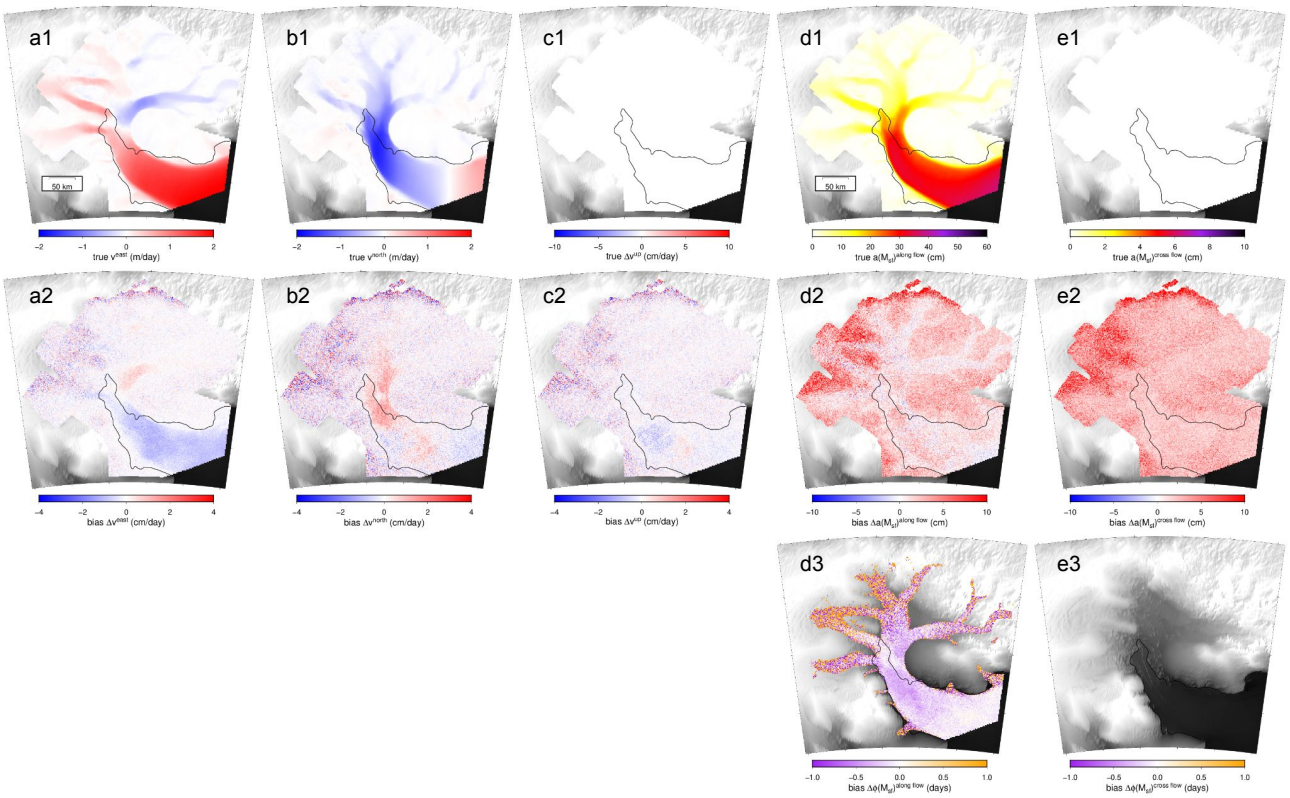

Figure S4.19: Input and the bias of estimated secular and tide-induced M_{sf} displacement using the nonlinear model with ephemeral grounding. (a1-c1) Input secular horizontal and vertical velocity. (d1-e1) Input amplitude of horizontal sinusoidal displacements at M_{sf} period. Input phases of all sinusoidal displacement are spatially constant and are not shown. The bias of estimation is defined as the inferred value minus the input value. (a2-c2) Bias of estimated secular velocity. (d2-f2) Bias of estimated amplitude of vertical sinusoidal displacements. (d3-e3) Bias of estimated phase of horizontal sinusoidal displacement. Phase estimates which correspond to small amplitude estimates and large uncertainties are not shown.

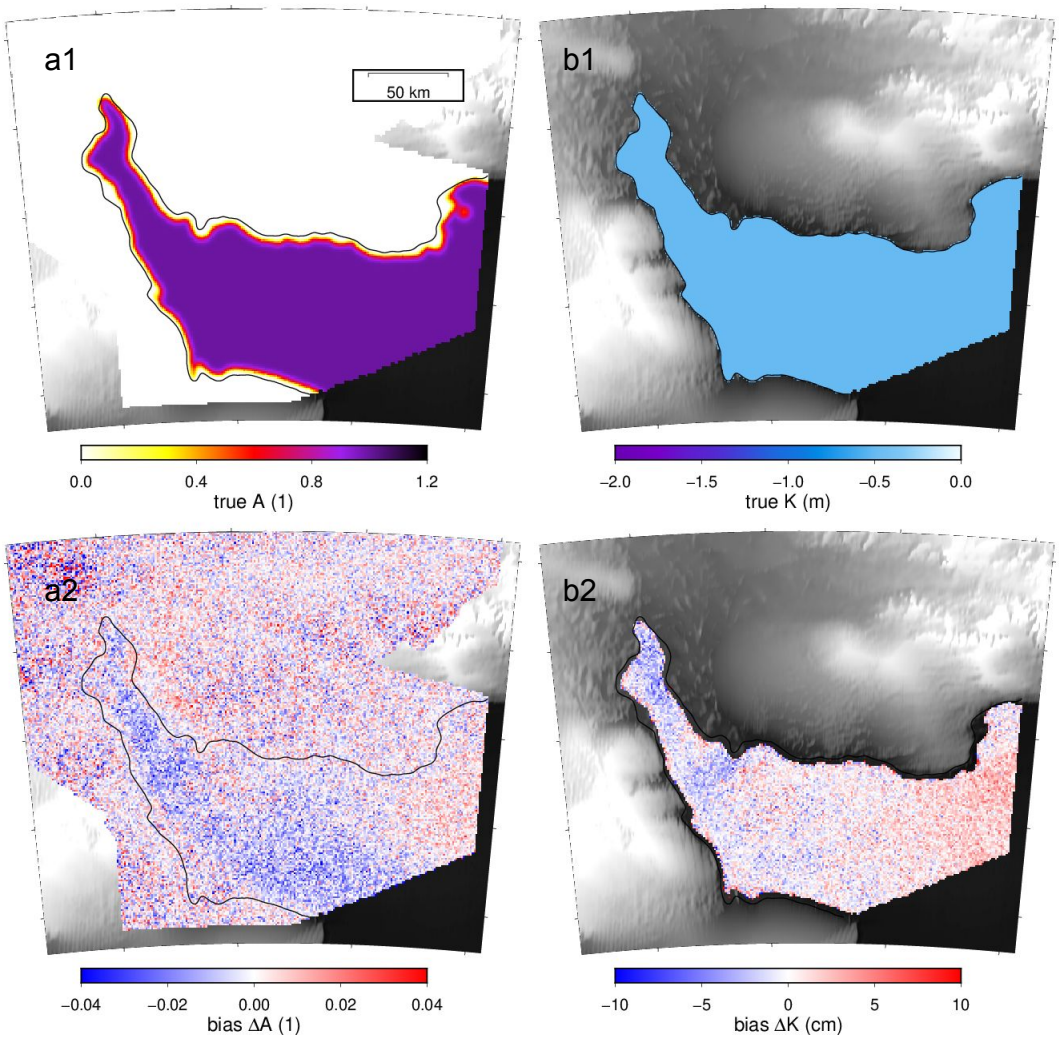

Figure S4.20: Input and the bias of estimated vertical displacement using the non-linear model. (a1-b1) Input amplitude scaling and the level of ephemeral grounding. (a2-d2) Bias of inferred amplitude scaling and the level of ephemeral grounding.

S4.7.6 The Calculation of Error Model

With the assumption of Gaussian distribution for all uncertainties, we have the following relationship:

$$\mathbf{C}_\chi = \mathbf{C}_d + \mathbf{C}_p \tag{S4.16}$$

where $\mathbf{C}_d$ is the covariance matrix for measurement error and $\mathbf{C}_p$ is the covariance matrix for modeling error, which is also referred to as prediction error.

We assume the error to be independent (i.e. $\mathbf{C}_\chi$ is diagonal) and calculate $\mathbf{C}_\chi$ using residual analysis which is discussed in Chapter 3. We employ the following approach for inversion at EIS:

1. Assuming 20 cm error for all displacement data along LOS direction and 60 cm error for all displacement data along azimuth direction, conduct the first inversion and find the residual of each data point.

2. For the data on the same grid point, group the data points according to the observational unit, which is determined by track and LOS/azimuth measurement. Assuming data in the same group share the error model, calculate the error for each group using the residual from the initial inversion. The diagonal entries of $\hat{\mathbf{C}}_\chi$ are the variances of the residual in the corresponding groups.

3. Conduct the second inversion using the empirically estimated error model $\hat{\mathbf{C}}_\chi$.

S4.7.7 Inferred Secular Velocity and Fortnightly Flow Variability from the Linear Model

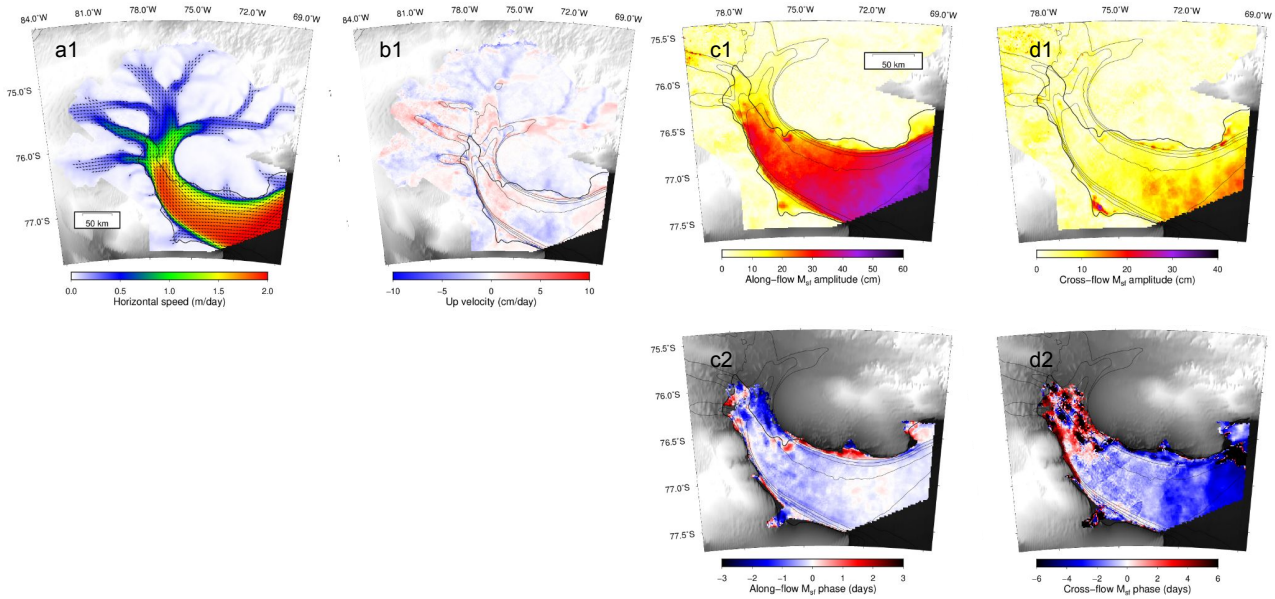

Figure S4.21: (a1) Horizontal velocity where the color indicates speed and arrows show flow direction. (b1) Vertical velocity, where the positive values indicate moving upward. (c1-d1) The amplitude of horizontal displacement variation at M_{sf} period. (c2-d2) The phase of horizontal displacement variation at M_{sf} period.

S4.7.8 Derived Grounding Line from M_2 Displacement Amplitude

We derive updated grounding line at Evans Ice Stream using the 10 cm contour of M_2 vertical displacement amplitude.

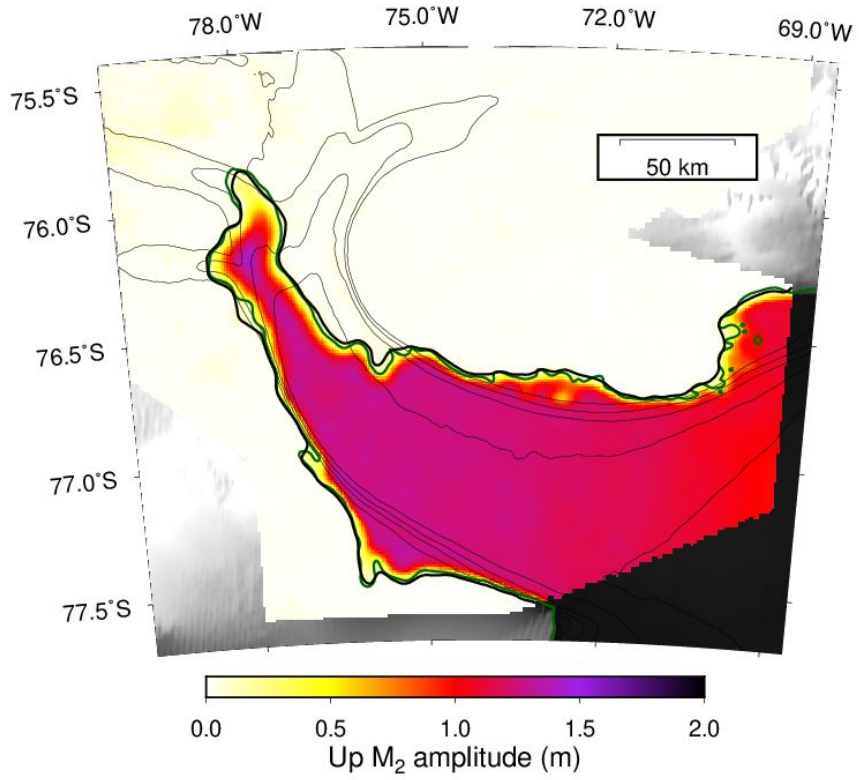

Figure S4.22: Grounding line at Evans Ice Stream. Grounding line derived from M_2 displacement amplitude is in black. Grounding line from Bedmap2 (Fretwell et al., 2013) is in green.

S4.7.9 Construction of the Nonlinear Vertical Displacement Model

We follow the same procedures for deriving relative phase variations and construct a vertical displacement model in our RIS study. Please refer to Chapter 3, section S3.7.7 for details.

The only difference with the RIS study is that we use the relative variation in M_2 phase (Figure S4.23) for all semidiurnal constituents, because the inferred N_2 phase has artifacts.

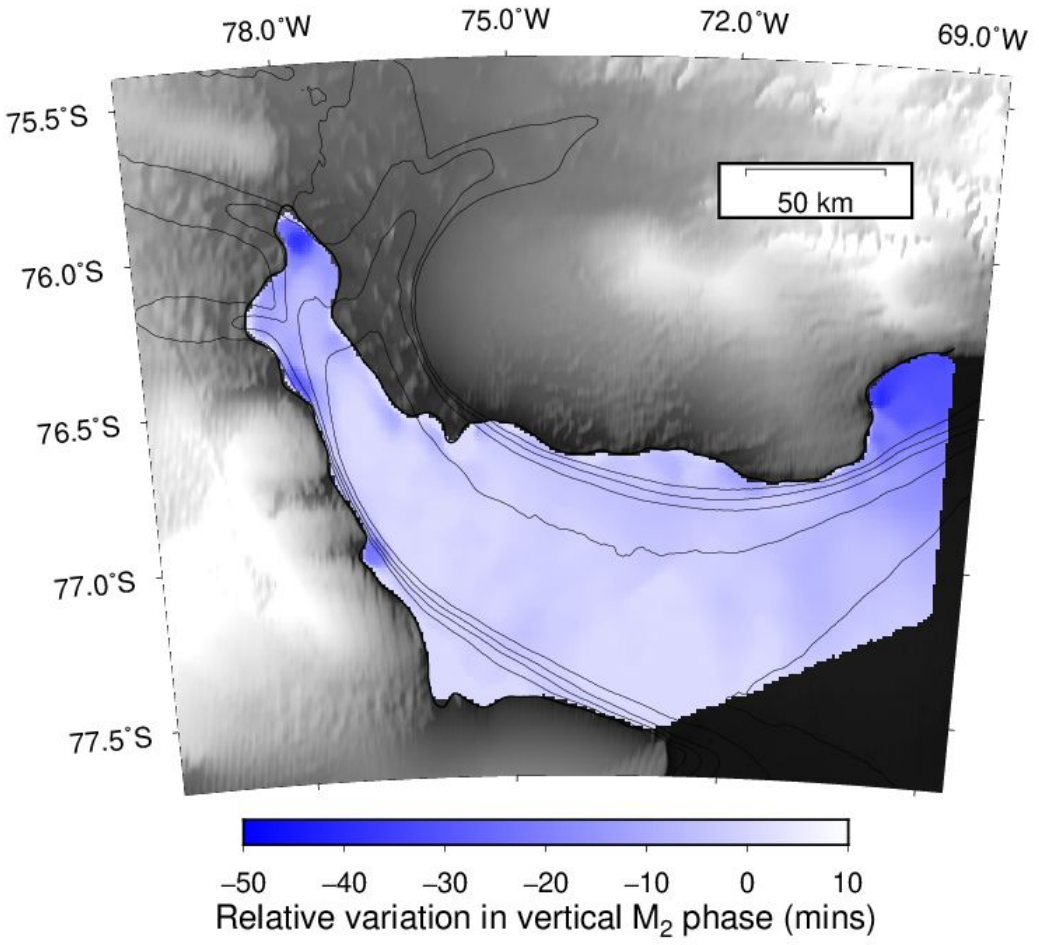

Figure S4.23: Relative variation in M_2 phase at EIS.

S4.7.10 Difference of Inferred Secular Velocity with Reference Secular Velocity

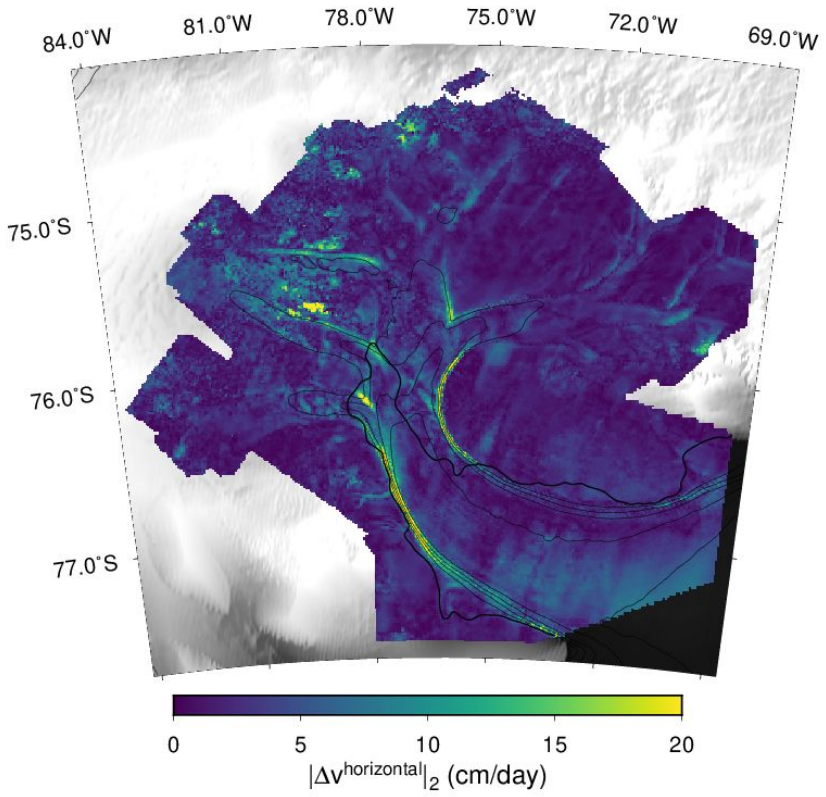

Figure S4.24: Differential map of inferred secular horizontal velocity with reference velocity (Mouginot et al., 2012).

S4.7.11 Discussion of Inferred Vertical Velocity

The east component has relatively small correlations with other components, presumably because it is constrained mostly by the azimuth component of the displacement fields which is free from the influence of vertical displacement. The north and up components sharing the LOS component showing large correlation (> 0.9) between the two components. North and up components are less reliable than the east component. The correlation between north and up components is present in both upstream tributaries and downstream ice shelf. Along the flow over ice shelf, the up component goes from positive to negative, and then positives, which is presumably associated with first the decrease, and then the change from negative to positive of north component.

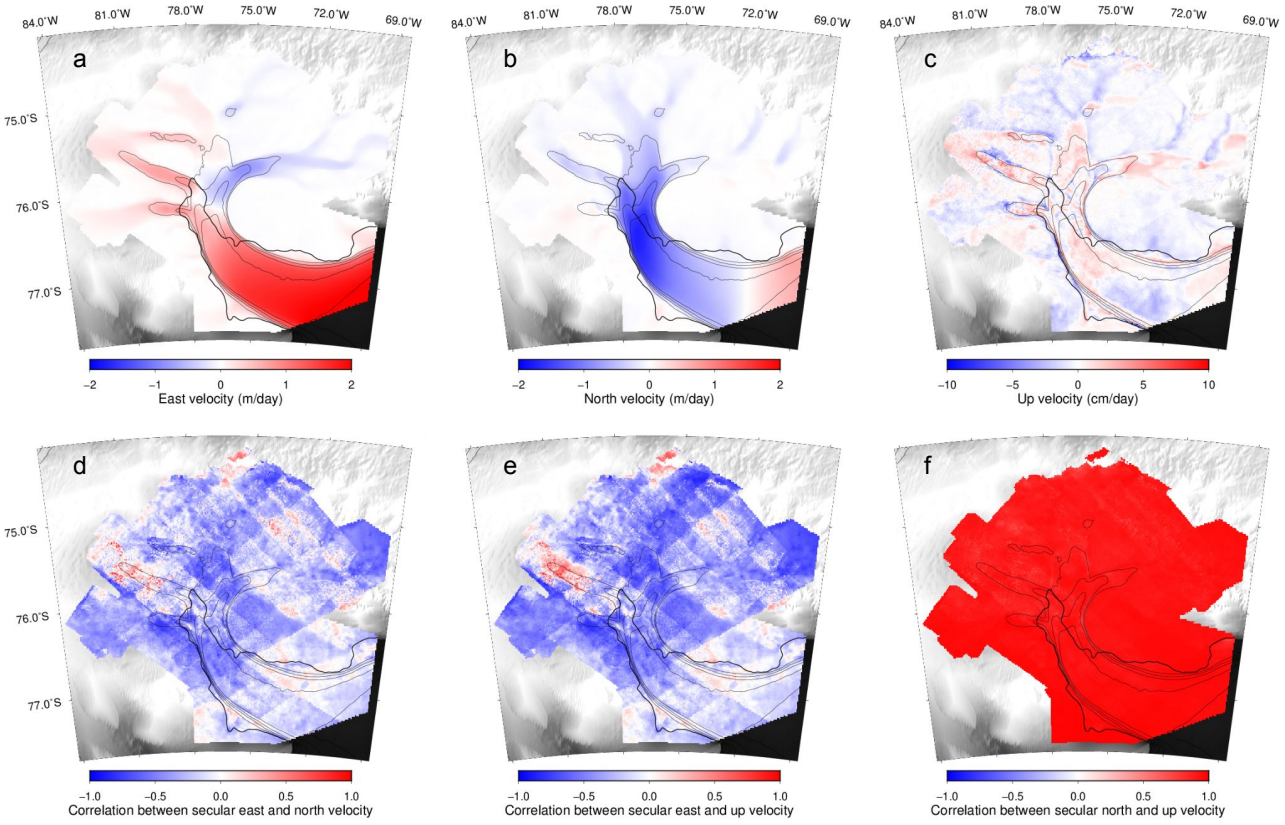

Figure S4.25: (a-c) inferred east, north, and up velocity. (d-f) The correction of east-north, east-up, north-up velocity.

S4.7.12 Sampling of Tide Hights by S1 and CSK Data Acquisitions

In our study, we find that CSK data has better ability to sample low tides at all locations in the domain imaged by CSK. Figure S4.26 is an example showing all the SAR acquisitions and the corresponding tide heights at reference point in Figure 4.1b. All the S1 acquisitions are plotted. Our available CSK acquisitions is a subset of the total archive of CSK acquisitions. When requesting CSK data, we optimized the sampling of low tide. This example shows that CSK acquisitions have better sensitivity to low tides.

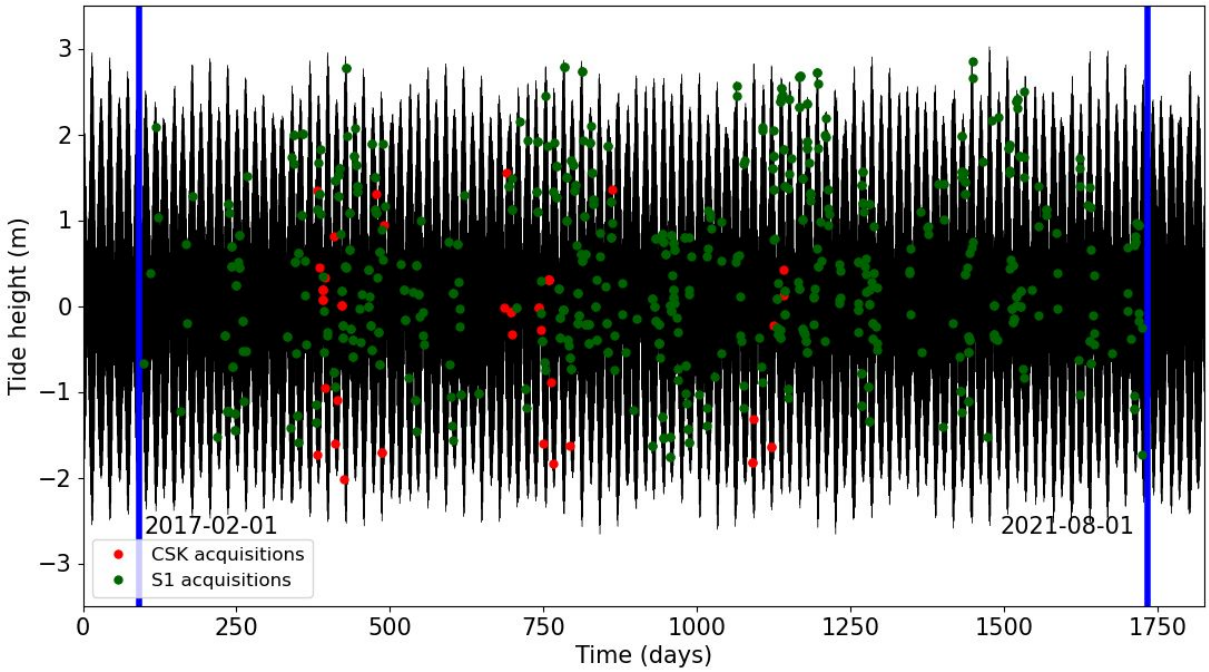

Figure S4.26: The sampling of tide height by CSK and S1 acquisitions.

S4.7.13 Archive and Ordered CSK Data at EIS

The dedicated CSK SAR observational campaign over EIS started in November 2017 has lasted nearly 4 years making more than 5000 acquisitions which corresponds to more than 30000 archive standard frames (40 km × 40 km). The data are acquired from 11 ascending tracks and 11 descending tracks covering the upstream tributaries and 150-km-long ice shelf downstream of the grounding line.

All the acquired CSK data and those data we ordered until July 2021 are shown with the corresponding tide height in Figure S4.28 and S4.29. We find the descending tracks (track 12-22) has higher sensitivity than the ascending tracks (track 1-11). For our study, we ordered and utilized 543 acquisitions (2500 standard frames). To maximize the sensitivity to low tide and ephemeral grounding, most of the ordered data are from descending tracks. The ordered data includes key acquisitions sampling the low tide below −1.6 m and acquisitions neighboring to those key acquisitions with time interval no greater than 8 days.

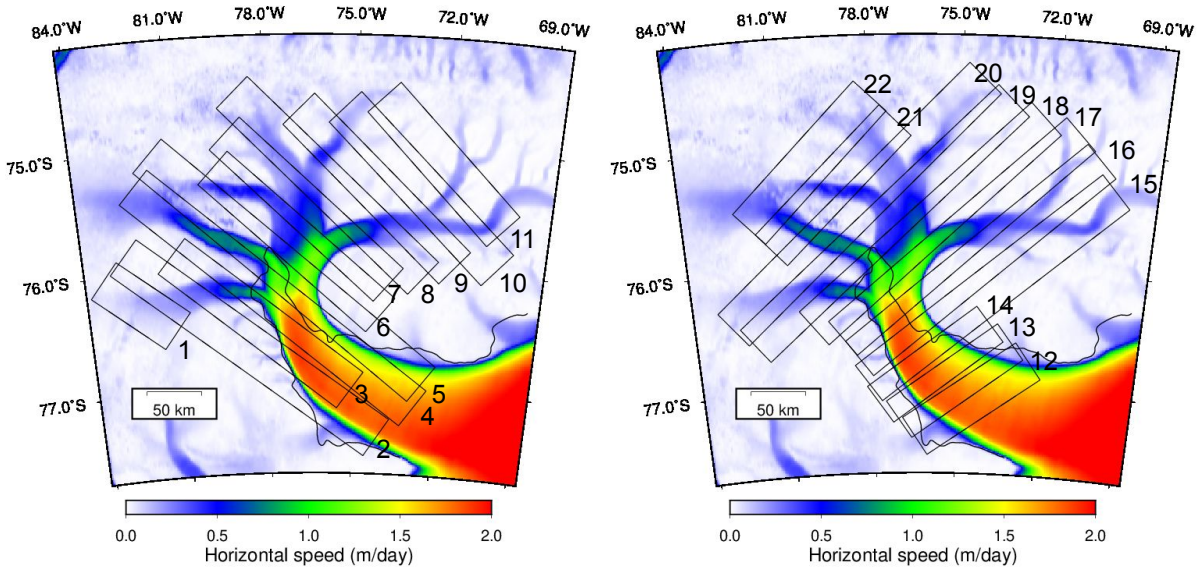

Figure S4.27: Footprints of acquisitions at Evans Ice Stream. (a) Footprints of acquisitions from 11 ascending tracks (1-11). (b) Footprints of acquisitions from 11 descending tracks (12-22).

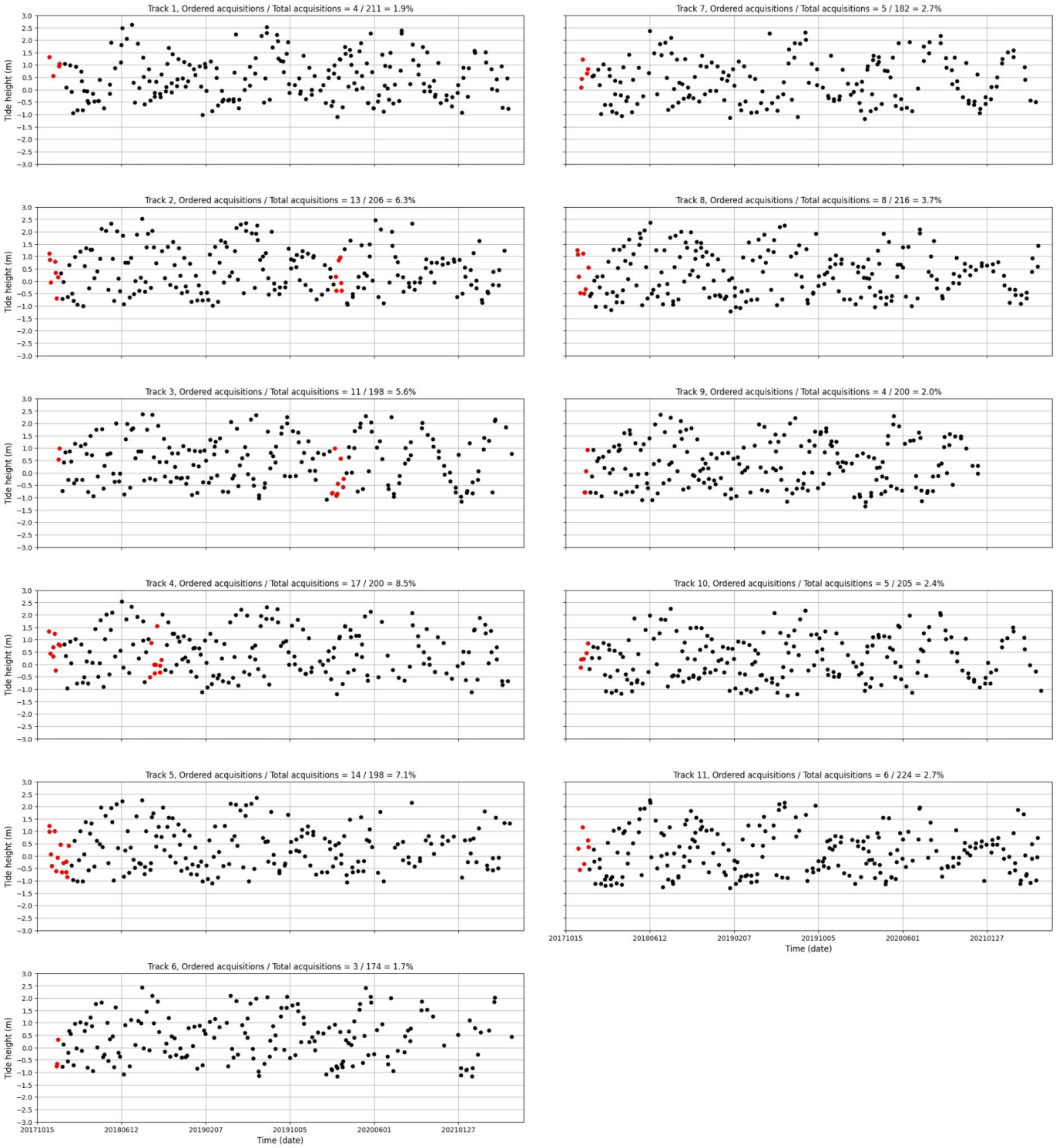

Figure S4.28: Acquisitions from 11 ascending tracks and the corresponding tide heights. Each figure shows acquisitions in one track. Red dots and black dots indicate indicate ordered and unordered acquisitions, respectively. The subtitle of each figure indicates the track number, the number of ordered acquisitions, the total number of acquisitions, and the percent of ordered acquisitions.

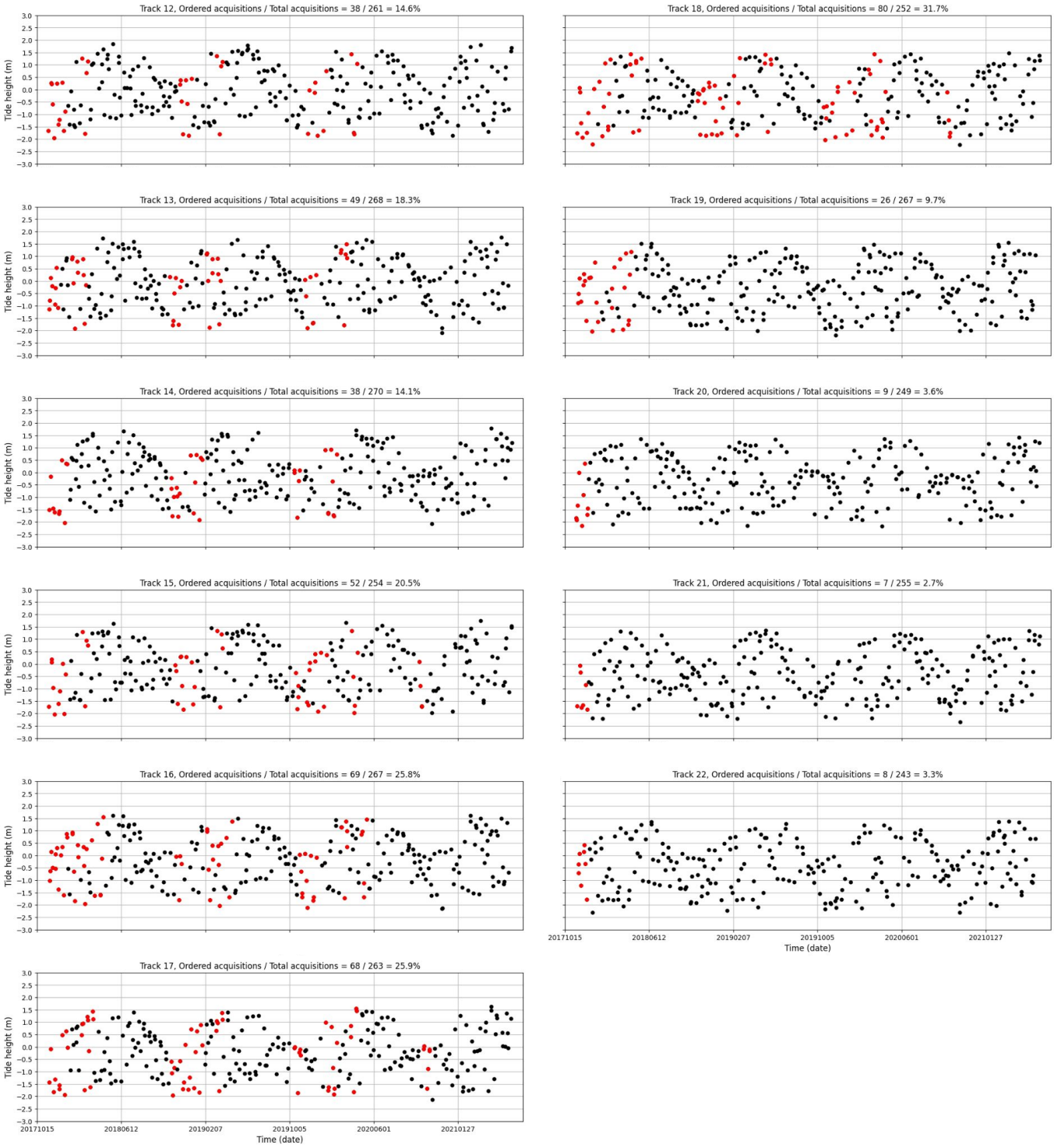

Figure S4.29: Acquisitions from 11 descending tracks and the corresponding tide heights. Each figure shows acquisitions in one track. Red dots and black dots indicate indicate ordered and unordered acquisitions, respectively. The subtitle of each figure indicates the track number, the number of ordered acquisitions, the total number of acquisitions, and the percent of ordered acquisitions.

S4.7.14 Potential Improvement from Utilizing More Archive CSK Data at EIS

Because the spatial and temporal information of archive CSK data can be gathered from the online catalog, we can set up synthetic tests to discuss the potential improvement from adding more archive CSK data into our study. We compare the results from using the currently ordered CSK data and results from using all achieve CSK data. In all tests, all available S1 data are jointly used with CSK data.

S4.7.14.1 Synthetic Tests Using the Linear Model

The synthetic tests are set up in the same way as those in section S4.7.2. For the linear model, we do not introduce ephemeral grounding and focus on the inference of secular velocity and fortnightly flow. Figure S4.30 S4.31 S4.32 and S4.33 show the results from using the ordered CSK data. Figure S4.34 S4.35 S4.36 and S4.37 show the result from using all archive CSK data. Compared with using ordered CSK data only, the accuracy of both secular velocity and fortnightly flow are clearly improved from using the archive CSK data:

1. The ~2 cm/day bias in all three components in secular velocity is reduced to be close to zero.

2. The large correction (~1) between secular north and up velocity is significantly reduced to be ~0.5. Thus, the current artifacts in secular up velocity due to the large correlation between the two components discussed in section S4.7.11 should be reduced with additional data. The well-resolved secular velocity will also open the opportunity for detecting any temporal variation in secular velocity, such as seasonal changes or secular increase/decrease in flow rate.

3. The 5 cm bias in the amplitude of fortnightly flow is reduced be to less than 1 cm. The bias in the phase of fortnightly flow which can be up to 0.5 day is reduced to be less than 0.2 day.

4. The bias in the amplitude of vertical M_2, N_2 and O_1 displacement are reduced from 2 cm to 5 cm to be less than 1 cm. The bias in the phase of vertical displacement of M_2, N_2 and O_1 are reduced from a 5 min to 15 min to be close to 0 min for M_2 and O_1 and 5 min for N_2.

5. The formal error in secular velocity, fortnightly flow and vertical displacement which is independent of data are reduced by more than 50%. (The error should

be approximately scale with $\frac{1}{\sqrt{N}}$, where N is number of data points or SAR acquisitions).

We note that, due to the sparse sampling of displacement fields by SAR acquisitions, large bias can exist from using a small number of SAR acquisitions, for example, the discontinuity between two ascending tracks in the inferred amplitude of the fortnightly flow using only the ordered data (Figure S4.30d2). Using sufficient data, the bias can be significantly reduced (Figure S4.34d2).

S4.7.14.2 Synthetic Tests Using the Nonlinear Model

We also test the nonlinear model to discuss the potential improvement in constraining ephemeral grounding. The synthetic tests are set up in the same way as those in section S4.7.5. We prescribe the ephemeral grounding level at -1.8 m. At this level, S1 data does not have any sensitivity to ephemeral grounding, so the constraint on ephemeral grounding is completely from CSK data. We perform experiments comparing results from ordered and archive CSK data at two patches centered at two points. One point is in the northern horn of the grounding line and the other point is in the central trunk of the ice shelf (Figure S4.38). Figure S4.39 S4.40 show results at the two patches respectively. The additional CSK data improves the constraint to ephemeral grounding resulting in smaller credible interval size and much more resolved ephemeral grounding points.

Because we have ordered a large number of acquisitions sampling low tide from descending tracks (Figure S4.29), we expect that the major zones of ephemeral grounding are already detected in the current result (Figure S4.20). The additional CSK will help reduce the uncertainty in estimation (i.e., the size of credible interval) leading to more resolved ephemeral grounding points, especially at low grounding level. The better resolved zones of ephemeral grounding along the ice shelf margins will be wider than the currently resolved zones.

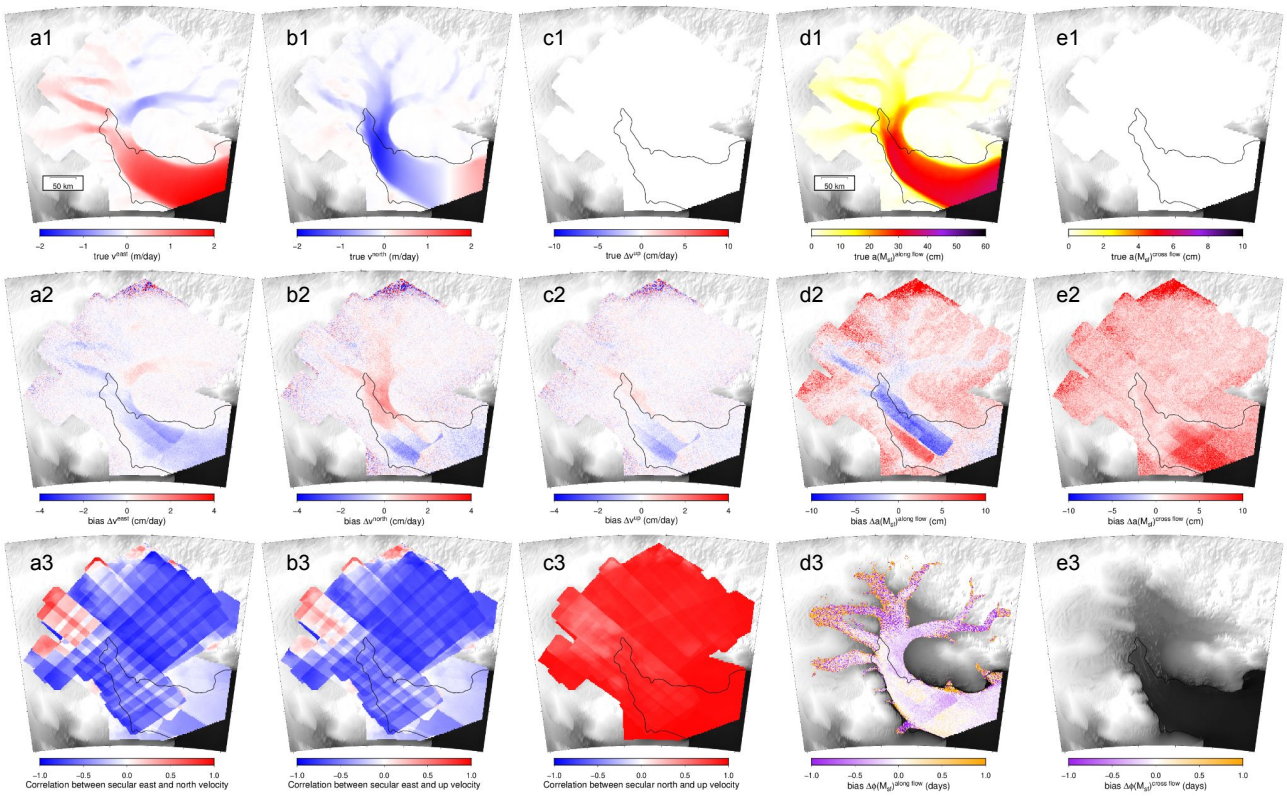

Figure S4.30: Input and the bias of estimated secular velocity and tide-induced M_{sf} displacement from the linear model using the ordered data. (a1-c1) Input secular horizontal and vertical velocity. (d1-e1) Input amplitude of horizontal sinusoidal displacement at M_{sf} period. Input phases of all sinusoidal displacement are spatially constant and are not shown. The bias of estimation is defined as the inferred value minus the input value. (a2-c2) Bias of estimated secular velocity. (d2-f2) Bias of estimated amplitude of vertical sinusoidal displacements. (a3-c3) The correlation between inferred secular east, north and up velocity. (d3-e3) Bias of estimated of phase of horizontal sinusoidal displacement. Phase estimates at where amplitude is small has large uncertainty and are not shown. The input M_{sf} cross-flow displacement has zero amplitude, so the input phase the bias of phase estimates are not available.

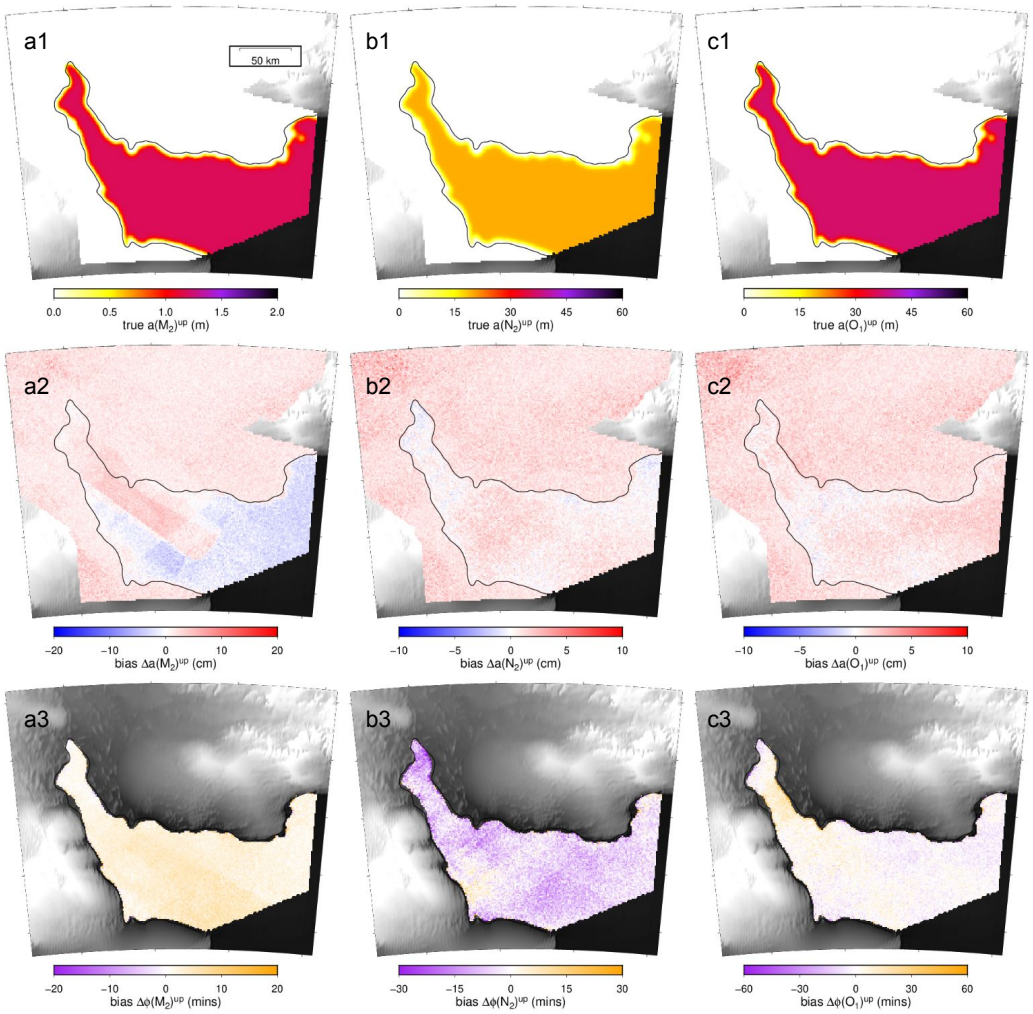

Figure S4.31: Input and the bias of estimated vertical displacement from the linear model using the ordered data. (a1-d1) Input amplitude of vertical displacement at M_2, N_2, O_1, and M_{sf} periods. (a2-d2) Bias of inferred amplitude of vertical displacement at M_2, N_2, O_1, and M_{sf} periods. (a3-d3) Bias of inferred phase of vertical displacement at M_2, N_2, O_1, and M_{sf} periods.

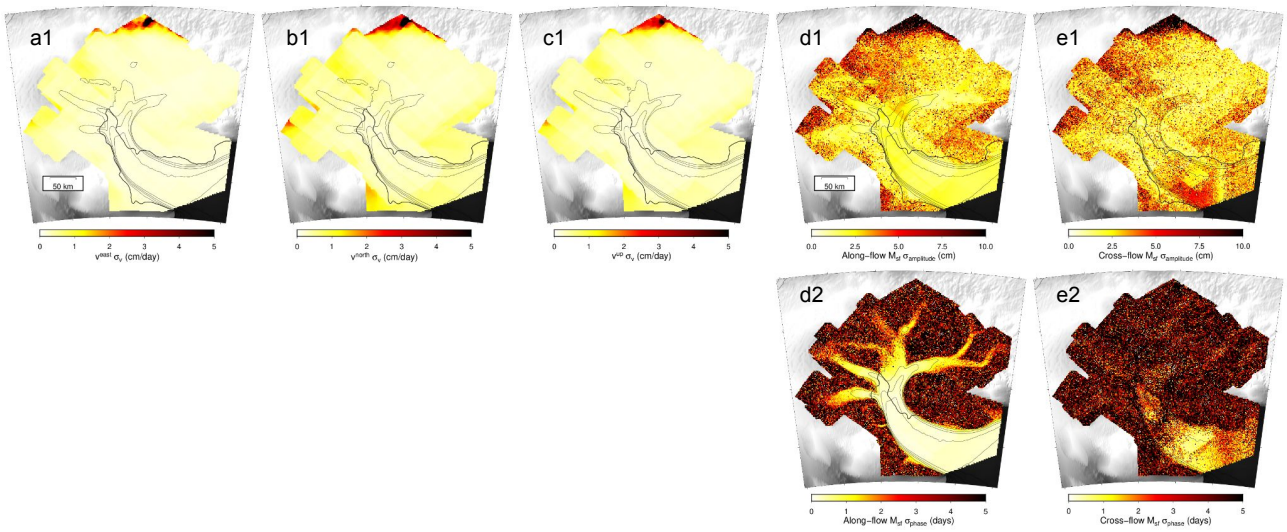

Figure S4.32: Formal error (1-σ) of the inferred secular velocity and fortnightly flow from the linear model using the ordered data.(a1-c1) Error in secular velocity. (d1-e1) Error in along-flow and cross-flow amplitude of fortnightly flow. (d2-e2) Error in along-flow and cross-flow phase of fortnightly flow.

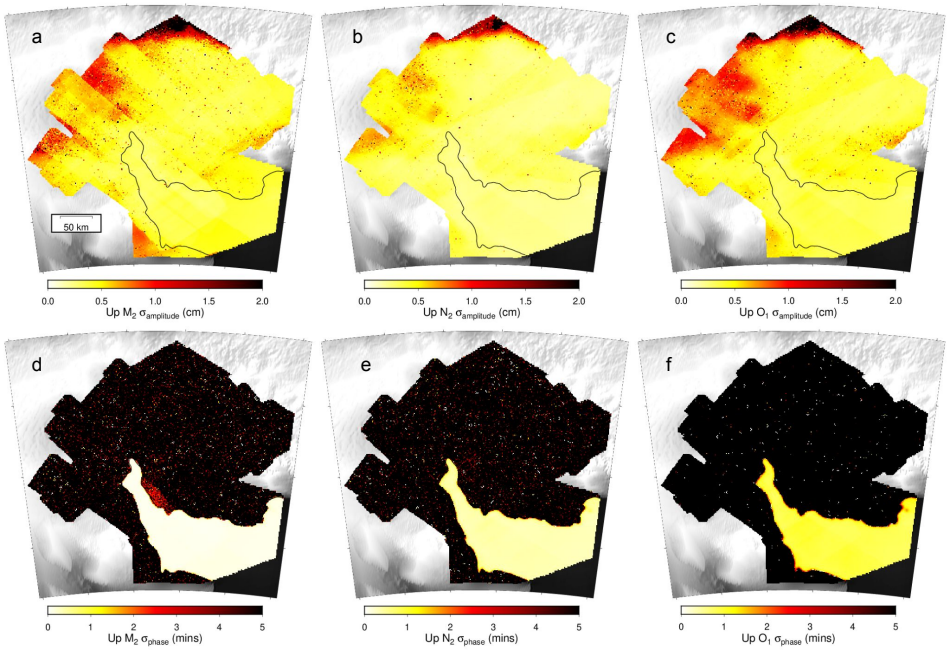

Figure S4.33: Formal error (1-σ) of the inferred vertical displacement from the linear model using the ordered data. (a-c) Error in the amplitude of M_2, N_2 and O_1. (d-f) Error in the phase of M_2, N_2 and O_1.

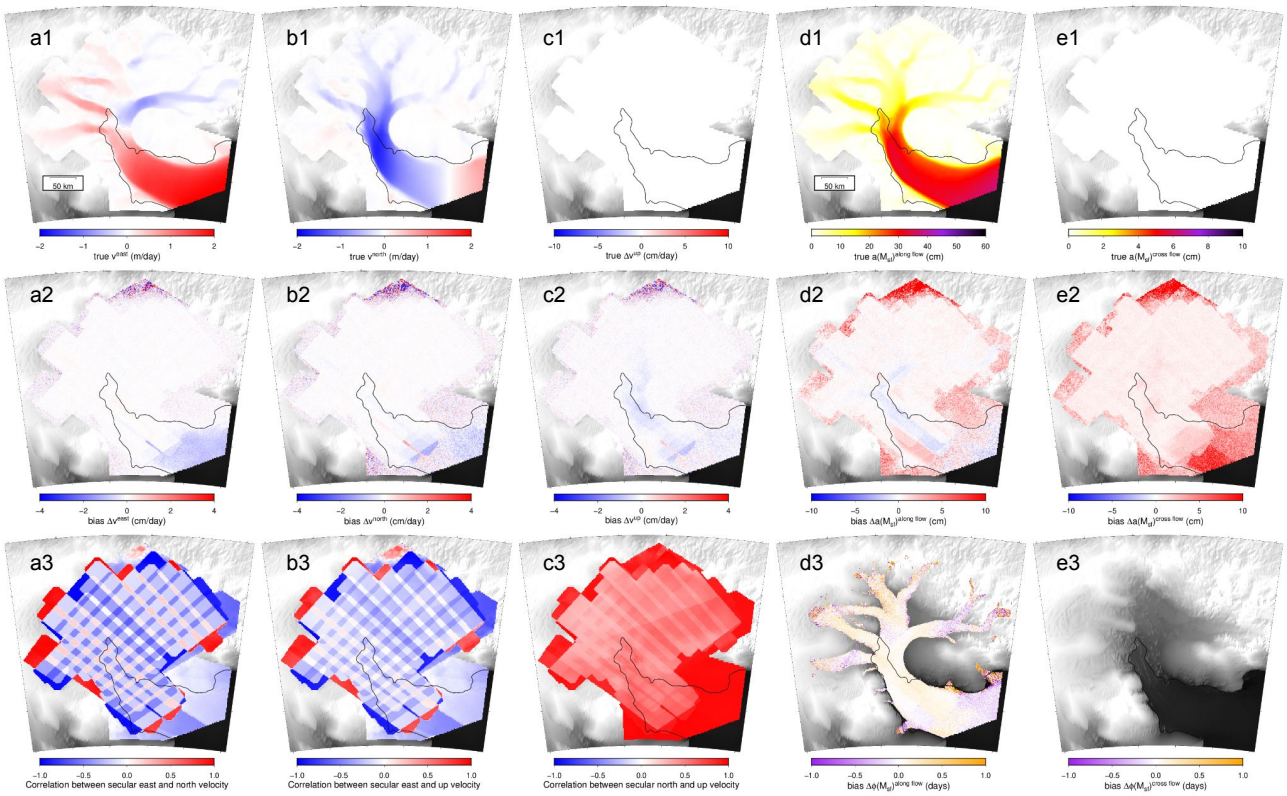

Figure S4.34: Input and the bias of estimated secular velocity and tide-induced M_{sf} displacement from the linear model using the all archive data. (a1-c1) Input secular horizontal and vertical velocity. (d1-e1) Input amplitude of horizontal sinusoidal displacement at M_{sf} period. Input phases of all sinusoidal displacement are spatially constant and are not shown. The bias of estimation is defined as the inferred value minus the input value. (a2-c2) Bias of estimated secular velocity. (d2-f2) Bias of estimated amplitude of vertical sinusoidal displacements. (a3-c3) The correlation between inferred secular east, north and up velocity. (d3-e3) Bias of estimated of phase of horizontal sinusoidal displacement. Phase estimates at where amplitude is small has large uncertainty and are not shown. The input M_{sf} cross-flow displacement has zero amplitude, so the input phase the bias of phase estimates are not available.

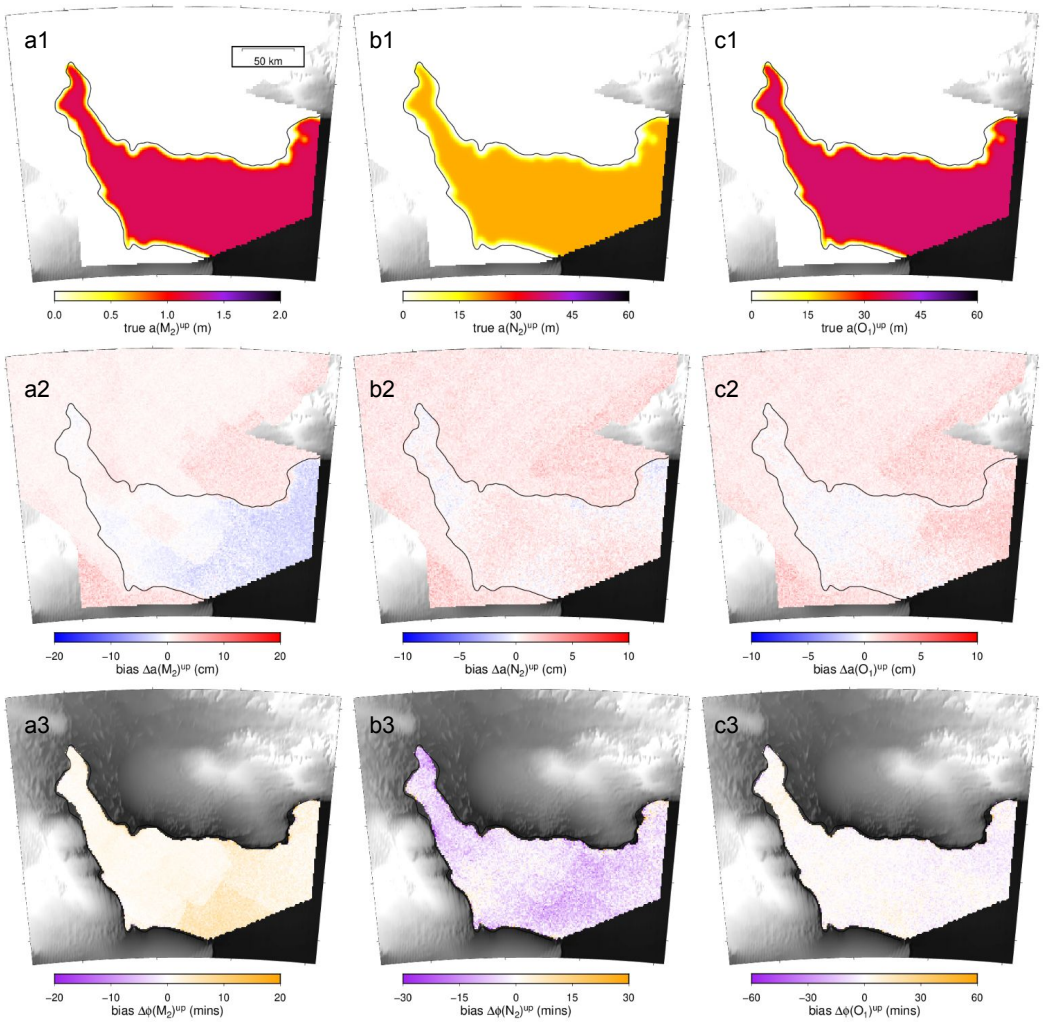

Figure S4.35: Input and the bias of estimated vertical displacement from the linear model using all archive data. (a1-d1) Input amplitude of vertical displacement at M_2, N_2, O_1, and M_{sf} periods. (a2-d2) Bias of inferred amplitude of vertical displacement at M_2, N_2, O_1, and M_{sf} periods. (a3-d3) Bias of inferred phase of vertical displacement at M_2, N_2, O_1, and M_{sf} periods.

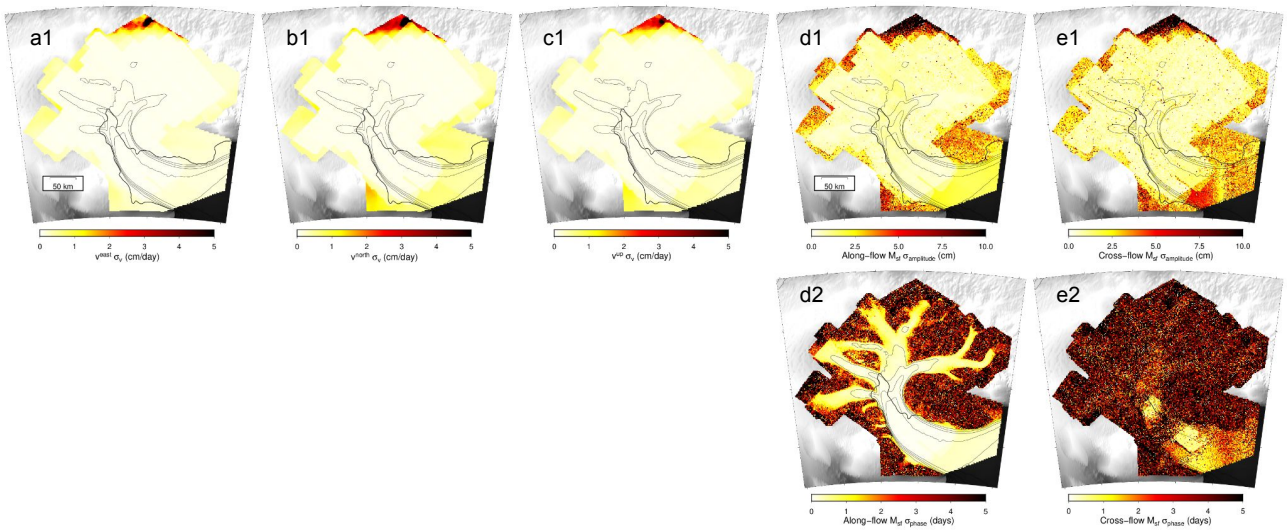

Figure S4.36: Formal error (1-σ) of the inferred secular velocity and fortnightly flow from the linear model using all archive data.(a1-c1) Error in secular velocity. (d1-e1) Error in along-flow and cross-flow amplitude of fortnightly flow. (d2-e2) Error in along-flow and cross-flow phase of fortnightly flow.

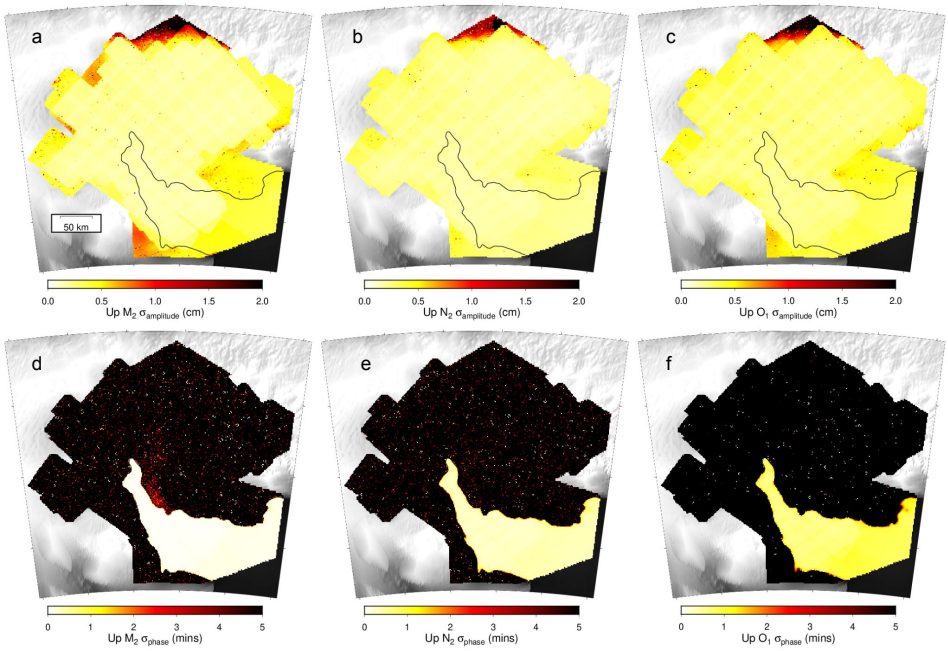

Figure S4.37: Formal error (1-σ) of the inferred vertical displacement from the linear model using all archive data. (a-c) Error in the amplitude of M_2, N_2 and O_1. (d-f) Error in the phase of M_2, N_2 and O_1.

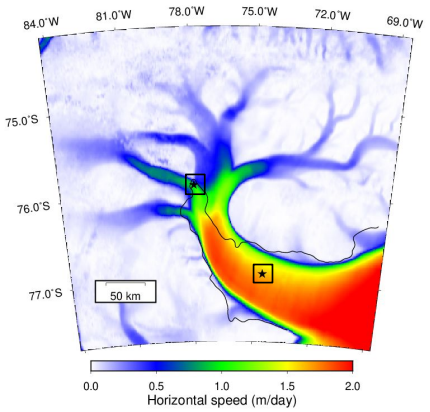

Figure S4.38: The two patches centered at two points in the northern horn of the grounding line and in the central trunk of the ice shelf for synthetic tests.

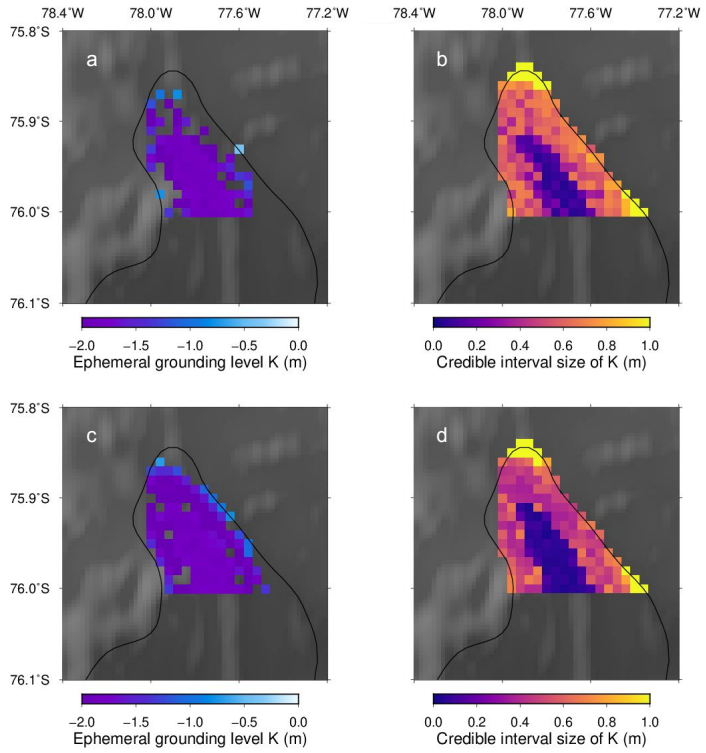

Figure S4.39: The inference of ephemeral grounding at the patch in the northern horn of the grounding line. True ephemeral grounding level is -1.8 m. (a) Inferred ephemeral grounding level from ordered data. (b) The size of 68% credible interval of ephemeral grounding level constrained by the ordered data. (c) Inferred ephemeral grounding level from all achieve data. (b) The size of 68% credible interval of ephemeral grounding level constrained by all achieve data.

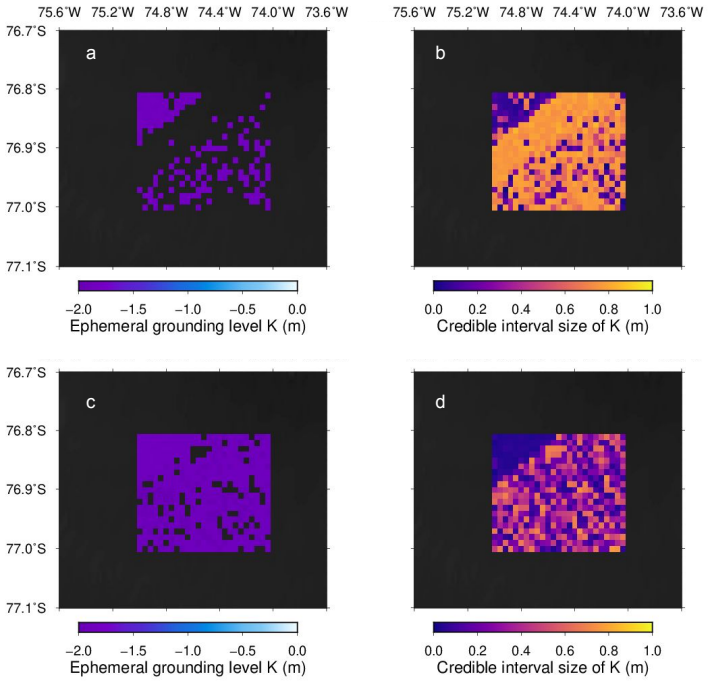

Figure S4.40: The inference of ephemeral grounding at the patch in the central trunk of the ice shelf. True ephemeral grounding level is -1.8 m. (a) Inferred ephemeral grounding level from ordered data. (b) The size of 68% credible interval of ephemeral grounding level constrained by the ordered data. (c) Inferred ephemeral grounding level from all achieve data. (b) The size of 68% credible interval of ephemeral grounding level constrained by all achieve data.

BIBLIOGRAPHY

Bamber, J. L. et al. (2000). Widespread complex flow in the interior of the antarctic ice sheet. In: *Science* 287.5456, pp. 1248–1250. ISSN: 00368075. DOI: 10.1126/science.287.5456.1248.

Bindschadler, R. A. et al. (2003). Tidally driven stick–slip motion in the mouth of Whillans Ice Stream, Antarctica. In: *Annals of Glaciology* 36, pp. 263–272. ISSN: 0260-3055. DOI: 10.3189/172756403781816284.

Doake, C. S. M. et al. (2002). Tide-induced lateral movement of Brunt Ice Shelf, Antarctica. In: *Geophysical Research Letters* 29.8, pp. 67–1–67–4. ISSN: 00948276. DOI: 10.1029/2001GL014606.

Fattahi, H. et al. (2017). InSAR time-series estimation of the ionospheric phase delay: An extension of the split range-spectrum technique. In: *IEEE Transactions on Geoscience and Remote Sensing* 55.10, pp. 5984–5996. ISSN: 0196-2892. DOI: 10.1109/TGRS.2017.2718566.

Fretwell, P. et al. (2013). Bedmap2: improved ice bed, surface and thickness datasets for Antarctica. In: *The Cryosphere* 7.1, pp. 375–393. ISSN: 1994-0424. DOI: 10.5194/tc-7-375-2013.

Gardner, A. S. et al. (2018). Increased West Antarctic and unchanged East Antarctic ice discharge over the last 7 years. In: *Cryosphere* 12.2, pp. 521–547. ISSN: 19940424. DOI: 10.5194/tc-12-521-2018.

Gudmundsson, G. H. (2006). Fortnightly variations in the flow velocity of Rutford Ice Stream, West Antarctica. In: *Nature* 444.7122, pp. 1063–1064. ISSN: 0028-0836. DOI: 10.1038/nature05430.

Gudmundsson, G. H. (2007). Tides and the flow of Rutford Ice Stream, West Antarctica. In: *Journal of Geophysical Research* 112.F4, F04007. ISSN: 0148-0227. DOI: 10.1029/2006JF000731.

Hellmer, H. H. et al. (2012). *Twenty-first-century warming of a large Antarctic ice-shelf cavity by a redirected coastal current*. DOI: 10.1038/nature11064.

Joughin, I. (2002). Ice-sheet velocity mapping: A combined interferometric and speckle-tracking approach. In: *Annals of Glaciology* 34, pp. 195–201. ISSN: 02603055. DOI: 10.3189/172756402781817978.

Joughin, I. and J. L. Bamber (2005). Thickening of the ice stream catchments feeding the Filchner-Ronne Ice Shelf, Antarctica. In: *Geophysical Research Letters* 32.17, pp. 1–4. ISSN: 00948276. DOI: 10.1029/2005GL023844.

Joughin, I. et al. (2006). Integrating satellite observations with modelling: Basal shear stress of the Filcher-Ronne ice streams, Antarctica. In: *Philosophical Transactions of the Royal Society A: Mathematical, Physical and Engineering Sciences* 364.1844, pp. 1795–1814. ISSN: 1364503X. DOI: 10.1098/rsta.2006.1799.

Joughin, I. et al. (2014). Marine ice sheet collapse potentially under way for the thwaites glacier basin, West Antarctica. In: *Science* 344.6185, pp. 735–738. ISSN: 10959203. DOI: 10.1126/science.1249055.

Lipovsky, B. P. and E. M. Dunham (2017). Slow-slip events on the Whillans Ice Plain, Antarctica, described using rate-and-state friction as an ice stream sliding law. In: *Journal of Geophysical Research: Earth Surface* 122.4, pp. 973–1003. ISSN: 2169-9003. DOI: 10.1002/2016JF004183.

Matsuoka, K. et al. (2015). *Antarctic ice rises and rumples: Their properties and significance for ice-sheet dynamics and evolution*. DOI: 10.1016/j.earscirev.2015.09.004.

Milillo, P. et al. (2019). Heterogeneous retreat and ice melt of thwaites glacier, West Antarctica. In: *Science Advances* 5.1, eaau3433. ISSN: 23752548. DOI: 10.1126/sciadv.aau3433.

Minchew, B. M. et al. (2017). Tidally induced variations in vertical and horizontal motion on Rutford Ice Stream, West Antarctica, inferred from remotely sensed observations. In: *Journal of Geophysical Research: Earth Surface* 122.1, pp. 167–190. ISSN: 21699003. DOI: 10.1002/2016JF003971.

Morlighem, M. et al. (2020). Deep glacial troughs and stabilizing ridges unveiled beneath the margins of the Antarctic ice sheet. In: *Nature Geoscience* 13.2. ISSN: 17520908. DOI: 10.1038/s41561-019-0510-8.

Mouginot, J. et al. (2012). Mapping of ice motion in Antarctica using synthetic-aperture radar data. In: *Remote Sensing* 4.9, pp. 2753–2767. ISSN: 2072-4292. DOI: 10.3390/rs4092753.

Padman, L. et al. (2002). A new tide model for the Antarctic ice shelves and seas. In: *Annals of Glaciology* 34, pp. 247–254. ISSN: 02603055. DOI: 10.3189/172756402781817752.

Padman, L. et al. (2018). Ocean tide influences on the Antarctic and Greenland Ice Sheets. In: *Reviews of Geophysics* 56.1, pp. 142–184. ISSN: 19449208. DOI: 10.1002/2016RG000546.

Robel, A. A. et al. (2017). "Tidal modulation of ice shelf buttressing stresses". In: *Annals of Glaciology*. Vol. 58. 74. Cambridge University Press, pp. 12–20. DOI: 10.1017/aog.2017.22.

Rosier, S. H. R. et al. (2014). Modeling Antarctic tides in response to ice shelf thinning and retreat. In: *Journal of Geophysical Research: Oceans* 119.1, pp. 87–97. ISSN: 21699275. DOI: 10.1002/2013JC009240.

Rosier, S. H. R. et al. (2017). Strong tidal variations in ice flow observed across the entire Ronne Ice Shelf and adjoining ice streams. In: *Earth System Science Data* 9.2, pp. 849–860. ISSN: 1866-3516. DOI: 10.5194/essd-9-849-2017.

Rosier, S. H. and G. H. Gudmundsson (2020). Exploring mechanisms responsible for tidal modulation in flow of the Filchner-Ronne Ice Shelf. In: *Cryosphere* 14.1, pp. 17–37. ISSN: 19940424. DOI: 10.5194/tc-14-17-2020.

Sutterley, T. C. et al. (2014). Mass loss of the Amundsen Sea Embayment of West Antarctica from four independent techniques. In: *Geophysical Research Letters* 41.23, pp. 8421–8428. ISSN: 0094-8276. DOI: 10.1002/2014GL061940.

Tarantola, A. (2005). *Inverse problem theory and methods for model parameter estimation*. Society for Industrial and Applied Mathematics, p. 342. ISBN: 0898715725.

Thompson, J. et al. (2014). Modeling the elastic transmission of tidal stresses to great distances inland in channelized ice streams. In: *The Cryosphere* 8.6, pp. 2007–2029. ISSN: 1994-0424. DOI: 10.5194/tc-8-2007-2014.

Vaughan, D. G. et al. (2003). Acoustic impedance and basal shear stress beneath four Antarctic ice streams. In: *Annals of Glaciology* 36, pp. 225–232. ISSN: 02603055. DOI: 10.3189/172756403781816437.

Warburton, K. L. P. et al. (2020). Tidal grounding-line migration modulated by subglacial hydrology. In: *Geophysical Research Letters* 47.17, e2020GL089088. ISSN: 0094-8276. DOI: 10.1029/2020GL089088.

Wiens, D. A. et al. (2008). Simultaneous teleseismic and geodetic observations of the stick-slip motion of an Antarctic ice stream. In: *Nature* 453.7196, pp. 770–774. ISSN: 14764687. DOI: 10.1038/nature06990.

Chapter 5

CLOSING THOUGHTS

1. *On the application of array-based receiver function estimation*

I present one application of imaging sedimentary structures in the Oklahoma basin in this thesis, and have also applied the array-based RF estimation to several more seismic dense-array datasets. Some of those experiments produce promising results, exhibiting coherent phases that are contaminated in RFs estimated from traditional methods. But some experiments still show suspicious artifacts. Below are some of my thoughts on the applications of this method as well as possible future work.

The coherency of RFs at neighboring stations and the data error model (i.e., Gaussian distribution estimated from pre-event noise) are two main assumptions of our methodology. When these assumptions are severely violated, the artifacts in RFs may be augmented and spurious coherent phases may be introduced from array-based RF estimation. For example, we can consider the situation where the data error in the seismic waveforms at one station is significant. When estimating RFs using conventional RF practices, only RF at this single station is problematic. However, when estimating in the array-based manner, multiple RFs at neighboring stations are affected. It is possible that spurious coherent phases will appear.

The two main assumptions of our methodology correspond to two common situations where array-based RF estimation does not perform well: (1) The spacing of the station is not dense enough to satisfy the assumption of RF coherency. (2) The error model is not realistic enough which typically underestimates the actual error.

In my experiences (1) examining whether the assumption of RF coherency is well satisfied and (2) performing well quality control on data with focus on waveform coherency are two usually necessary steps before applying the method. In addition, an RF phase of high-fidelity should be able to improve fitting to multiple seismic waveforms within the subarray. This criterion can be used to identify spurious phases caused by problems in data.

Because of our assumption of RF coherency (i.e., constant slowness, same amplitude within a subarray) is simple, we cannot neglect the bias in estimated RFs. A common question people may have when using the methodology is: whether the

obtained phases are spurious/shifted due to extrapolation caused by the enforced RF coherency. I think a suite of synthetic tests quantifying the bias in estimation in different scenarios, for example, a step change in the horizontal discontinuity, will be a helpful complement to the methodology. These synthetic tests, which are essentially quantifying the model (prediction) error, will also benefit the development of more realistic error models.

2. *On parameter estimation of displacement models for SAR observations*

Reconstructing surface displacement/deformation using SAR observations involves inversion of displacement model at a large number (e.g., tens of thousands to millions) of grid points defined at surface. Displacement models for SAR observations are typically linear, thus, solving the inverse problems which have closed-form solutions at all grid points is computationally tractable.

In our study to identify zones of ephemeral grounding beneath ice shelves, we need to infer the clipping level of a time series, which requires us to adopt a nonlinear displacement model. Nonlinear inverse problems do not have closed-form solutions. Solving Bayesian nonlinear inverse problems often requires sampling of the posterior probability distributions using Monte Carlo methods. Naive application of Monte Carlo methods on all grid points is computationally very expensive and far from being tractable on our computational architecture.

I address this issue by linearizing the inverse problem through adopting an alternative form of the model and discretizing one nonlinear parameter. This strategy has implications for solving similar problems in the future. However, it is not a general approach. Our study, which should be one of the earliest ones adopting a nonlinear displacement models for SAR observations, indicates the paucity of the available computational methodologies and tools for such problems.

With the rapid increase in the availability of SAR observations, inferring time-dependent complex surface displacement/deformation will become possible in the future, and adopting more complex (e.g., nonlinear) displacement models will be necessary. How to efficiently solve millions of similar small-scale inverse problems may be an important problem we need to work on in the future.

3. *On the observed ice-shelf ephemeral grounding and fortnightly flow variability*

Our study reveals large amounts of undocumented areas of ephemeral grounding at Rutford Ice Stream (RIS) and Evans Ice Stream (EIS) which can play a key role in generating the observed fortnightly flow. Given that the fortnightly flow variabil-

ity is present over the entire Filchner-Ronne Ice Shelf (FRIS) System, ephemeral grounding is likely to exist at many other tributary ice streams as well as the margin of the main trunk of FRIS. The prevalent existence of ephemeral grounding also suggests that the potential decrease in buttressing stress due to ice shelf thinning may induce significant increase in ice flow rate. Follow-up modeling work on estimating the basal traction provided by the areas of ephemeral grounding and understanding the mechanical controls of the observed ephemeral grounding on the ice flows in general are important. The employed mechanical model for modeling should adopt realistic short-time ice rheology and utilizing the bathymetry inferred at areas of ephemeral grounding. Pinning points and ice-shelf buttressing stress are critical for making realistic projection of the response of ice-sheet to changes in climate. Ephemeral grounding, which has not been systematically observed before, may be ubiquitous over Antarctic Ice Sheet playing an important role in ice-shelf buttress effect and should be an important component in the future ice-sheet models.

Tide-induced ephemeral grounding and asymmetric migration of grounding line are two most promising underlying mechanisms proposed so far that can give rise to the asymmetric response of ice flows to tidal forcing leading to fortnightly flow variability. These two mechanisms can coexist, and further work on evaluating the individual importance of the two, is needed. Asymmetric migration of grounding line is difficult to observe from remotely sensed observations, because it is likely to be associated with processes in subglacial hydrological environments without inducing apparent surface displacement. We may need to rely on in situ experiments monitoring the sub-glacial environments to observe this process.

At RIS, we observe tide-induced periodic divergence and convergence of the horizontal ice flow, which implies that the principal axes of stress of ice are constantly rotating. Because tide-induced variability in flow is common in Antarctic glaciers, the observed cross-flow variability may be a common process of Antarctic ice flows which was not observed or discussed. The widely used rheology of ice, such as Glen's Law, are based on experiments without considering the constant temporal change in the principal axes of stress. Our observation may indicate an important aspect to consider in developing more realistic rheological models for Antarctic ice flows.